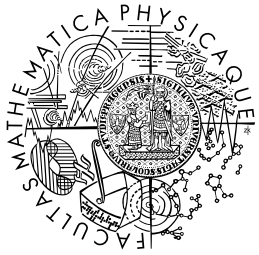

FACULTY
OF MATHEMATICS
AND PHYSICS
Charles University

DOCTORAL THESIS

Roman Fiala

Investigation of new catalysts for polymer membrane fuel cells

Department of Surface and Plasma Science

Supervisor of the doctoral thesis:	Prof. RNDr. Vladimír Matolín, DrSc.
Study programme:	Physics
Study branch:	4F5 Physics of Surfaces and Interfaces

Prague 2017

I declare that I carried out this doctoral thesis independently, and only with the cited sources, literature and other professional sources.

I understand that my work relates to the rights and obligations under the Act No. 121/2000 Coll., the Copyright Act, as amended, in particular the fact that the Charles University in Prague has the right to conclude a license agreement on the use of this work as a school work pursuant to Section 60 paragraph 1 of the Copyright Act.

In Prague date 26.9. 2017 signature of the author

Název práce: Studium nových katalyzátorů pro palivové články s polymerní membránou

Autor: Roman Fiala

Katedra: Katedra fyziky povrchů a plazmatu

Vedoucí disertační práce: Prof. RNDr. Vladimír Matolín, DrSc., Katedra fyziky povrchů a plazmatu

Abstrakt:

Palivové články jsou slibným alternativním zdrojem elektrické energie. I přes výrazné zlepšení, které bylo dosaženo výzkumem v posledních desetiletích, technologie ještě není připravena pro široké komerční využití. Katalyzátor palivových článků (FC) by měl být stále zkoumán kvůli skutečnosti, že jediným spolehlivým funkčním katalyzátorem je platina, ušlechtilý a drahý kov, což znemožňuje masové použití této technologie. V této práci je prezentován výzkum platinového katalyzátoru dopovaného oxidem ceričitým a jeho modifikace připravované magnetronovým naprašováním, což je technika fyzikální depozice. Katalyzátor byl studován za použití standardních technik povrchové analýzy (PES, SEM, AFM, XANES) a elektrochemického měření (CV, PEIS). Hlavní část práce popisuje analýzy katalyzátoru přímo v palivových článcích pomocí individuálně navržené testovací stanice. Vzhledem k vysoké hustotě energie (PD) asi 1 W cm^{-2} a podstatně vyššímu specifickému výkonu na gram platiny (SP) 1,6 kW mg^{-1} ve srovnání s komerčním referenčním katalyzátorem Pt-Ru / Pt-C a navíc díky relativně dlouhé stabilitě, byl naprašovaný katalyzátor na bázi oxidu ceričitého dopovaný platinou shledán jako vhodný katalyzátor pro PEM FC. Navíc byla ukázána možná náhrada Pt a CeO_2 jinými prvky. Vedle těchto výsledků byl prezentován návrh automatizované zkušební stanice a delších technických zařízení.

Klíčová slova: vodíkový palivový článek, oxid céru, platina, katalyzátor

Title: Investigation of new catalysts for polymer membrane fuel cells

Author: Roman Fiala

Department: Department of Surface and Plasma Science

Supervisor: Prof. RNDr. Vladimír Matolín, DrSc., Department of Surface and Plasma Science

Abstract:

Fuel cells are a promising alternate power source of electricity. Despite of significant improvement that was reached by research throughout recent decades, the technology is not still ready to large scale commercial use. The catalyst of fuel cell (FC) should be still investigated due to fact that the only reliable functional catalyst is Platinum, a noble and expensive metal, which makes the use of this technology not competitive. In this thesis, investigation of Platinum doped ceria catalyst and its modification prepared by physical technique of deposition which is magnetron sputtering is presented. The catalyst was studied using standard surface analytic techniques (PES, SEM, AFM, XANES) as well as electrochemical measurement (CV, PEIS). The principal part of this thesis reports direct analyses of catalyst in fuel cell using an individually designed fuel cell test station. Considering the high power density (PD) about 1 W cm^{-2} and substantially higher specific power per gram of Platinum (SP) 1.6 kW mg^{-1} in comparison with commercial Pt-Ru/Pt-C reference catalyst and additionally the relatively longtime stability, the sputtered Platinum doped cerium oxide based catalyst was found a suitable catalyst for PEM FC. Moreover, possible substitution of Pt and CeO_2 by other elements was shown. Beside of these results, the designs of automatized test station with more technical developments were presented.

Keywords: proton exchange membrane fuel cell, cerium oxide, platinum, catalyst

Děkuji všem členům kolektivu katedry za přátelský přístup a pomoc během studia a vedoucímu Prof. Vladimírovi Matolínovi za vřelé a odborné vedení. Jmenovitě děkuji Mgr. Michalovi Václavů za pomoc s technickými řešeními a Dr. Jakubovi Drncovi za umožnení NEXAFS experimentů na ESRF.V neposlední řadě bych rád poděkoval také svým rodičům a své přítelkyni za podporu.

Rád bych také poděkoval všem grantům za finanční podporu:

Projekt č. 388711 – Grantová agentury Univerzity Karlovy
Projekt č. 942214 – Grantová agentury Univerzity Karlovy
Projekt č. 13-10396S – Grantová agentury České republiky
Projekt SVV-2010-365307
– Univerzita Karlova, Specifický vysokoškolský výzkum
Projekt č. 0021620834 – Ministerstvo školství a tělovýchovy české republiky
Projekt chipCAT (FP-7-NMP-2012) – Evropské unie

I thank to all the team members of the department for friendliness and help during the study and supervisor Prof. Vladimir Matolín for a kind and professional leadership. I thank Mgr. Michal Václavů for help with technical solutions and Dr. Jakub Drnec for enabling NEXAFS experiments at the ESRF. Last but not least, I would also like to dedicate this thesis to my parents and my girlfriend for support.

I would like to thank to grant agencies for financial support:

Project n. 388711 – Charles University Grant Agency
Project n. 942214 – Charles University Grant Agency
Project n. 13-10396S – Grantová agentury České republiky
Project SVV-2010-365307
– Charles University, Specifický vysokoškolský výzkum
Project n. 0021620834 – Ministry of Education, Youth and Sports of the Czech Republic
Project chipCAT (FP-7-NMP-2012) – European Union

Contents

I Introduction

"Some people like the sci-fi
but scientists make the fiction true."

The human being and our activity have been connected with an energy consuming since time immemorial. It is really impossible to try to imagine modern civilization without energy sources such as petrol, gas or coal. Our civilization, as we know it, would be collapsed without electricity. Unfortunately, the sources of conventional energy are depleting relatively fast. For example, the Hubbert theory estimates the worldwide peak of oil production between years 2010 and 2030 and most probably before year 2020 [1, 2]. After approaching this peak the production of oil is going to be decreasing again. In addition, the energy demand is increasing year by year. Nowadays the worldwide energy consumption is 1.4×10^{14} kWh·year^{-1} [3]. This amount of energy corresponds to chemical energy that can be released from 3.4×10^{10} tons of coal which corresponds to 6.8×10^{8} wagons and such a train would be 336 longer than circumference of the Earth.

There exists another reason why the alternative energy solution should be found. The global warming is reality and the global temperature is increasing faster that it was in last 180 years due to increasing emission of *Green House Gases* GHGs (mainly CO_2, CH_4). In figure 1 there is seen comparison the fastest global change on the Earth ever which is happen in the end of Paleocene[1] 55 millions year ago also called as *Paleocene–Eocene Thermal Maximum* PETM with a nowadays temperature raising. As it has been proved by carbon isotope ratio mass spectrometry[2] the PETM was caused by burring of organic-based carbonaceous species such as fossil fuel (petroleum or coal) or biomass or permafrost that could be initialized by volcanic activity [4]. The investigation of geological sedimentation shows that PETM, which lasted 10 000 years, 5 Tt of carbon was released into atmosphere (estimated maximum of emission was 2 Gt of carbon annually but the average emission was 0.5 Gt of carbon annually) while nowadays 10 Gt of carbon is releasing annually which is 20 times higher in comparison with PETM [4]. In addition, the figure 1 illustrated that the nowadays temperature raising is 100 times higher in comparison with PETM. It should be noted that the maximum concentration of CO_2 in Eocene (700 ppm) was decreasing 40 millions years by natural way up to the preindustrial concentration of CO_2 (280 ppm). The actual concentration of CO_2 is higher than 400 ppm [5]. According to the mentioned facts it would be even better do not use the rest of fossil fuels does not matter how much is still remains.

[1] Paleocene is a geologic epoch (from about 66 to 56 million years ago) which is the first epoch of the Paleogene Period.

[2] The photosynthetic reaction prefers lighter isotope C^{12} to C^{13} [4]

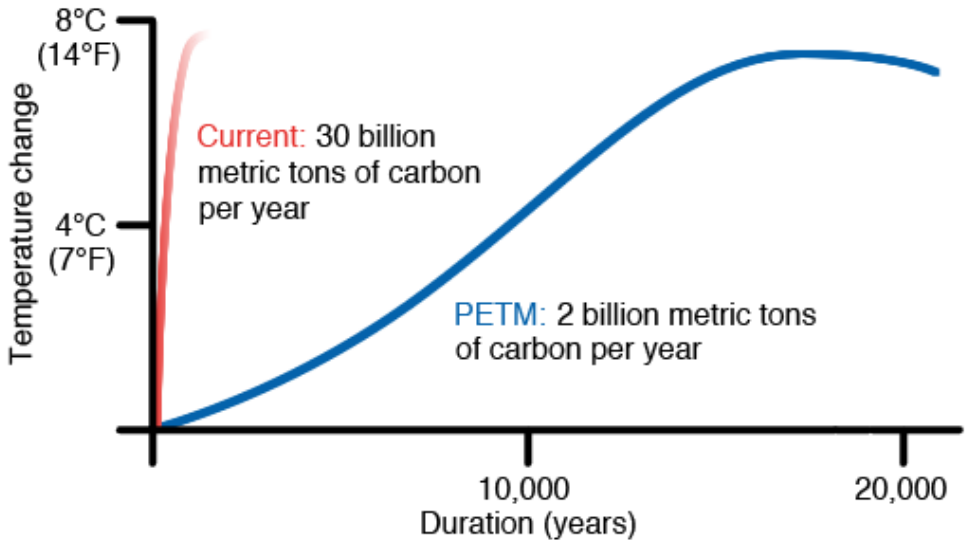

Fig. 1: The comparison of time dependence of temperature rise during PETM (–) and nowadays temperature rise (–) [4].

The solution of energy issue and establishment of new future energy conception are essential to keeping our civilization as we know it.

Might the solution be the use of *green energy*, which is nowadays so popular, in much larger scale? It can been shown that the worldwide energy demand could be met by building a hypothetical large-scale solar power plant. With using known worldwide energy demand (1.4×10^{14} kWh·year^{-1} [3]) mentioned above and electric power density per area unit of a solar panel (0.56 kWh·d^{-1}·m^{-2} [6]) the size of this hypothetical solar plant would be calculated as (830×830) km^2. If we want to imagine such a big area, it may help us comparison with some piece of real land. This area of hypothetical solar plant that ought to be met the worldwide energy demand would be as large as 7% of Sahara desert [3]. It should be noticed that such a similar plans for constructing of large-scale solar power plant in Sahara really exist and this project is known as *Desertec* [8, 9]. However, how to transport energy produced in this remote part of the Earth to the place of use? Similarly, what happens during the night or when it is cloudy? This energy must be stored somehow.

The another solution might be water power plants. Due to its location and orography in the middle of Europe and with mountains along boundaries the water power plants are still suitable in our country [4]. If we calculate the energy benefit of potential energy of annual precipitation in our country during the year according to the middle see level in our country and according to the lowest see level at our boundaries, the amount of generated electricity by water power plants (45.6 TWh) cannot met the electricity demand of our country (66 TWh [10]). That means that the theoretical maximum of electrical energy which can be produced using such a way would be the 68% of total energy demand in our country only. It is obvious that Czech energetic industry definitely could not work

[3]Sahara is the biggest desert in the world. It is located in the north Africa. The total area is $(9.2 \cdot 10^6$ km$^2)$ [7]

[4]The annual production of electricity using water plants in The Czech republic is 3.3 TWh [10]. This production is 3% of annual electricity demand (66 TWh) [10]

with using water plants these days only.

The next near future solution may be expansion of using nuclear power plants. It is estimated that there are enough nuclear sources to meet current demand for next 150 year [11].

Finally, the solution of future energy issue, which might be more important than we admit now, would be an use of thermonuclear fusion power plants [12–14]. Unfortunately, the civil purpose of this technology has been under investigation since early 1950s and it has not been finished yet. The first experiments using "burning" a mixture of deuterium and tritium is estimated in 2032 (project ITER, Cadarache, France)[15].

Leaving aside nuclear energy and still undeveloped fusion energy, it is obvious that there exist alternate power sources and electricity could be produced using above mentioned technology. However, the characteristic attribute of *green energy* sources is its dependence on nature conditions[5] such as solar radiation, precipitation and weather generally. Hence, this kind of power plants usually works instantly and there are peaks of overproduction and stretches of time when the production is not high enough. This irregularity is reason why there is definitely needed some possibility how to store the produced energy. In addition, the energy generated in remote places like the north Africa in the project *Desertec* especially as well as energy generated by using big nuclear power plants must be transported to the place of use or to the vehicle directly. We simply need to make the generated energy mobile being ready in place of consumption so we need to have a appropriate energy carrier.

Both assumptions - the energy storage and the transportation - can be met through a new convenient energy carrier which might be hydrogen. Now some attributes of hydrogen will be explained and the comparison with convectional hydrogen carriers and casual transportation system will be discussed.

- **Hydrogen Energy storage**
  With using the tabulated data of the heat of combustion is easy to show that hydrogen has the best mass density of energy in comparison with other convenient energy carriers [17–19]. Contrary to this fact, the hydrogen spatial density of energy ranks among the worst due to its low mass density. However, hydrogen can be stored under high pressure. The common pressure of hydrogen storage in industry is about 700 Bar [6] [20]. The compression of hydrogen can improve spatial density of energy, unfortunately even under such high pressure hydrogen can not approach the same spatial density of energy as world-wide-use gasoline. In addition, hydrogen can be stored using different method. Hydrogen might be transformed in to liquid form (LH_2), which improves the balance of energy density two times approximately [17]. Another storage procedure is the use of metal hydrides [20]. Moreover, there exists the solution based on liquid organic hydrogen

[5] Admittedly, apart from solar, wind and water energy there are existed other sources that could be also called *green* or *renewable* sources such a use of biomass and others [16] but these energies still need to be stored somehow.

[6] Unfortunately, the storage of hydrogen under high pressure needs relatively heavy gas cylinders or tanks with safety equipment which make the final storage system heavy and bigger [20].

carrier (LOHC)[21] that have the similar spatial density of liquid hydrogen but under ambient conditions. Considering these facts, the hydrogen is really suitable alternative energy carrier of nearest future.

- **Transportation of energy**
  Nowadays, the energy is produced by power plants distributed by the high voltage transmission system. However, it was shown that hydrogen as an energy carrier can be transported using gas pipelines [22, 23] so the energy produced by power plants might be distributed by this worldwide gas pipelines network. In addition, it is easy to show that the energy flow transmitted in form of hydrogen would be 5 fold greater in comparison with the high voltage transmission system. Besides, hydrogen can be still transported by common cargo shipment in forms of LH_2, high pressured hydrogen, metal hydrides or LOHC (discussed in previous paragraph). In view of this fact, hydrogen may be the suitable energy carrier for transportation of energy for long distance.

It was shown that H_2 is supposed to be really suitable energy carrier for storage as well as it is promising for energy transportation. The energy is stored in form of chemical energy of hydrogen but how this energy can be released from this form and transformed into useful work? There exists the basic procedure how to do it which is combustion with using heat engine[7]. The efficiency of heat engine is limited by efficiency of Carnot cycle. This efficiency is relatively low (less than 40%) and it decreases with temperature of cooler. In addition, apart from heating or combustion application the energy in form of electricity is needed and generating of electricity using the final device consisted of heat engine where the transformation into electricity using some turbine and/or electric generator makes the efficiency even lower. The efficiency of standard coal power plant is about 37% [24]. Considering the fact that in most of application the energy in form of electricity is needed we ought to ask if there exists some other solution how transform chemical energy into electricity directly.

1. The Fuel Cell Basics

The technology that makes direct transformation of chemical energy into electricity possible really exists and it is called the fuel cell (FC). As it was indicated the FC is a power source that performs direct transformation of chemical energy of fuel into electricity. The fuels are usually hydrogen and hydrocarbons such as methane, ethane and others. In addition, the efficiency is not limited by efficiency of the Carnot cycle and it is usually higher in comparison with efficiency of standard heat engine (vapor producing→turbine→generating electricity) which is limited by Carnot cycle. It can be shown that the theoretical maximum efficiency of fuel cell is about 77% at working condition of 70°C while the efficiency of heat engine is impossible to determine at this low temperature since it is lower than

[7]Heat engine is a thermodynamics term. It is a system that performs the conversion of thermal energy to mechanical energy which can be used to do useful mechanical work

temperature of heat engine cooler. Considering this the FC technology is really suitable for low temperature applications such as mobile applications (mobile phone, laptops, remote radio transmitter or locator) and as well as for automotive application. In addition, fuel cell technology is not basically consisted of moving mechanical components so there are not any mechanical wears and any noise pollution in contrast to gasoline engine. The next advantage of this technology is fact that the waste products are heat and pure water[1] which makes this power source CO_2 free and environmental friendly.

It was just described that chemical energy of hydrogen fuel can be easily transformed into electricity directly by fuel cell and additionally it could be transformed under higher efficiency in comparison with the system based on heat engine and turbine generator. However, how hydrogen can be fabricated? Or more precisely according to the fact that hydrogen is supposed to be energy carrier, let us ask how the electricity, which is produced by conventional power plants and the overproduction of alternated power plants, can be transformed into hydrogen in order to store it in this form as an energy carrier and/or then transport it? While the fuel cell can transform hydrogen in to electricity and into waste in form of pure water (power source mode) this technology can be used as well as in reverse way (reverse mode). If the fuel cell is used in reverse mode, the electricity is consumed and water is transformed into oxygen and hydrogen keeping the high efficiency comparable with power source mode additionally. This reverse mode of fuel cell is known as the Polymer Electrolyte Membrane Electrolysis (PEM EL) [25, 26]. The already known setup, which may be suitable, is using of solar power plants for producing electricity which is then use for hydrogen and oxygen evolution by PEM EL [27].

In view of this fact, the fuel cell technology is suitable transformer between chemical energy of fuel and electricity in both directions. Considering these facts, fuel cell and PEM FC, which is main topic of this thesis, is a promising power source of electricity that can help to solve energy issue of nearest future. And the thesis is about improving of PEM FC (see goals of thesis 4).

The principle of fuel cell was found in 19 century. Christian Friedrich Schönbein referred to this phenomena in 1839 [29, 30], using it to explain the electrical current measured in experiment with platinum electrodes. However, Sir William R. Grove constructed the first experimental prototype of fuel cell only one year later in 1839 [28, 30–32]. The original scheme of Grove's prototype is shown in fig. 1.1. Those days it was presented that also variation of different kind of fuel such as H_2 and camphor can be used but the performance of cell was too low (a few mW). The expansion and improvement in surface analysis techniques in recent decades made the next investigation and much more precarious research of this field possible. The laboratories as well as companies all around the world have been focused on this topic. Moreover, the idea of fuel cell technology found its place even in an energy politics in world-important countries e.q. in the USA represented by Fuel Cell and Hydrogen Energy Association (FCHEA)[33] that was formed in 2010 following the merger of two former associations representing different sectors of the industry, the U.S. Fuel Cell Council (USFCC) and the National Hydrogen

[1] There are several types of fuel cells with different working conditions, the fuel that is used and the waste products. In the case of proton exchange membrane fuel cell (PEM FC), the waste products are just pure water and heat. More details about it is presented in chapter 5.

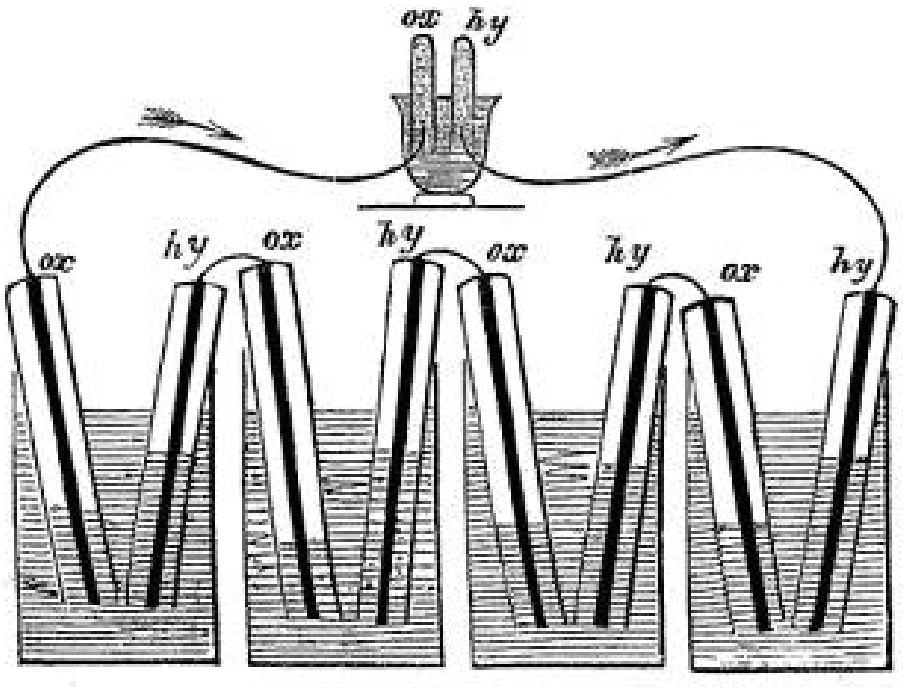

Fig. 1.1: The Sir William R. Grove's diagram of *the gas voltaic battery* from 1839 publish in [28].

Association (NHA) or German Hydrogen and Fuel Cell Association (DWV) [34] and National Organization Hydrogen and Fuel Cell Technology [35] in Germany.

The fuel cell is consisted of two electrodes coated by catalyst and of an electrolyte (see the next part 5). The catalyst is crucial part because without it the chemical reaction could not work and the FC would not produce any electricity. Unfortunately, there is only one general known really functional and stable catalyst for PEM FC and this catalyst is platinum. Platinum is really noble metal and due to its rarity it is also expensive. In view of this fact, the important parameter of FC is power per mass unit of platinum as is called specific power (SP). The specific power (SP) of the state of the art of nowadays automotive application is 6 W/mg(Pt) which was 2012 milestone [36]. The price of 1 g platinum is 35 EUR/g [37]. The world-wide reserve of platinum is 66 000 tons [38] which means that if we calculate with 1 000 millions car on the world it would not be enough platinum to meet the demand. It is clear that using of platinum makes the commercial production of FC technology limited. In addition, it should be also mentioned that after expansion of FC technology the price of platinum would be growing up rapidly due to increasing of demand and the price of final device based on FC could be much higher than we could suppose. It is obvious that if this technology is used in large scale, the amount of platinum must be rapidly decreased or platinum should be replaced by other cheaper catalyst keeping the same activity and stability. **The decrease of amount of platinum using other suitable additive oxides which would be kept the performance and stability as high as in the case of pure platinum catalyst is the main goal of this thesis.**

2. Nowadays FC in use

Despite the unfinished investigation of proper inexpensive catalyst, the fuel cell technology is supposed to be an alternate technology that should help to solve energy issue of nearest future. There exist many examples of use of PEM FC. For example the hydrogen bus from Škoda Electric company in our country and car powered by PEM FC from Honda company planed as the first serial production of such a car by year 2015 [39](See the fig.2.1). These vehicles use hydrogen as a fuel

Fig. 2.1: Examples of use of trihybride: fule cell/energy storage element/super capacitor. On the left is example of the trihybrid bus which is constructed by Škoda Electric Pilsen trolley bus and Fuel cell manufacturer is Proton Motors [40]. On the right is a sport car Honda Clarity with PEM FC solution of 80 kW [41].

and fuel cell is keeping running under stable optimal conditions during the whole time while the vehicle is working. The overproduction of electricity generated by PEM FC during the drive is stored in lithium traction batteries and acceleration, which consumes more electric energy than PEM FC could generated, is provided by super capacitors[1] that are continuously fed by PEM FC. The super capacitor is also used for deceleration which is carried out by a regenerative break[2]. This system: fuel cells and energy storage elements with super capacitors is called *trihybride*. Additionally, both vehicles are emission free because they use a fuel cell. Moreover, we could say that all reasonable automotive companies are trying to develop the fuel cell car. The overview is shown e.q. in [43]. In addition, there exist much more applications which was already used such as stationary unit for houses and small and middle size power plants [33, 43]. Then there are portable or mobile fuel cells: little source for laptops [44] or military application e.g. radio [45], military submarine [46, 47] or public submarine ready for serial production [48]. The fuel cell is supposed to be solution for houses based on combination

[1]The super capacitor, also known as ultra-capacitor, is an element of energy storage which has much smaller capacity than lithium traction batteries but which can involve much higher current. It is usually used as a buffer of energy between electric motor and batteries. See [42].

[2]The regenerative break is a way how to slow vehicle down which is based on transformation of kinetic energy of vehicle into electricity. The electricity is stored in batteries or distributed back to the electric-power transmission (in the case of trains and others using overhead lines). The regenerative break is usually performed by using an electric motor as an electric generator. In case of regenerative break, the excess kinetic energy is saved which is in stark contrast to conventional braking systems which is characteristic for vehicles with combustion engine where the excess kinetic energy is converted to the heat only and therefore wasted.

of solar panels and fuel cells as it was described above [27]. See the scheme in fig. 2.2. The fuel cell can be powered by hydrogen from methanol steam reformer

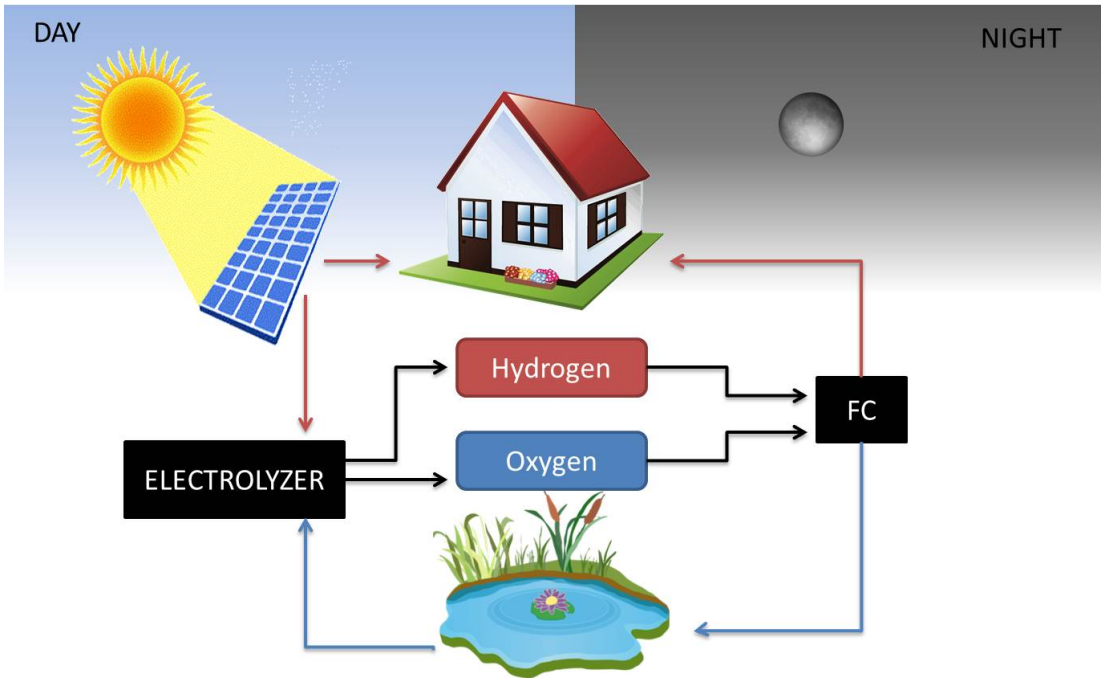

Fig. 2.2: The scheme of solution for houses based on combination of solar panels and fuel cells.

based on solar heat, which is possible to use as a house complementary solution [49].

3. The state of the art

The fuel cell is a global topic which is investigated worldwide and many efforts have been made to improve this system as it is evidenced by hundreds of thousands of published articles in this filed. The database web of knowledge returned 98 710 for keys *fuel cell* (till 8.8. 2016).

The research is divided into some main subfields as follows :

- anode catalyst
- cathode catalyst
- membrane investigation
- flowfields development with fluid simulations and water management.

It is obvious that Pt is the most convenient element for hydrogen oxidation reaction (HOR) as it is seen in fig. 3.1 where it is illustrated the comparison between Pt and another elements for HOR (left) and ORR (right) [50]. There are lots of reviews about Pt and Pt-based fuel cell electrocatalyst [53, 54]. It has been shown that amount of platinum could be decreased by improving morphology of carbon substrates and by increasing specific surface area [55, 56]. The typical catalyst support is carbon nanoparticles known as *Carbon Black* or *Vulcan Carbon*

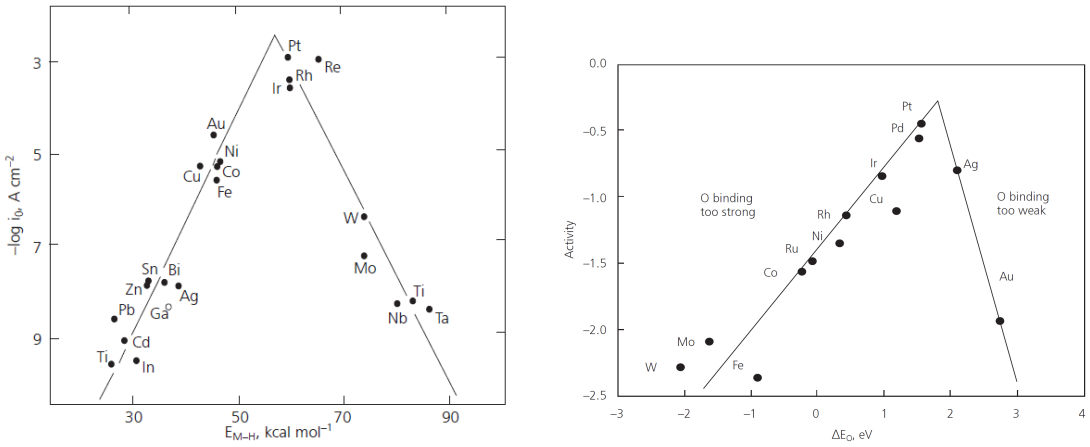

Fig. 3.1: On the left there is the logarithm of exchange current densities ($\log i_0$) for hydrogen evolution vs. the bonding adsorption strength of intermediate metal-hydrogen bond formed during the reaction itself [51] and on the right there are trends in oxygen reduction activity plotted as a function of the oxygen binding energy [52].

(XC-72 and others) and the widely used catalyst is platinum in the form of nanoparticles of diameters about 4 nm known as platinum on carbon black (Pt-C) from e.g. (Johnson Matthey Co, E-TEK Inc.). The scheme of Pt-C catalyst with carbon support is seen in fig. 3.2. It is seen that platinum is situated on the carbon particle surface in the form of small particles.

The new cutting edge automotive loading of catalyst is 0.3 mg·cm^{-2} for cathode and 0.025-0.05 mg·cm^{-2} for anode as it has been demonstrated without degrading the cell performance and life-time [58–60]. It could be seen that main bottleneck in the fuel cell technology is high loading of platinum on the cathode. However, considering the fact that hydrogen is supposed to be also produced from bio-ethanol [1] the demands placed on anode catalyst is increasing and anode catalyst becomes important again [55, 61, 62]. Hydrogen produced from bio-ethanol using reformer is contaminated by carboneaous species such as CO, so the anode catalyst exhibiting higher resistance for CO poisoning is needed. The CO tolerance could be partially increased by using higher loading of platinum on the anode side or by using of certain platinum alloys that some of them are also known as catalysts for direct methanol fuel cell (DMFC). The CO and CO-like species are adsorbed irreversibly on the catalyst surface and critically poison Pt that causes a significant reduction of the electrical efficiency and power density. It can be summarized that for hydrogen contaminated with CO there are Pt-based catalysts that give performance equal or similar to the performance given by Pt/C with pure hydrogen cell: Pt-Ru/C, Pt-Mo/C, Pt-W/C, Pt-Ru-Mo/C, Pt-Ru-W/C, Pt-Ru-Al_4, and Pt-Re-(MgH_2) [63]. In another report it is described the use of Ru-Pt, Ru-Sn and Mo-Pt alloys for PEM FC based on hydrogen contaminated by CO coming from steam reformer fabrication procedure [61, 62]. The general role of bimetallic alloys is shift of the onset potential for CO oxidation to lower potential which reduces CO poisoning [64–67]. In the detail, onset potential for OH adsorption is for Ru lower than for Pt, which leads to increase of OH

[1] Bio-Ethanol is produced by microbial fermentation of the sugar coming from appropriate plants.

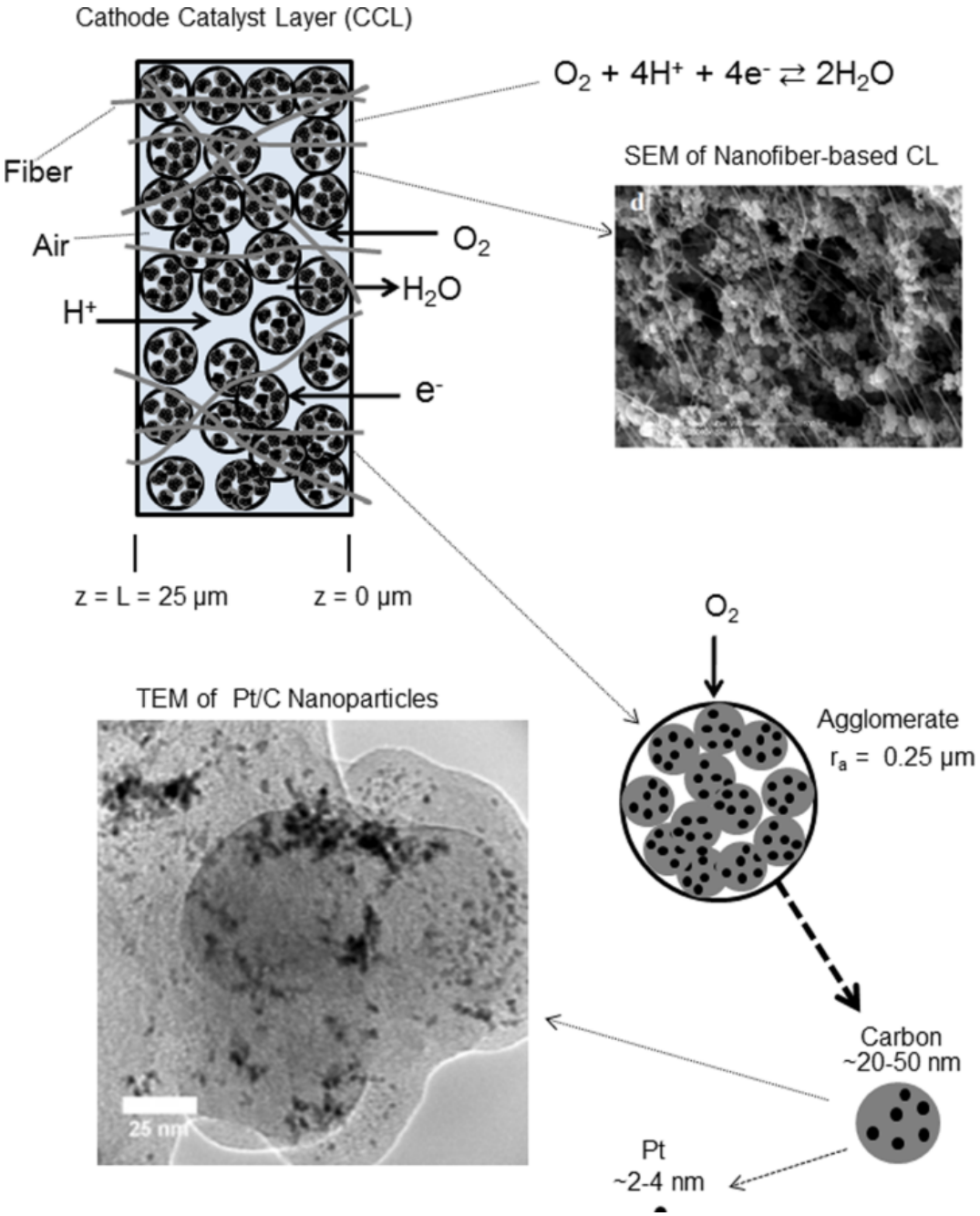

Fig. 3.2: The scheme of Pt-C catalyst with carbon support. The TEM images left below and Pt-C catalyst on carbon support illustration in the right below [57].

species adsorbed on the surface which prevent to CO poisoning [68] by reaction

$$\mathrm{Ru} - (\mathrm{OH})_{ad} + \mathrm{Pt} - (\mathrm{CO})_{ad} \longrightarrow \mathrm{Pt} + \mathrm{Ru} + \mathrm{CO_2} + \mathrm{H^+}_{aq} + \mathrm{e^-} \qquad (3.1)$$

According to the fact that the state of the art platinum loading on anode for hydrogen of highest purity is still significant (only 6 - 12 × less than cathode loading) and fact that better CO tolerance for hydrogen produced by reformates is needed and catalyst stability needs to be improve, the investigation of anode catalyst is main topic of this study.

The another solution is the use of Pt doped metal oxides. The selection criteria for appropriated metal oxides are described in [54] and it is listed below:

- High stability in acidic media for acidic fuel cells or in alkaline media for alkaline fuel cells
- High resistance against electrochemical corrosion: metal oxides should be electrochemically stable under the working conditions of PEM FCs, or metal nanoparticles supported on them should not peel off from them and should not agglomerate, leading to the degradation of catalytic performance.
- Good electronic conductivity
- Good proton conductivity
- High specific surface area
- Porosity: appropriate porosity of metal oxides is favorable for mass transfer of liquid fuels or oxygen gas and the minimization of water flooding in electrodes.
- Compatibility with electrodes: metal oxides should bond well with noble metal nanoparticles to maintain adhesion and a conductive link to noble metal nanoparticles, and to form a good three-phase boundary.

All these criteria are fit by CeO_2 which is used in this thesis. The investigation of catalytic performance for some metal oxides (TiO_x, WO_x, MoO_x, RuO_x, SnO_x and CeO_2) as a co-catalyst and support for various reactions including HOR, ORR, EOR is summarized in [54]. The co-catalytic behavior of WO by the formation HWO_3 for anode oxidation was publicized even in 1960s [69] and similar behavior was also observed for SnO_x [54]. The role of co-catalytic oxides is similar to bimetallic alloy - the onset potential for oxidation of carboneous species is shifted to the lower potential in comparison with standard Pt-C as it is described for Pt-SnO_2 electrocatalyst [70, 71]. The CeO_2 is readily reducible into Ce_2O_3 so it can be easily switched between two chemical states Ce_{3+} and Ce_{4+} with small energy needs. The chemical state depends on whether its presence is in reducing or oxidizing environment as it is seen in eq. 3.2.

$$CeO_2 \longleftrightarrow CeO_{2-x} + \frac{x}{2}O_2 \quad (0 \leq x \leq 0.5) \tag{3.2}$$

The ability to store and release oxygen is also known as *oxygen storage* and the quantum origin of this phenomenon is described in [72]. Additionally, it contains many oxygen vacancies leads to high oxygen mobility. The oxygen storage and high oxygen mobility make ceria possible to use for the ORR and for the oxidation of the adsorbed CO from hydrogen contaminated with remaining CO [54]. This ability might help to stabilize doped platinum which is also reason why this thesis is focused on use of Pt doped CeO_2 prepared by physical way. The preliminary quantum study about Pt-CeO_2 structure was presented [73].

Many efforts have been directed toward enhancing the catalytic activity by developing advanced cathode catalyst. There are reviews about bimetallic platinum alloys as an alternation to pure Pt/C catalyst [54, 55, 58]. The main bimetallic alloys investigated as cathode electrocatalyst are Pt_3-M (M: Ti, V, Fe, Co, Ni) [74, 75] but there is also study about use of Pt-Cu alloy [76]. There are another studies about platinum transition metallic alloys Pt-Fe, Pt-Cr and Pt-Cr-Co presented higher specific activities for oxygen reduction comparable with platinum [59, 77–79].

There are two approaches how to explain the better catalytic activity of binary alloys comparing to Pt/C. First approach is based on de-alloying of transition

metal from platinum alloy while the less stable elements are intentionally or unintentionally dissolved out to leave a nanoporous film, skeletal surface or core–shell particle configuration which increase the specific area of remaining platinum [53, 76, 80, 81]. Second, there is suggested occurrence of a lower Pt valence band center relative to the Fermi level in Pt skin layer-based alloys by the underlying transition metal which increase the efficiency for ORR [74]. Unfortunately, all these Pt-M alloys are unstable and reasonable degradation occurs in comparison with Pt/C catalyst [82]. However, it was recently shown that the stability might be improve by creation of structural defects and micro-strain in alloy because the defects are more stable and active than pure alloy [83, 84]. The relation between the electrocatalytic properties of the oxygen reduction reaction and the electronic band structure of Pt_3M (M: transition metal) alloys are seen in fig. 3.3. It is seen that Pt_3Co exhibits the highest performance which is the reason why in this study it is also investigated the Pt-Co alloy for cathode catalyst but prepared by different way.

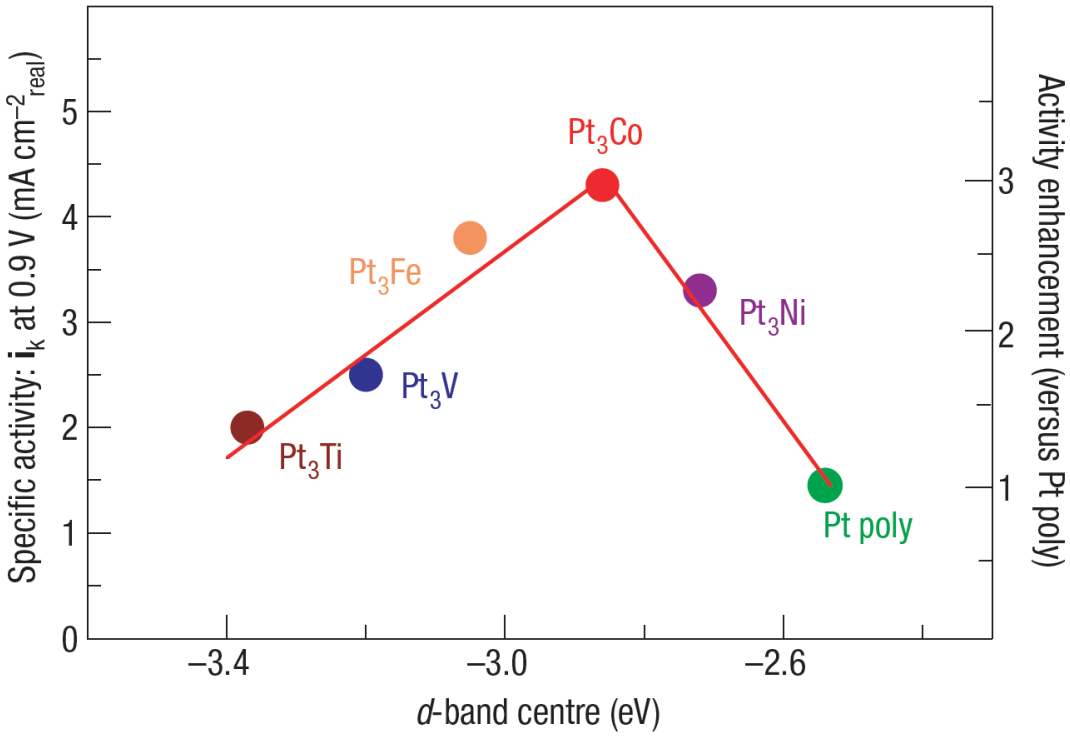

Fig. 3.3: The relation between the electrocatalytic properties of the oxygen reduction reaction and the electronic band structure of Pt_3M alloys. Experimentally measured specific activity for the ORR on Pt_3M surfaces in 0.1M $HClO_4$ at 333 K versus the d-band center position [74].

There exist some platinum free catalysts but they are not stable enough. They are also dissolved and degraded rapidly and the performance is much lower in comparison with noble metal based catalyst [85]. Despite the fact, that there has been done progress with non-noble metal catalyst [86, 87] the platinum based catalyst still remains at the center of research interest [88–90]. The promising alternative cathode platinum-free catalyst might be e.g. M–N_4 (M: Co or Fe) [91] and anode platinum-free catalyst alternations are e.q. Co-Mo-C [85] or M-WC/KC (M: Ni, Co or Mo) [92–95].

There is review about platinum supported on doped or non-doped graphene for ORR [96] but this catalyst is supposed to work in alkaline solution. The scheme of this catalyst is seen on the left in fig. 3.4. Platinum free cathode catalyst for

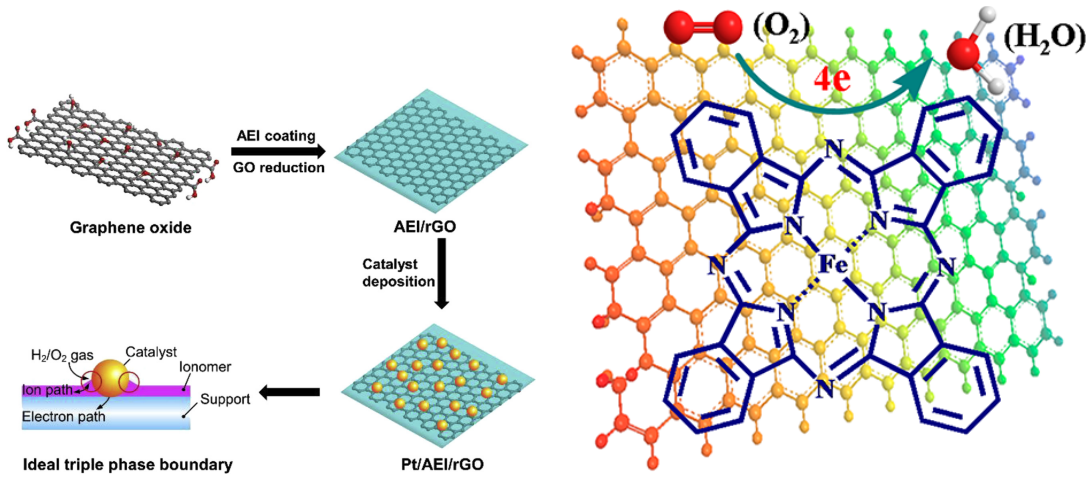

Fig. 3.4: Examples of graphene supported catalyst. On the left it is an illustration of preparation of the Pt/AEI/rGO catalyst with ideal triple phase boundaries (AEI - anion exchange ionomer, rGO - reduced graphene oxide) [97]. On the right there is a schematic illustration of the interaction between Pt-Fc and graphite [98].

alkaline solution studied recently is based on transition metal nitrogen carbon complex (graphene-iron phthalocyanine (g-FePc) in the case of Fe) and it has been shown as a promising non-platinum catalyst [98, 99]. For the illustration of the catalyst structure see the fig. 3.4. The junction between Fe-Pc and graphene is mediated by $\pi - \pi$ orbital interaction. Unfortunately, this complex still has not exhibited efficiency and stability comparable with platinum based catalyst [96].

4. The Goals of the Thesis

Considering the facts mentioned above, the fuel cell technology is a promising alternation of the energy solution for near future because of many reasons - power source diversification and autonomy, technical, ecological and economic reasons. Unfortunately, as it was already described, there still exists just one suitable catalyst material enabling to get a reasonable power density for automotive industry. This catalyst is platinum. Platinum is a rare and expensive material and the price is even going to increase when the serial production starts as it was also explained above. So the discovery of a less expensive catalyst or decreasing of the amount of platinum while the power density is comparable with pure platinum catalyst is crucial. **The main general target of this thesis is decreasing of the amount of platinum which is used as a catalyst in proton exchange membrane fuel cell (PEM FC).**

Especially, investigation of the new platinum cerium oxide alloy for fuel cell anode and its comparison with commercial platinum catalyst. The convenient experiment method is a direct test in fuel cell test station. The supplementary methods are scanning electron microscopy (SEM) helps to control the structure

of catalyst layer and photoelectron spectroscopy (PES) enables to control chemical composition of catalyst material. Complementary, X-ray absorption near edge spectroscopy (XANES) is strong effective instrument to study chemical composition of catalyst film *in-operando*. Moreover, the additional another goal is investigation of Pt-Co as cathode catalyst. Finally,the important and necessary aim is also developing of experimental setup for PEM FC analyzing.

Main individual goals of theses are listed below:

- Improve measurement system for fuel cell.
- Pt-CeO_2 samples preparation using magnetron sputtering.
- Analysis of samples using SEM, XPS, PES.
- Direct test in PEM FC test station.
- Compare results with commercial Pt catalyst.
- Investigate behavior of catalyst in real conditions with use of XANES.
- Investigate a low platinum content cathode and test PEM FC with own low platinum content catalyst on both, anode and cathode, sides.

II Theory

"If we knew what it was we were doing,
it would not be called research, would it?"
— Albert Einstein

The historical background of fuel cell technology and its meaning in global point of view were described in the previous part. However, the principle in detail was left unclear and it is going to be described in this chapter. The detailed explanation of principle of fuel cell is described on the case of PEM FC, which is the type of fuel cell used in this thesis. Additionally, the comparison of different types of fuel cells is shown. Moreover, the author's mathematical derivation of cell voltage and efficiency and basic fuel cell model are shown in individual chapters. Besides that, methods of characterization of fuel cell performance are described.

5. Theory of Fuel cell

5.1 Fuel cell principle

The fuel cell is a device enabling a direct transformation of chemical energy of hydrogen or of hydrocarbons fuel into electricity. The fuel cell has a sandwich-like structure which is consisted of an anode electrode, a cathode electrode and an electrolyte which is placed in the middle and makes ion conductive junction between both sides. Both anode and cathode electrodes are composed of *gas diffusion layer* (GDL) and of thin catalyst film. In the case of PEM FC, ion conductive membrane is used as an electrolyte. The membrane pressed between anode electrode and cathode electrode is called *membrane electrode assembly* MEA and this MEA is clamped between two stainless steel or graphite gas distributors. The structure of PEM FC is illustrated in fig 5.1. Catalyst film, which is placed between membrane and gas diffusion layer, is usually coated on GDL or for some applications is coated onto a membrane directly.

The principle of PEM FC is as follows: Hydrogen flows to the anode where it is adsorbed on catalyst layer where it is decomposed into protons and electrons 5.1.

$$2H_2 \longrightarrow 4H^+ + 4e^- \tag{5.1}$$

Protons can go through ion conductive membrane while electrons cannot pass because membrane is an insulator. At the same time, oxygen flows on the cathode

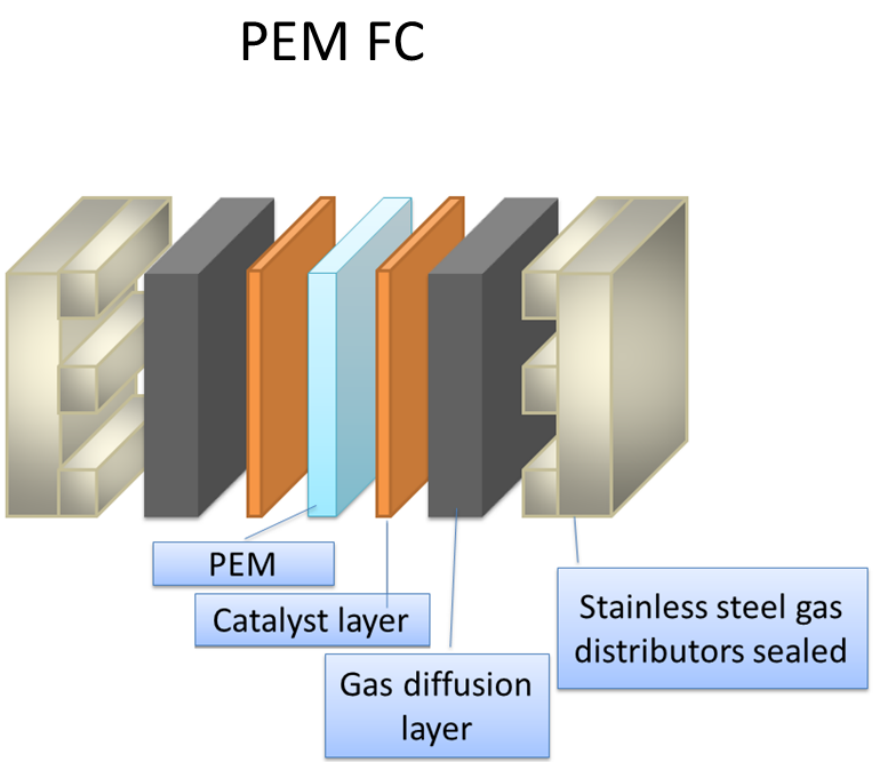

Fig. 5.1: The sandwich-like structure of PEM FC: both, the anode electrode and the cathode electrode, consisted of the gas diffusion layer and of the catalyst film, the ionconductive membrane in the middle, gas distributors on both sides.

catalyst where it is reduced and reacts with protons to form water 5.2

$$4H^+ + 4e^- + O_2 \longrightarrow 2H_2O \tag{5.2}$$

However, this reaction needs two more electrons so they are taken from the cathode surface and this way the potential difference between anode and cathode are created. While the protons go through the membrane, electrons go along the external circuit and do useful electric work (see 5.2). The well-know equation summarizing the fuel cell reaction is as folows (5.3):

$$2H_2 + O_2 \longrightarrow 2H_2O \tag{5.3}$$

The other explanation can be seen e.g. in [20, 100]. The reaction pathway is explained in detail in the following section 5.3.

5.2 PEM FC summary

There exist more types of fuel cell than PEM FC. Despite the fact that this thesis is about PEM FC, the main other types of fuel cell are briefly described in order to get basic overview. Type of fuel cell are different to each other from several criteria such as scale of use, working temperature, electrolyte, fuel which is used and etc.

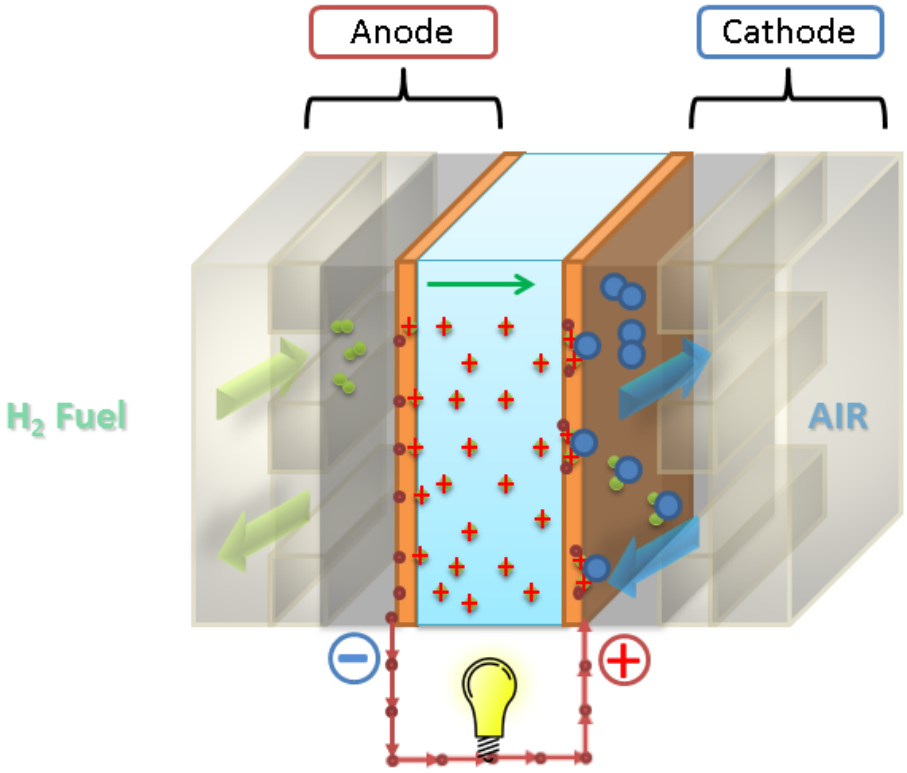

Fig. 5.2: The principle of fuel cell. Hydrogen ( ) is oxidized to form protons ( ) and electrons( ). Protons go thought the membrane and oxygen ( ) is reduced to form water ( ) while electrons cannot pass thought the electrolyte and go along the external circuit instead where do useful electrical work.

Based on the review (not shown) of the other type of fuel cells can be seen that the PEM FC can operate in wide power range. For the better illustration see the the figure 5.3 where is the summary of fuel cells characterizations. It is seen that PEM FCs are suitable for small mobile devices through the cars to the backup power sources of power of hundreds of kilowatts. This fact together with zero CO_2 emission makes PEM FC very convenient power source of electricity. The other advantage of PEM FC is low working temperature of range from room temperature to less than 100°C (typically 80 °C). The working temperature around room temperature is important for mobile application like laptops or mobile phone where is necessary to keep lower temperature. The working temperature around 80 °C at which the PEM FC reaches high power density around 1-2 $W\,cm^{-2}$ (which is the highest value in comparison to the others type of fuel cell) is still appropriate temperature for automotive industry and power generation in large scale. The indisputable advantage is the stable electrolyte which is ion conductive membrane - mainly NAFION®. The other and more general information about PEM FC is described in chapter 1.

On the other hand, there are disadvantages. The necessary use of pure hydrogen fuel without any carbonate impurities and especially the use of expensive platinum catalyst are the main disadvantages which is the reason why the decrease of platinum amount is the main goal of this theses (see the chapter 4).

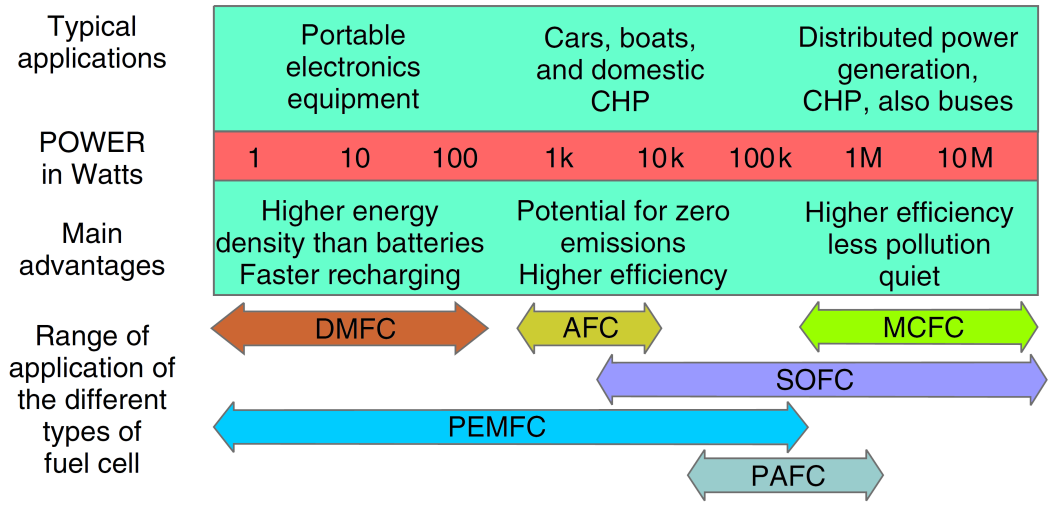

Fig. 5.3: The summary of applications and main advantages for different type of fuel cell. Reprinted from [20].

5.3 3 phases interface

The PEM FC reaction mechanism for the anode reaction 5.1 and cathode reaction 5.2 described in the previous section 5.1 puts high claims for specific solution of the environment of reaction. For the better understanding see the fig. 5.4 where are the anode (a) and cathode (b) mechanisms in the detail. In the case of anode, it is seen that hydrogen in its gas phase has to get from GDL to the place of reaction through the combination of contiguous pore space. When it reacts on Pt particle and it is dissociated into protons and electrons, the electrons have to get out through electron conductive channel to the electrode which is realized by GDL. Complementary, the protons have to get to electrolyte through ionconductive channel as it is illustrated in figure 5.4. In the case of cathode it is similar but in addition, the water which is formed on the cathode has to get out. Given this fact, the porous space should enable the transport of fuel/oxygen in gas phase and simultaneously the transport of water mainly in liquid phase between the GDL and place of reaction. It can be summarized that the appropriated place of reaction is catalyst particle connected to the ioncoductive network, electron conductive network and combination of contiguous porous network. Should be noted, that simple connection is not enough, it is crucial that the network is ended at the GDL or complementary at the electrolyte.

The complex interplay between particle size, pore size distribution and ionic/electronic conductivity, in fuel cell electrodes is called the triple face interface (TPI). The total length of this TPI is essential due to the fact that it is only at this region, where the electron conductive phase, ion conductive phase and contiguous combination of porous space structure, which charge transfer reactions can be proceed. Thus, the length of TPI of each PEM FC is crucial because the performance of PEM FC grows with increasing length of the TPI. More details can be found e.g. [20, 101].

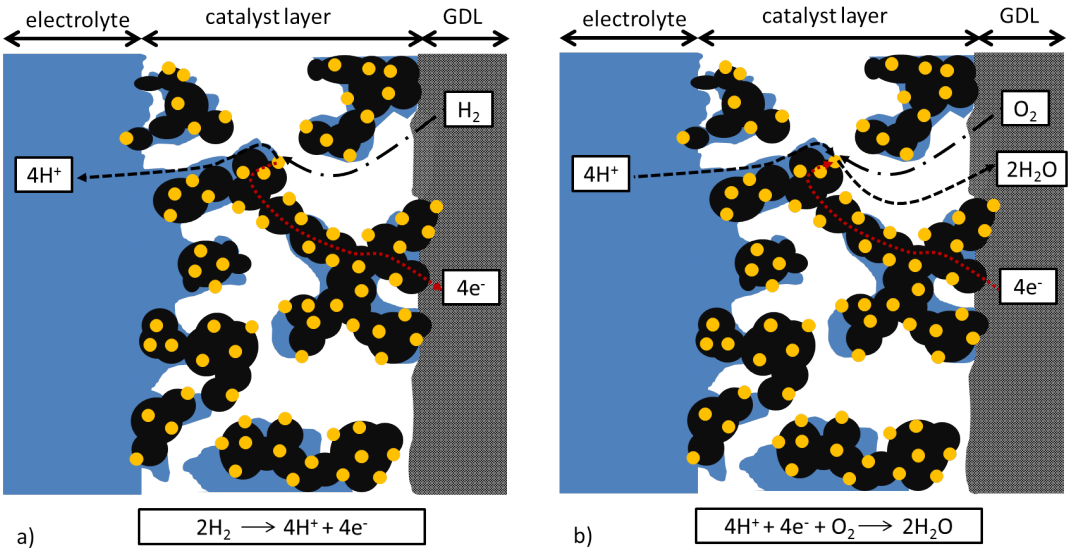

Fig. 5.4: Schematic view of reaction pathway for: a) PEM FC anode; b) PEM FC cathode. Platinum catalyst nanoparticles(●), carbon support (●). The carbon and platinum particles are bonded together using a NAFION® solution which provides ion conductivity(▬). Contrary, the carbon support particles together with platinum particles provide electron conductivity

5.4 Proton Exchange Membrane

The PEM FC electrolyte is realized by proton exchange membrane which is made from ionomers[1] and it is designed to be proton conductive. This ionomer is known as NAFION®. It has been developed by E.I. DuPont company and currently it is still produced by the same company.

Nafion is a sulfonated tetrafluoroethylene based fluoropolymer-copolymer which is consisted of nonpolar *tetrafluoroethylene* (TFE) segments $CF_2{-}CF_2$ and polar *perfluorosulfonic vinyl ether* (PSVE) segments ($CF_2{-}CF(OCF_2{-}CF(CF_3)O)$-$-CF_2{-}CF_2{-}SO_3H$) and its chemical formula is below in fig 5.5.

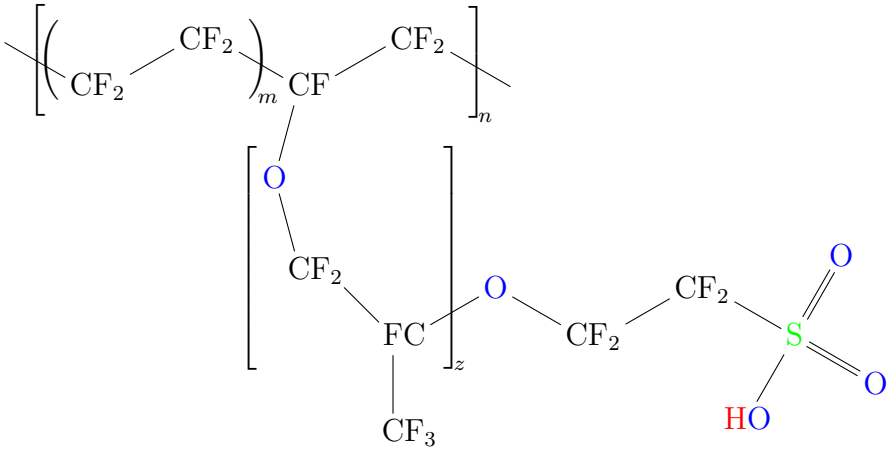

Fig. 5.5: The structual chemical formula of Nafion.

The Nafion has hydrophobic and hydrophilic parts. The hydrophobic part is

[1] An ionomer is a polymer comprising fraction of ionized units in additional to normal polymer.

situated around the TFE (whose behavior is known from behavior of PTFE) and hydrophilic part is well defined by each sulfonate group around PSVE. The segregation of the ionic groups (SO_3^-) occurs and a better segregation of these hydrophobic and hydrophilic patches is produced in the water-polymer interface [102]. The protons can be transported along SO_3^- ionic groups. However, the natural bond between SO_3^- and H^+ is strong because of its ionic character and proton is not mobile. Nevertheless, the attraction between SO_3^- and H^+ or better between SO_3^- and H_3O^+ in water environment is getting weaker by increasing of humidity and protons are able to move (increasing the dry weight of the material by up to 50%). If the membrane is well hydrated, there are occurred more complex mechanism of proton conductivity and apart from proton as a part of water molecule H_3O^+, proton could be between two water molecules $H_5O_2^+$ or it is a part of $H_5O_2^+$ comprised of an H_3O^+ ion and three H_2O molecules [103, 104]. For better understanding the mechanism of proton conductivity is illustrated in fig. 5.6 a) where is nanoscopic hydrated network. In fig. 5.6 b) is seen the cross-section of channel of cluster network. The typical conductivity of well hydrated membrane is 0.1 S cm^{-1} [105]. If the membrane is less hydrated, the water clusters

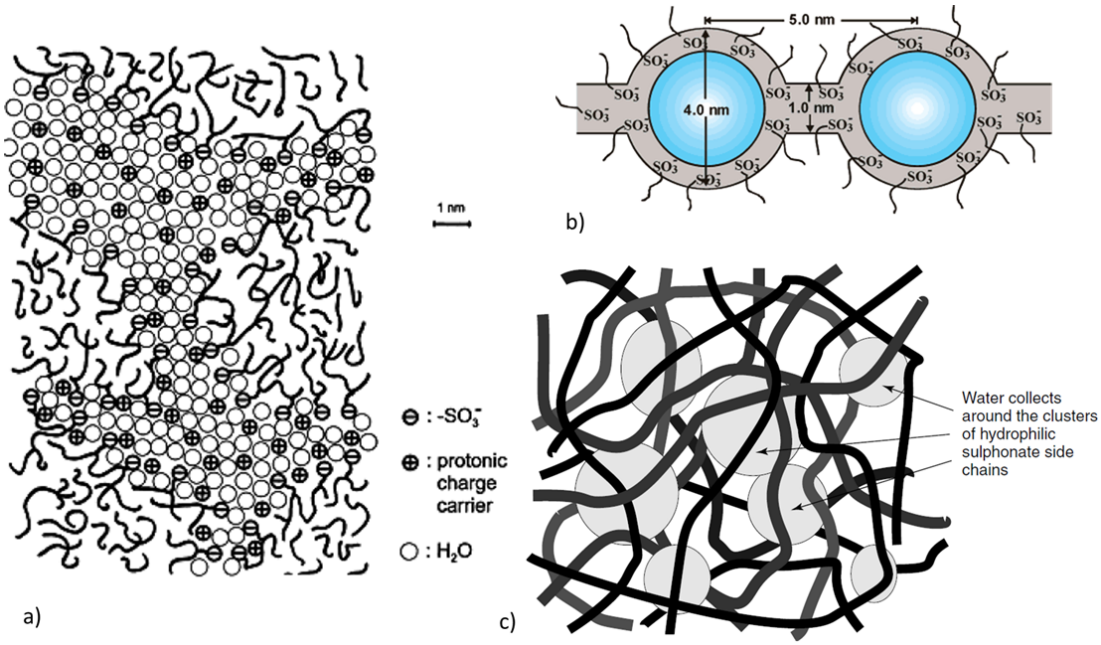

Fig. 5.6: Proton conductivity mechanism in Nafion: (a) Stylized view of the nanoscopic hydrated structures of Nafion and sulfonated polyetherketone [106]; (b) Cluster-network model for the morphology of hydrated Nafion [107]; (c) The structure of Nafion-type membrane materials. Long chain molecules containing hydrated regions around the sulphonated side chains [108].

around hydrophilic ionic chains are formed as it is illustrated in fig. 5.6 c). It is obvious that in this case the water regions are separated so the conductivity is lower but it is still possible because H^+ ions can move through the supporting long molecule structure as a diffusion of H_3O^+. This mechanism is called *vehicle mechanism* [109, 110].

Given the facts above mentioned, it is necessary used well hydrated membrane for PEM FC application. Hence, water management makes PEM FC technology more complicated and some other problems can occurred.

Another effect which is typical for PEM membrane is water crossover which means that water goes through the membrane from the anode side to the cathode side. Especially, while the fuel cell is operated H^+ ions go through the membrane and pull water molecules with them by electro-osmotic drag [105]. Furthermore, for high current density it can happen that the anode side of the electrolyte gets dried out although the cathode side is well hydrated.

It is important to keep appropriated humidity of both sides anode and cathode which means the use of moistened gases on both sides of fuel cell. In the best case, moistened gases according to the current real current density.

It should be noted that the mechanism of PEM membrane has not been perfectly clearified yet and there still exist new model studies that try to explain the membrane behavior e.q. [102, 111–113]. The more information about PEM and nafion membrane can be found in [102, 103, 107, 114, 115].

There are different types of Nafion that are differentiated by *equivalent weight* (EW) which is the number of grams of dry Nafion per mole of sulphonic acid groups when the material is in the acid form and by the thickness of membrane. For example the Nafion 117 has 1100 EW and it is 0.007 inch thick.

5.5 Gas Diffusion Layer

The role of *Gas Diffusion Layer* (GDL) is also important. The function of GDL is the diffusion of reactants to the place of reaction and consequently the diffusion of products out of cell. Thus, GDL should be porous enough with combination of contiguous porous creating network important for diffusion of hydrogen/water on anode and for air/water on the cathode. Additional, the GDL is bound to provide an electric conductivity. Moreover, the material of GDL should be mechanically firm in order to protect the porous structure from a collapse due to pressure which is used for a clamping of the MEA in the cell. Usually, the operating pressure of PEM FC is up to 1.5 MPa. The material widely used as a best solution for GDL is *carbon paper* or *carbon cloth*. Carbon cloth is usually thicker (less than 0.5 mm) and the mechanical assembly could be easier since it fills small gaps and irregularities between bipolar plates. However, the carbon cloth is not suitable for the thin modern design of the fuel cell and the most favorite GDL is a carbon paper. The thickness of the carbon paper is about 0.2-0.3 mm, after assembling is usually pressed to $^4/_5$ of its thickness which is still at the elastic deformation region and while the conductivity usually increasing approximately four times (see the data-sheet for carbon paper [116]).

For better water flow through the material the carbon paper has hydrophobic surface by coating of Teflon on its surface. The fig 5.7 a) shows the structure of carbon paper. The individual carbon fibers coated by Teflon are visible.

The next function of GDL is support for catalyst layer so the specific surface area of the upper side of carbon paper ought to be as high as possible. From this reason, the carbon paper is usually coated by micro-porous carbon-based layer (MPL) for fuel cell application. Carbon coated by such a MPL is seen in fig. 5.7 b), where is shown carbon paper 29 BC from SIGRACET® and its detail is in fig. 5.7 c) (the same carbon paper was used in experiments in this thesis). If the carbon paper with MPL is compared with carbon paper without MPL, the significant increasing of specific surface area is obvious.

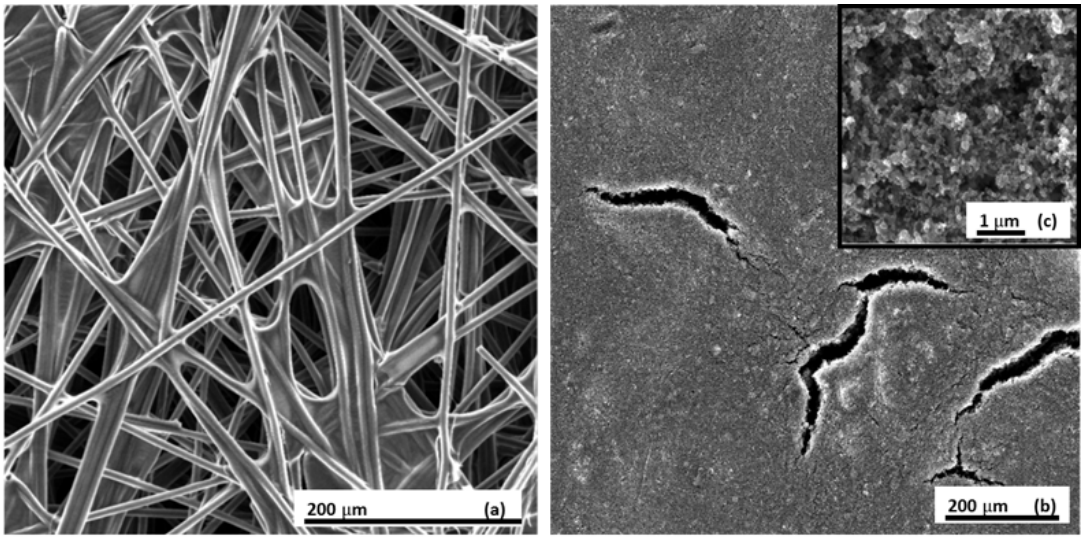

Fig. 5.7: The SEM images of carbon paper: Alfa Aesar, Toray Carbon Paper, tefloned, TGP-H-60 (a); carbon paper 29 BC from SIGRACET® with a micro-porous layer (b) and the detail of the micro-porous layer (c).

III Experimental Part

"I would rather have questions that can't be answered than answers that can't be questioned."

— Richard Feynman

In this chapter it is presented how the fuel cell is characterized, which procedures are normally used and which dependencies and quantities describe quality of fuel cell. The experimental setup is illustrated. Additionally, the design of our new piston cell is presented. Moreover, the design of our laboratory is shown and development of the new automatized test station is briefly presented. The sample preparation is summarized.

6. Cell characterization

6.1 IV curve

Fuel cell is a source of electricity so it is characterized by quantities which are known from battery field as a voltage of unloaded cell (OCV - Open Circuit Voltage) and voltage dependency on current. For characterization of fuel cell it is used the plots of voltage and power dependency in one graph as it is illustrated in fig. 6.1. The open circuit voltage and a maximum power are marked. The relation between power and cell voltage is illustrated for graphical determination of cell voltage at maximum power.

As regards the fact that fuel cell technology is supposed to be used in applications where the size of device is important, appropriate quantities are current density and *power density* (PD) 6.1

$$P_{PD} = \frac{P}{A} \tag{6.1}$$

where P is power of fuel cell and A is the area of electrodes. This PD roughly corresponds to the power gained from a volume unit. Since the platinum catalyst is rare and expensive material, the determination of power per unit of mass of noble metal is useful (see I): the *specific power* (SP) is defined 6.2

$$P_{SP} = \frac{P_{PD}}{M_L(Pt)} \tag{6.2}$$

where $M_L(Pt)$ is loading of Platinum. Thus, the SP characterizes the price of power gained by fuel cell.

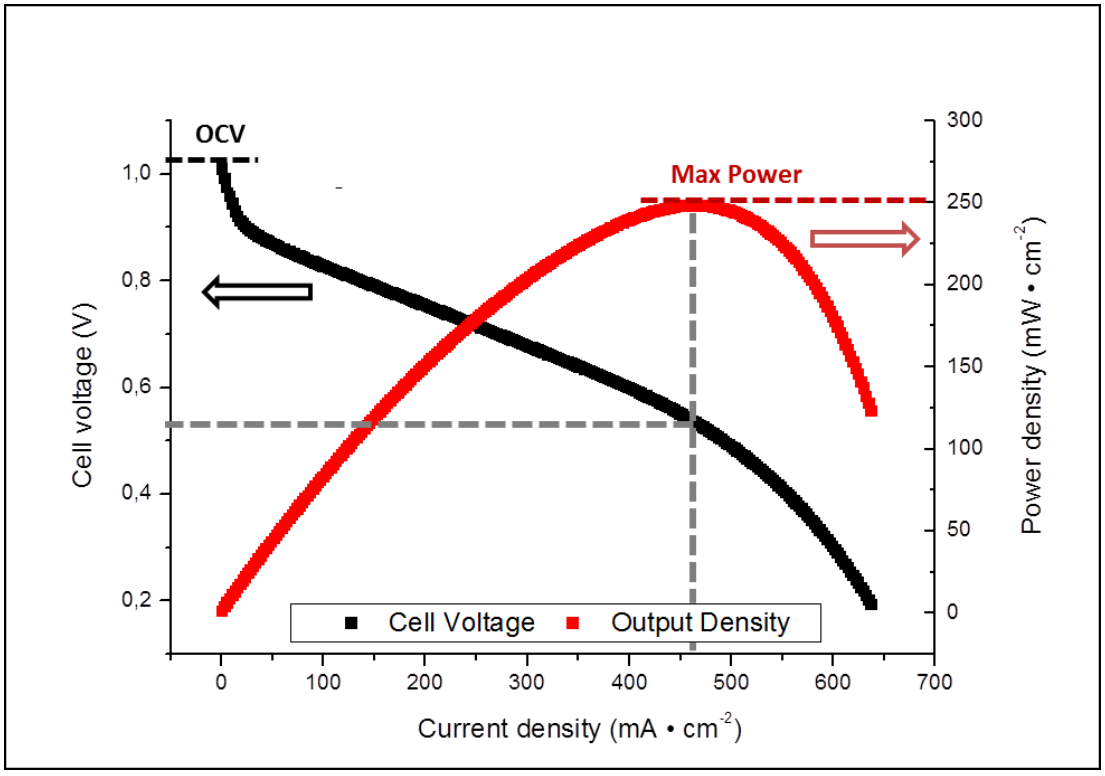

Fig. 6.1: Typical result of testing of PEM FC. The *Open Circuit Voltage (OCV)* and a maximum power are marked. The graphical determination of voltage at maximum power is illustrated.

With respect to fig. 6.1 it is seen a general obvious phenomenon that power increase with decreasing cell voltage up to its maximum. However, should be noted that efficiency of fuel cell decreases with decreasing cell voltage as it was explained in the section **??**. So the real practical use is about the balance between the efficiency and power density and specific power density that is wanted.

6.2 Cyclic voltammetry

The *cyclic voltammetry* (CV) is derived from polarography which is method that was discovered by Czech Jaroslav Heyrosvký who was awarded for this invention by the Nobel Prize in 1959. The CV belonges to the group of potential-dynamic electrochemical experimental methods. The investigated surface is placed in the electrolyte and it is called the working electrode. The general schema of setup is in fig. 6.2 on the left. The voltage on the working electrode is measured relative to the reference electrode. The current thrgough the working electrode and counter electrode is applied with respect to the voltage between the working electrode and the reference electrode. The reference electrode is usually made from silver-silver chloride (Ag-AgCl) or calomel (Hg_2Cl_2, SCE) and more. The counter electrode can be simply made from Pt and support for working electrode is usually consisted of glassy carbon, carbon paste, Au, Pt and crystals that are coated with investigated catalytic powder.

The CV measurements are performed with using potentiostat following way: the voltage at working electrode related to the reference electrode is periodical-

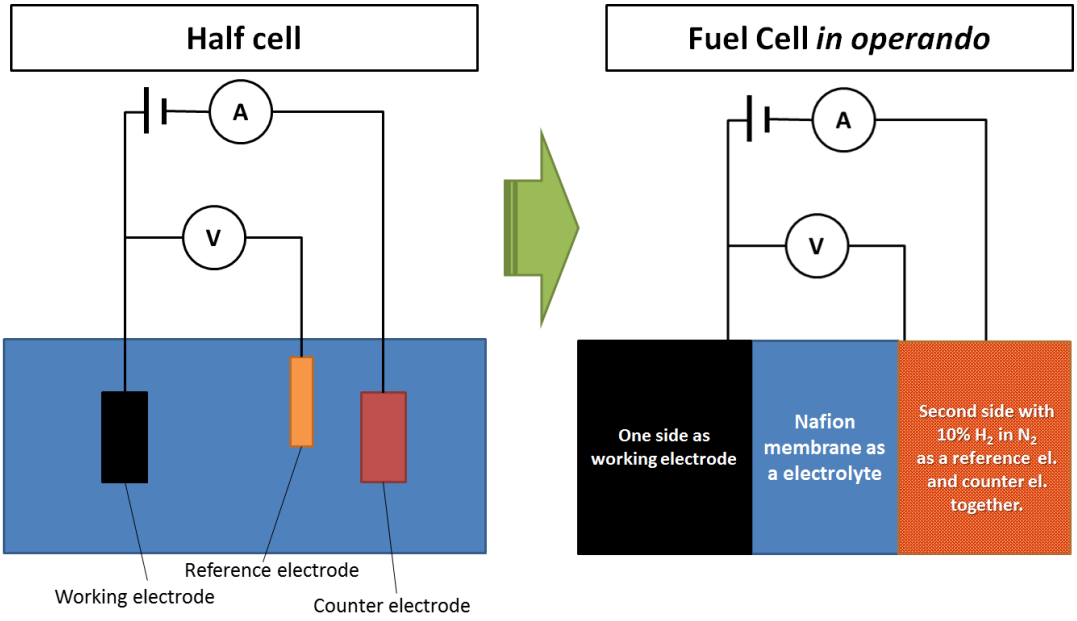

Fig. 6.2: The illustration of experimental setup for cyclic voltammetry (left) and its adaptation for *in operando* measurement in fuel cell directly (right). Setups are consisted of working electrode (■), reference (■) electrode and counter electrode (■) placed in electrolyte (■). In the case of setup for *in operando* measurement the reference electrode and the working electrode are shared and they are represented by one side of the fuel cell (■).

ly cycled between two values (see the fig. 6.3 top) while the current through the working electrode changes accordingly. The first half of cycle is called the forward scan (voltage increases) and the second part of cycle is the reverse scan (voltage decreases). The scan rate is generally from 10 to 200 mV s^{-1}. The current dependency on such a voltage of the periodic triangle wave is called voltammogram. Because of space reason the cycling voltammetry was briefly only explained. For more information about this method see [117].

For the needs of catalyst investigation of fuel cell it was better to use CV directly in fuel cell without the disassembly of the cell. The experimental setup is explained by illustration in fig. 6.2 right. As a working electrode is used the side of fuel cell with catalyst of interest under nitrogen atmosphere. As the reference electrode is used the opposite side of a fuel cell filled with a mixture of 10% hydrogen and 90% nitrogen. With regard to the fact that the catalyst is Pt based, the platinum dynamic hydrogen reference electrode is created. As the electrolyte is used ion-conductive membrane (Nafion). During my study all *in operando* voltammograms were determined this way.

The example of voltammogram which was obtained *in operando* in the fuel cell directly in the case of our Pt reference sample is shown in fig. 6.3 bottom. Let's briefly explain what can be seen. First, in region 0-0.4 V hydrogen is desorbed from the catalyst surface. Then while the voltage is increasing all hydrogen atoms left the surface but the voltage is still too low to attract the anions from the electrolyte. When the voltage increases enough, it is higher than 0.75 V (maximum at 0.81 V), the Pt surface stares oxidizing by reductive species as OH^- and for higher voltage simply by O^{2-} and Pt-OH and PtO are formed, respectively. When

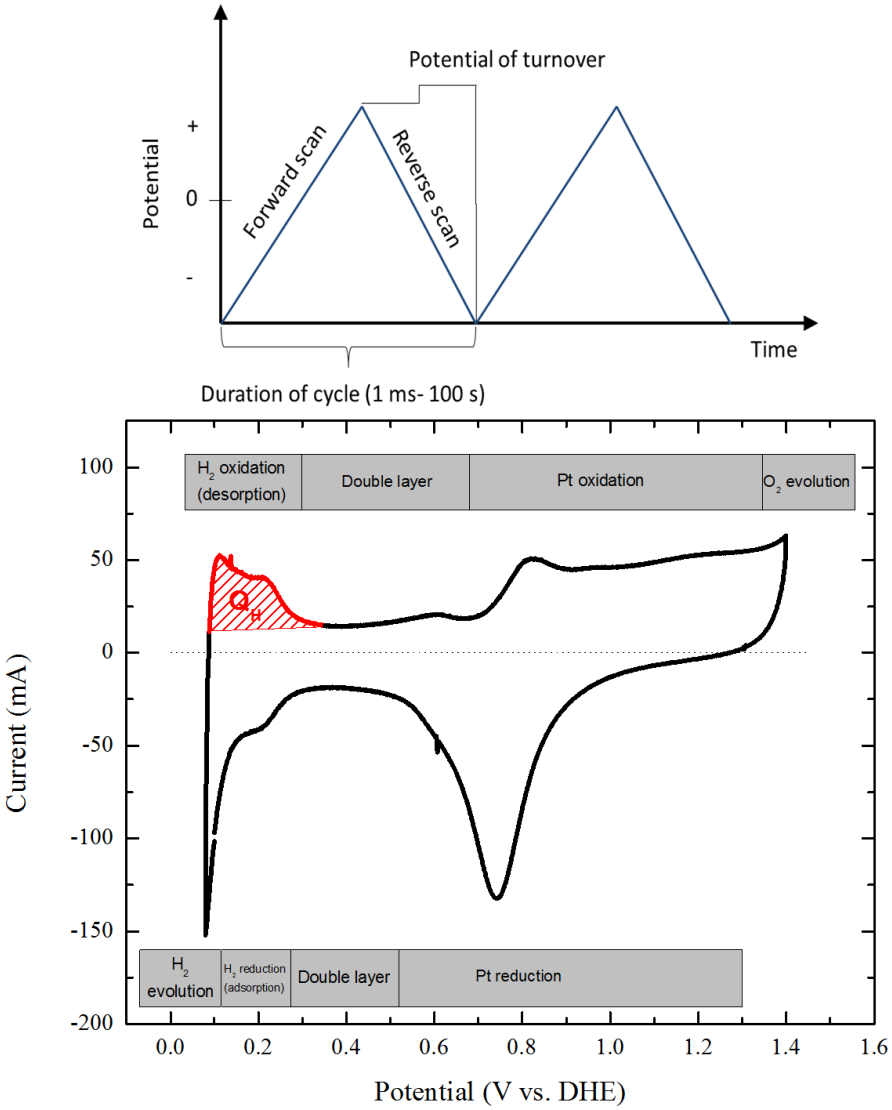

Fig. 6.3: The illustration of the periodic triangle wave of voltage between the working electrode and the reference electrode (top). The example of voltammogram of the commercial Platinum anode obtained *in operando* in a fuel cell (bottom). The scan rate is $100\,\mathrm{mV\,s^{-1}}$. The specific regions of Pt voltammograms are labeled. The hatched area represents integrated part of voltammogram used for determination of charge Q_H of adsorption of one monolayer of hydrogen cations.

the voltage reaches the thermoneutral voltage for electrolysis (1.45 V) the oxygen evolution startes to be possible and for higher voltage the oxygen evolution is appeared. When the voltage starts to decrease, the oxygen evolution is stopped and Pt surface starts to be reduced at voltage lower than 1 V (maximum reducing peak appear at 0.75 V). During the next decrease of voltage again no reaction appears on the surface because the voltage is still too high to attract the cations from the electrolyte but already low to attract anions. When the voltage decreases below 0.4 V the hydrogen cations adsorption (H_3O^+) is appeared and below 0 V the hydrogen evolution is started. The region between 0.4 V and 0.6 V is called *double layer region* because no reaction appears on the surface and the current is

caused by charging of capacitor created by this double layer.

It should be noticed that the difference between oxidizing and reducing peak of Pt is equal to $0.81 - 0.75 = 0.6\,\mathrm{V}$ which is in agreement with theory: $2.3\frac{RT}{zF} = 59\,\mathrm{mV}$ (at $25\,^{\circ}\mathrm{C}$) for one electron ($z = 1$) reversible *redox* couple.

Additionally, voltammogram contains more information about the catalyst. Focusing on the hydrogen adsorption/desorption region (0-0.4 V) the electrochemically active surface area (ECSA) could be estimated. Assuming monolayer adsorption of hydrogen cations on the surface (it is good physical reason for this assumption) the charge which is needed for desorption of such adsorbed hydrogen can be determined with use of red hatched area 6.3. The charge needed for desorption of monolayer of hydrogen cations is given as follows

$$Q_H = \frac{A_H}{S_r} \tag{6.3}$$

where A_H is the integral of the red hatched area in figure 6.3 after subtracting the charge of double layer and S_r is the scan rate. The specific charge of Platinum is known $Q_{spec} = 210 \cdot 10^{-6}\,\mathrm{C\,cm^{-2}}$ so the electrochemically active surface area of catalyst can be expressed as

$$ECSA = \frac{Q_H}{Q_{spec}} \tag{6.4}$$

The obtained value can be divided by loading of Platinum. Sometimes the determination of A_H is much more difficult than in the presented case. The electrochemists do not agree on the accuracy of absolute value of ECSA determined by this way. Be that as it may, the relative comparison still makes sense. Especially, for comparison of voltammograms obtained with the same scan rate the comparison of maximal current of features is also possible.

Similarly, the ECSA can be determined using so called CO stripping, which is method based on CO uderpotential deposition (UPD); the adsorbed CO is desorbed and the charge of desorption is integrated but the specific charge of Platinum is two-times higher in the case of CO.

It should be noted that for our Pt doped oxides catalyst the determination of ECSA is not correct principally due to fact that specific charge of our catalyst material is unknown.

6.3 Crossover determination

As it has been already explained in chapter 3 the crossover of hydrogen from the anode side to the cathode side could cause dramatic decrease of performance of fuel cell. For these reasons, it is necessary to keep this phenomenon under control.

The physical cause of this drop of performance is given by hydrogen molecules that passed through the ionomer membrane to the cathode side where they were dissociated on the cathode catalyst as it was on the anode side and react with oxygen to form water without electron charge transfer along external electrical circuit. However, the reaction runs on the surface with the hydrogen which is adsorbed on it so under appropriate potential the charge transfer of adsorbed hydrogen and surface can be measured.

This is indeed possible and the experimental setup is as follows. The anode is filled by hydrogen as it is at normal operating condition but the cathode is filled by pure nitrogen flow (30 sccm[1]) which is free of oxygen. The experimental setup is same like for CV experiment *in operando* as it has been described in the previous section (6.2 in figure 6.2 right) apart from the hydrogen mixture on the anode side, in this case fuel at operating condition is used (pure hydrogen). From the potentiostatic point of view the measurement is also same as it was for CV measurement but, in contrast, the first quadrant is used only and the linear sweep rate of potential is much smaller ($0.5\,\mathrm{mV\,s^{-1}}$). The current corresponds to crossover effect is obtained as current at potential in the middle of the region of hydrogen adsorption/desorption, at 0.22 V, where the hydrogen adsorption and desorption are in the balance.

The illustration of the crossover determination is shown in fig. 6.4. Hydrogen is at low potential (100 mV) adsorbed and dissociated on the cathode catalyst. When the potential is increasing the H^+ are going out of the surface as a H_3O^+. As potential is growing up more H^+ are leaving the surface. When current is stable (plato) the adsorption and dissociation (H_2 is dissociated because potential is low; lower then UPD) of H_2 is equal to desorption and the current divided 2 means exactly the H_2 transfer through membrane. Ought to admit that no all hydrogen passed though the membrane to the cathode side is adsorbed and dissociated by potential but only adsorbed hydrogen that could react with oxygen cause the current loss in operated fuel cell. Thus, from this point of view, this method calculates exactly the crossover current that we are interested in.

6.4 Impedance spectroscopy

For better understanding of inner processes of electrical sources the impedance spectroscopy (*electrochemical impedance spectroscopy* EIS) can be used. The principle of the EIS is illustrated in figure 6.5 top. The working point is set and sinusoidal waveform is added. The amplitude of wave should be low to prevent an influence of chemical processes, less than 10 mV or equivalent of current. The current of the cell can be expressed as

$$i = I_{DC} + I_m sin(\omega t) \tag{6.5}$$

where I_{DC} is current working point, I_m is a current amplitude, ω is angular frequency and t is time. The voltage of the cell is given analogously as follows

$$u = U_{DC} + U_m sin(\omega t + \theta) \tag{6.6}$$

where U_{DC} is the voltage working point, U_m is the voltage amplitude, θ is the phase shift between current and voltage. Impedance spectroscopy can be current controlled *galvanostatic* GEIS or voltage controlled *potentiostatic* PEIS. One of the quantities 6.5 and 6.6 is controlled and the other one is dependent on it.

Assuming Ohm's low the impedance can be expressed as

$$Z = \frac{u}{i} \tag{6.7}$$

[1]The unit sccm means standard cubic centimeter per min. Sometimes the unit mL $\mathrm{min^{-1}}$ are simply used where is supposed that volume is also standard volume.

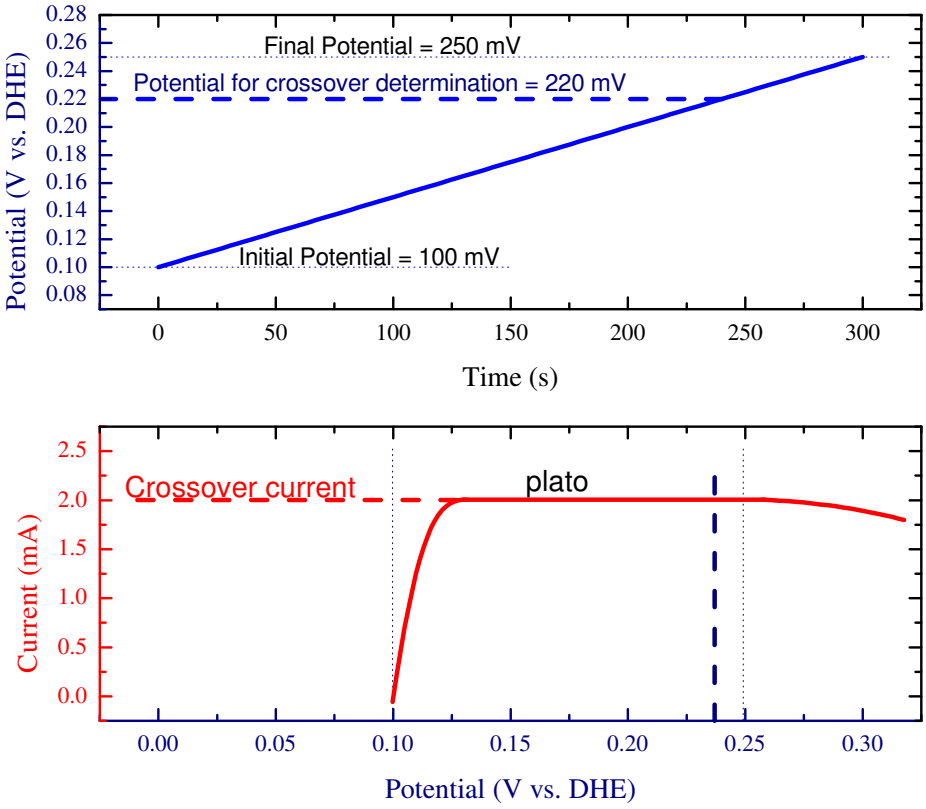

Fig. 6.4: Illustration of determination of crossover current. The time dependency of potential for linear sweep (top) and its corresponding current dependency on potential (bottom). The crossover current and potential are marked; additionally initial and final potentials.

where impedance is a complex number. Example of determined impedance is shown in figure 6.5 bottom in its natural axes, which is called Nyquist plot. If the cell is characterized by impedance, the cell behavior must be explained by analogy using electronic components as it is shown in fig. 6.5 below plot. Resistance R_1 is usually called internal resistance R_i of the cell and represents the shift of spectrum on real-part axis. This spectrum contains information about the systems frequency response. On the left there is the response of the fast process which is anode activation and its reaction rate; for the lower frequency it is seen the response of the rate of cathode reaction and for lower frequency (more on the right) the effect of diffusion is seen. However, the determination of analog electronic scheme with physical meaning is not an easy task and even if the electronic model is known it has bad convergence because it is a complex problem. The one of the models used in this work is shown in figure 6.5 bottom where the physical meaning is described. R_1 represents mainly the resistance of ion conductive membrane as internal resistance R_i. Parallel combination of R_2 and constant phase element CPE_1 correspond to the anode reaction rate, parallel combination of R_3 and constant phase element CPE_2, R_3 corresponds to the cathodic reaction rate and warburg element W_{w1} represents the diffusion. The inductance L_1 is additional inductance for better convergence of the model.

The calculation of phase shifts/phase angle, power factors and plotting Bode

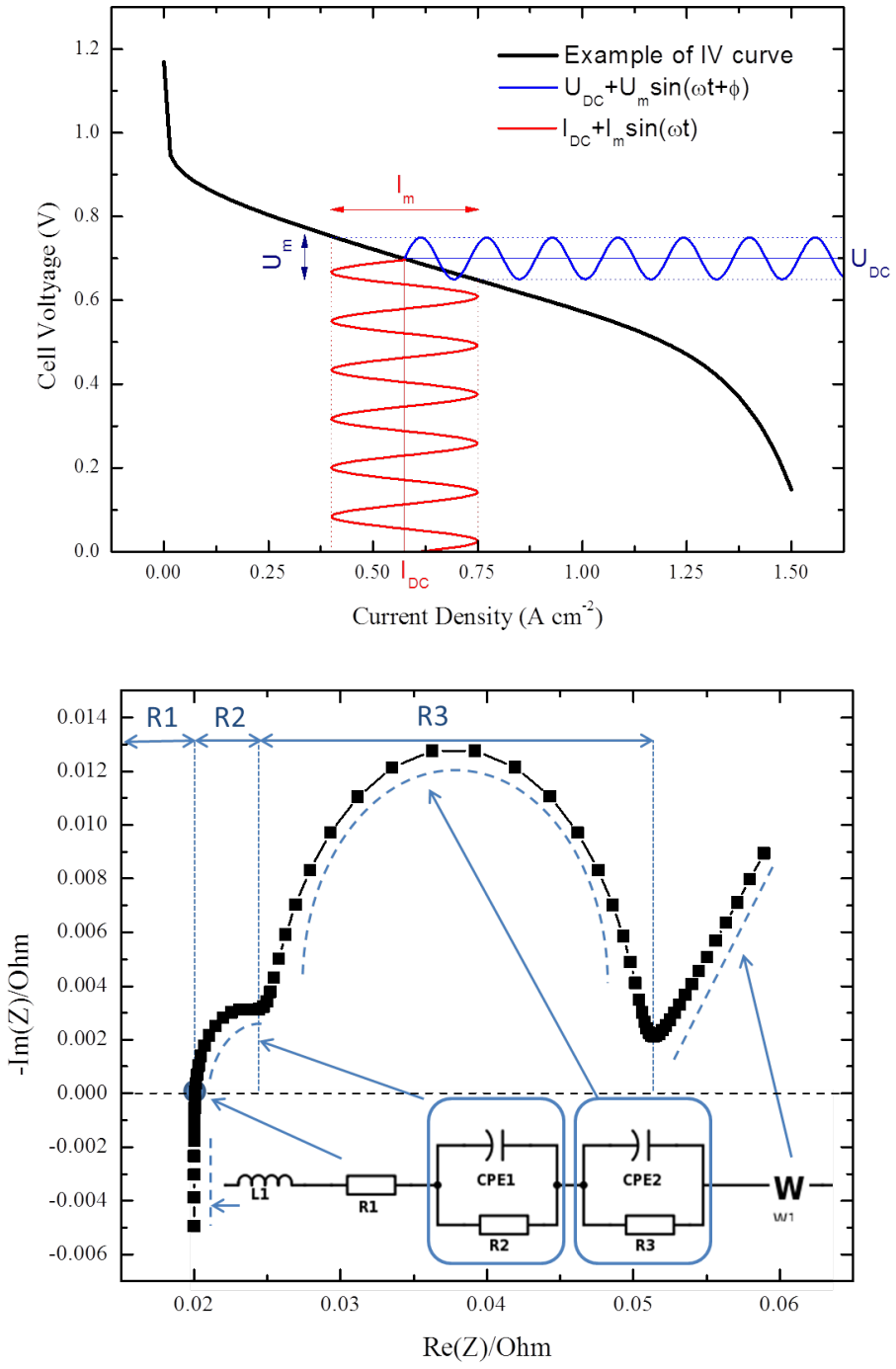

Fig. 6.5: The illustration of determination of electrochemical impedance spectroscopy (top); the potential or current working point is periodically changing using harmonic sinusoidal waveform. In the bottom figure there is Nyquist plot as a typical result of impedance spectroscopy measurement for PEM FC single cell; on the x-axis there is a real part of the impedance and on the y-axis there is in the negative imaginary part. The analogy based on the use of electronic conventional passive components is shown.

plot are not shown here because it is basic knowledge of complex numbers.

6.5 Test protocol

The testing protocol of presented samples in this thesis is based on the publicized protocol of fuel cell measurement U.S. Fuel Cell Council (USFCC) [118], information that was given personally in SolviCore GmbH & Co. KG (currently Greenerity GmbH) and our own invention.

In figure. 6.6 the scheme of fuel cell testing is shown. Individual procedures are described in the following list.

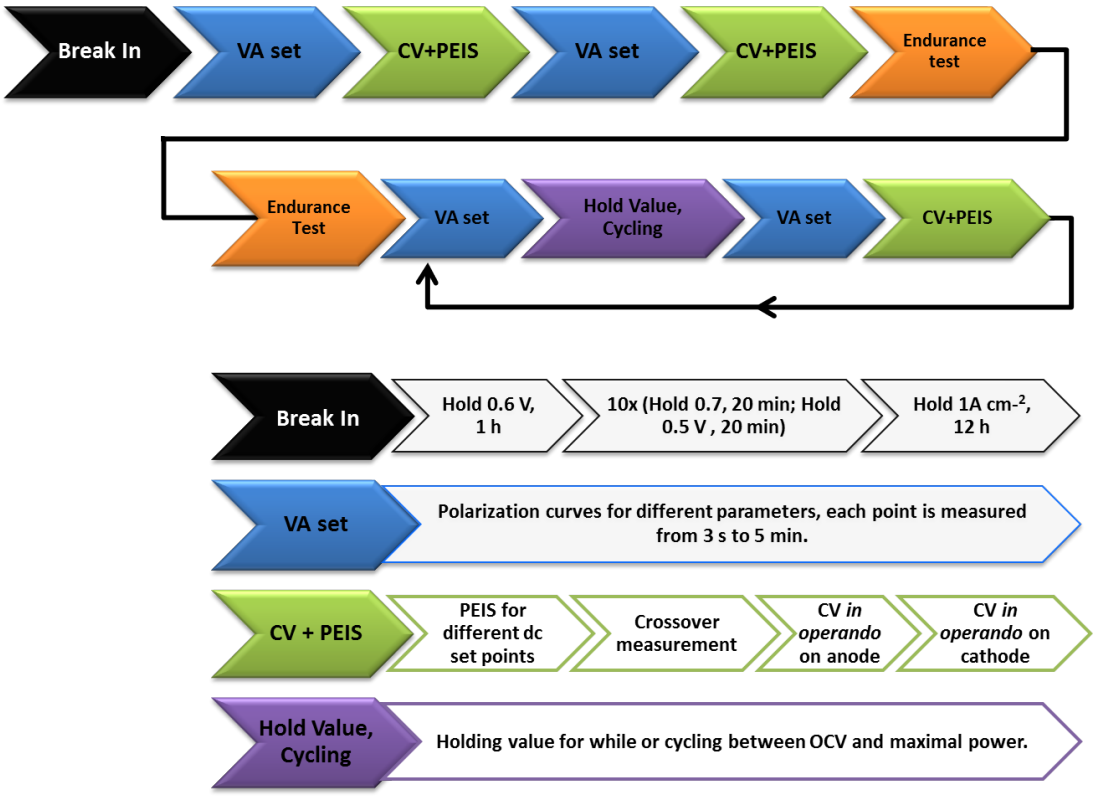

Fig. 6.6: The scheme of protocol of measurement in fuel cell. In top part is diagram of procedure and the descriptions of individual procedures are listed in bottom part.

- The first step is humidification of membrane. For several hours (4 hours at least) is used nitrogen of 100% RH for humidification of the membrane.

- The next step is *Break-In* which is procedure for starting the cell before the relevant data are obtained. At the first, the voltage of 0.6 V is held for 1 h. Secondly, 10 cycles which are consisted of voltage hold of 0.7 V for 20 min and voltage hold of 0.5 V for 20 min. Last, the current of 1 A cm^{-2} is held for 12 hours. Thus, the Break-In procedure takes almost 20 hours.

- In this step the set of IV curves are determined (in figure labeled as VA set). More than dozen polarization curves with different parameters are obtained. The measurement time for each point (current step) in polarization curve is various from 3 s over 5 min to 20 min. In this work this measurement time is 3 s unless otherwise stated. Obtaining of IV curves is current controlled with current step 0.5 mA unless otherwise noted.
- The next step is determination of potential electrochemical impedance spectroscopy.
- Then crossover current is measured.
- In this step the cyclic voltammetery is obtained. Despite of the fact the anode side is investigated mainly both side of fuel cell are checked.
- Following is the measurement of the IV curves as it was described 4 bullets above.
- Last step is the endurance test which was optional. The endurance test consists of PEIS, crossover determination, CV on both sides of cell followed by two sets of IV with the hold current/hold voltage or special accelerated procedure for longer time as durability test as it is illustrated in figure 6.6. The accelerated procedure is switching between maximal power and unloaded cell. These procedures are repeated until the degradation is appeared.

7. Experimental Setup

7.1 Basic Experimental Setup

At the beginning of my doctoral study the experimental setup presented for fuel cell measurement in [119] or published online in [120] was used and some data were obtained using this experimental setup. For better control of operating conditions during fuel cell test the test station was upgraded. The scheme of the experimental setup for fuel cell testing is shown in figure 7.1. All gases are humidified before entering the cell. Back pressures regulators set the working pressures in the cell. The cell and humidifiers are heated by heaters with PID[1] controller to set its temperature working point.

The possible inlet gases are hydrogen, additive, nitrogen for anode and oxygen, air, nitrogen for cathode. Nitrogen is included to experimental setup because of purging by nitrogen or for electrochemistry experiment as CV 6.2 or PEIS 6.4. The methanol line with its humidifier (on the right in figure 7.1) was installed because of methanol poisoning experiment. As an electronic load the BK precision 8500 was used. All parameters as temperature, pressure in cell, current and voltage are controlled by computer with software already developed during the

[1]Controller calculate the error between setpoint and process variables and applies the correction to reach the setpoint value. The determination of correction is based on proportional P, integral I, and derivative D terms which give their name to the controller type.

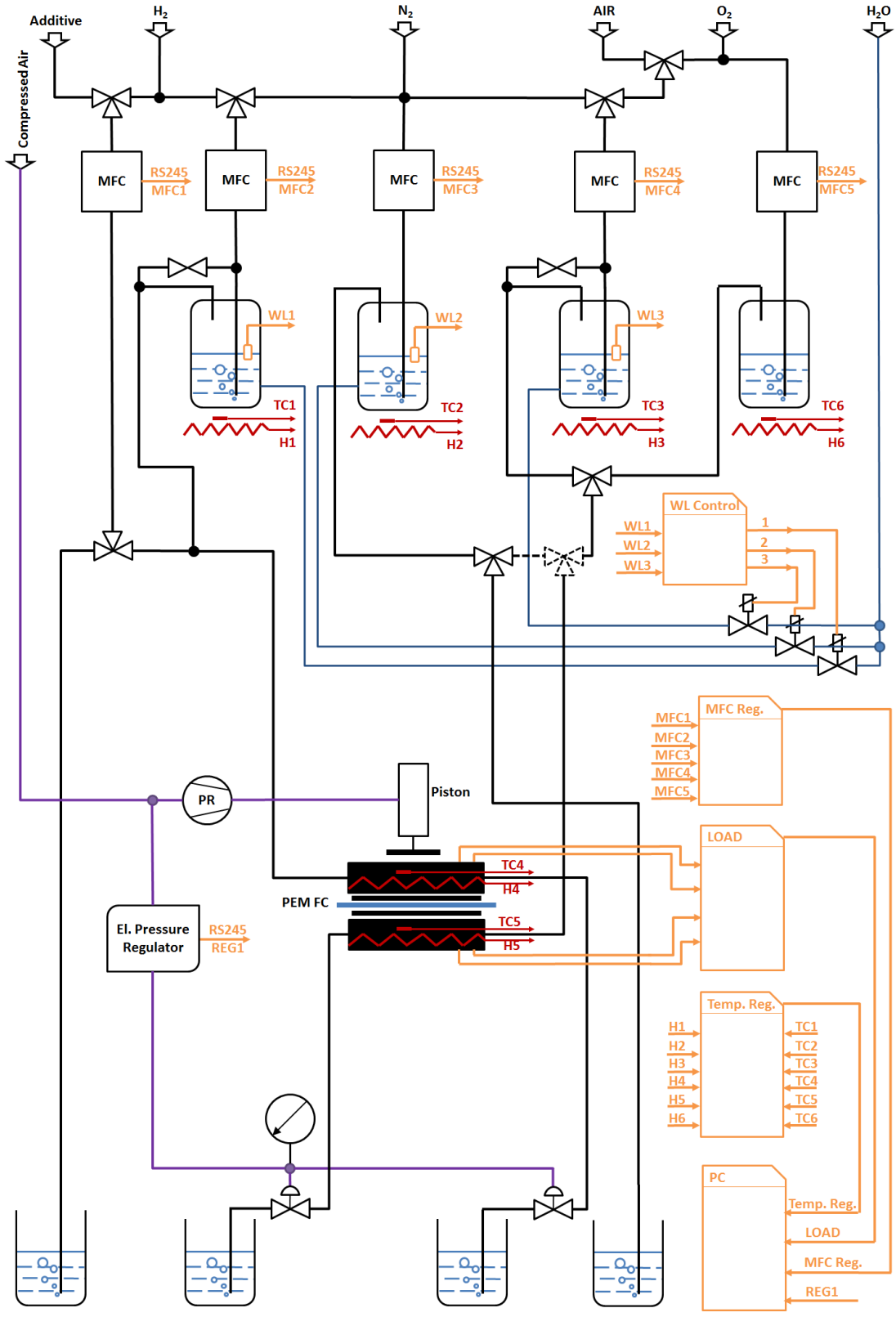

Fig. 7.1: The scheme of the experimental setup for testing of PEM fuel cell. **PR** symbolizes manually operated pressure regulator. The valve with dashed lines is realized by manual re-connection of tubes. Similarly, the cell connection can be easily reconnected for needs of experiment.

master degree which was extended by option to programmable own batch of operation and processes. All valves are manually operated apart from two for additive gas selection. Automatically operated valves are also used for filling of water in humidifiers. The cell inlets and outlets are connected by SuperLock® connectors enabling fast re-connection so the cell can be easily reversed or reconnected for electrochemical measurement. The technical pressed air is used as reference for backpressures and it is also used for piston cell which is described in the next section 7.2. During the study the thousands of IV curves were obtained so some program for post processing analyses should have been developed. The program for data processing was written in C++ with the use of libraries in Origin® from OriginLab and it was compiled directly by compiler provided with Origin 8.5.

7.2 Design of Piston Cell

For an appropriate control of working conditions of the cell we decided to use our special design piston cell 7.2 (right) instead of cell tightened by bolts. The design was derived from similar solution from GreenLight, Ltd. Additionally, this cell enables to perform tests depending on the pressure.

The limits of operating conditions are given by the pressure limit of a piston and temperature limit of silicon *o-ring* gaskets: 10 Bar, 150-200 °C which is enough to meet the fuel cell testing ranges: up to 8 Bar and up to 80 °C. The normal operating condition used in this work is 8 Bar and 70 °C.

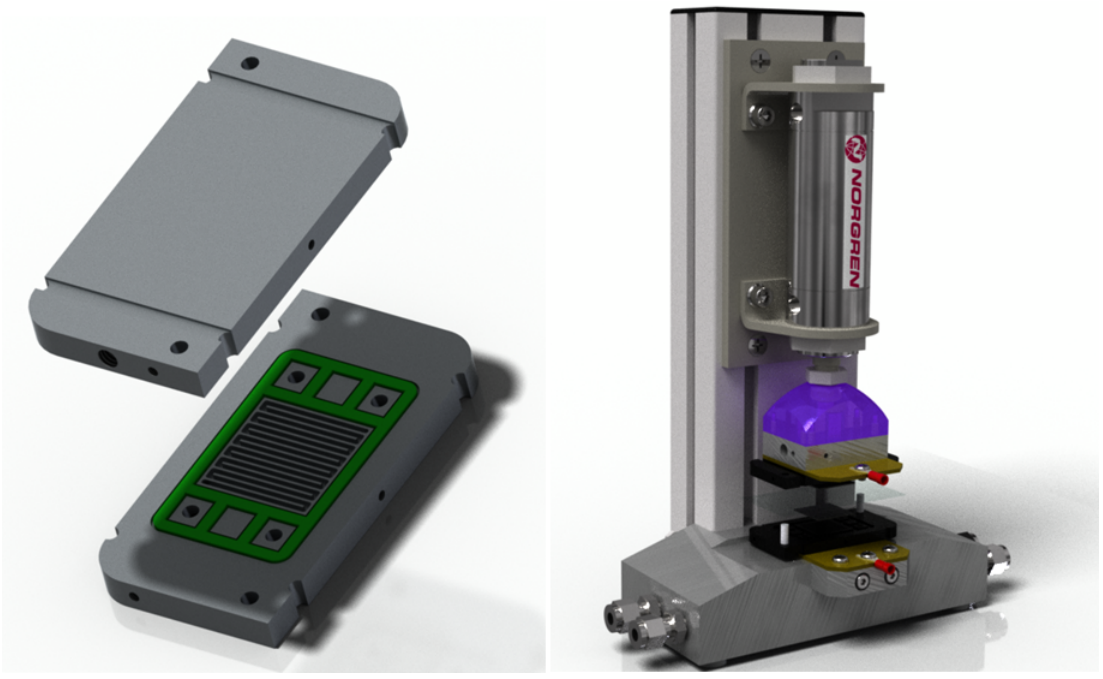

Fig. 7.2: The 3D model of our own piston device for testing of single fuel cell (right) and 3D model graphite plates used as a gas distributors (left).

This device enables better control of operating condition in comparison with bolt tightened cell and additionally the quick change of tested sample is possible.

New design of cell needs new design of graphite plates as gas distributors. The 3D model of graphite plates is introduced in figure 7.2 (left). The active area is 5

cm^2 normally used for samples of $(2.1 \times 2.1)\,cm^2$ as a channel was chosen a single serpentine. Between these two graphite plates the membrane electrode assemble (MEA) is clamped and sealed by silicon gaskets (in figure colored by green).

The PEM FC stack was designed at the end of the study so there was not time to obtain some results with the use of it. Be that as it may, the 3D models of designed stack is in the attachment VII.

7.3 Design of Automatized Test Station

It is obvious that testing of fuel cell that usually run 24 h per day and 7 days a week is also very time consuming for operator. The upgraded test station presented in the section 7.1 help to user with automatic water refilling in water management and the SW helps to use basic batch protocol experiment and the new piston cell described in the previous section helps to control operating conditions. However, all valves were still manual operated and for electrochemical experiment was user's attendance necessary because gases have to be changed manually and potentiostat must be connected. We should not forget that the electrochemical experiments like CV, crossover and PEIS should be performed in the same point of testing protocol which sometimes (often) means night measurement of CV or impedance spectroscopy. Based on these facts we decided to develop full automatized *"push & play"* test station which could save time of users.

In this section it is presented the result of our development. The simplified scheme of fully automatized test station is seen in figure 7.3. All valves are operated automatically. The pressure control and gas selection and mixing arrangement and water management are automatized. Besides automatization of mechanical parts, the test station contains humidifier for pure nitrogen which is ready for electrochemical experiment immediately. Thus, after installation of the cell and selection of the test protocol 6.5 and pushing *"run"* all experiments including electrochemical measurement like CV, PEIS, crossover determination are processed without user participation. The proposed design of automatized test station contains more than 600 unique individual parts in form of 3D model and the assembling contains 2130 parts so more explanation is not shown here due to the space reason. The test station is on the marked now and the technical specification can be also seen online on the web page: `http://www.lean-cat.com/fuel-cell-test-station`. Additionally, our own humidification system, back pressure regulating system and piston testing cell (already introduced in 7.2) were designed.

This test station has been multiplied ten times and in our current laboratory was not space anymore so the new laboratory was designed. Some parts of technical proposal of laboratory are presented in the attachment VII.

However, there was no time to obtain any data for needs of this thesis with the use of this new designed automatized test station.

All 3D models and technical drawings have been created using Autodesk® Inventor.

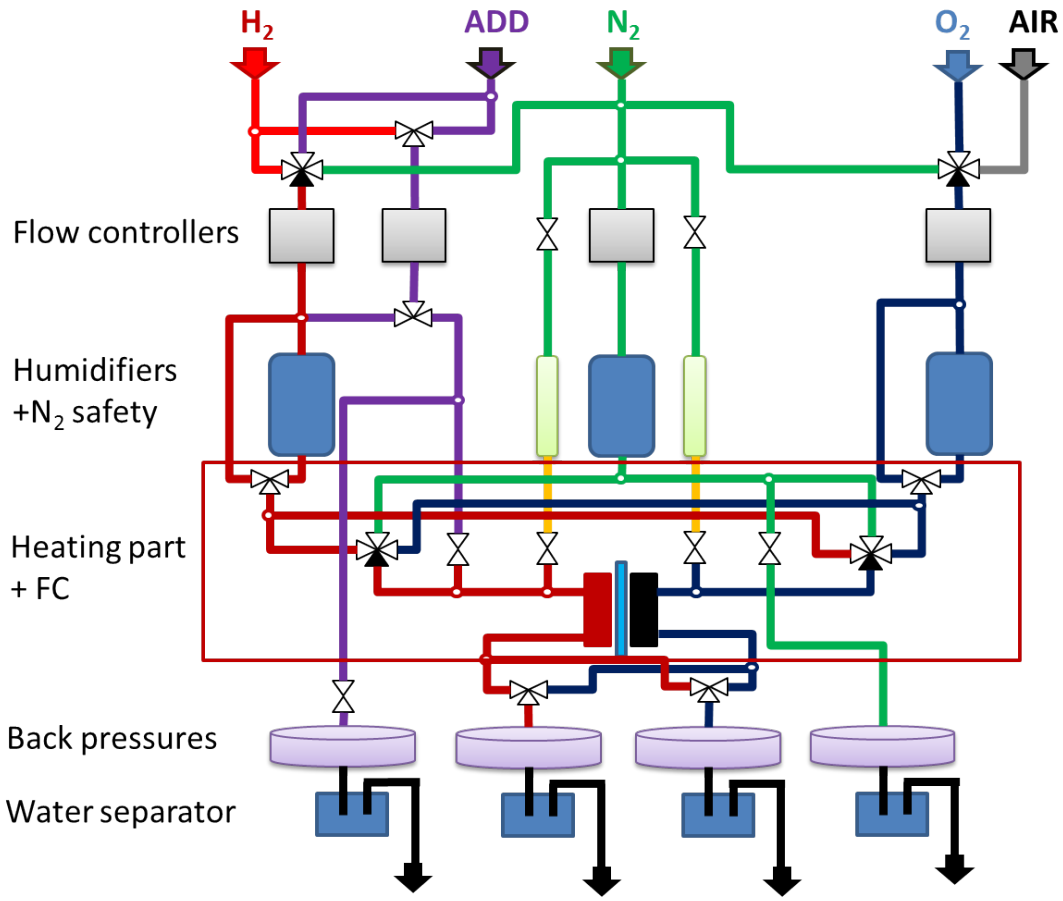

Fig. 7.3: The simplified scheme of automatized test station. Five main modules are labeled: flow control and input tracing of gases, humidification system, heating system and cell input gas tracing, back pressure control and water separator with automatic water filling system.

7.4 Equipments and Materials

Main materials and devices used in laboratory experiments are listed in the table 7.1. The errors of voltage and current determination do not effect on the results and they were estimated less than 1%. Error of of obtained power densities, internal resistance, crossover current are about ∼5% (less than 10%) and they are given by statistic analyses of repeated experiment. The error of determined metal loading by photoelectron spectroscopy is about ∼ 30% due to big uncertainty of obtained elements ratio with the use of this methode. A notation of temperature condition of fuel cell experiment was used: $T_1/T_2/T_3$°C where T_1 is the temperature of the anode humidifier, T_2 is the temeprature of the the cell and T_3 is the temeprature of the cathode humidifier. The gas flow rate is given unit sccm which is standard cubic centimeters per minute.

X-ray photoelectron spectroscopy (XPS) was performed in an ultrahigh vacuum (UHV) experimental chamber operating at base pressures $< 5 \cdot 10^{-10}$ mbar and equipped with a SPECS Phoibos MDC 9 electron energy analyzer and a dual Mg/Al X-ray source.

Morphology and structure of samples were observed by means of *Scanning Electron Microscopy (SEM)* Tescan MIRA I or MIRA III microscope operating at 10-30 keV electron beam energy.

Transmission Electron Microscopy (TEM) using the 200 kV JEOL 2100F microscope with a Scherzer resolution of 0.19 nm. The samples for TEM observation have been prepared by using Focus Ion Beam (FIB) (Tescan LYRA FIB-SEM) technique of thin lamellas cut from the catalyst films (not by me but by colleagues J. Lavková).

Electrochemical analyses as CV i EIS, linear sweep were performed by potentiostat Bio-Logic SP-150 and increasing of current range to 10 A the Booster Booster VMP3B-10 was used. Usual scan rate for CV was 100 $\mathrm{mV\,s^{-1}}$.

8. Samples Preparations

Samples with thin catalyst layer were prepared by rf-magnetron sputtering. Magnetron sputtering is a physical vapor deposition method which is generally known method in this field and more information about this method can be found in [121, 122].

The basic principle of sputtering is illustrated in figure 8.1. The deposition is performed at lower pressure with special atmosphere which is usually Argon. Magnetic field around magnets has an influence on electron's trajectory (Lorentz-force) in this region and transform it to the spiral. Hence, the probability of gas ionization is maximized at this point, and due to applied stress, glowing discharge occurs and plasma is formed in this area. Cations hit the target and if the energy is high enough atoms of target are released. The sputtered atoms condense at the surface of a substrate, which is placed in front of the target.

The preparation of composite catalyst layers were necessary for presented study. Any other material can be placed on the target in order to preparation of composite layer with two components or two magnetrons for simultaneous sputtering process can be used (see the fig. 8.1).

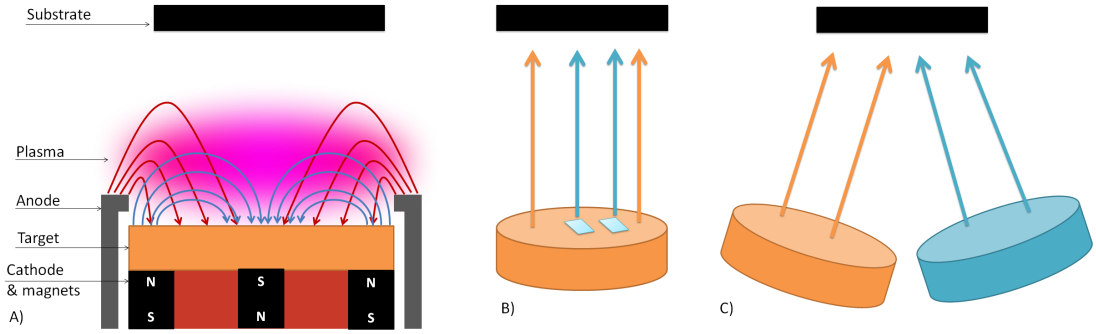

Fig. 8.1: The illustration of magnetron sputtering principle used in presented study. Basic setup (a) and illustration of simultaneous sputtering using adding material on the target (b) and with use of two magnetrons (c).

The process chamber was pumped to a residual gas pressure range $5 \cdot 10^{-5} - 2 \cdot 10^{-4}$ Pa before the process gas was used. The process gas was Ar at pressure

0.4 Pa. For sputtering of conductive material the DC current was used and in the case of non-conductive material the AC current was necessary. The AC voltage was usually in the range of hundreds volts and frequency of AC current usually was $f = 13.56$MHz, which is high frequency from the radio broadcast band which is the reason why AC current based sputtering is also called RF-magnetron sputtering.

Individual special parameters of preparation if they were used are attached in each chapter in the result parts. The thickness of prepared catalyst layers is from several nm to tens nm. The substrates were usually *gas diffusion layer (GDL)* with *carbon ionomer nanoporose layer (CIL)* as a commercial product Sigracet® 29 BC or 25 BC (see figure 8.2) which is in this work called as *nGDL*.

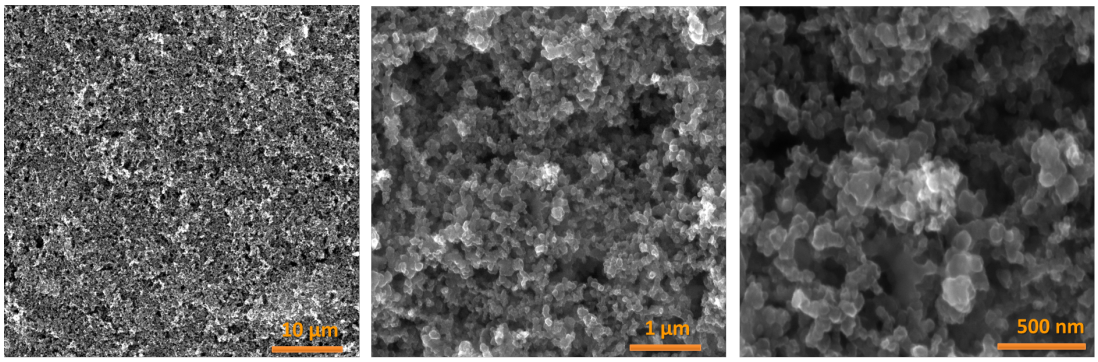

Fig. 8.2: The SEM images of commercial catalyst support Sigracet® 25 BC for three different magnifications.

Name	Description
Reformate Anode	Alfa Aesar, Platinum Ruthenium black, nominally Pt 400μg cm^{-2}, Ru 200μg cm^{-2}
Reformate Cathode	Alfa Aesar, Platinum, minimally Pt 400μg cm^{-2}
NAFION NR212	Alfa Aesar, Nafion® membrane, 0.05 mm thick, recast
nGDL	SGL TECHNOLOGIES GmbH, Sigracet GDL 25 BC or 29 BC
GDL	Gas Diffusion Layer, Alfa Aesar Toray Carbon Paper, TGP-60
CF	Graphite foil from Alfa Aesar
MWCNT	Multi-Walled Carbon Nanotubes from Sigma Aldrich
Pt,CeO2,Pd,..	sputtering targets from Kurt J. Lesker and Safina
Hydrogen	purity of 5N0
Oxygen	purity of 4N5
Nitrogen	purity of 5N0
NaOH	Penta, Sodium hydroxide
Metanol	Alfa Aesar, Ultrapure Spectrometric Grade, 99.8%
$HClO_4$	SigmaAldich, Ultrapure Spectrometric Grade, 99.8%
H_2SO_4	SigmaAldich, Ultrapure Spectrometric Grade, 99.8%
H_2O_2	Penta, Hydrogen peroxide, 30%
NAFION – solution.	Alfa Aesar, Perfluorosulfonic acid – PTFE copolymer, NAFION 5% w/w solution
H_2SO_4	Penta, Kyselina sírová, 99.97%
Peristaltic pump	VINTRUM®, PCD 22
Heaters	MANEKO LTHS 500
Heating regulators	SELEC PID 500
Mass Flow Controllers	Alicat Scientific 50
AD/DA converter	BMC Messsysteme PCI-BASE 1000
Potentiostat	Bio-Logic,SP-150 with booster VMP3B-10
Reference electrode	Ag/AgCl leak free, KRD diameter 2 mm, length 65 mm
Load	BK Precision 8500
SEM images	MIRA I or MIRA III from TESCAN

Tab. 7.1: List of main materials and device that were used in laboratory experiment.

IV Experimental Results

"Little things often harbour a great secret
- the physics of nanoword."

9. PEIS and Crossover

In this chapter the impedance spectroscopy analyses and the hydrogen crossover determination for our experimental test cell are present in order to show how the PEIS and crossover depends on different catalyst. It helps to understand results presented in following chapters. MEAs with several different anodes are examined while the cathode (Alfa Aesar with loading of $400\,\mu g(Pt)\,cm^{-2}$) as well as Nafion membrane NR212 which was used in most of our PEMFCs were kept the same.

As anode the catalysts with different loadings were studied: $300\,\mu g(Pt)\,cm^{-2}$ (from FC store), $110\,\mu g(Pt)\,cm^{-2}$ (sputtered Pt on nGDL) and $20\,\mu g(Pt)\,cm^{-2}$ (sputtered Pt on nGDL).

Procedure of crossover determination has been already described in the section 6.3. The results of crossover analyses are presented in figure 9.1 for 30 sccm of N_2(cathode) and 80 sccm of H_2 80 (anode) at 70/70/70 °C[1] and at 0.5 Bar. As a cathode Alpha Aesar with loading of $400\,\mu g(Pt)\,cm^{-2}$ was used. Linear sweep was performed from 100 mV to 250 mV with sweep rate of $500\,\mu V\,s^{-1}$. Determined crossover currents (value of current at 220 mV) were $I_{cross} = 1.27\,mA\,cm^{-2}$ for $20\,\mu g(Pt)\,cm^{-2}$ on the anode, $I_{cross} = 1.29\,mA\,cm^{-2}$ for $110\,\mu g(Pt)\,cm^{-2}$ and $I_{cross} = 1.25\,mA\,cm^{-2}$ for $300\,\mu g(Pt)\,cm^{-2}$.

Usually, crossover current less than $I_{cross} = 2\,mA\,cm^{-2}$ is good result showing good assembling of the fuel cell as it was advised by Dr. Christian Eickes from SolviCore GmbH & Co. KG. Therefore we can see that the determined crossovers in our experiments did not cross this limit.

Despite the fact that Platinum loading on the anode could be 30 times higher (according investigated different anodes), the crossover current is comparable. The reason is that crossover effect depends on the membrane parameters and due to the nature of the measurement it depends also on the cathode catalyst. As it has been mentioned at the begging of this chapter the same membrane and cathode catalyst were used for all presented measurements in this chapter therefore with respect to this fact we have confirmed that crossover effect is mainly caused by membrane and it does not depend on the anode catalyst. We admit that crossover

[1]Notation of FC temperature condition: first value is temperature of the anode humidifier, middle value is temperature of the cell and last value is temperature of the cathode humidifier.

effect can depend on an anode catalyst and its porosity but for normally used material (material used in this work) the effect of anode is negligible as we have just shown. The significance of these results for this work is discussed in the last paragraph of this chapter.

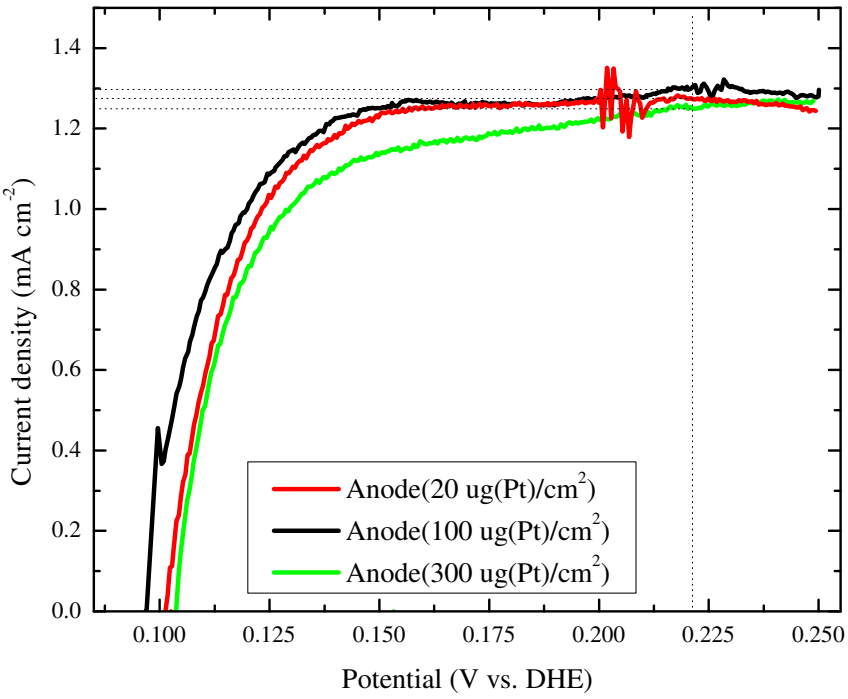

Fig. 9.1: Crossover determination for the anode $20\,\mu g(Pt)\,cm^{-2}$ (-) ($I_{cross} = 1.27\,mA\,cm^{-2}$), anode $110\,\mu g(Pt)\,cm^{-2}$ (-) ($I_{cross} = 1.29\,mA\,cm^{-2}$) and anode $300\,\mu g(Pt)\,cm^{-2}$ (-)($I_{cross} = 1.25\,mA\,cm^{-2}$). The Nafion NR212 membrane and commercial cathode catalyst with loading of $400\,\mu g(Pt)\,cm^{-2}$ were used at condition 70/70/70 °C and 0.5 Bar.

Method of impedance spectroscopy determination has been already described in the section 6.4. The result of impedance spectroscopy with the use of Nafion NR212 is shown in figure 9.2. Three different anode loadĩngs $20\,\mu g(Pt)\,cm^{-2}$, $110\,\mu g(Pt)\,cm^{-2}$, $300\,\mu g(Pt)\,cm^{-2}$ were used while a cathode catalyst was the same for all samples, commercial cathode ($400\,\mu g(Pt)\,cm^{-2}$). The operating conditions were 70/70/70 °C at 0.5 Bar. Two different working points were used, 0.5 V and 0.7 V. It is seen that individual internal resistances are equal and this test revealed that internal resistance is independent on presented catalyst loadings and on tested working points. This observation is in agreement with the theoretical assumption that the internal resistance is given by the contact resistance and membrane conductivity. Since the membrane conductivity (described in the section 5.4 is orderly lower than the contact one (gold plate and graphite plate of area of 35 cm^2) the internal resistance R_i is given mainly by conductivity of the membrane. The internal resistance is estimated $R_i = (0.021 \pm 0.002)\Omega$ and after taking account of the active area $A = 4.41\,cm^{-2}$ we obtain the internal resistance as $R_i^A = (0.093 \pm 0.009)\Omega\,cm^2$. It should be noted that the difference of

impedance spectroscopy results (arches radius) in the case of presented samples must be primarily caused by the anode properties because the rest parameters are the same or vice versa by different behaviors of cathodes due to different anode (source of hydrogen cations).

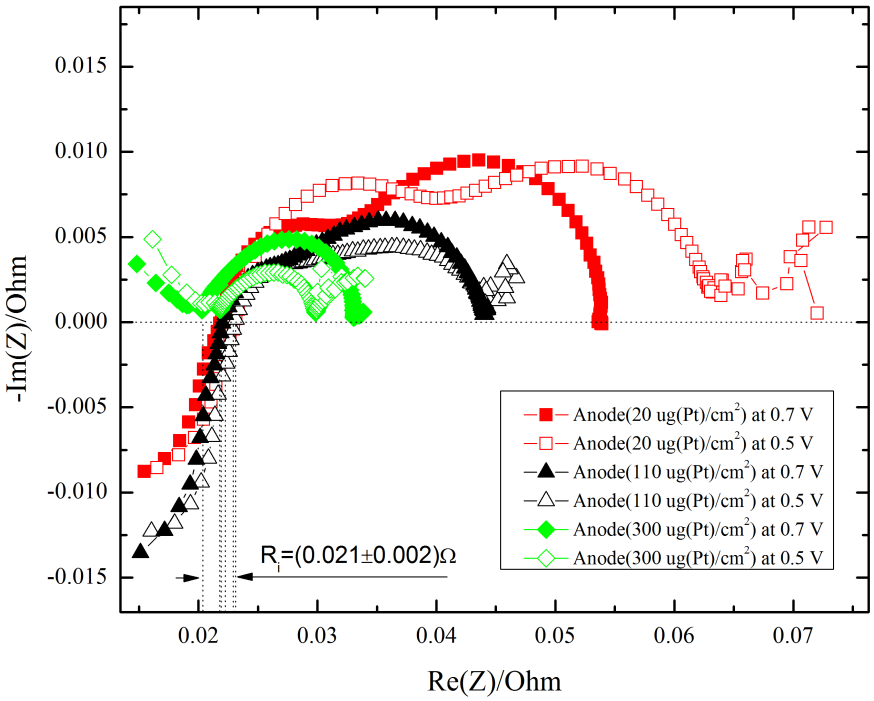

Fig. 9.2: The results of impedance spectroscopy for different anode catalysts: $20\,\mu g(Pt)\,cm^{-2}$ (-), $110\,\mu g(Pt)\,cm^{-2}$ (-), $300\,\mu g(Pt)\,cm^{-2}$ (-) at two different working points: 0.7 V with filled symbols (■▲◆), 0.5 V with no-filled symbols (□△◇). In all cases the same membrane and cathode catalyst were used: Nafion NR212, commercial cathode catalyst ($400\,\mu g(Pt)\,cm^{-2}$). The operating conditions were 70/70/70 °C at 0.5 Bar. The determined serial resistance is $(0.021 \pm 0.002)\Omega$. Frequency range was 200 kHz - 200 mHz. The active area was $4.41\,cm^{-2}$.

It can be seen that internal resistance, which is given mostly by conductivity of Nafion membrane, and crossover current, which is also the effect of the membrane, are comparable for all samples shown in this chapter. With respect to the fact that the anode catalyst is investigated in this study while the rest of conditions (the same conditions as conditions that were used in presented impedance spectroscopy) were kept the same, the obtained values of internal resistance and crossover current can be used for verification of good assemblage of the cell. Obtained internal resistances and crossover currents were similar for all samples tested in this work so impedance spectroscopy analysis and crossover determinations are not shown in next chapters due to the space reason but both analyses were performed for all individual testing samples (according to the test protocol 6.5) and used for checking of right testing conditions and proper assemblage.

10. Pt vs. PtO_x

In this chapter the use of a sputtered thin film of PtO_x as an anode catalyst for PEM FC is presented. The comparison with metallic platinum is discussed.

Samples were prepared with the use of magnetron sputtering (see 8). The deposition of Pt layer was proceeded at pressure $4 \cdot 10^{-1}$ Pa of Argon atmosphere and discharge power was set to 10 W (2.9 nm min^{-1}). Similarly, PtO_x was deposited at the same pressure $4 \cdot 10^{-1}$ Pa but in Oxygen atmosphere and discharge power was set to 10 W (2.5 nm min^{-1}). The residual background pressure before the chamber was filled by the working gas was $5 \cdot 10^{-4}$ Pa and Platinum target was used in both cases (Pt 2 inch diameter, Safina). The samples were placed 90 mm away from the target and the discharge voltage was 280 V. The thickness of both layers was equivalent of 30 nm Pt.

As a substrate and support for catalyst layers the sedimented Multi-Walled Carbon Nanotubes (MWCNT) from Sigma Aldrich supported on GDL was used. The deposition process has been already explained in my previous works [119, 123]. The nanotubes were dispersed in N,N-dimethylformamide (DMF) at a concentration of 1 mg in 30 ml and the GDL was submerged in the solution using the ultrasonic bath. Next step was an evaporation of solvent until the dry GDL coated by MWCNT was acquired (usually during one night). The obtained sedimented MWCNT are shown in figure 10.1 using two different magnification. The homogeneously dispersed carbon nanotubes are clearly seen.

The reason why we used MWCNT was to increase surface area of GDL.

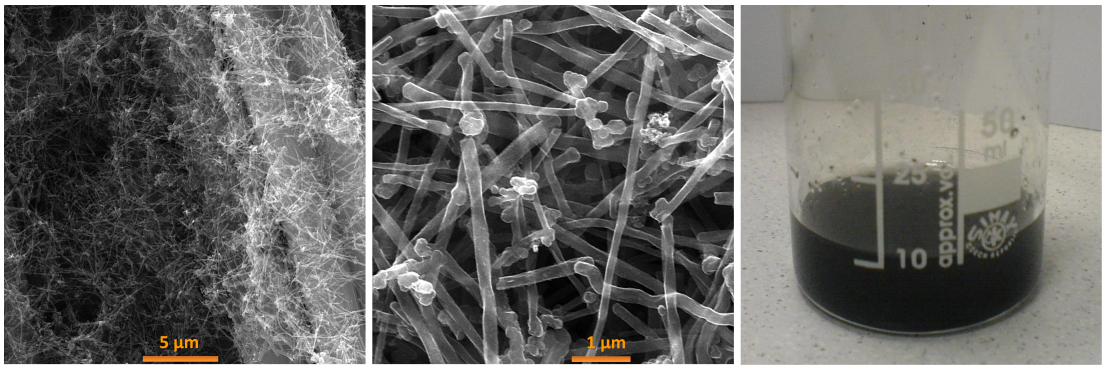

Fig. 10.1: The SEM images of sedimented MWCNT for two different magnification (left) and (middle) and photography of sedimentation process (right).

The FC testing cell used in this experiment was the cell from Quintech with active area of 1 cm^2 and the cell was tightened by bolts with the use a torque of 3 N m. This cell was already described in previous works [119, 124, 125] so the details are not shown here. As a membrane Nafion 0.125 mm thick (Alfa Aesar, Nafion NE-1035 perfluorosulfonic acid-PTFE copolymer) was used. Before the membrane was used in fuel cell the special treatment was necessary (already published in our several works [124–126]). The treatment consisted of 4 steps. First, there was 1 h long treatment in 3% solution of H_2O_2 at 80 °C to get rid of organic impurities. Secondly, the membrane was cleaned for 1 h in pure deionized water at 80 °C. Next step was 1 h long treatment with 10% solution of sulfuric acid at 80 °C in order to activate Nafion and get rid of metallic cations impurities

in sulfonic groups in Nafion structure ($SO_3^-M^+ \longrightarrow SO_3H$). Last step was cleaning by water at 80 °C for 1 h.

Presented FC analyses were performed at following conditions: hydrogen flow rate 40 sccm, oxygen flow rate 30 sccm, the pressure was ambient pressure and commercial cathode from Alfa Aesar (2 mg cm^{-2}) was used. Temperature of the anode humidifier was 70 °C and temperature of the cathode humidifier was 65 °C. The results obtained for PtO_x anode catalyst for two different cell temperatures and two different tests are presented in figure 10.2. In the top row there are results that were acquired at cell temperature of 70 °C while in bottom row there are I-V curves obtained at 27 °C (room temperature). I-V curves determined by acquiring and averaging each current step for 50 ms[1] are on the left column and on the right column there is I-V curve where each point is result of statistical analyses of 20 min time scan (*long scan* called in this work). It is shown that achieved maximum power densities for both type of scans are comparable which signalized the good stability of catalyst.

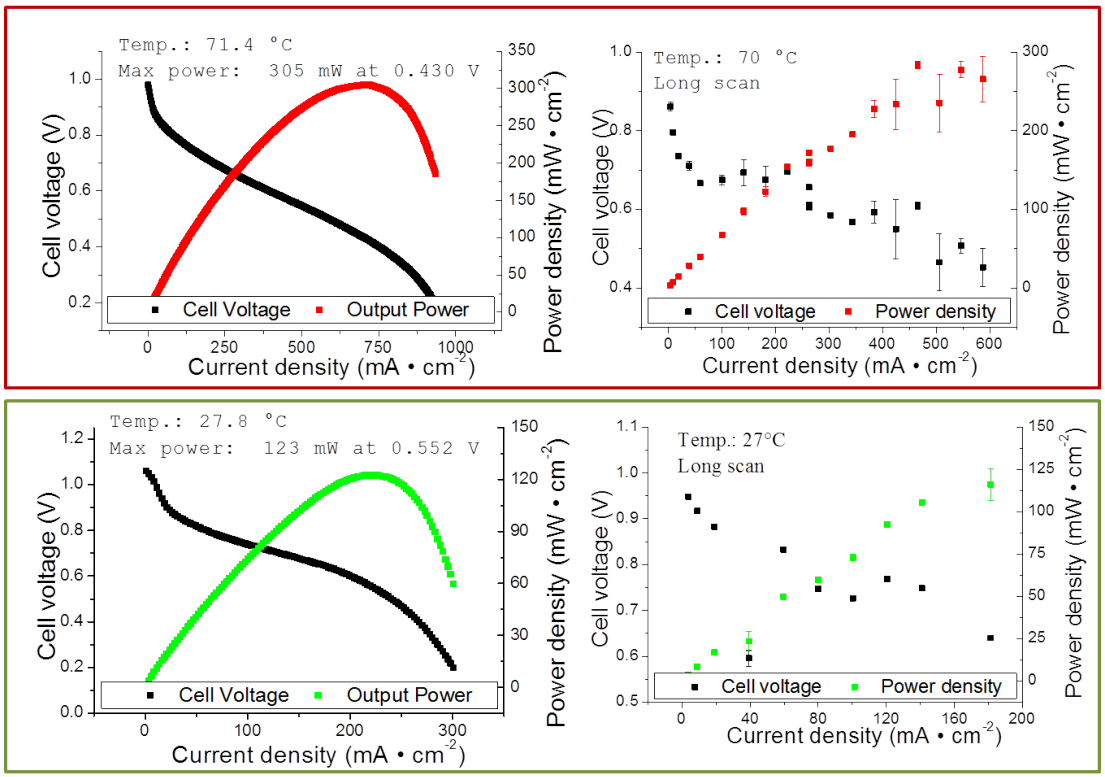

Fig. 10.2: The results of fuel cell test of Pt sputtered in oxygen atmosphere as an anode catalyst in PEM FC for two different temperatures: 70 °C (top), 27 °C -room temperature (bottom). On the left there is IV curve determined by measuring and averaging each current step for 50 ms and on the right there is IV curve where each point is result of statistical analyses of 20 min time scan (called *long scan*).

Due to fact that performance of operating fuel cell can be shortly unstable for different reasons e.g. improper water management conditions (condensed wa-

[1]There were performed analyses how the time of measuring of each current step depends on reached maximum power. The 50 ms for each point has been found as still reasonable period if the amount of points is higher because the time scan could be also long in sum and additionally it is more smooth because of small current steps.

ter appears), lack of oxygen or fuel because of insufficient diffusion; the 20 min time scans have to be analyzed properly because simple average is not sufficient method in this case. The example of result of statistical analysis of two 20 min time scans representing 2 points are shown in figure 10.3. In the top figure an instability caused by appearing of condensed water is seen and in the bottom figure an example of quite stable behavior is shown. The mean, median and weighted arithmetic mean with standard deviations and with their confidence intervals are shown. Obtained data are presented in the table and in plots: time scan (top) and distribution function (bottom). There are lots of such graphs obtained for each IV curve *time scan* (39 individual statistical analyses of 20 min *time scans* for IV curve, see figure 10.2 (top-right)).

The comparison of fuel cell tests performed at 70 °C for pure Platinum and PtO_x anode catalysts are seen in figure 10.4. The Pt loading for of 60 μg(Pt) cm^{-2} was the same for both pure Platinum and PtO_x catalysts. The recorded power densities and specific powers are summarized in the table 10.1. It is seen that acquired maximum power density for PtO_x is 1.08 times higher in comparison to pure Platinum catalyst.

	Power Density mW cm^{-2}	**At Voltage** V	**Specific Power** W mg^{-1}
PtO_x	305	0.43	5.08
Pt	282	0.45	4.7

Tab. 10.1: The obtained power densities and specific powers of anode catalyst: pure Platinum and PtO_x at 70 °C.

It is generally known that PtO and PtO_2 oxides are unstable and they are transformed to the more stable form Pt_3O_4 [127, 128]. Thus, it can be also supposed that the as prepared PtO_x catalyst is reduced in the hydrogen atmosphere on the anode side of the fuel cell. This assumption is also supported by evidences given in the literature [127]. The XPS analysis reveals described reduction effect in hydrogen atmosphere (see fig. 10.5). In figure Pt 4f XPS spectrum of PtO_x as prepared anode catalyst is shown. The spectrum exhibits Pt $4f_{7/2} - 4f_{5/2}$ doublet at 72.5 - 75.8 eV corresponding to Pt^{2+} [126] and second doublet at energies of 74.4-77.7 eV, which can be attributed to the Pt^{4+} species [125]. It is clearly seen that Pt^{2+} and Pt^{4+} states appear while the metallic state is missing, which is in agreement with our assumption that reactive sputtering of Platinum in oxygen atmosphere should produce platinum oxides. After fuel cell experiment the cell was disassembled and the XPS analysis has been acquired after fuel cell treatment. However, the most of catalyst was sticking on the membrane instead of on GDL. Thus, we decided to obtain XPS spectra with the use of the membrane instead of nGDL 10.5 (top). Comparison of the normalized intensity of individual chemical states of Pt before and after fuel cell analyses is summarized in the table 10.2. It seems that Platinum was also little bit oxidized (Pt^{2+} occurred) after the fuel cell test which can be explained by oxidizing of Platinum surface in ambient condition after the cell disassembling because the metallic Platinum

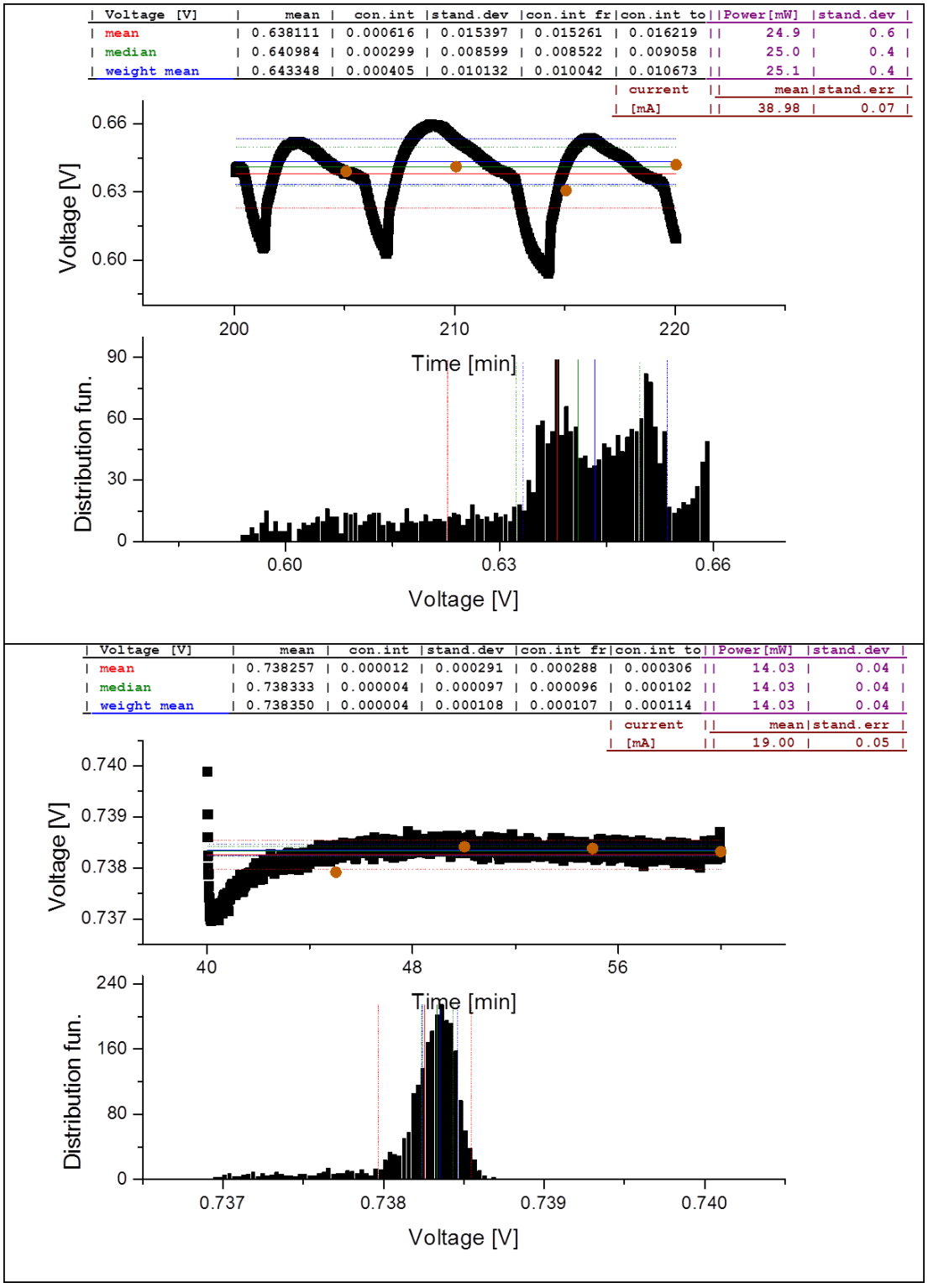

Fig. 10.3: The examples of graphical results of statistical analysis of obtained data from fuel cell test for two different current steps are seen. The voltage dependency on time (top) and its distribution function (bottom). In both plots data (black) recorded each 0.5 s, mean, median and weighted arithmetic mean are seen, dashed lines represent standard deviations. Brown points (•) symbolize mean after each 5 min of data.

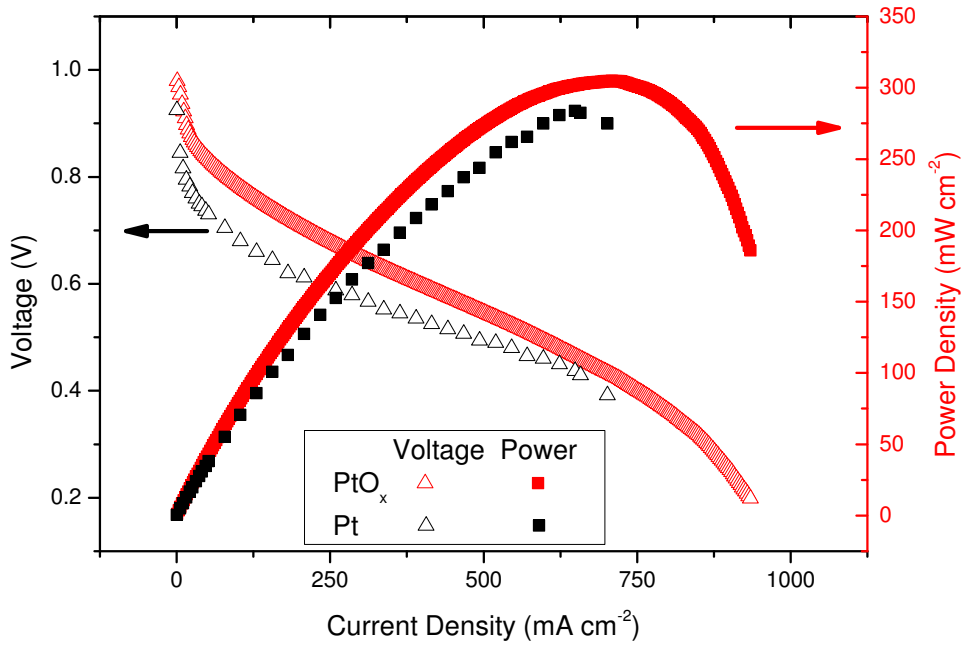

Fig. 10.4: The comparison of the use of Pt sputtered without oxygen and Pt sputtered with the use of oxygen for 70 °C.

surface is unstable and thin oxides films is creating relatively fast and because of the fact that XPS method is very surface sensitive [129]. Otherwise, it is possible that this feature is not representing Pt^{2+} but it represents the rest of asymmetry peak of metallic Platinum instead despite the fact that it has been already fitted by asymmetric feature Doniach-Sunjic curve convoluted with Gaussian doublet. Similarly, it is seen that Platinum catalyst as prepared is not fully oxidized up to Pt^{4+} which is given also by the fact that Pt_3O_4 mix oxide is preferred [127, 128]. For quantitative analysis, relative factors of sensitivity given by [130] and corrected according to our experimental setup by formula reported in the reference [131] were used.

	$\mathbf{Pt^0}$	$\mathbf{Pt^{2+}}$	$\mathbf{Pt^{4+}}$
Before	0.00	0.20	0.80
After	0.83	0.17	0.00

Tab. 10.2: The Pt 4f XPS spectra of PtO_x (30 nm) before (below) and after treatment by H_2 during FC test obtained from Nafion membrane (top). The investigated doublets are $4f_{7/2} - 4f_{5/2}$ for Pt^0, Pt^{2+} and Pt^{4+}.

It was shown that sputtered PtO_x catalyst is reduced in hydrogen atmosphere of the anode side of fuel cell and it exhibits similar behavior like Adam's PtO_2 catalyst [132]. Moreover, the increase of power density in comparison with the

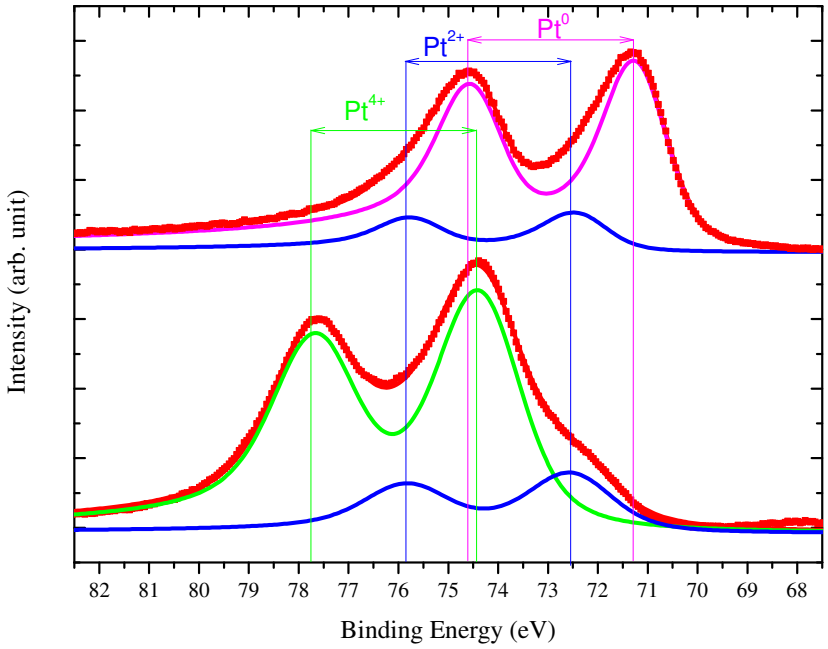

Fig. 10.5: The Pt 4f XPS spectra of PtO_x (30 nm)/nGDL before (below) and after treatment by H_2 during FC test obtained from Nafion membrane (top). The doublets $4f_{7/2} - 4f_{5/2}$ of Pt^0, Pt^{2+} and Pt^{4+} are labeled.

catalyst layer consisted of metallic Platinum allows us to suppose the increase of specific surface area of our PtO_x catalyst after treatment by H_2. Thus, the observed increase of power density in the case of PtO_x catalyst comparing to the pure metallic sputtered catalyst is caused by increase of specific area after reduction of PtO_x.

11. Pt-CeO_2

11.1 Different Pt Loading

In this chapter the Platinum doped Cerium oxide as a node catalyst for PEM FC is presented. First section characterizes Pt-CeO_2 anode catalyst for different Platinum loadings from point of view of FC, XPS analyses. Additionally SEM and HTREM image are discussed. Results of density function theory are provided by group of Konstantin M. Neyman from Barcelona whom we co-operate with is discussed. These results are already published in [133] and in previous works [124, 125, 134, 135]. Therefore only most important results and conclusions are presented in this chapter.

Pt-Ce_2 thin catalyst layers were prepared by rf-magnetron sputtering as it has been described in section 8. Layers were sputtered using two targets simultaneously. Radio frequency (13.56 MHz) sputtering of ceria was performed by using a

2 inch diameter CeO_2 (Kurt J. Lesker, 2 inches) target installed on a TORUS 2 inches UHV magnetron (Kurt J. Lesker) with applied power of 50 W at distance of 90 mm from substrates. Pt was added by using the second DC homemade magnetron at the distance of 200 mm from substrates and tilted by 45° relative to the CeO_2 target, the power applied to the Pt target was 10 W. The sputtering was carried out in Ar atmosphere with total pressure of $4 \cdot 10^{-1}$ Pa. The sputtering chamber was always evacuated up to $5 \cdot 10^{-4}$ Pa before starting the deposition. The described sputtering conditions gave a growth rate of the Pt-doped cerium oxide films of 1 nm min^{-1}. As a substrate nGDL was used in all cases. The thickness of films was determined as 30 nm by using AFM (Atomic Force Microscopy) analysis of the same layer prepared simultaneously on Si substrate.

We prepared series of three samples with different platinum loadings: 0.6-Pt-CeO_2 (0.6 μg(Pt) cm^{-2}), 2-Pt-CeO_2 (2 μg(Pt) cm^{-2}) and 4-Pt-CeO_2 (4 μg(Pt) - cm^{-2}). Loading of Platinum was determined by calculating element concentration ratio given by XPS analyses (see section 19.1). For comparison sputtered pure Platinum 2-Pt (2 μg(Pt) cm^{-2}) and commercial anode Alfa Aesar 2mg-Pt (2.7 mg cm^{-2} of Pt) were used as references. Nafion membrane NR212 and commercial cathode Alfa Aesar (2.0 mg(Pt) cm^{-2}) were used in all cases.

Figure 11.1 shows SEM images of nGDL (a) and sputtered Pt doped cerium oxide (b). The sputtered layer created cauliflower-like/cerebral-cortex-like structure which caused an increase of the specific area as it is seen in figure 11.1(b).

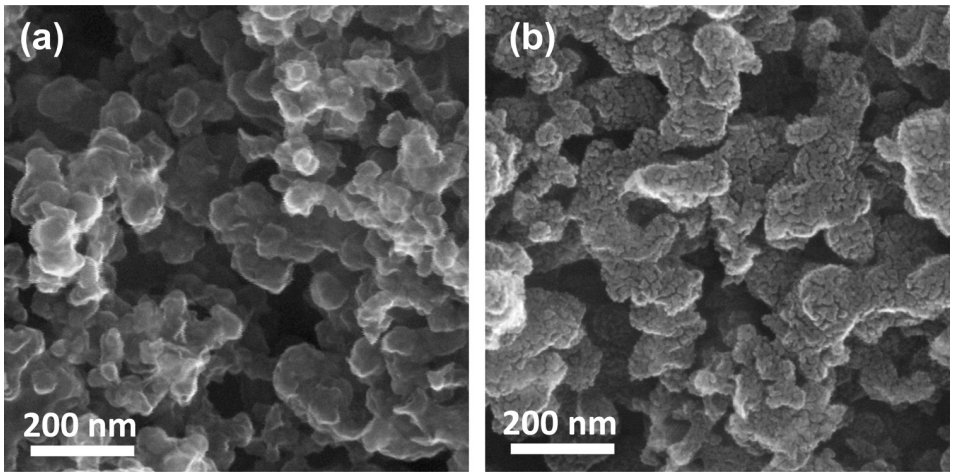

Fig. 11.1: The SEM images of nGDL catalyst support (a) and 30 nm thick sputtered Pt-CeO_2 layer on nGDL (b).[133]

HRTEM images of 2-Pt-CeO_2 and 4-Pt-CeO_2 (see fig. 11.2) shows atomic resolution pictures of the cerium oxide nanoparticle lattice in {1 1 0} plane. It can be seen that the surface of nanoparticles (NPs) exhibits {1 1 1}×{1 0 0} facets which have been shown to expose specific sites anchoring atomically dispersed ionic Pt^{2+} [136]. The statement that Platinum is in the layer in the form of dispersed ionic Pt^{2+} is supported by the fact that HRTEM images did not show any traces of Pt or Pt oxide particles in thin films of ceria with low Pt loadings. (HRTEM measurement has been done by colleague J. Lavková).

The fuel cell analyses were performed using experimental setup shown in the section 7.1 and a piston operated cell (described in section 7.2) and it was pro-

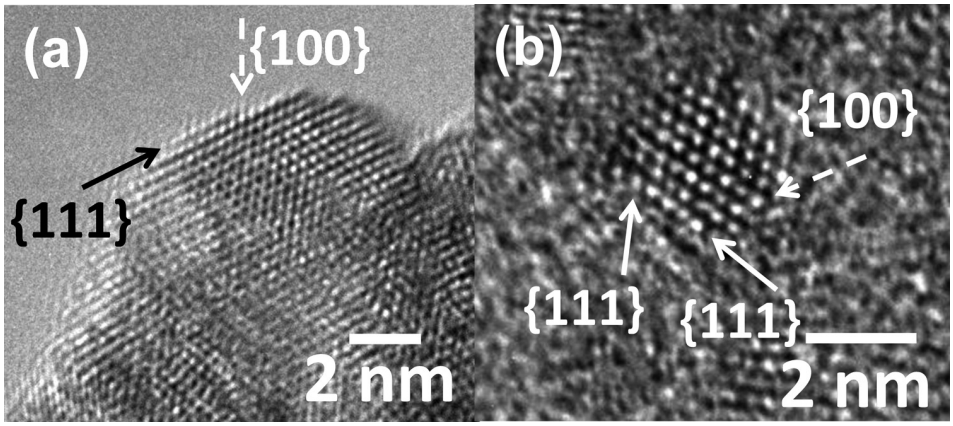

Fig. 11.2: HRTEM images of 2-Pt-CeO_2 and 4-Pt-CeO_2 sputtered layer. The facets 111 and 100 are marked by arrows [133].

ceeded by testing protocol presented in the chapter 6.5. Experimental conditions were the same for all series of samples: 70/70/70 °C at feed gas pressure 0.5 Bar and a piston pressure of 8 Bar. The flow rates were 40 sccm (1.2 Stoich) of H_2 and 30 sccm (2.0 Stoich) of O_2. The summary of results of fuel cell tests are presented in figure 11.3. It is obvious that maximum power density was obtained for commercial catalyst. However, what is interesting, there is a non-monotonous power dependency on Pt contents in the Pt-CeO_2 catalyst films. Obtained power densities follow order: 2mg-Pt, 2-Pt-CeO_2, 4-Pt-CeO_2, 0.6-Pt-CeO_2, 2-Pt. 2-Pt-CeO_2 exhibits maximum power densities from all Pt-CeO_2 catalyst and exceeds power density 0.41 W cm^{-2}.

Notable, 2-Pt reached 5.5 times less power density (0.075 W cm^{-2}) than 2-Pt-CeO_2 (0.41 W cm^{-2}) which is also prove of positive influence of CeO_2 in the catalyst to obtain good performance. Calculated specific powers are listed in the table 11.1. For better investigation of observed phenomena obtained power densities and specific powers of tested catalysts are graphically presented in figure 11.4. It is seen that the highest specific power was obtained for sample 0.6-Pt-CeO_2 and the obtained specific powers for all samples are ordered as follows: 0.6-Pt-CeO_2, 2-Pt-CeO_2, 4-Pt-CeO_2, 2-Pt, 2mg-Pt. If we look at the figure 11.4 we can conclude that the best Pt-CeO_2 sample was 2-Pt-CeO_2 because it exhibited the highest power densities while the specific power was still high (the second highest). Additionally, power density obtained for the sample 2-Pt-CeO_2 was only 1.1 times lower relative to the reference catalyst while the specific power was more than 900 times higher in comparison to the commercial catalyst.

The XPS results showing the Pt 4f states shown in figure 11.5 (left), revealed that sputtered Pt-CeO_2 contained $Pt^{2,4+}$ cations. All spectra of ceria-based catalysts exhibited two $4f_{7/2} - 4f_{5/2}$ doublets at binding energies (BEs) of 72.5–75.8 eV and 74.2–77.5 eV corresponding to Pt^{2+} and Pt^{4+} species, respectively [126]. The relative intensities of the Pt^{2+} and Pt^{4+} peaks in Pt 4f spectra can be used to calculate the Pt^{2+} /Pt^{4+} concentration ratios, given as 2.15, 1.21 and 0.7 for the 0.6-Pt-CeO_2, 2-Pt-CeO_2 and 4-Pt-CeO_2 catalysts, respectively. These results show that lower Pt loadings lead to higher relative abundance of Pt^{2+} species

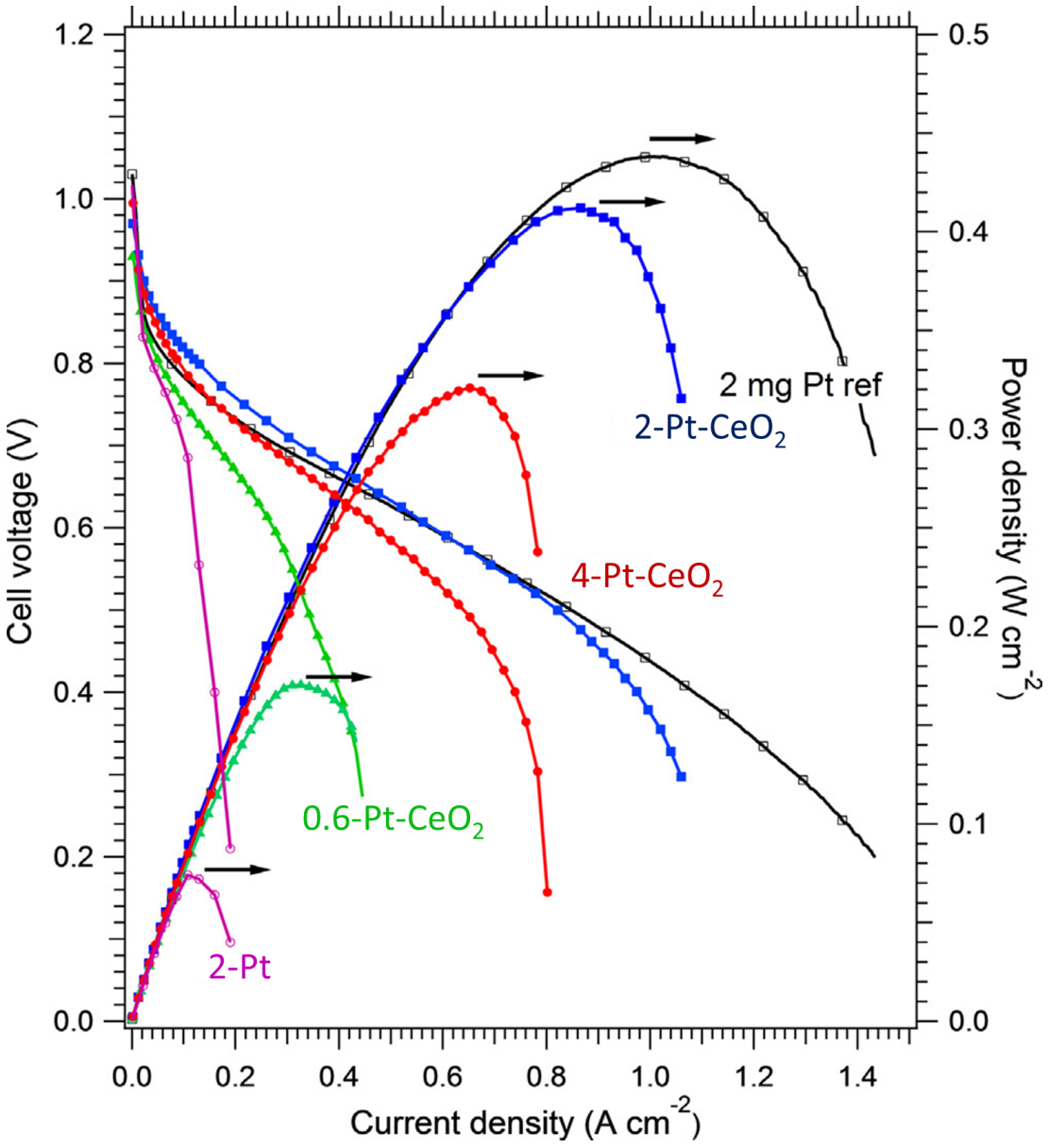

Fig. 11.3: The fuel cell results as polarization I–V curves (left Y-axis) and the corresponding power density(right Y-axis) measured for the three ceria based anode catalysts prepared with different Pt loading: 0.6-Pt-CeO_2 (0.6 μg(Pt) cm^{-2}), 2-Pt-CeO_2 (2 μg(Pt) cm^{-2}) and 4-Pt-CeO_2 (4 μg(Pt) cm^{-2}), pure Platinum 2-Pt (2 μg(Pt) cm^{-2}) and commercial anode Alfa Aesar 2mg-Pt (2.7 mg(Pt) cm^{-2}). Nafion membrane NR212 and commercial cathode Alfa Aesar (2.0 mg(Pt) cm^{-2}) were used. Conditions: 70/70/70 °C at pressure 0.5 Bar and at pressure 8 Bar in piston operated cell. The flow rates were 40 sccm (1.2 Stoich) of H_2 and 30 sccm (2.0 Stoich) of O_2. [133]

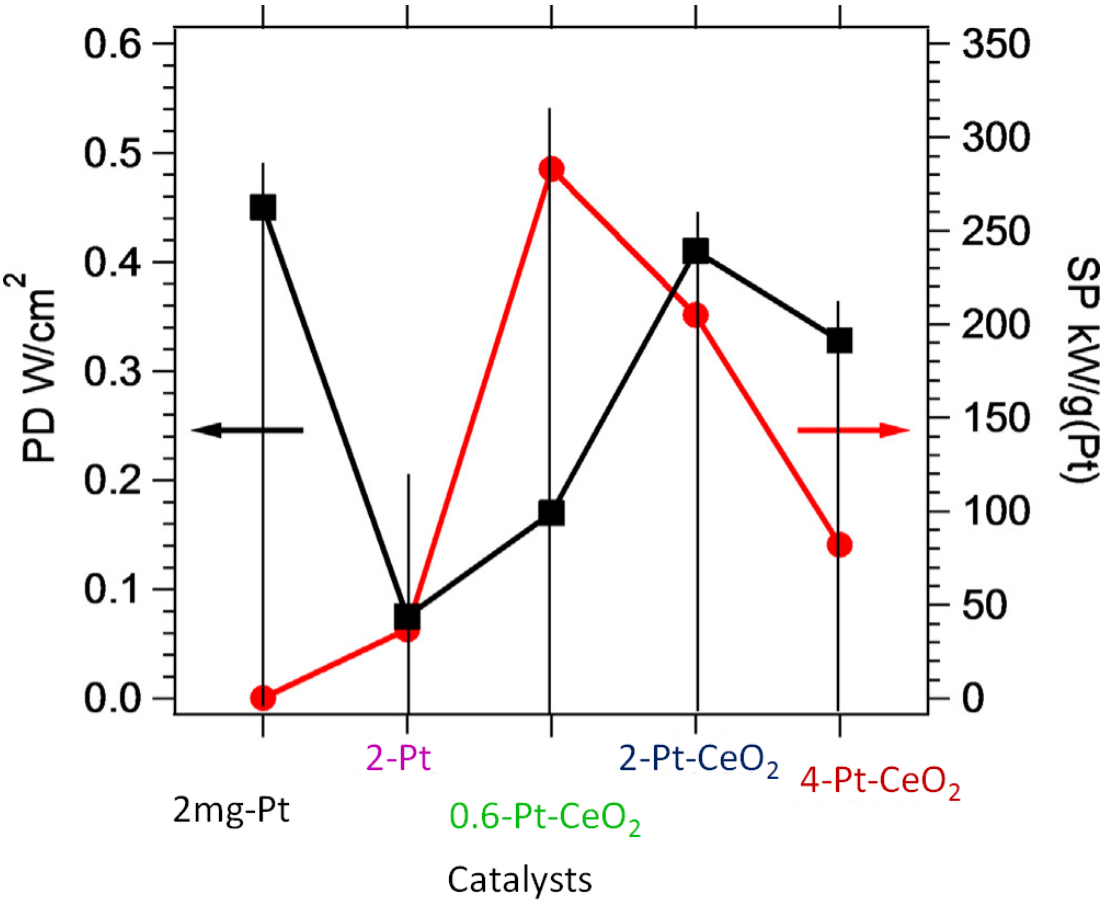

Fig. 11.4: Graphical demonstration of obtained power densities (left axis) and specific powers (right axis) for investigated catalysts: 2mg-Pt, 2-Pt-CeO_2, 4-Pt-CeO_2, 0.6-Pt-CeO_2, 2-Pt. 2-Pt-CeO_2.

Sample wt%	**Power Density** W cm^{-2}	**Loading** μg(Pt) cm^{-2}	**Specific Power** W $mg(Pt)^{-1}$
2mg-Pt	0.44	2000	0.22
2-Pt-CeO_2	0.41	2	205
4-Pt-CeO_2	0.33	4	83
0.6-Pt-CeO_2	0.17	0.6	283
2-Pt	0.075	2	38

Tab. 11.1: The obtained power densities and specific power of Pt-CeO_2 sputtered anode catalyst in PEM FC. As a cathode commercial catalyst Alfa Aesar (2.0 mg(Pt) cm^{-2}) was used. Data were obtained at 70/70/70 °C and at pressure 0.5 Bar. The flow rates were 40 sccm (1.2 Stoich) for H_2, 30 sccm for O_2 (2.0 Stoich).

in the sputtered Pt-CeO_2 films. In contrary as expected, the pure Pt film 2-Pt contains only metallic Platinum, which is identified by its characteristic doublet at BEs 71.2–74.5 eV and an asymmetric shape of the Pt 4f peaks.

Because disassembling of the MEAs for the XPS measurement of used catalyst samples was not easy we decided to simulate the FC conditions by using the flow reactor. The Pt doped cerium oxide catalysts were heated in the humidified hydrogen flow of 30 sccm at 65°C for 24 h. The figure 11.5 (right) shows the Pt 4f spectra of the catalyst films recorded after such annealing process. If we compare this results with results obtained before the FC test (11.5 (left)), it is seen that after wet hydrogen annealing the Pt^{4+} species disappeared. In the case of low Pt loading (samples 0.6-Pt-CeO_2 and 2-Pt-CeO_2), annealing results in Pt^{2+} as the only Pt state is presented, whilst for the 4-Pt-CeO_2 sample the disappearance of Pt^{4+} is concomitant with the formation of Pt^{2+} and Pt^0.

The results clearly show that Pt^{4+} is not a stable component under the simulated FC operating conditions, while Pt^{2+} and partially Pt^0 are stable even after the sample transfer in air. Although the exposure to H_2 cannot fully simulate the operation conditions of the catalyst in the PEM FC (potential was not applied), this test can suggest that sputtered Pt-ceria catalysts with higher Pt loading (above 2 μg(Pt) cm^{-2} in this case) are composed of ionic and metallic Pt.

These structural units of Pt-CeO_2 have been fully characterized by DFT *Density functional theory* modeling (as in the model presented in figure 11.6) and they were exposed at {1 0 0} facets of ceria, which are also detected on the nanostructured thin film catalysts presented in HRTEM imaging (the fig. 11.2). The ceria nanoparticles (NP) model exhibits 4 anchoring sites (or 6 if we also consider the substitutions of corner Ce atoms by Pt atoms) occupied by Pt^{2+} species and additional Pt atoms would be adsorbed in metallic form. DFT calculations suggest that the great stability of Pt^{2+} species on ceria makes them resistant to reduction by hydrogenation and that the formation of such stable surface complexes prevents to degradation of the nanostructured composite. Moreover, if we look at the Platinum/Cerium concentration predicted by model, we obtain easily at. 4.8% of Pt in catalyst layer. With the use of interstitial model presented in section 19.1 this concentration corresponds to the loading 1.2 μg(Pt) cm^{-2} in 30 nm thick layer. Based on this fact we can suggest the optimal Platinum loading for 30 nm thick layer is even lower than 2 μg(Pt) cm^{-2} but still higher than 0.6 μg(Pt) cm^{-2} according to the FC analyses.

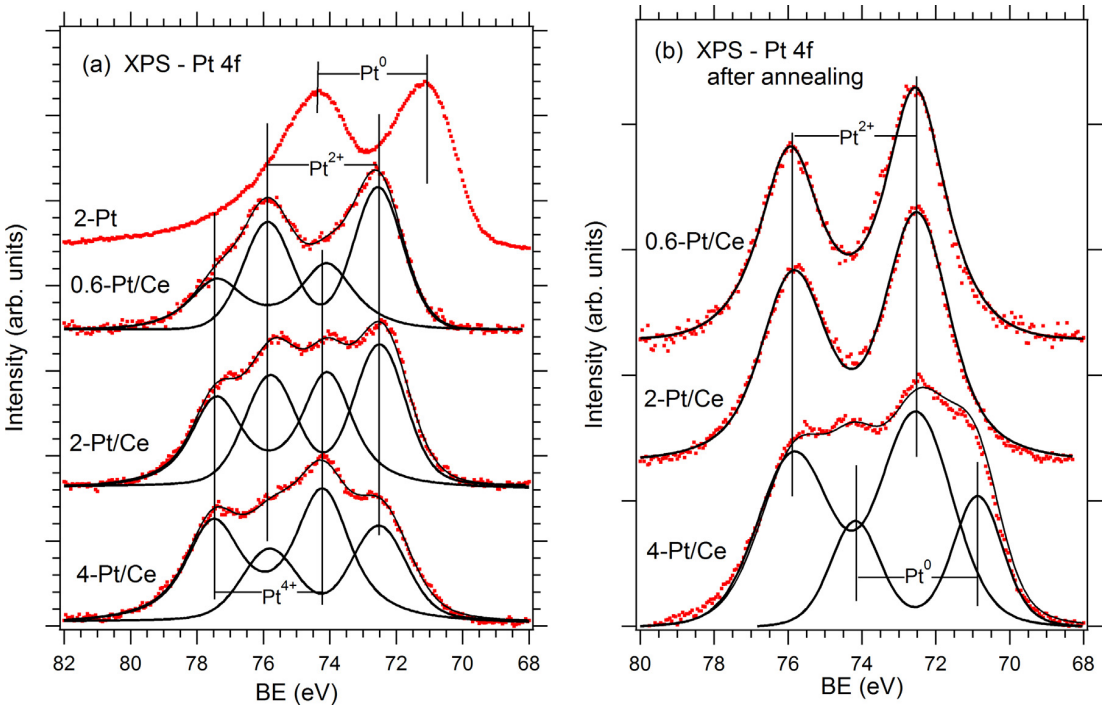

Fig. 11.5: XPS Pt 4f spectra of the sputtered reference pure Pt film 2-Pt (2 μg(Pt) cm^{-2}) and the three ceria based anode catalysts with different Pt contents 0.6-Pt-CeO_2 (0.6 μg(Pt) cm^{-2}), 2-Pt-CeO_2 (2 μg(Pt) cm^{-2}) and 4-Pt-CeO_2 (4 μg(Pt) cm^{-2}) as-prepared (a) and after wet hydrogen annealing simulating anode conditions of the PEM FC operation (b). All the catalysts films were sputter deposited on the nGDL. The doublets $4f_{7/2} - 4f_{5/2}$ for Pt^0, Pt^{2+} and Pt^{4+} are marked. [133]

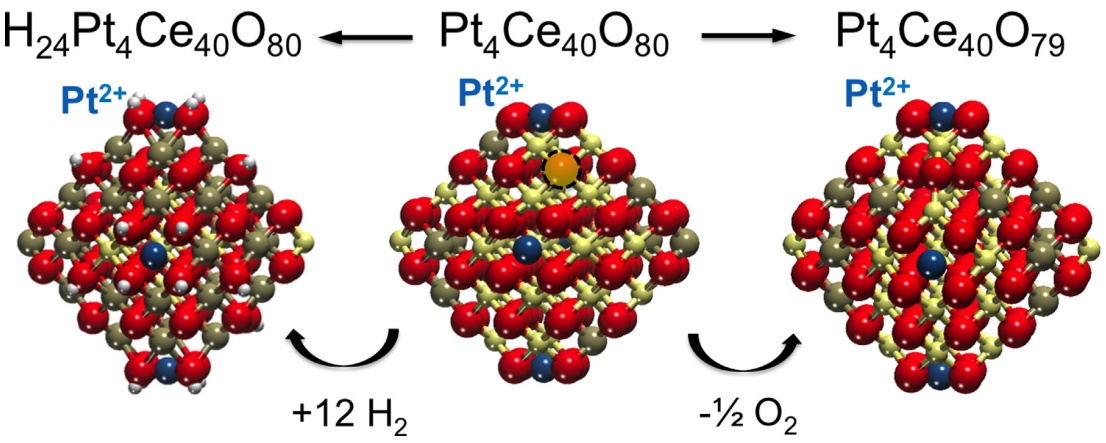

Fig. 11.6: Structure of the $Pt_4Ce_{40}O_{80}$ model with 4 Pt atoms in the 2+ state (center). 24 Ce^{4+} cations are reduced to the Ce^{3+} state upon dissociative adsorption of 12 H_2 molecules (left) resulting in $E_{ad}(H_2) = 156kJ\ mol^{-1}$ per H_2 molecule. Nevertheless, the four atomic Pt^{2+} species retain their oxidation state and very strong bonding to the ceria substrate. Note that the adsorption of 24 H and 4 Pt leads to the reduction of 32 Ce^{4+} to Ce^{3+} state. The removal of an oxygen atom to form $Pt_4Ce_{40}O_{79}$ (right) results in a dramatic increase of the vacancy formation energy ($E_f(O_{vac}) = 210kJ\ mol^{-1}$) with respect to the bare $Ce_{40}O_{80}$ NP ($E_f(O_{vac}) = 79kJ\ mol^{-1}$). White, blue, red, beige, and brown spheres depict H, Pt, O, Ce^{4+} , and Ce^{3+} , respectively and position of the removed O atoms is indicated by a circle. [133].

11.2 Endurance experiment

The most optimal sample revealed by the study presented in the previous chapter was Pt-CeO_2 anode catalyst dedicated 2-Pt-CeO_2 with loading 2 μg(Pt) cm^{-2} therefore this sample was chosen for endurance study which is presented in this chapter.

Measurement was performed at the same condition as described in chapter 11.1. Figure 11.7 shows the comparison of 2-Pt-CeO_2 (2 μg(Pt) cm^{-2}) anode and commercial anode catalyst from Alfa Aesar (2.7 mg(Pt) cm^{-2}). The cathode was commercial from Alfa Aesar (2.0 mg(Pt) cm^{-2}) in both cases. It is clearly seen that power density of 2-Pt-CeO_2 (0.44 W cm^{-2}) is 1.5 times lower than power density of commercial catalyst (0.65 W cm^{-2}). For better comparison, the obtained values together with calculated specific powers are listed in table 11.2. It is seen that specific power of 2-Pt-CeO_2 (220 W mg(Pt)$^{-1}$) is still 670 times higher than specific power of commercial catalyst (0.33 W mg(Pt)$^{-1}$). We should admit that standard deviation obtained by statistical analyses of FC results is about 5%.

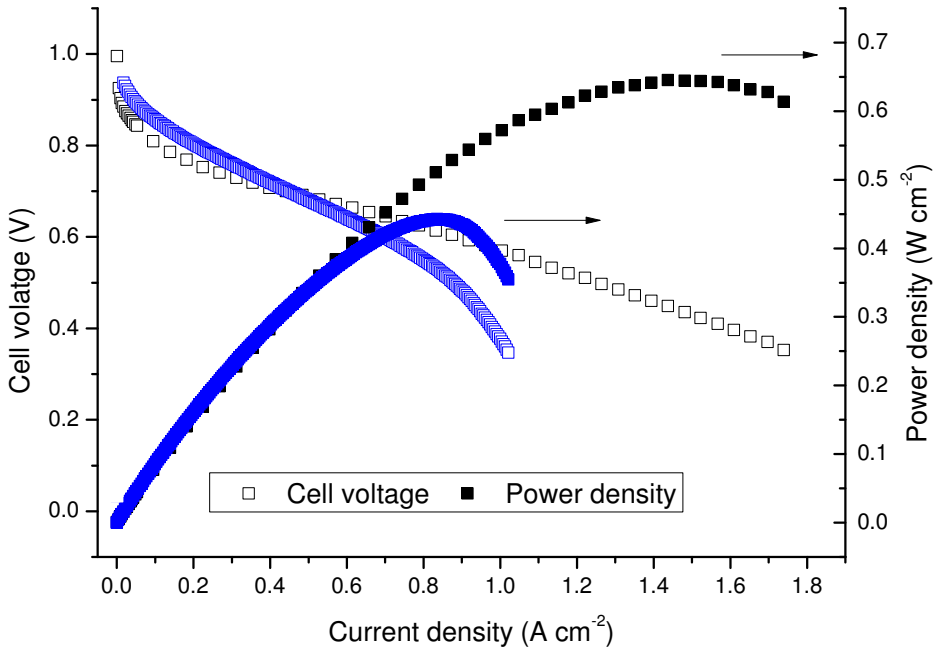

Fig. 11.7: The comparison of polarization curves and power density dependencies on current density for 2-Pt-CeO_2 (2 μg(Pt) cm^{-2}) anode and commercial anode catalyst from Alfa Aesar (2.7 mg(Pt) cm^{-2}). The cathode was commercial from Alfa Aesar (2.0 mg(Pt) cm^{-2}) in both cases. Data were obtained at temperatures 70/70/70 °C and at pressure 0.5 Bar. The flow rates were 40 sccm (1.2 Stoich) for H_2, 30 sccm for O_2 (2.0 Stoich). Pressure in piston was 8 Bar and active area was 4.41 cm^2.

The endurance test of Pt-CeO_2 sputtered anode catalyst (2 μg(Pt) cm^{-2}) has been proceeded by using the method already described in chapter 6.5. The

Sample wt%	Power Density W cm^{-2}	Loading μg(Pt) cm^{-2}	Specific Power W $mg(Pt)^{-1}$
2mg-Pt	0.65	2000	0.33
2-Pt-CeO_2	0.44	2	220

Tab. 11.2: The obtained power densities and specific powers of Pt-CeO_2 sputtered anode catalyst (2 μg(Pt) cm^{-2}) and commercial catalyst from Alfa Aesar (2.7 mg(Pt) cm^{-2}). As a cathode commercial catalyst Alfa Aesar (2.0 mg(Pt) cm^{-2}) was used. Data were obtained at 70/70/70 °C at pressure 0.5 Bar. The flow rates were 40 sccm (1.2 Stoich) for H_2, 30 sccm for O_2 (2.0 Stoich).

figure 11.8 shows power densities of fuel cell after selected cycles of the endurance procedure. One cycle is consisted of 30 s long load of the cell at maximum power density and of 30 s long period of unloaded cell. It seen that even after 6000 cycles of this accelerated endurance test any drop of performance was not appeared. Thus, the Pt-CeO_2 catalyst has been found as a stable anode catalyst in PEM FC. We admit that much longer test is necessary before the commercial application.

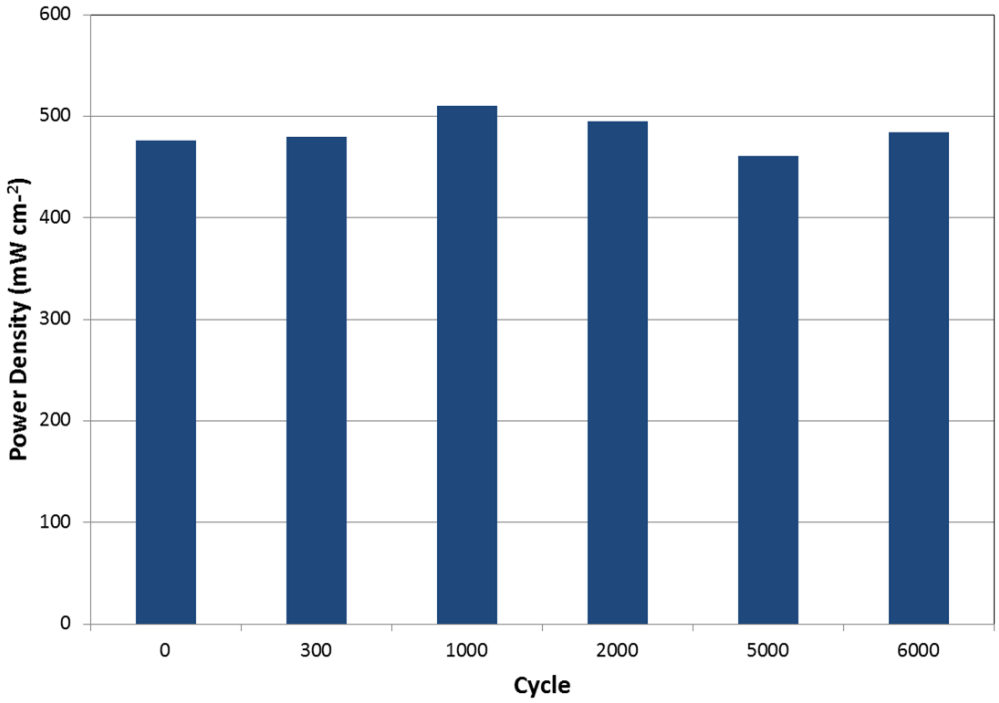

Fig. 11.8: The bar plot representing power density after selected loops of endurance cycles for Pt-CeO_2 (2 μg(Pt) cm^{-2}) anode and commercial cathode catalyst from Alfa Aesar (2.0 mg(Pt) cm^{-2}). The conditions were: temperatures 70/70/70 °C at pressure 0.5 Bar. The flow rates were 40 sccm (1.2 Stoich) for H_2, 30 sccm for O_2 (2.0 Stoich). Pressure in the pistion cell was 8 Bar.

After selected loops in figure 11.8 electrochemical analyses have been proceeded: EIS, Crossover determination and CV. The voltammograms obtained after selected cycles of endurance test are shown in figure 11.9. It is clearly seen

that voltammograms are mostly same and any significant differences have not appeared. The hydrogen onset adsorption/desorption region has been investigated and current densities (after stabilization) at potential marked by black vertical line are listed in the table 11.3 as I_H. It is seen that after stabilization the current densities representing hydrogen desorption are the same which confirms the stability that was observed in figure 11.8. Currents representing hydrogen crossover and internal resistances given by impedance spectroscopies have been determined according to the testing protocol described in chapter 6.5 and the results are summarized in table 11.3. It is clearly seen that internal resistances have after stabilization the same values ($R_i^A = (89 \pm 7)\Omega\ \mathrm{cm}^2$) for all cycles of endurance test.

Observation of stable internal resistance is also in agreement with assumption in section 9. The internal resistance is given mostly by conductivity of the membrane which is orderly lower in comparison with junction resistance and resistance of catalyst.

Similarly, the crossover analyses exhibit after some stabilization a stable behavior $I_{cross} = (0.54 \pm 0.04)\mathrm{mA\,cm}^{-2}$, which is also in agreement with results reported in chapter 9. Voltammograms in figure 11.9 are shifted vertically by current of hydrogen crossover which is determined as $\sim 0.5\,\mathrm{mA}$.

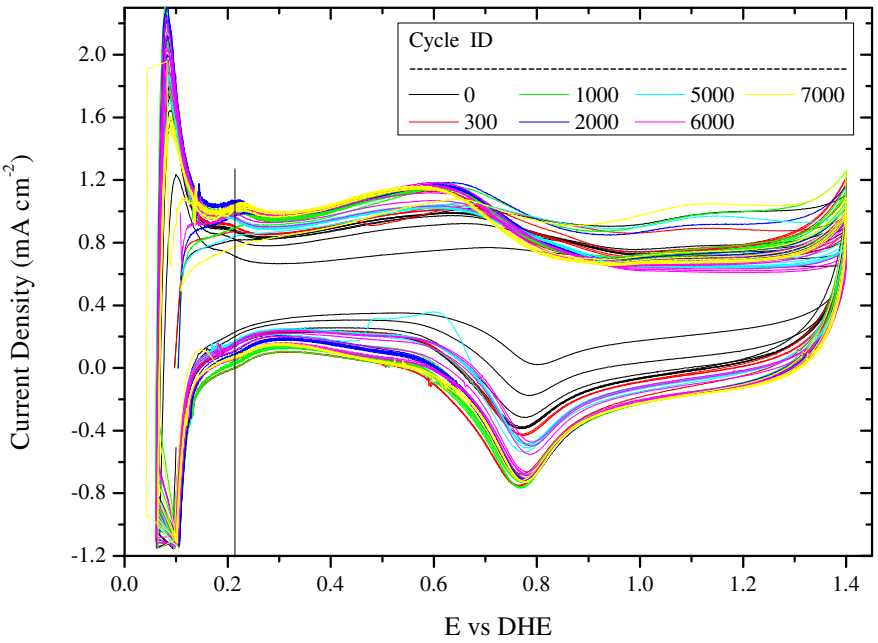

Fig. 11.9: The voltammograms for Pt-CeO_2(2 μg(Pt) cm^{-2}) (left) obtained *in operando* after selected cycles of the endurance test. Flows of gases were 30 sccm of N_2 on the side of interest and 30 sccm of H_2 as dynamic hydrogen reference electrode on the second side. The other condition: ambient pressure, 70/70/70 °C and the scan rate of $100\,\mathrm{mV\,s}^{-1}$. Potential (0.22 V vs DHE) used for determination of current representing hydrogen oxidation reaction activity is marked by black vertical line.

Cycle	R_i^A Ω cm^2	I_H mA cm^{-2}	I_{cross} mA cm^{-2}
0	0.110	0.39	0.32
300	0.101	0.50	0.52
1000	0.081	0.50	0.59
2000	0.090	0.49	0.55
5000	0.097	0.43	–
6000	0.081	0.49	0.59
7000	0.083	0.49	0.45

Tab. 11.3: Summarization of obtained internal resistances (R_i^A), current at 0.22 V (I_H) vs DHE determined from CV and crossover current (I_{cross}) for selected cycles of endurance experiment. Standard deviation of obtained values are ∼5%.

11.3 CO poisoning

Resistance of the anode catalyst 2-Pt-CeO_2 (2 μg(Pt) cm^{-2}) described in the previous chapter 11.2 to CO poisoning was investigated. Experimental setup for the CO poisoning effect characterization has been already described in the section 7.1. Pure H_2 and mixture of 1% CO in H_2 were mixed by using two mass flow controllers in order to prepare 25 ppm of CO in hydrogen flow. The cell operating condition were the same as in the previous case 11.2: temperatures 70/70/70 °C at pressure 0.5 Bar. Cathode catalyst was commercial catalyst from Alfa Aesar (2 mg cm^{-2} of Pt). The flow rates were 50 sccm for H_2 (or mix H_2+CO), 40 sccm for O_2. Pressure in piston was 8 Bar and active area was 4.41 cm^2.

Example of result of CO poisoning effect on Pt-CeO_2 anode catalyst is shown in figure 11.10. There is shown the dependence of current density on time at 0.75 V. 25 ppm mixture of CO and H_2 was started in 610 s and after 20 s the current was dropped down from 0.21 A cm^{-2} to 0.007 A cm^{-2}. The CO poisoned H_2 flow was stopped in 870 s. This experiment revealed relatively week resistance to CO and catalyst was rapidly poisoned. However, if this catalyst is exposed for such very short exposure the catalyst was regenerated.

In order to compare Pt-CeO_2 sputtered catalyst with commercial PtRu commercial catalyst with Pt loading (0.45 mg cm^{-2}) figure 11.11 was reprinted from [137]. It is clearly seen that this catalyst exhibits lower drop of current density than our Pt-CeO_2 catalyst at even higher CO concentration (50 ppm). While our Pt-CeO_2 exhibits drop of current density from 0.21 A cm^{-2} to 0.007 A cm^{-2} at 25 ppm of CO and at 0.75 V, the commercial catalyst showed decrease of current density from 0.735 A cm^{-2} to 0.37 A cm^{-2} at 50 ppm of CO and at 0.7 V. In addition, what is important, the current decreases to the minimum after 20 s in the case of our Pt doped ceria catalyst while in the case of commercial catalyst the stabilization at minimal current was appeared after 3500 s. Thus, if we compare our Pt-CeO_2 sputtered anode catalyst with commercial PtRu catalyst [137, 138] we can conclude that our catalyst is not suitable for hydrogen fuel contaminated with carbonaceous species impurities because the significant poisoning effect is appeared at 25 ppm. The more complex analyses of CO poisoning effect of our catalyst is seen in chapter 13.2

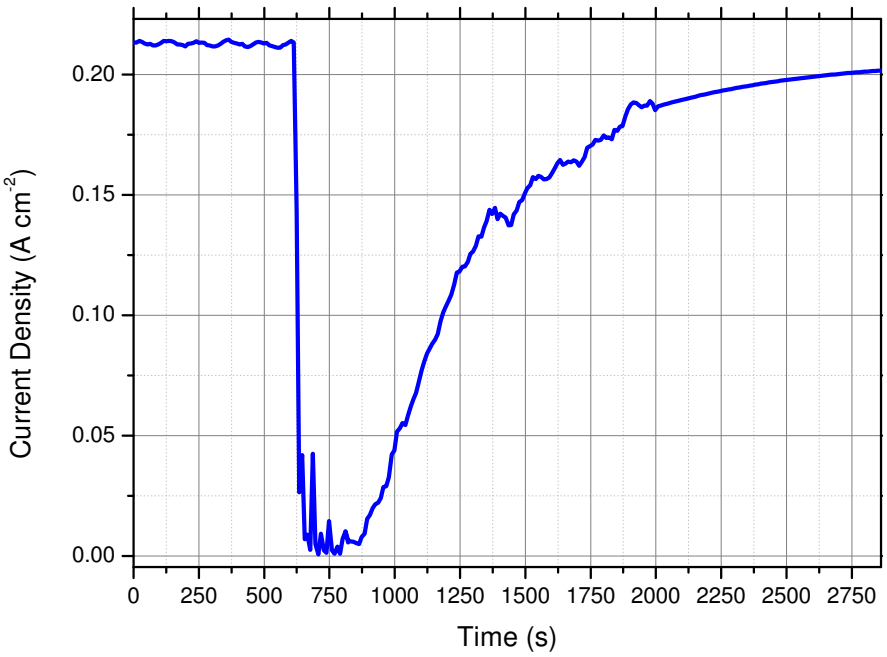

Fig. 11.10: Current density dependency at 0.75 V on time, which shows poisoning effect with the use of 2-Pt-CeO_2 (2 μg(Pt) cm^{-2}) sputtered anode catalyst. H_2 with CO of 25 ppm concentration was used for experiment. CO was used from time of 610 s to 870 s. FC operating conditions were 70/70/70 °C at presure 0.5 Bar. Cathode catalyst was commercial catalyst from Alfa Aesar (2 mg cm^{-2} of Pt). The flow rates were 50 sccm for H_2 (or mix H_2+CO), 40 sccm for O_2. Pressure in piston was 8 Bar and active area was 4.41 cm^2.

12. Fully thin catalyst PEM FC

This chapter presents the investigation of the cathode catalyst in the first part and the second part is focused on PEM FC made exclusively from thin film catalysts with the use of our Pt-CeO_2 sputtered catalyst film as an anode and Pt-Co sputtered film as a cathode catalyst.

12.1 PtCo as Cathode

The influence of Pt-Co alloy on its catalyst structure and oxygen reduction has been already described in the section 3. We have analyzed Pt-Co thin layer for several different Platinum/Cobalt ratio at the same thickness of the catalyst film.

The nonreactive magnetron sputtering was used to prepare Pt-Co thin film catalysts. The Pt-Co cathode catalyst layer was prepared by means of two magnetrons working simultaneously. DC sputtering of Co was performed by using Co target (diameter of 52 mm, Kurt J. Lesker) at distance of 90 mm from substrates. Pt was added by using the second DC operated magnetron with Pt target (2 inches, Safina) at distance of 200 mm from substrates and tilted by 45° relative to

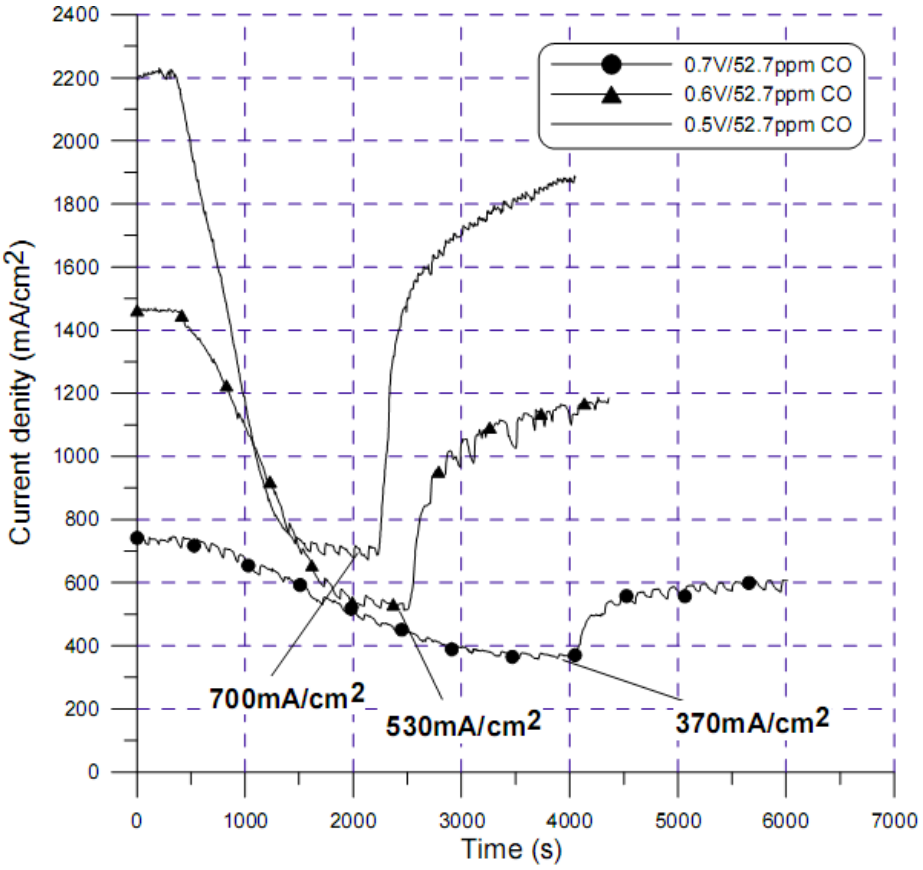

Fig. 11.11: FC analyses of CO poisoning effect with the use of PtRu alloy (1:1) (0.45 mg cm^{-2}) at 50 ppm of CO for different voltages (Reprinted from [137]). Flow rates: 20 sccm (1.4 Stoich) for anode, 15 sccm for O_2 (1.85 Stoich). Temperature was 80/65/70 °C and pressure was ambient.

the Co target. Support for sputtered catalyst layer was the commercial nGDL (Sigracet, GDL 25 BC).

The catalyst film thicknesses were determined by Atomic Force Microscopy (AFM) from the reference films deposited on the silicon substrate simultaneously. Thickness of Pt-Co sputtered catalyst film was determined as 50 nm. Concentration of Pt has been obtained from calibration of growth rate for both magnetrons and checked by XPS analyses.

The fuel cell experiment was performed with the use of experimental setup shown in the section 7.1 presenting testing protocol introduced in chapter 6.5. Experimental conditions were the same for all series of samples: 70/70/70 °C at ambient pressure and at pressure 8 Bar in the piston operated cell. The flow rates were 40 sccm (1.2 Stoich) for H_2, 30 sccm for O_2 (2.0 Stoich). As a membrane Nafion NR212 (0.05 mm thick) was used. Anode catalyst was commercial catalyst from Alfa Aesar (2.7 mg(Pt) cm^{-2}). Results of fuel cell experiments for sputtered cathode Pt-Co catalysts with Platinum content of 100 wt% (110 μg(Pt) cm^{-2}), 87 wt% (85 μg(Pt) cm^{-2}), 60 wt% (50 μg(Pt) cm^{-2}) and 40 wt% (30 μg(Pt) cm^{-2}) are summarized in figure 12.1. It is clearly seen that power density is slowly decreasing with decrease of Pt content but this decrease is not proportional to the loading of Platinum. This phenomenon is explained by positive influence of Co and its Pt-Co alloy on oxygen reduction. For better understanding the calculated

power densities and specific powers are listed in the table 12.1. The non-linear dependence of power density of Platinum loading is revealed by increase of specific power. Specific power increases with decreasing loading of Platinum. The Pt-Co (6 wt%, 3.8 μg(Pt) cm^{-2}) has been also tested but due to too low power density (less than 0.05 W cm^{-2}) it was omitted in the plot 12.1.

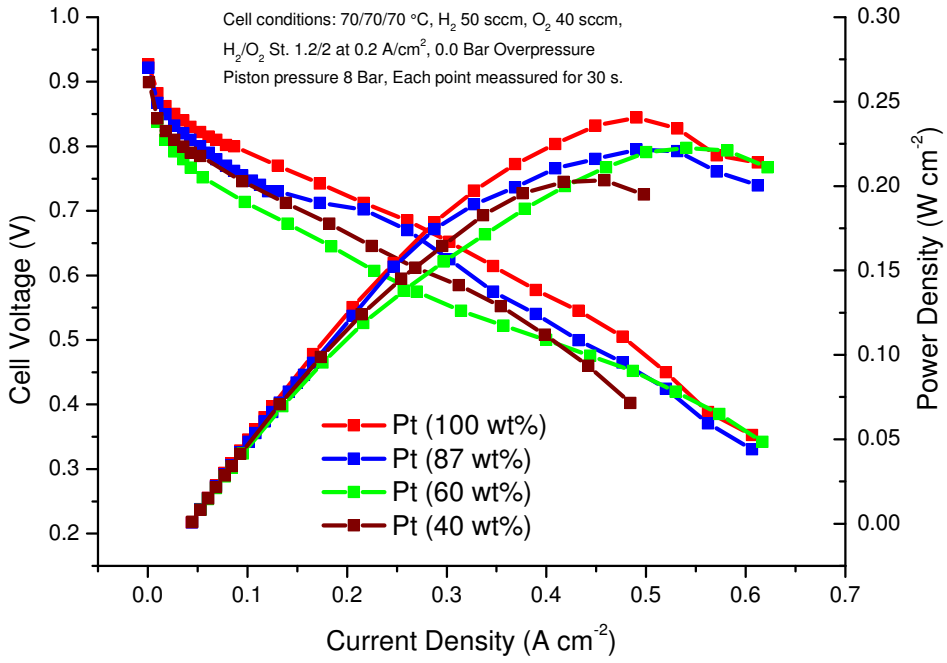

Fig. 12.1: Results of fuel cell experiments for 50 nm thin sputtered cathode Pt-Co catalyst with Platinum content of 100% (-■-, 110 μg(Pt) cm^{-2}), 87% (-■-, 85 μg(Pt) cm^{-2}), 60% (-■-, 50 μg(Pt) cm^{-2}), 40% (-■-, 30 μg(Pt) cm^{-2}) . Anode catalyst was commercial catalyst from Alfa Aesar (2.7 mg(Pt) cm^{-2}). The conditions were: temperatures 70/70/70 °C at **ambient** pressure. The flow rates were 40 sccm (1.2 Stoich) for H_2, 30 sccm for O_2 (2.0 Stoich).

Pt content wt%	**Power Density** W cm^{-2}	**At Voltage** V	**Specific Power** W mg(Pt)$^{-1}$
100%	0.24	0.51	2.2
87%	0.22	0.47	2.3
60%	0.21	0.43	4.2
40%	0.20	0.46	6.7

Tab. 12.1: The obtained power densities and specific powers of Pt-Co cathode catalyst in PEM FC. As an anode the commercial catalyst Alfa Aesar (2.7 mg(Pt) cm^{-2}) was used. Data were obtained at 70/70/70 °C at **ambient** pressure. The flow rates were 40 sccm (1.2 Stoich) for H_2, 30 sccm for O_2 (2.0 Stoich).

Complementary fuel cell analysis obtained at pressure 0.5 Bar is shown in figure 12.2 and calculated power densities and specific power are summarized in

the table 12.2. In contrast to the results obtained at ambient pressure (shown in figure 12.1) maximal power density was not reached by Pt (100 wt%) with the highest loading of Pt but Pt-Co (87 wt%) exhibited maximum power of $0.38\,\mathrm{W\,cm^{-2}}$ which corresponds to $4.5\,\mathrm{W\,mg(Pt)^{-1}}$. Obtained maximal performances were analyzed using statistic and determined standard deviance was lower than $0.03\,\mathrm{W\,cm^{-2}}$ for all presented samples in both operating pressures.

In order to understand the observed behavior of Pt-Co the cyclic voltammetry was performed directly in the fuel cell (see figure 12.3). Voltammograms were obtained by the method described in the section 6.2 and they are presented as measured (left) and divided by platinum loading (right). Vertical shift is caused by hydrogen crossover. It is clearly seen that maximum current (corresponding to the charge) in the hydrogen adsorption/desorption region was reached for Pt-Co (87 wt%). The same sample exhibits also maximum specific current and specific charge in the hydrogen adsorption/desorption region.

In the hydrogen underpotential deposition region, all samples clearly exhibit features associated with hydrogen adsorption and desorption on Pt{100} (a broad peak at ∼0.3 V vs. RHE) [139, 140] while a peak between ∼0.1 and ∼0.2 V vs. RHE associated with hydrogen adsorption and desorption on Pt{110} [139, 140] facets is partially hidden in hydrogen evolution.

The shift of the onset potential for reduction of oxygenated species on Pt (∼0.8 V vs. RHE)[141, 142] was observed: Pt-Co (87 wt%) shifts to the higher potential; Pt-Co (60 wt%) and Pt-Co (40 wt%) shift to the lower potential relative to the Pt (100 wt%). The shift of reducing peak for Pt-Co (60 wt%) and Pt-Co (40 wt%) to the lower potential can be given by higher upper voltage of CV in this case (1.4 V) but according to the literature [143] it should not cause bigger shift than 12 mV. Remind theory described in the section 3 (see figure 3.1) oxygen is bonded on Co surface stronger than in the case of pure Pt which could explain the shift to the lower potential due to high atomic concentration of Co in Pt-Co (individual atomic ratio: $Pt_{45}Co_{65}$ for Pt-Co 60 wt% of Pt and $Pt_{25}Co_{75}$ for Pt-Co 40 wt% of Pt). However, Pt-Co 87 wt% of Pt corresponds to $Pt_{75}Co_{25}$ and there are lots of evidence in the literature that maximal performance is reached by optimal Pt_3-Co phases ($Pt_{75}Co_{25}$) [74, 75](see also figure 3.3). What is new in our work is the fact that we have been able to prepare this active phase by magnetron sputtering without annealing at 600°C which is necessary for other techniques [144–146]. We should note that oxygen reduction study with the use of rotated disc electrode (RDE) could obtain the potential shift more precisely. However, optimal strength of oxygen bond to the surface for this sample (Pt-Co 87 wt% of Pt) can be seen in voltammogram which reveals almost the same week adsorption/desorption process of oxygen comparable with hydrogen adsorption/desorption instead of strong chemical bond (compare redox couple marked by black and blue lines in both figures in 12.3). This observed shifts of potential can be also affected by little drifting of potential of DHE reference electrode and they could be inaccurate. Nevertheless, the weaker bond between oxygen species and surface than in the case of pure Pt but still strong enough to proceed surface reaction can be supposed. The similar observation of potential shifts on Pt_3Co phase that we have just discussed was also shown in [147]. There is no doubt that Pt-Co (wt. 87% of Pt) corresponding with $Pt_{75}Co_{25}$ exhibited higher power performance in comparison with other investigated Pt-Co samples

including pure Platinum catalyst regarding to obtained current densities and specific current in CV and in FC analyses at 0.5 Bar.

The reason why we did not obtain higher performance for Pt-Co (87 wt%) according to the cyclic voltammetry results can be explained by a not sufficient diffusion of reactants and products through the sputtered layer of 50 nm. Good diffusion is even more crucial on the cathode side than on hydrogen side. Thus, it could be possible that a higher power density could be obtained by using thinner layers.

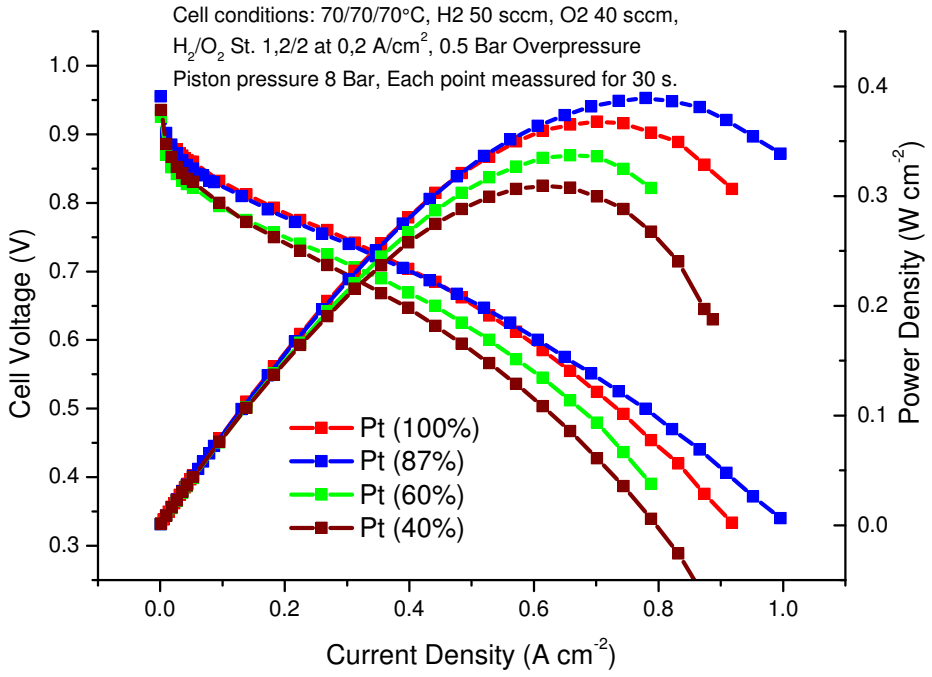

Fig. 12.2: Results of fuel cell experiments for 50 nm thin sputtered cathode Pt-Co catalyst with Platinum content of 100% (-■-, 110 μg(Pt) cm^{-2}), 87% (-■-, 85 μg(Pt) cm^{-2}), 60% (-■-, 50 μg(Pt) cm^{-2}), 40% (-■-, 30 μg(Pt) cm^{-2}) . Anode catalyst was commercial catalyst from Alfa Aesar (2.7 mg(Pt) cm^{-2}). The conditions was: temperatures 70/70/70 °C at pressure **0.5 Bar**. The flow rates were 40 sccm (1.2 Stoich) for H_2, 30 sccm for O_2 (2.0 Stoich).

Pt content wt%	**Power Density** W cm^{-2}	**At Voltage** V	**Specific Power** W mg(Pt)$^{-1}$
100%	0.37	0.52	3.4
87%	0.38	0.50	4.5
60%	0.34	0.51	6.8
40%	0.31	0.50	10.3

Tab. 12.2: The obtained power densities and specific powers for Pt-Co cathode catalyst in PEM FC. As an anode commercial catalyst Alfa Aesar (2.7 mg(Pt) cm^{-2}) was used. Data were obtained at 70/70/70 °C at pressure **0.5 Bar**. The flow rates were 40 sccm (1.2 Stoich) for H_2, 30 sccm for O_2 (2.0 Stoich).

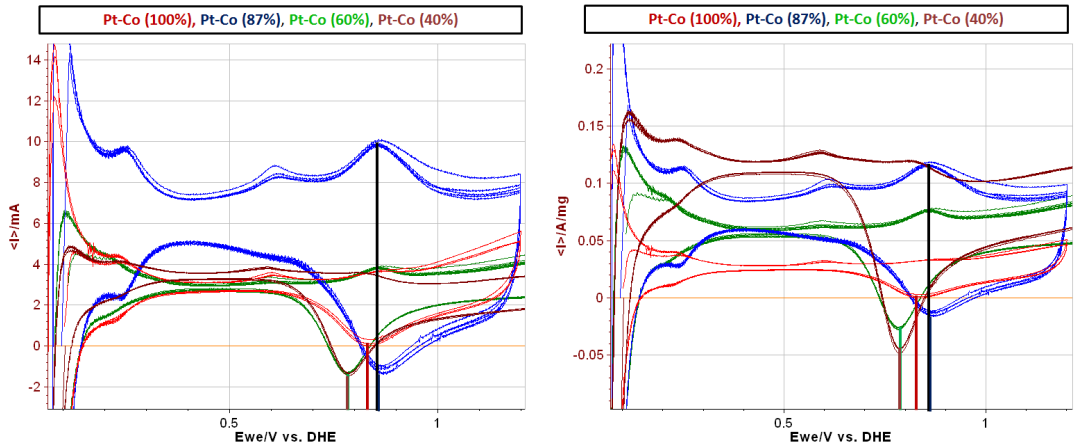

Fig. 12.3: Results of cyclic voltammetry obtained directly in FC *in operando* for 50 nm thin sputtered cathode Pt-Co catalyst with Platinum content of 100% (- 110 μg(Pt) cm^{-2}), 87% (- 85 μg(Pt) cm^{-2}), 60% (- 50 μg(Pt) cm^{-2}) and 40% (- 30 μg(Pt) cm^{-2}). Voltammograms as measured (left) and divided by loading of Platinum (right). Anode catalyst was commercial catalyst from Alfa Aesar (2.7 mg(Pt) cm^{-2}). The conditions was: temperatures 70/70/70 °C at ambient pressure. The flow rates were 30 sccm of N_2, on the cathode side and 30 sccm of H_2 on the anode side. Features corresponding to reduction of surface oxides (series of colored vertical lines) and oxygen species formation on the surface (black line) are marked.

We can conclude that Pt-Co prepared by magnetron sputtering can significantly improve oxygen reduction on the cathode side of fuel cell in comparison with pure sputtered Platinum. Additionally, we have shown that optimal Pt_3Co phase was obtained without any annealing procedure but for direct evidence of presence of Pt_3Co phase *the high resolution transmission microscopy (HRTEM)* or *the x-ray diffraction (XRD)* is necessary.

12.2 PtCeO$_2$ anode + PtCo cathode

The nonreactive magnetron sputtering was used to prepare Pt-CeO_2 thin films and Pt-Co thin film catalysts. The Pt-CeO_2 anode catalyst layer was prepared by means of two magnetrons working simultaneously. RF sputtering of ceria was performed by using CeO_2 target (52 mm diameter, Kurt J. Lesker) at distance of 90 mm from substrates. Pt was added by using the second DC operated magnetron with Pt target (2 inches diameter, Kurt J. Lesker) at distance of 200 mm from substrates and tilted by 45° relative to the CeO_2 target. RF power (13.56 MHz) applied to the CeO_2 target was 50 W while power applied to the Pt target was 10 W. The sputtering was carried out in Ar atmosphere with total pressure of $4{\cdot}10^{-1}$ Pa. The sputtering conditions gave a growth rate of the Pt-doped cerium oxide films of 1 nm min^{-1}. The cathode Pt-Co catalyst was prepared by using the same procedure as it has been already described above. Power of 20 W was applied to the both Co and Pt targets; the total pressure of argon working atmosphere was kept at $6{\cdot}10^{-1}$ Pa. The sputtering conditions gave a growth rate of the

Pt-Co films of 3.3 nm min^{-1}. The both catalyst layers were carried on commercial nGDL support (Sigratec, GDL 25 BC). The catalyst film thicknesses were determined by Atomic Force Microscopy (AFM) from the reference films deposited on the silicon substrate simultaneously as it has been already described above.

As we have shown previously, sputtered Pt doped cerium oxide contains Pt in $Pt^{2,4+}$ states [124, 126, 148]. In the PEM FC a mixture of hydrogen and water vapor is used as a feed stream due to necessity to keep the proton exchange membrane wet. Consequently during the FC working conditions the anode catalyst is reduced and for very low loading (case of this work) Pt^{4+} is transformed to Pt^{2+}. Figure 12.4 (top-left) shows Pt 4f spectrum obtained after annealing in wet H_2 at 65 °C in the flow reactor simulating anode conditions of the PEM FC operation .The spectrum of hydrogen annealed Pt-CeO_2 confirms that there is only one $4f_{7/2}$ - $4f_{5/2}$ doublet at binding energy (BE) 72.5 - 75.8 eV corresponding to Pt^{2+} [126]. XPS analysis of the Pt-Co alloy thin film used as a cathode is shown in fig. 12.4. The Pt 4f spectrum presented in fig. 12.4 (bottom-left) shows that Pt has metallic character which is seen from doublet at BEs 71.2 - 74.5 eV and asymmetric shape of the Pt 4f peaks characteristic for metallic Pt. The Co $2p^{3}/_{2}$ region of the XPS spectrum in fig. 12.4 (bottom-right) can be fit by four peaks, two peaks at 780.9 eV and 786 eV indicating Co^{2+} as predominant species, one peak at 779.9 eV corresponding to Co^{3+} and a peak of metallic Co at 778.6 eV [149]. The highest peak at 780.9 eV is a Co^{2+} main peak whilst 786 eV peak corresponds to the satellite structure characteristic of octahedral Co^{2+} cations [150]. The O 1s spectrum in fig. 12.4 (top-right) shows two peaks at 529.6 eV and 531 eV that could be assigned to Co_2O_3 and CoO, respectively [151]. It is evident that amount of cobalt oxides in the Pt-Co catalyst is substantially higher in relation to the metal Co content. The presence of high amount of oxidized Co in the Pt-Co catalyst could be explained by its exposure to air due to the sample transfer to the XPS spectrometer through air. We note that it is difficult to assign any of the mentioned XPS peaks to eventual Pt-Co alloy formation because Pt-Co alloy binding energy shifts for Pt 4f $^{7}/_{2}$ and Co 2p $^{3}/_{2}$ in relation to pure metals are very small, 0.1 eV and 0.2 eV, respectively [152].

Fuel cell measurement was proceed with the use of our piston cell described in chapter 7.2. The piston pressure was set to 8 Bar. Operating over pressure of both feed gases (H_2 and O_2) was 0.5 Bar and flow rates were 40 sccm for H_2, 30 sccm for O_2. The temperature conditions was 70 °C of operating cell and dew points of 70 °C for both humidifier systems (70/70/70 °C). The active area of MEA was 4.62 cm^2 and it was consisted of magnetron sputtered 30 nm thick Pt-CeO_2(2 μg(Pt) cm^{-2}) layer as an anode and magnetron sputtered 50 nm Pt-Co (46 μg(Pt) cm^{-2}) layer as a cathode. Hence, the total loading was 48 μg(Pt) cm^{-2} of MEA. Pt loadings were calculated from the film thickness and Pt concentration determined by XPS. As a electrolyte Nafion membrane (DuPont Inc., Nafion NR-212, perfluorosulfonic acid-PTFE copolymer) with thickness of 0.05 mm was used.

The results of fuel cell analysis for fully thin catalyst fuel cell are presented in fig. 12.5 which reveals power densities $PD = 0.125$W cm^{-2}. This power density corresponds to specific power of MEA $SP = 2.5$W $mg(Pt)^{-1}$. For better understanding of the results the comparison with commercial catalyst and results from the chapter 12.1 is summarized in the table 12.3. It is seen that combination of Pt-Co cathode and Pt-CeO_2 anode exhibited lower power density than lowest power

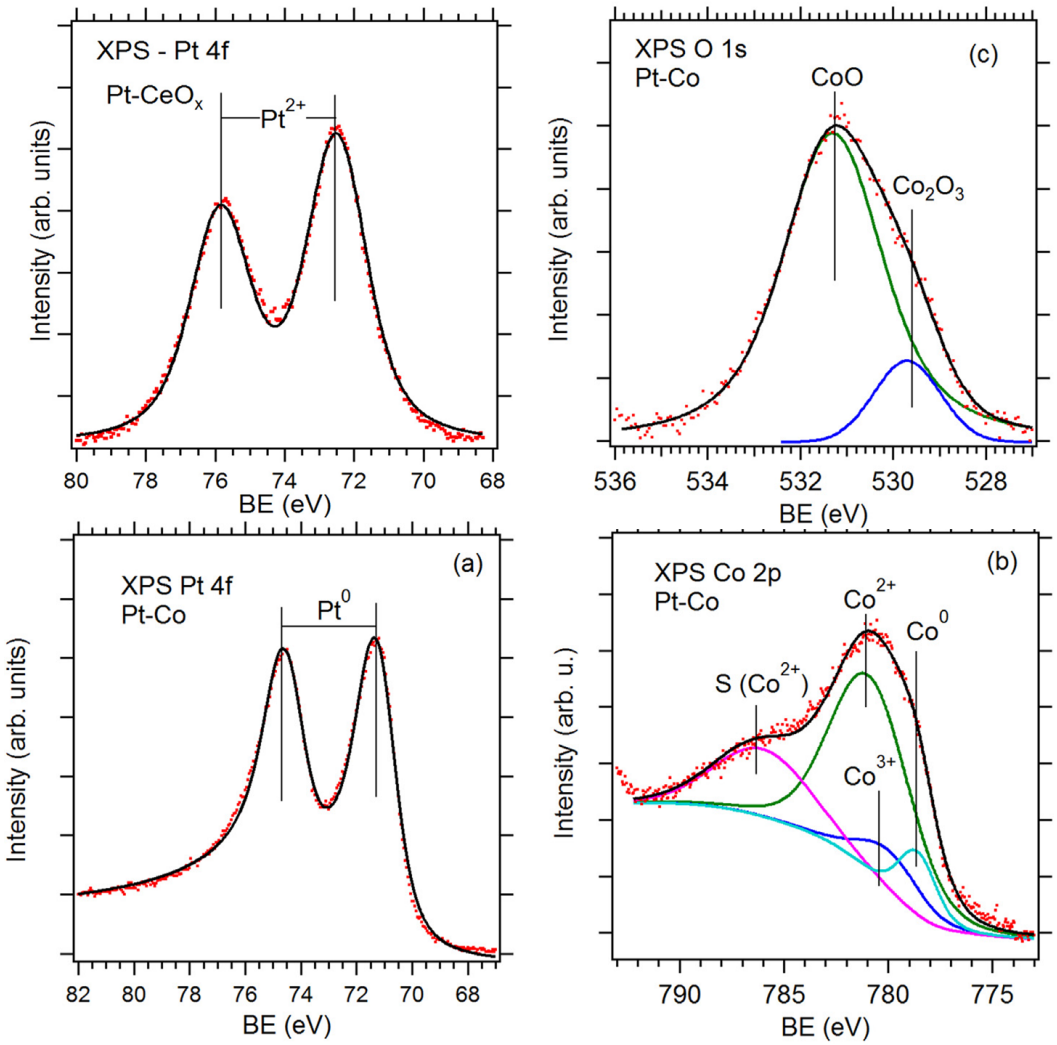

Fig. 12.4: The spectra: Pt 4f in Pt-CeO_2 (left-top), O 1s in Pt-Co (right-top), Pt 4f in Pt-Co (left-bottom) and Co 2p in Pt-Co. Pt-CeO_2 (30 nm, 2 μg(Pt) cm^{-2}) and Pt-Co (50 nm, 46 μg(Pt) cm^{-2}) sputtered layers are carried on nGDL.

density obtained with cell contained only one of our thin catalyst accompanied by commercial catalyst, Pt-CeO_2 anode + commercial cathode and commercial anode + Pt-Co. If we try to express this phenomenon by mathematical formula representing this observation (parallel combination of obtained performances) that I have found, we obtain

$$\frac{1}{(PD_{Fully\_thin})^q} = \frac{1}{(PD_{Pt-CeO2+com.cathode})^q} + \frac{1}{(PD_{Pt-CeO2+com.cathode})^q} \quad (12.1)$$

where $q = 1.618$ is correction parameter (by coincidence this value is equal to the Golden ratio). The reason why with the use of combination of our sputtered anode and cathode catalyst fuel cell a lower performance was obtained in comparison with both their combination with commercial catalyst is clear. There is not any strong commercial catalyst on the second side that could improve the performance. Be that as it may, the power density of 0.125 W is relatively good result in comparison with commercial catalyst and according to the fact that only 48 μg(Pt) cm^{-2} loading was used for all MEA.

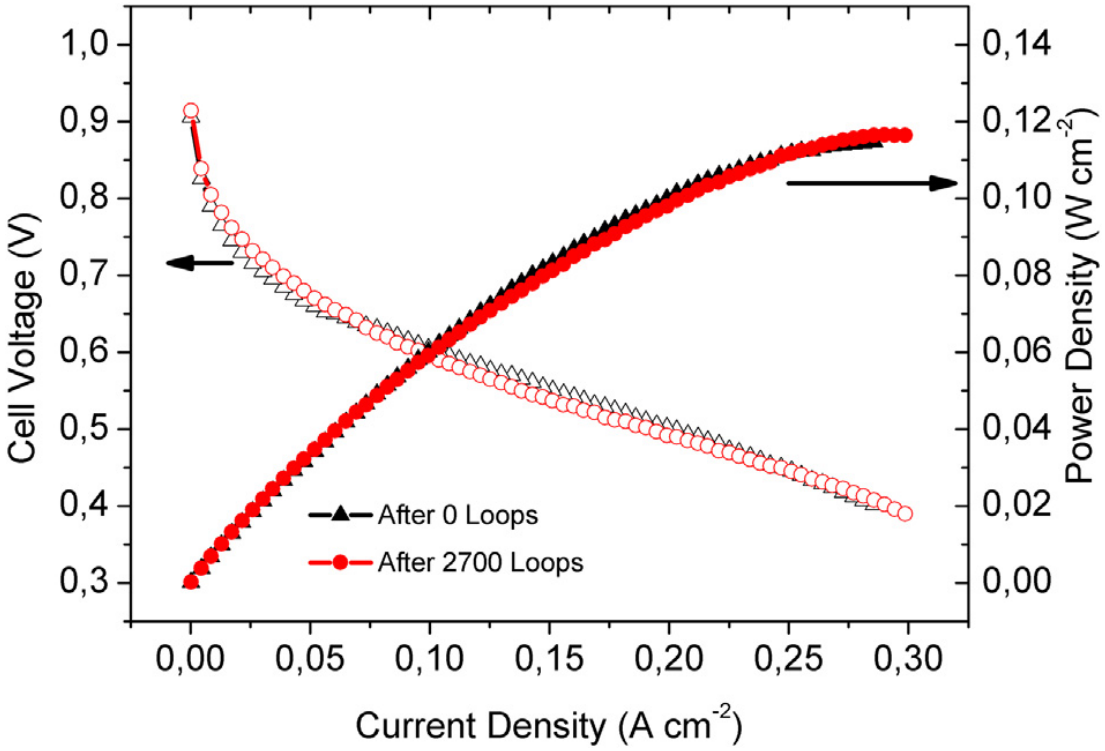

Fig. 12.5: The result of fuel cell test before endurance test (black) and after 2700 cycles of endurance test (red) for fuel cell consisted of 30 nm thick Pt-CeO_2(2 μg(Pt) cm^{-2}) sputtered layer as an anode and 50 nm sputtered Pt-Co (46 μg(Pt) cm^{-2}) layer as a cathode. The conditions was: temperatures 70/70/70 °C at pressure 0.5 Bar. The flow rates were 40 sccm for H_2 (Stoich 1.2), 30 sccm for O_2 (Stoich 2.0).

Anode	**Cathode**	**Power Density** W cm^{-2}	**Pt Loading** μg(Pt) cm^{-2}	**Specific Power** W mg(Pt)$^{-1}$
Com. Ref.	Com. Ref.	0.65	4700*	0.14*
Pt-CeO_2	Com. Ref.	0.45	2	225
Com. Ref.	Pt-Co	0.34	50	6.8
Pt-CeO_2	Pt-Co	0.125	48*	2.7*

Tab. 12.3: The obtained power densities and specific powers for Pt-CeO_2 anode, Pt-Co cathode catalyst and its combination as fully thin catalyst film PEM FC compared with commercial reference catalyst Alfa Aesar (2.7 mg(Pt) cm^{-2}) as an anode and Alfa Aesar (2.0 mg(Pt) cm^{-2}) as a cathode. Data were obtained at 70/70/70 °C at pressure 0.5 Bar. The flow rates were 40 sccm for H_2 (Stoich 1.2), 30 sccm for O_2 (Stoich 2.0). *Platinum loading and specific power are calculated for all MEA.

Figure 12.6 shows result of the endurance test of the fuel cell. The measurement has been proceed by protocol described in chapter 6.5. Each bar represents average of power densities obtained after finishing 300 of endurance cycles consisted of periodically changing working conditions (maximal performance <-> non-loaded cell). It is clearly seen that there did not appear any significant and statically approved drop of performance for all 2700 measured cycles despite some fluctuation was revealed. This fact is confirmed in figure 12.5 where fuel cell polarization curve and current power density dependency on current density before

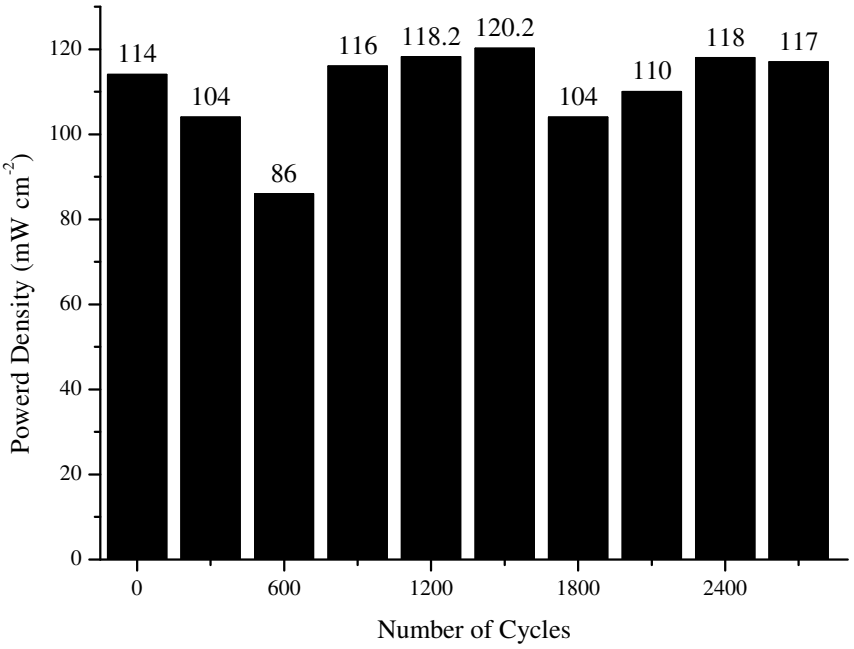

Fig. 12.6: The result of endurance durability test according to the procedure described in 6.5 for fuel cell consisted of 30 nm thick Pt-CeO_2 (2 μg(Pt) cm^{-2}) sputtered layer as an anode and 50 nm sputtered Pt-Co (60% of Pt) layer as a cathode. The conditions was: temperatures 70/70/70 °C at pressure 0.5 Bar. The flow rates were 40 sccm for H_2 (Stoich 1.2), 30 sccm for O_2 (Stoich 2.0).

and after endurance test are shown; any performance decrease was not seen.

The *in situ* characterization of catalysts films by the cyclic voltammetry performed directly in the fuel cell was used to clarify the electrochemical activity of the catalyst. The CV experiment was performed using the standard two-electrode setup: The counter electrode and the reference electrode together were connected to the side fed by a humidified moistened hydrogen flow and the working electrode was connected to the side of interest keeping under a humidified moistened nitrogen flow as it was described in the section 6.2. The conditions of CV measurement were as follows: the flow rates were 30 sccm of moistened hydrogen and 30 sccm of moistened mixture 10% H_2 and 90% N_2 on the side of reference-counter electrode and on the side of working electrode respectively; The pressure of gases was ambient pressure; The temperature was 70 °C and pressure in the piston was 8 Bar; the scan rate was 100 mV s^{-1}. The CV from Pt-CeO_2 anode is shown in figure 12.7 (left) and the CV from Pt-Co cathode is shown in the same figure (right). It is clearly seen that both materials are catalytically active. Both CVs clearly show PtO reduction and high hydrogen adsorption/desorption features in the region 0-0.4 V. Similarly to FC tests, these results confirm high catalytic activity of both materials. In the case of both CVs, relatively high hydrogen evolution appeared. The reason was that the non-standard dynamic platinum-hydrogen electrode consisted of Platinum based catalyst (Pt-CeO_2 or Pt-Co) was used as reference and set the accurate and proper zero potential was difficult.

Similarly, the exact potential against to reversible hydrogen electrode (RHE) was difficult to determine and the data are shown as obtained. The shift to the positive current of both obtained voltammograms was due to crossover of hydrogen that was 0.6 mA cm^{-2} which can explain the shift $\sim$ 2.6 mA. The CV profile obtained for Pt-Co in fig. 12.7 (right) is similar to that of the active disordered Pt_3Co cubic phase CV in [146] confirming suggestion of a Pt rich skin formation. In the case of Pt-CeO_2 (see fig. 12.7 (right)) the hydrogen adsorption/desorption region is substantially shifted to the positive current in comparison with the rest of curve while this behavior is not seen in the case of Pt-Co (see fig. 12.7(left)) which is most likely by due to faster kinetics of hydrogen oxidation on Pt-CeO_2 in comparison with Pt-Co. The reaction kinetics can be compared using the slope of hydrogen evolution (comparison is not shown).

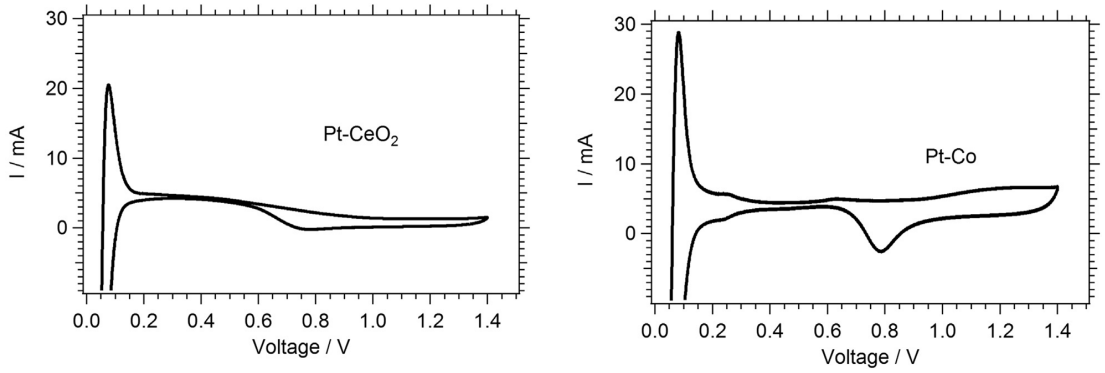

Fig. 12.7: The voltammograms for Pt-CeO_2 (2 μg(Pt) cm^{-2}) (left) and Pt-Co (46 μg(Pt) cm^{-2}) (right) obtained in-operando with the use of 30 sccm of N_2 on the side of interest and with 30 sccm of (10% H_2,90% N_2) as dynamic hydrogen reference electrode on the second side. The other condition: ambient pressure, 70/70/70 °C and the scan rate of 100 mV s^{-1}. Active area is 4.41 cm^2

We have presented our first experiment of fully thin catalyst fuel cell. My opinion is that after optimization of Pt-Co with respect to the previous section 12.1 the presented performance could be exceeded.

Some of results presented in this chapter have been already published and more details can be found directly in the article [153].

13. Pt-SnCeO$_x$

13.1 FC perfomance

In this chapter the FC study of alternative material Pt-SnCeO$_x$ thin anode catalyst layers are investigated.

Samples of Pt-SnCeO$_x$ were prepared by magnetron sputtering (described in chapter 8) based on simultaneous sputtering procedure from two targets: SnO_2 target (2 inches Kurt J. Lesker) and CeO_2 (2 inches Kurt J. Lesker) with two Platinum wires (diameters: 0.35 mm, length: 2 cm, from Alfa Aesar) placed on the target in radial direction. Residual pressure was $2{\cdot}10^{-4}$ Pa. The process gas

was Ar at pressure $6{\cdot}10^{-1}$ Pa. Power applied to magnetron with SnO_2 was P_{DC} = 20 W and power applied to magnetron with composite target consisted of CeO_2 +2× Pt wires was P_{RF} = 120 W. Pt-CeO_2 catalyst layer was prepared by the same way but without the use of SnO_2 target using the discharge power set to 70 W. The catalyst film thicknesses were determined as 25 nm by Atomic Force Microscopy (AFM) from the reference films deposited on the silicon substrate simultaneously and Pt loading was determined from XPS analysis by method described in chapter 19.1 as 2 μg(Pt) cm^{-2} and 2 μg(Pt) cm^{-2} for Pt-$SnCeO_x$ and of Pt-CeO_2, respectively. The atomic ratio of Pt-$SnCeO_x$ and of Pt-CeO_2 given by XPS is (Pt:Sn:Ce) = (7.5:4.9:87.6) and (Pt:Ce)=(7.5:92.5), respectively.

As a substrate a commercial nGDL was used.

The comparison of XPS Ce 3d spectra obtained for Pt-$SnCeO_x$ and Pt-CeO_2 is presented in figure 13.1. The characteristic $3d_{5/2} - 3d_{3/2}$ doublets attributed to Ce^{4+}: (882.1-900.6) eV, (888.8-907.2) eV, (898.2-916.6) eV and attributed to Ce^{3+}: (880.4-999.2) eV, (885.3-903.9) eV are shown [154, 155]. The doublet (883.3-901.8) eV was used to approximate of natural asymmetry of the doublet 882.1-900.6 eV. The fit has been proceeded with the procedure published in [155] and it is similar to the procedure presented in chapter 14 where fully oxidized Pt-CeO_2 was shown. Thus, we can see that both ceria based samples (Pt-$SnCeO_x$ and Pt-CeO_2) ware partially reduced. The ratio of Ce^{3+}/Ce^{4+} is 0.4 and 0.2 for Pt-$SnCeO_x$ and Pt-CeO_2, respectively. The fact that Ce^{3+}/Ce^{4+} for Pt-$SnCeO_2$ is higher than in the case of Pt-CeO_2 is also in agreement with the literature [148].

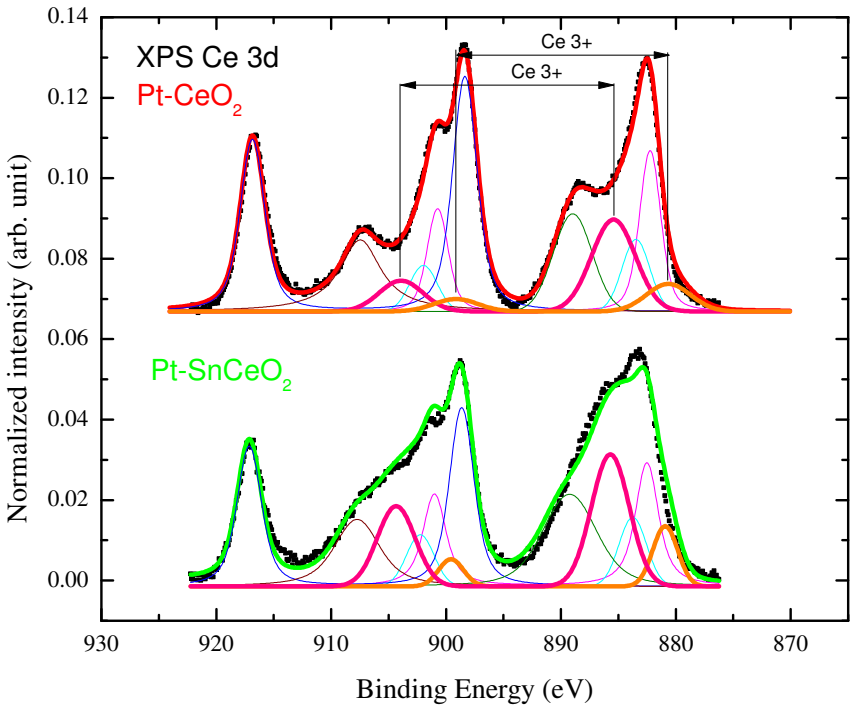

Fig. 13.1: The Ce 3d XPS spectra of Pt-CeO_2 (25 nm) (top) and Pt-$SnCeO_x$ (25 nm) (bottom). Three doublets $3d_{5/2}-3d_{3/2}$ contributed to Ce^{4+} and two doublets $3d_{5/2}-3d_{3/2}$ representing Ce^{3+} are shown.

XPS of Pt 4f of Pt-$SnCeO_2$ (25 nm) (see figure 13.2 (top)) revealed three doublets $4f_{7/2} - 4f_{5/2}$ representing Pt^{2+} (72.6-75.9) eV [125, 126], (74.4-78.0) eV [125, 126] Pt^{4+} and Pt state attributed to Pt-Sn alloy [148]. The Pt 4f feature attributed to Pt-Sn alloy was determined by using the same fitting parameters for Pt^2+ and Pt^4+ obtained for XPS of Pt 4f of Pt-CeO_2 (25 nm) presented in fig. 13.2 (top) as a reference. Without this procedure with reference fitting parameters the Pt-Sn feature cannot be found (only doublets corresponding with Pt^{4+} would be slightly shifted to the higher binding energy) due to the fact that XPS is not as precise as HXPES used by authors [156]. The chemical states concentration was determined: (Pt^{2+}:Pt^{4+}:Pt-Sn) as (0.37:0.23:0.40) and (Pt^{2+}:Pt^{4+}) as (0.39:0.61) for Pt-$SnCeO_2$ (25 nm) and Pt-CeO_2 (25 nm), respectively. Figure 13.2 (bottom) shows XPS Sn 3d. One observed doublet $3d_{5/2} - 3d_{3/2}$ (486.4-495.0) eV was attributed to Sn^{4+} [157, 158].

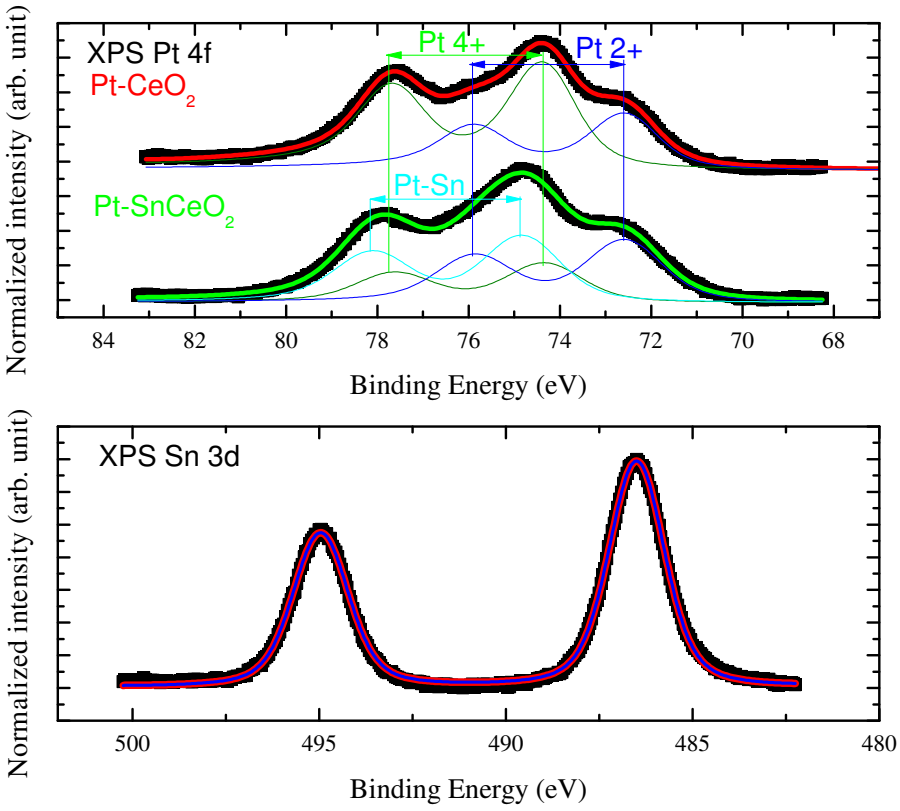

Fig. 13.2: The comparison of XPS result for Pt 4f in Pt-CeO_2 (25 nm) and in Pt-$SnCeO_2$ (25 nm) (top). The doublets $4f_{7/2} - 4f_{5/2}$ representing Pt^{2+}, Pt^{4+} and Pt-Sn are shown. XPS of Sn 3d in Pt-$SnCeO_2$ (25 nm) (bottom). The doublet $3d_{5/2} - 3d_{3/2}$ contributed to Sn^{4+} is shown.

The FC analysis was performed with the use of Quintech commercial cell with active area of 1 cm^2 and the cell was tightened by bolts using torque of 3 N m. As a membrane, 0.125 mm thick Nafion (Alfa Aesar, Nafion NE-1035 perfluorosulfonic acid-PTFE copolymer) was used. Before the membrane was used in fuel cell, the special treatment was necessary (already published in our works [124–126] and in the previous chapter 10). Cathode catalyst was commercial catalyst from Alfa Aesar (2 mg cm^{-2} of Pt). The temperatures of anode humidifier and

cathode humidifier were 70 °C and 65 °C, respectively. Experiment was proceeded with flow rates of 40 sccm (1.2 Stoich) for H_2, 30 sccm for O_2 (2.0 Stoich) at ambient pressure. Figure 13.3 shows FC test results for two different cell temperatures: room temperature and 70 °C. The obtained power densities and specific powers are summarized in the table 13.1 where the comparison with commercial anode catalyst and Pt-CeO_2 is presented (IV curves obtained for Pt-CeO_2 and commercial catalyst is not presented because they have been already investigated previous chapters). It is clearly seen that Pt doped tin cerium mix-oxide exhibited slightly lower power densities than Pt doped cerium oxide.

However, specific power of both prepared catalysts has still exceeded the specific power of commercial catalyst more than 700 times. This fact clarified Pt-$SnCeO_x$ anode sputtered catalyst as a promising anode catalyst and as an alternation to the Pt-CeO_2.

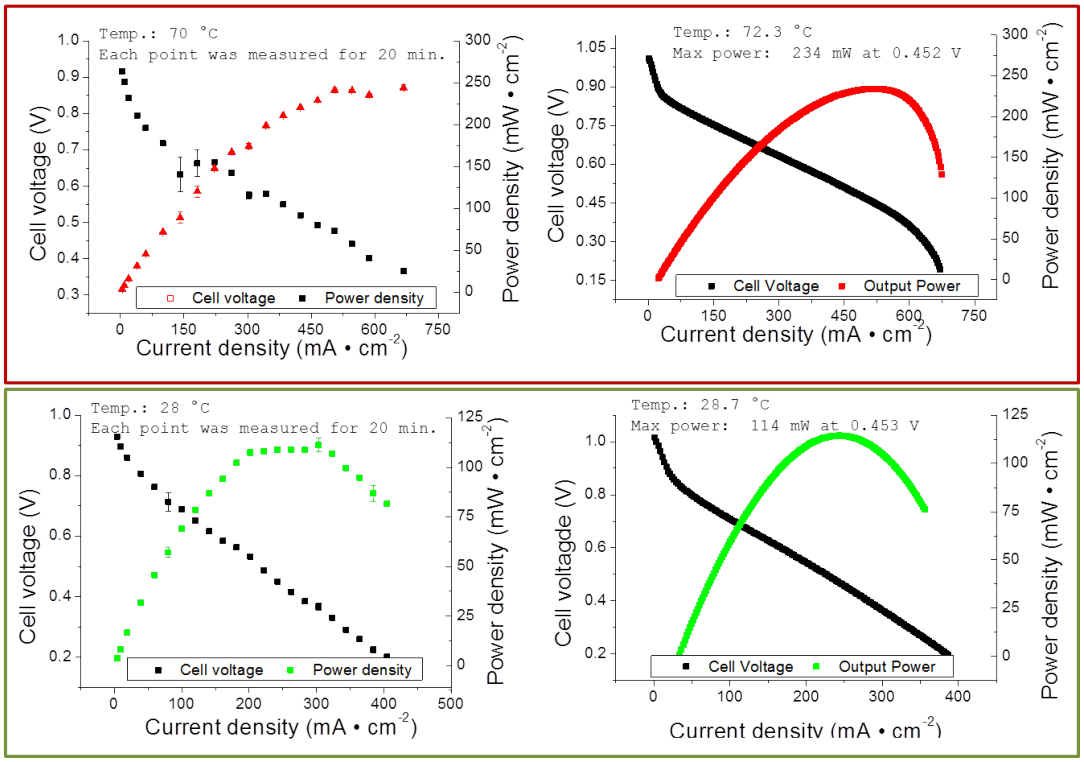

Fig. 13.3: The results of fuel cell analyses for Pt-$SnCeO_x$ anode catalyst at ambient pressure for two different temperatures: 70 °C (top), 27 °C -room temperature (bottom). On the right there is IV curve determined by measuring and averaging each current step for 50 ms and on the left is IV curve where each point is result of statistical analysis of 20 min time scan. Cathode catalyst was commercial catalyst from Alfa Aesar (2 mg cm^{-2} of Pt). The flow rates were 50 sccm (1.2 Stoich) for H_2, 40 sccm for O_2 (2.0 Stoich). As a membrane Nafion of 0.125 mm thick (Alfa Aesar, Nafion NE-1035 perfluorosulfonic acid-PTFE copolymer) was used.

	Power Density mW cm^{-2}	**Pt Loading** μg(Pt) cm^{-2}	**Specific Power** W mg^{-1}
Commercial Anode	450	2700	0.17
Pt-CeO_2	250	2	125
Pt-$SnCeO_x$	234	2	117

Tab. 13.1: The obtained power densities and specific powers of Pt-$SnCeO_x$ anode catalyst and its comparison with commercial catalyst and Pt-CeO_2 sputtered anode. Conditions of fuel cell experiment are the same as in figure 13.3 (70 °C).

13.2 CO poisoning

The effect of CO poisoning on Pt-$SnCeO_x$ is presented in this section. The same samples as in the previous section were used and the FC conditions were the same.

Figure 13.4 shows results of CO poisoning analyses for different anode catalysts presented in table 13.1. The data series are as follows: Pt-$SnCeO_x$ (I) (2 μg(Pt) cm^{-2}), Pt-$SnCeO_x$ (II) (2 μg(Pt) cm^{-2}), Pt-CeO_2 (2 μg(Pt) cm^{-2}) and commercial Alfa Aesar Pt-Ru alloy (1:1) (2.7 mg(Pt) cm^{-2}) anode catalyst. Data line labeled (I) and (II) are two different series of poisoning effect of the same catalyst. There are shown normalized current densities at 0.5 V for different concentration of CO. Label "0 ppm" means that no CO was used in this case and catalyst was regenerating. Absolute values of current densities are listed in the table 13.2. Each CO treatment was ∼3 h long.

The side result is also the comparison of current density dependencies on time for Pt-Ru alloy (1:1) commercial catalyst (2.7 mg(Pt) cm^{-2}) and Pt-$SnCeO_x$ sputtered catalyst which is shown in figure 13.5. It is seen that some periodical behavior which has influence on performance appeared in the case of Pt-Ru catalyst in contrast to sputtered Pt-$SnCeO_x$ layer where this phenomenon was not observed. These features are caused by inconvenient water management of Pt-Ru commercial catalyst operated in PEM FC, which was also proved later.

CO concentration ppm	**Pt-Ru comm.** mA cm^{-2}	**Pt-$SnCeO_x$ (I)** mA cm^{-2}	**Pt-$SnCeO_x$ (II)** mA cm^{-2}	**Pt-CeO_2** mA cm^{-2}
0	678	465	490	500
25	680	460	500	283
0	685	466	490	290
50	465	450	430	200
0	700	452	470	231
100	410	178	210	150
0	680	425	410	200
250	320	100	140	100
0	630	390	400	80
500	280	70	90	
0	607	420	461	
0 Next Day	700	504		

Tab. 13.2: Obtained current densities at 0.5 V for Pt-$SnCeO_x$ (I), Pt-$SnCeO_x$ (II), Pt-CeO_2 and commercial Alfa Aesar Pt-Ru alloy (1:1) (2.7 mg(Pt) cm^{-2}) anode catalyst for different CO concentration. The FC conditions are the same as in figure 13.4.

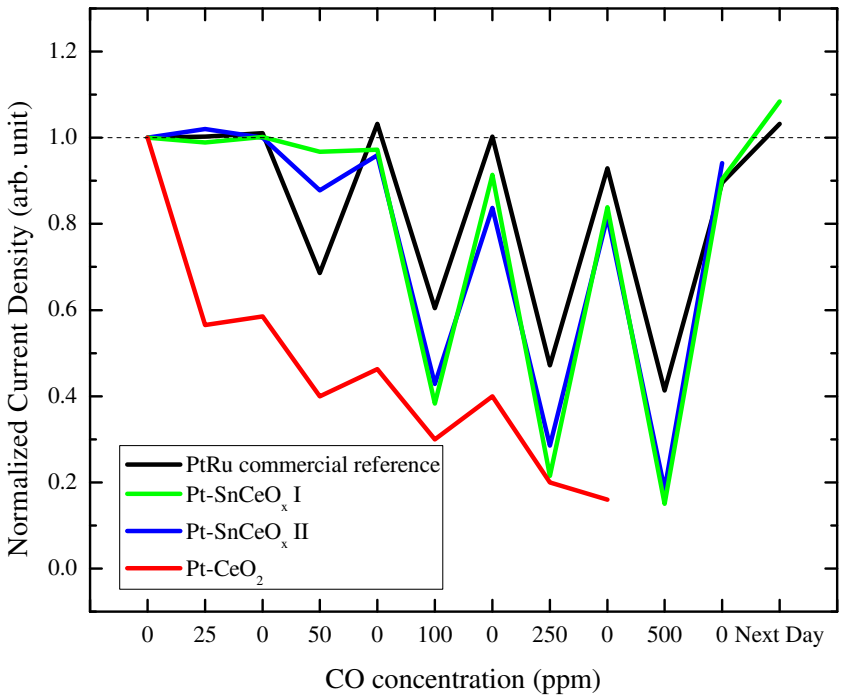

Fig. 13.4: The results of fuel cell CO poisoning effect analyses for Pt-SnCeO$_x$ (I), Pt-SnCeO$_x$ (II), Pt-CeO$_2$ and commercial Alfa Aesar Pt-Ru alloy (1:1) (2.7 mg(Pt) cm^{-2}) anode catalyst at temperatures 70/70/70 °C at ambient pressure. The flow rates were 50 sccm for H_2 (or mix H_2+CO), 40 sccm for O_2. Normalized current densities at 0.5 V for different CO concentration are shown. Cathode catalyst was commercial catalyst from Alfa Aesar (2 mg(Pt) cm^{-2}).

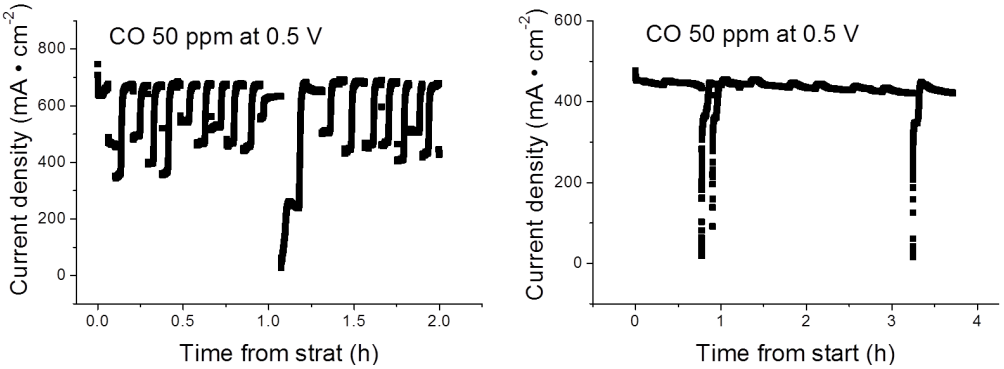

Fig. 13.5: The comparison of time dependency of current densities obtained for Pt-Ru (1:1) from Alfa Aesar (2.7 mg(Pt) cm^{-2}) (left) and Pt-SnCeO$_x$ sputtered anode catalyst 2 μg(Pt) cm^{-2}) (right). The FC conditions are the same as in figure 13.4.

Regarding the figure 13.4 and the table 13.2, it was confirmed that in the

case of Pt-CeO_2 the poisoning effect is significant and it starts at the lowest CO concentration (25 ppm) as it was also shown in chapter 11.3.

On the other hand, Pt-$SnCeO_x$ sputtered anode catalyst revealed comparable CO tolerance with Pt-Ru commercial catalyst. Moreover, at CO concentration of 50 ppm Pt-$SnCeO_x$ has exhibited higher CO tolerance than Pt-Ru commercial catalyst, which is important result.

Remind the comparable performance of Pt-$SnCeO_x$ and Pt-CeO_2 as it has been shown in the previous section, the Pt-$SnCeO_2$ is promising alternate catalyst revealing good stability and CO tolerance comparable with Pt-Ru (1:1) alloy. The function of Sn in our sputtered catalyst should be still more investigate but we can estimate that role of Sn in the Pt-$SnCeO_2$, where the alloy Pt-Sn seems to be created, is similar to the role of Ru in the Pt-Ru alloy commercial catalyst. Thus, Pt-Sn causes an increase of the probability of oxidation of carbonaceous species due to the lower onset potential for Sn-OH formation according to the equation 3.1. This hypothesis is also supported by the literature [159] where the Pt-$SnCe_2$ exhibits higher activity for ethanol oxidation reaction than Pt-CeO_2 catalyst.

14. Pd-CeO_x

In this chapter the possible alternation to Pt in Pt doped CeO_2 is presented. The Pd doped CeO_2 thin layer prepared by rf-magnetron sputtering as an anode catalyst for PEM FC was investigated.

Pd-CeO_2 thin layer was prepared by magnetron sputtering using 2 magnetrons simultaneously: one with CeO_2 target (2 inch diameter, Kurt J. Lesker, 99.9% pure) and second with Pd target (2 inch diameter Kurt J. Lesker, 99.9% pure). The deposition was proceeded at pressure $6 \cdot 10^{-1}$ Pa with Argon atmosphere and discharge power was set to 20 W and 50 W for Paladium and CeO_2 target, respectively. Voltage set on the samples holder was $V_{BIAS} = 17\,\mathrm{V}$. The residual pressure before the chamber was filled by process gas was $2 \cdot 10^{-4}$ Pa. The samples were placed 90 mm away from CeO_2 target and 200 mm from substrates and tilted by 45° relative to the CeO_2 target. As a substrate commercial nGDL was used.

The thickness of layer was determined as 25 nm by AFM of the same layer sputtered on Si substrate simultaneously.

SEM images of Pd-CeO_2 sputtered thin layer on nGDL are seen for two different magnifications in figure 14.1. It is clearly seen that the porous structure similar to the structure observed on Pt-CeO_2 sputtered thin film on nGDL has been appeared.

XPS analysis of the Ce 3d spectrum of Pd doped ceria film is presented in 14.2. The characteristic $3d_{5/2} - 3d_{3/2}$ doublets attributed to Ce^{4+}: (882.0-900.5) eV, (888.8-907.2) eV, (898.2-916.6) eV and attributed to Ce^{3+}: (880.4-999.2) eV, (885.3-903.9) eV are shown [154, 155]. The three doublets attributed to Ce^{4+} represent different 4f configurations in the photoemission final state and arise from the Ce 4f hybridization in both the initial and final states [154]. We subtracted a Shirley-type background and then fitted all peaks by using Voigt profile. Detailed description of the Ce 3d spectra fitting procedure is described in Skala et al. [155]. The Ce $3d_{5/2}4d^2$ at 882.0 eV and Ce $3d_{3/2}4d^2$ at 900.5 eV are fitted by adding an

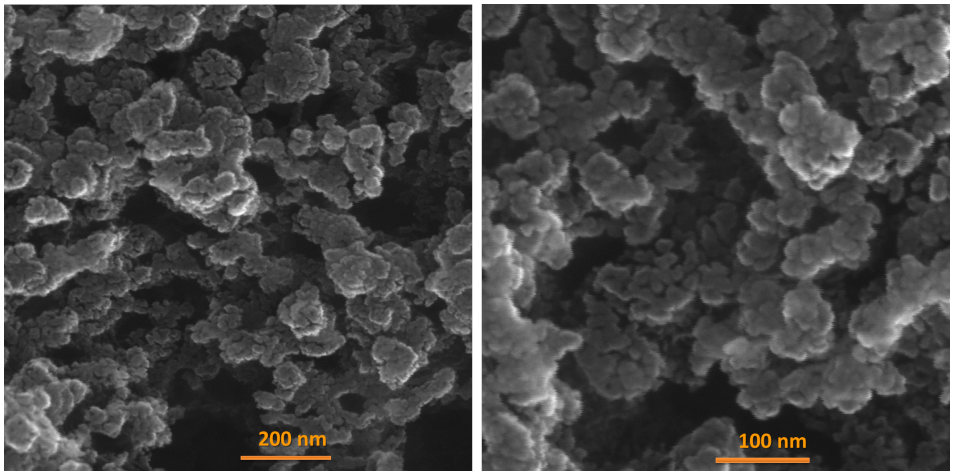

Fig. 14.1: The SEM images of 25 nm thick sputtered Pd-CeO_2 layer on nGDL for two different magnification.

extra pair of features (azur) because of its asymmetry [155]. Generally, there is no physical reason to suppose the same width of features because there are different spins of final states therefore also the lifetime of states can be different. This phenomenon is seen for peaks Ce $3d_{5/2}4f^1$ at 888.8 eV (green) and Ce $3d_{3/2}4d^1$ at 907 eV (brown) where different widths of peaks were fitted.

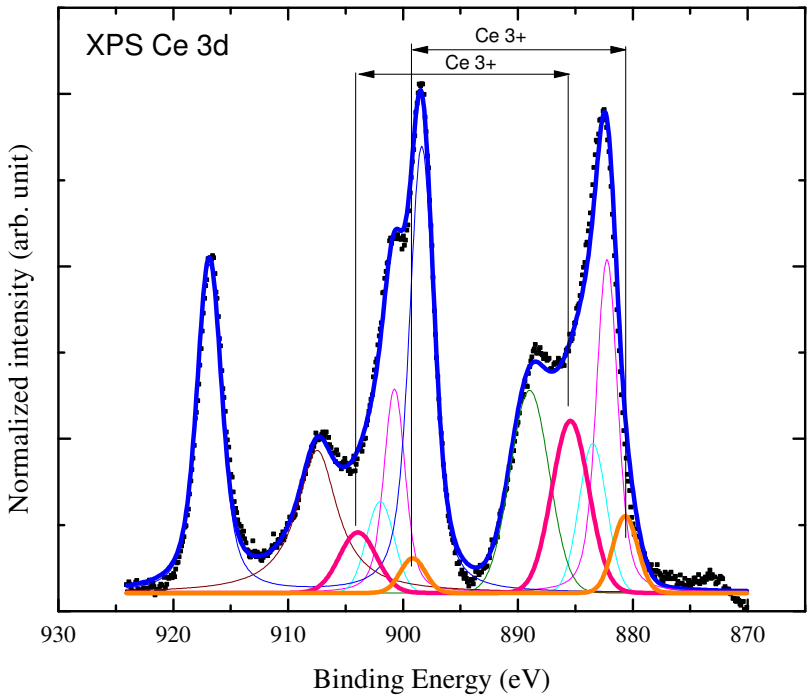

Fig. 14.2: The Ce 3d XPS spectra of Pd-CeO_x (25 nm)/CF. Three doublets $3d_{5/2}-3d_{3/2}$ contributed to Ce^{4+} and two doublets $3d_{5/2}-3d_{3/2}$ representing Ce^{3+} are shown.

Analysis of XPS spectrum of Pd 3d 14.3 reveals shift of binding energy for Pd

3d from 335.1 eV (metallic state) to 337.5 eV which corresponds to PdO (Pd^{2+}) which is the most stable oxidized form of Pd [160].

The ratio of Pd/Ce was determined as ratio of XPS peak area Pd 3d and Ce 3d divided by its sensitive factors. Hence, the ratio Pd/Ce was 4.7% which corresponds to loading of Palladium 0.5 μg cm^{-2}.

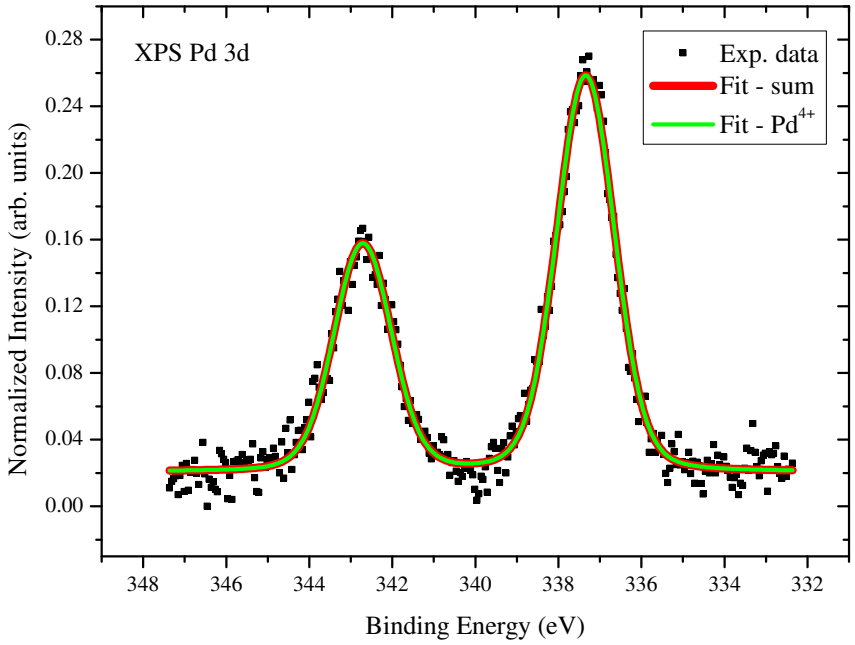

Fig. 14.3: The Pd 3d XPS spectra of Pd-CeO_x (25 nm)/CF. The doublets $3d_{5/2} - 3d_{3/2}$ are shown. Only Pd^{2+} is appeared.

Fuel cell measurement has been proceed using our piston cell described in chapter 7.2. The piston pressure was set to 8 Bar. Over pressure of both process gases (H_2 and O_2) was 0.5 Bar and flow rates were 50 sccm (1.2 Stoich) for H_2, 40 sccm for O_2 (2.0 Stoich). The temperature conditions were 70 °C of operating cell and dew points of 70 °C for both anode and cathode humidifier systems (70/70/70 °C). The Nafion NR212 (from Alfa Aesar), which is 50 μm thick, was used as a membrane.

The results of fuel cell analyses for Pd-CeO_2 sputtered thin layer on nGDL as an anode for PEM FC are presented in figure 14.4. It is seen that maximal power was reached at higher voltage (0.584 V) than 0.5 volt which means that the maximal power could be higher but the performance was dropping down due to diffusion limits for higher current density. The obtained results of fuel cell test of Pd-CeO_2 sputtered catalyst are compared with commercial catalyst (Alfa Aesar, 2.7 mg cm^{-2}of Pt) which is shown in figure 14.5. The gained power density and specific power are summarized in table 14.1. The power density for sputtered film $PD_{Pd} = 0.58\,\mathrm{W\,cm^{-2}}$ was 1.3 times less than power density of commercial catalyst $PD_{cmr} = 0.75\,\mathrm{W\,cm^{-2}}$ while the specific power of sputtered film $SP_{Pd} = 1160\,\mathrm{W\,mg(Pd)^{-1}}$ was 3900 times higher than the specific power of commercial catalyst $SP_{cmr} = 0.3\,\mathrm{W\,mg(Pt)^{-1}}$. Statistical analysis exhibits standard deviation

for obtained power density as 0.015 W cm^{-2}.

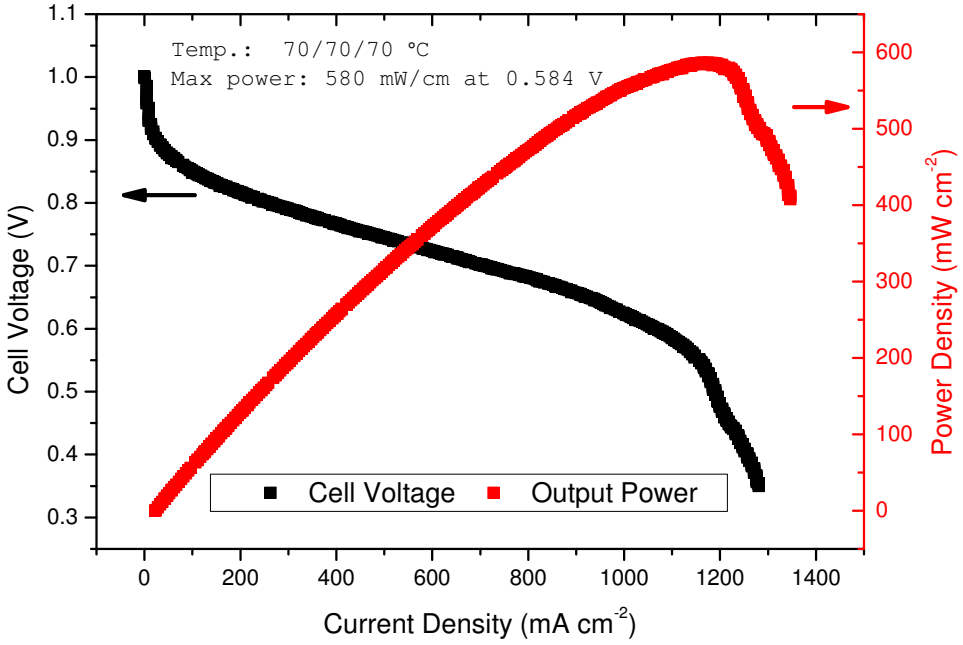

Fig. 14.4: The result of fuel cell analyses of Pd-CeO_2/nGDL anode catalyst at temperatures 70/70/70 °C at pressure 0.5 Bar. Cathode catalyst was commercial catalyst from Alfa Aesar (2 mg cm^{-2} of Pt). The flow rates were 50 sccm (1.2 Stoich) for H_2, 40 sccm for O_2 (2.0 Stoich). As membrane Nafion NR212 (from Alfa Aesar) was used.

	Power Density W cm^{-2}	**At Voltage** V	**Specific Power** W mg^{-1}
Commer. Ref.	0.75	0.518	0.3
Pd-CeO_2	0.58	0.584	1160

Tab. 14.1: The comparison of obtained power densities and specific powers of anode catalysts as commercial reference Anode (Alfa Aesar - 2.7 mg(Pt) cm^{-2}) and Pd-CeO_2 (25 nm thick layer, 0.5 μg(Pd) cm^{-2}) and commercial cathode (Alfa Aesar - 2.0 mg). The conditions were 70/70/70 °C and 0.5 Bar. As a membrane Nafion NR212 (from Alfa Aesar) was used.

The use of Pd in PEM FC as a catalyst for HOR as well as ORR has been already published [161, 162]. Authors presented the comparison of IV curves determined with the use of pure Pd and Pt-Pd alloys is shown. It is generally known that pure Pd is active for hydrogen oxidation but it exhibits lower performance than pure Pt because the overpotential of H-Pd formation is shifted and bond of H-Pd is too strong. On the other hand, it is clearly seen that the use of Pt-Pd alloy exhibits mostly the same performance as pure platinum. In addition, Pt-Pd alloy catalyst is more resistant to CO poisoning than Pt-Ru alloy as it is shown

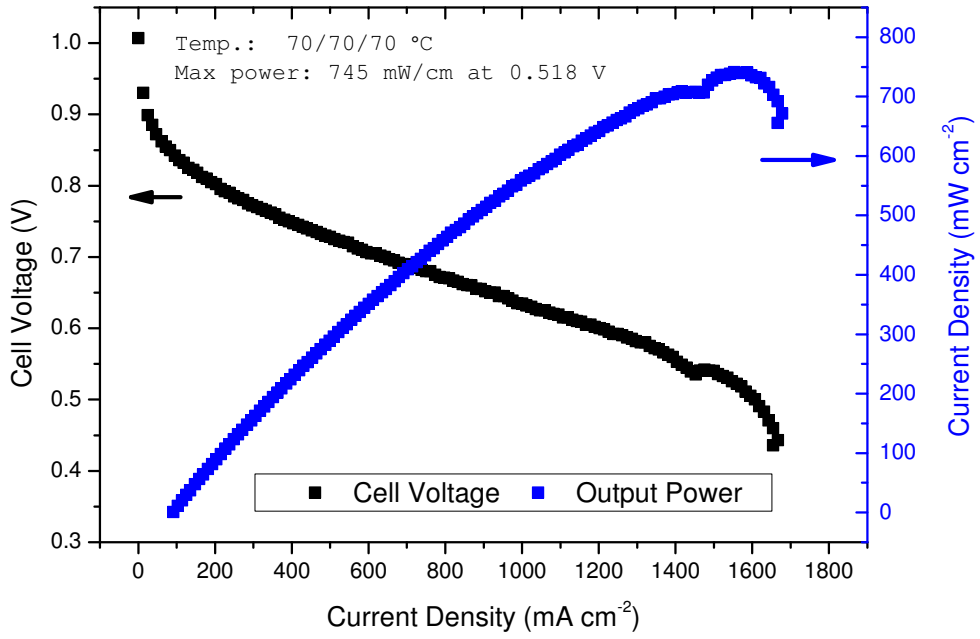

Fig. 14.5: The result of fuel cell analyses of commercial anode catalyst from Alfa Aesar (2.7 mg(Pt) cm^{-2}) at temperatures 70/70/70 °C at pressure 0.5 Bar. Cathode catalyst was commercial catalyst from Alfa Aesar (2 mg(Pt) cm^{-2}). The flow rates were 50 sccm (1.2 Stoich) for H_2, 40 sccm for O_2 (2.0 Stoich). As membrane Nafion NR212 (from Alfa Aesar) was used.

in the same literature [161].This fact could be useful for our DMFC FC anode or even cathode due to crossover effect (not shown).

We have shown that the use of Pd instead of Pt in Pt-CeO_2 sputtered catalyst is possible. Moreover, the price of Pd is 1.2 fold less than Pt [37]. Be that as it may, Pd-CeO_2 could help with diversification of sources of noble metals for PEM FC technology. Additionally, we have shown that the use of Pd-CeO_2 safes even much more Pt than in case of Pd-Pt alloy according to the literature . As a next step I suggest an investigation of another concentration of Pd (higher or lower) and comparison with pure Pd catalyst, and pure Pt about the same loading and do the comparison of Pt-CeO_2 and Pd-CeO_2 catalysts of the same atomic $\frac{\text{Pt}}{\text{Ce}} = \frac{\text{Pd}}{\text{Ce}}$ ratio.

15. Pt-WO_x

In this chapter the possible alternation to CeO_x is presented. The Pt doped WO_x thin layer prepared by rf-magnetron sputtering as an anode catalyst for PEM FC was investigated.

Thin layers of Pt doped tungsten oxide were prepared by reactive rf-magnetron sputtering from 1 inch WO_3 target (Kurt J. Lesker, 99.9% pure). More details

about this procedure have been already described in chapter 8. In the case of doped samples, 2 cm Platinum wire of 0.35 mm diameter was placed onto the target in radial direction. The processing atmosphere was composed of Ar and O_2 mixed with ratio $^{19}/_{1}$. Discharge power was set to 60 W which corresponds to 2.3 nm min^{-1} at this conditions. Commercial nGDL was used as substrate.

The thicknesses of layers were determined by AFM as 30 nm which corresponds to 26 μg cm^{-2} of Pt. SEM images for three different magnifications (shown in figure 15.1) revealed porous structure similar to structure observed for Pt-CeO_x deposited on nGDL.

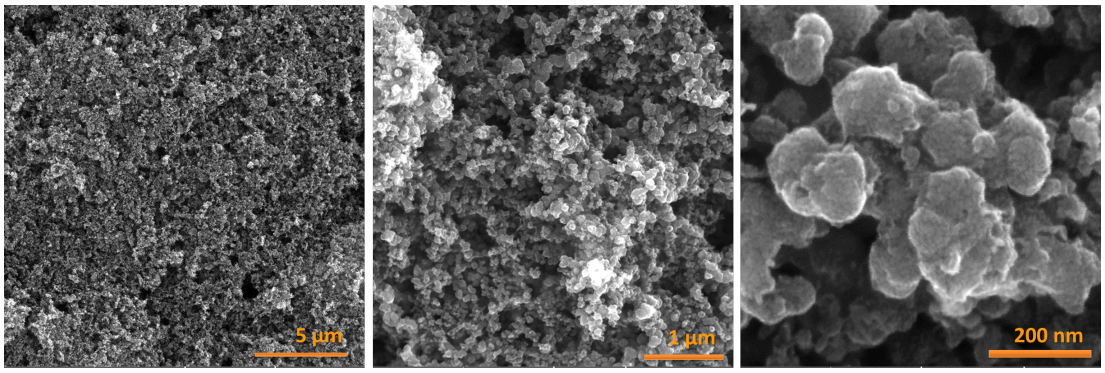

Fig. 15.1: SEM images for three different magnifications of Pt-WO_x sputtered on nGDL. The porous structure of layer is indicated (right).

The commercial cell tightened by bolts (Quintech, 1 cm^{-2}), which has been described in chapter 10, was used.

The cell was tightened by torque of 3 N m. As a membrane 0.05 mm thick Nafion membrane (DuPont, Nafion NR212) was used which had been pre-treated by manufacture therefore treatment procedure described in chapter 10 was not necessary.

The all fuel cell tests were performed at the same condition: hydrogen flow rate was 40 sccm, oxygen flow rate was 30 sccm and the pressure was 0.5 Bar with the use of commercial cathode from Alfa Aesar (2 mg cm^{-2}). The temperatures were set to 70/70/70 °C.

The example of fuel cell test analyses are shown in figure 15.2 where the comparison of Platinum doped tungsten oxide with commercial Pt reference catalyst is presented. The calculated power densities and specific power are summarized in the table 15.1. It is seen that while the power density for Pt-WO_x is 1.2 times less than the power density achieved by commercial reference catalyst, the specific power was 90 times higher in comparison with commercial reference catalyst.

Photoelectron spectroscopy analyses revealed cations of Platinum in the sputtered catalyst films (see XPS result in figure 15.3). The Pt 4f XPS spectrum exhibits Pt $4f_{7/2} - 4f_{5/2}$ doublet at 72.5 - 75.9 eV corresponding to Pt^{2+} [126] and second doublet at energies of 74.6-77.9 eV, which is attributed to the Pt^{4+} species [125]. The peaks were fitted using Doniach-Sunjic curve convoluted with Gaussian doublet and Shirley type background. The ratio Pt^{2+}/Pt^{4+} was 0.26.

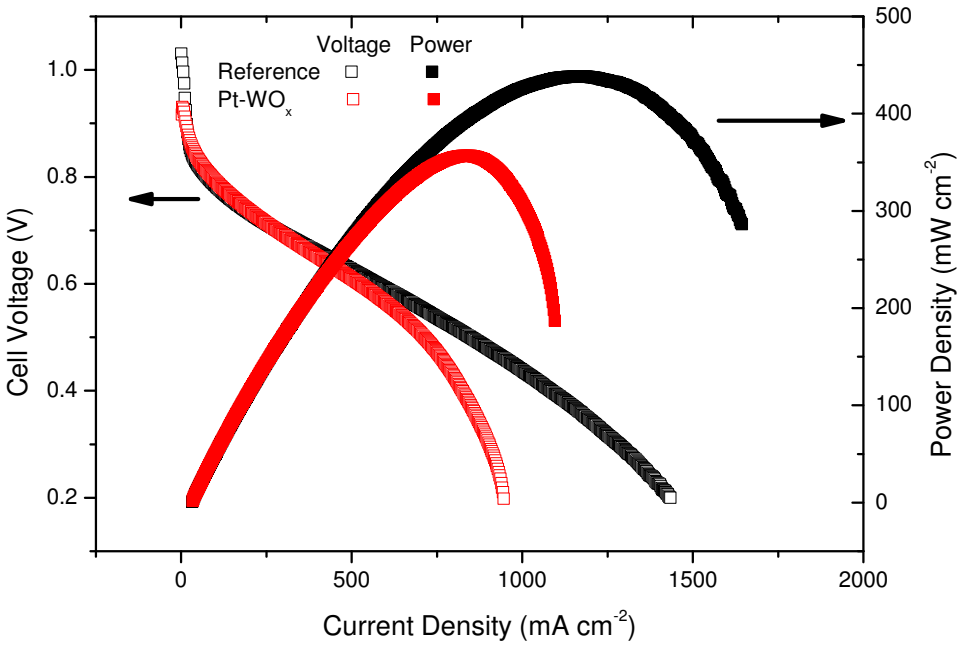

Fig. 15.2: The result of fuel cell analyses of Pt-WO_x/nGDL anode catalyst (red) and commercial anode catalyst from Alfa Aesar (2.7 mg cm^{-2} of Pt) (black) at temperatures 70/70/70 °C at pressure 0.5 Bar. Cathode catalyst was commercial catalyst from Alfa Aesar (2 mg cm^{-2} of Pt). The flow rates were H_2: 40 sccm, O_2: 30 sccm.

	Power Density W cm^{-2}	**At Voltage** V	**Specific Power** W mg^{-1}
Commer. Ref.	0.43	0.44	0.16
Pt-WO_x	0.36	0.50	14

Tab. 15.1: The comparison of obtained power densities and specific powers of anode catalysts: commercial reference anode (Alfa Aesar - 2.7 mg) and Pt-WO_x (30 nm thick layer, 26 μg cm^{-2}) 70/70/70 °C, pressure 0.5 Bar and commercial cathode (Alfa Aesar - 2.0 mg).

The result of XPS of W 4f is presented in figure 15.4. For peak analyzing procedure W $4f_{7/2} - 4f_{5/2}$ doublet having spin-orbit splitting of 2.15 eV and intensity ratio 0.75 was used. The peaks were fitted using pseudo-Voigt curves (product of Gaussian and Lorentzian functions) and Shirley type background [163]. Only W^{6+} state of tungsten occurred at binding energy 35.05-37.20 eV [163]. For quantitative analysis relative factors of sensitivity are given in [130].

Based on the result of fuel cell analyses, the use of Pt-WO_X as an anode catalyst for PEM FC was found promising. However, more analyses are needed.

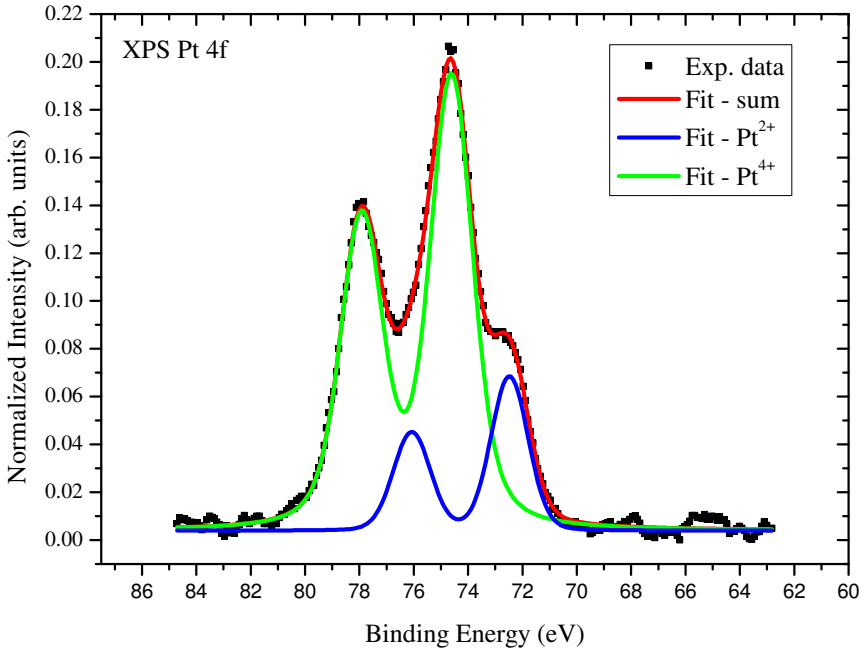

Fig. 15.3: The Pt 4f XPS spectra of Pt-WO_x (30 nm)/nGDL. The doublets $4f_{7/2} - 4f_{5/2}$ for Pt^{2+} and Pt^{4+} are shown.

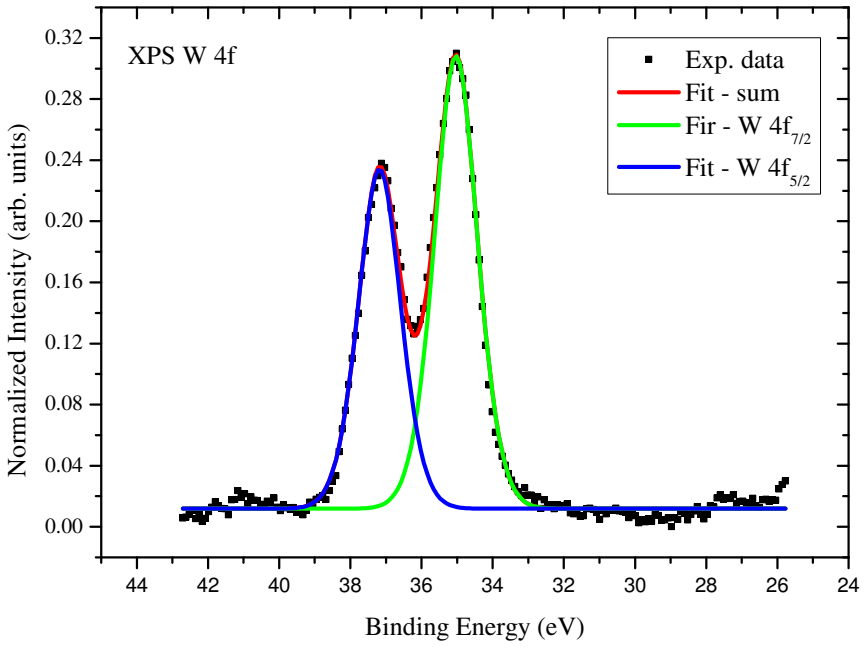

Fig. 15.4: The W 4f XPS spectra of Pt-WO_x (30 nm)/nGDL. The doublet $4f_{7/2} - 4f_{5/2}$ attributed to W^{6+} is shown.

16. Pt-CeO_x High PD

In this chapter the latest results from fuel cell analyses of Pt-CeO_2 sputtered catalyst layer are shown. Obtained power densities are statically analyzed and durability of catalyst was investigated. The cyclic voltammetry and impedance spectroscopy study are presented. In the next part the simple commercial nGDL and special carbon nitride (CN_x) catalyst supports are compared and possible application of CN_x is discussed. The last part shows difference between Pt-CeO_2 catalyst layers sputtered with or without presence of oxygen in process gas.

Apart from commercial catalyst, all catalyst layers were prepared by magnetron sputtering by procedures described in chapter 8. Conditions of sputtering were similar to them presented in chapter 11.1. Pt sputtered layers were prepared with the use of Platinum target (Safina, 2 inches). Pt-CeO_2 were sputtered with the use of a composed target prepared from CeO_2 target (Kurt J. Lesker, 99.9% pure, 2 inches) and small piece of sheet of Platinum placed on CeO_2 target (some samples were prepared by using two Pt wires placed on target in radial direction). The residual pressure inside the chamber was less than $1 \cdot 10^{-4}$ Pa then the chamber was filled by process gas. The samples were placed 90 mm away from targets. Sputtering process was proceeded with Ar atmosphere at pressure of $6 \cdot 10^{-1}$ Pa. In the case of CeO_2 sputtering, 0.25% of O_2 was added to the Ar atmosphere to obtain more porous structure which was investigated by colleagues M. Dubau and S. Haviar [122, 164, 165]. CN_x sublayers were prepared by sputtering with the use of Carbon target (Kurt J. Lesker, 99.9% pure, 2 inches) at Nitrogen atmosphere which is described in already published work of colleagues M. Dubau, S. Haviar [122, 164]. Illustration of layers arrangements for Pt-CeO_2 sputtered layer on nGDL is shown in figure 16.1 (left) and for Pt-CeO_2 sputtered on CN_x sublayer is seen in figure 16.1 (right). CN_x sublayer is normally almost diminished by magnetron sputtering process. Concentration of Pt was determined by XPS

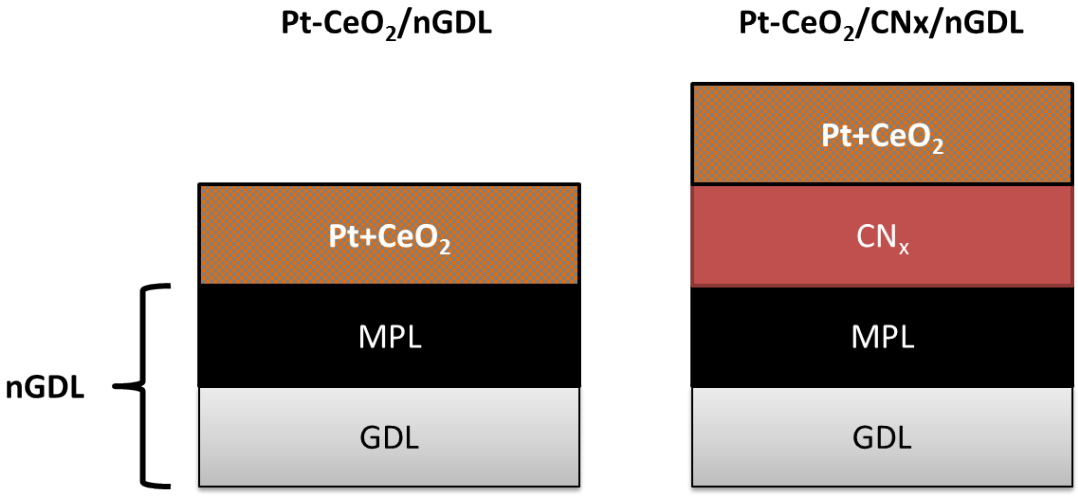

Fig. 16.1: Schematic illustration of sample composition: Pt-CeO_2 sputtered on nGDL (left) and Pt-CeO_2 sputtered on CN_x which is sputtered on nGDL (right). The commercial nGDL is consisted of micro-porous carbon layer (MPL) and carbon paper as gas diffusion layer (GDL).

analyses with the use of the calculation described in chapter 19.1. The thicknesses of layers were determined by AFM analyses of piece of silicon substrate sputtered simultaneously.

All prepared samples are listed in the table 16.1 and in the table 16.2. The contents of tables will be explain and described later in this chapter.

- Catalyst layers of samples Pt-CeO_2/CN_x/nGDL (I), Pt-CeO_2/CN_x/nGDL (II), Pt-CeO_2/nGDL (I) and Pt-CeO_2/nGDL (II) are 15 nm thick and they are prepared with the use of a sheet of Pt placed on CeO_2 target.
- Samples Pt(50nm)/nGDL, Pt(10nm)/nGDL and Pt(1nm)/nGDL are prepared with the use of Pt target and thicknesses of catalyst layers are 50 nm, 10 nm and 1 nm, respectively.
- Samples Pt-CeO_2(30nm)/CN_x/nGLD and Pt-CeO_2(30nm)/nGLD are prepared with the use of two Pt wires placed on CeO_2 target and the thickness of catalyst layers is 30 nm.
- Samples Pt-CeO_2(Ar)/nGLD and Pt-CeO_2(Ar+O_2)/nGLD are prepared with the use of a sheet of Pt placed on CeO_2 target and the thickness of catalyst layers is 25 nm.

Figure 16.2 shows SEM images of catalyst substrates: commercial nGLD (top-left) and nGDL coated by CN_x sublayer (top-right). The micro porous layer (MPL) on the surface of nGLD is clearly seen while CN_x creates specific porous layer. In the same figure Pt-CeO_2 sputtered thin film on the nGDL (bottom-left) and on the CN_x/nGDL (bottom-right) are shown. It is seen that CN_x/nGDL sublayer was completely changed by this procedure and the highly porous structure is formed. Similarly, highly porous structure seems to be appeared in the case of nGDL support due to natural high specific area of MPL.

XPS analyses of Pt 4f revealed Pt^{2+}, Pt^{4+} and absence of metallic states while investigation of Ce 3d showed CeO_2 partially reduced. Results are similar to them presented in chapter 11, 12.2 and 13 so they are not shown here because of space reason.

The data package presented in the tables 16.1 and 16.2 will be analyzed in following parts. First, the comparison of Pt-CeO_2 catalyst is compared and commercial pure Pt catalyst and investigation of difference of catalzst activity of theoretical ideal pure Pt catalyst and Pt doped ceria according its Pt loading **??**. In next section 16.2 the investigation of two different catalyst support, nGDL and nGDL coated by CN_x (see fig. 16.1), is presented. In the third section 16.3 an influence of Pt-CeO_2 sputtering procedure on fuel cell performance is investigated.

16.1 Pt-CeO_2/nGDL

FC experiments have been performed by experimental setup described in 7.1 with the use of the piston cell introduced in chapter 7.2. FC conditions were the same for all FC analyses and data were obtained at temperatures 70/70/70 °C and at pressure 0.5 Bar. The flow rates were 80 sccm for H_2 and 65 sccm for O_2. Pressure in piston was 8 Bar and active area was 4.41 cm^2. As a membrane Nafion NR212 of thickness 50 μm was used.

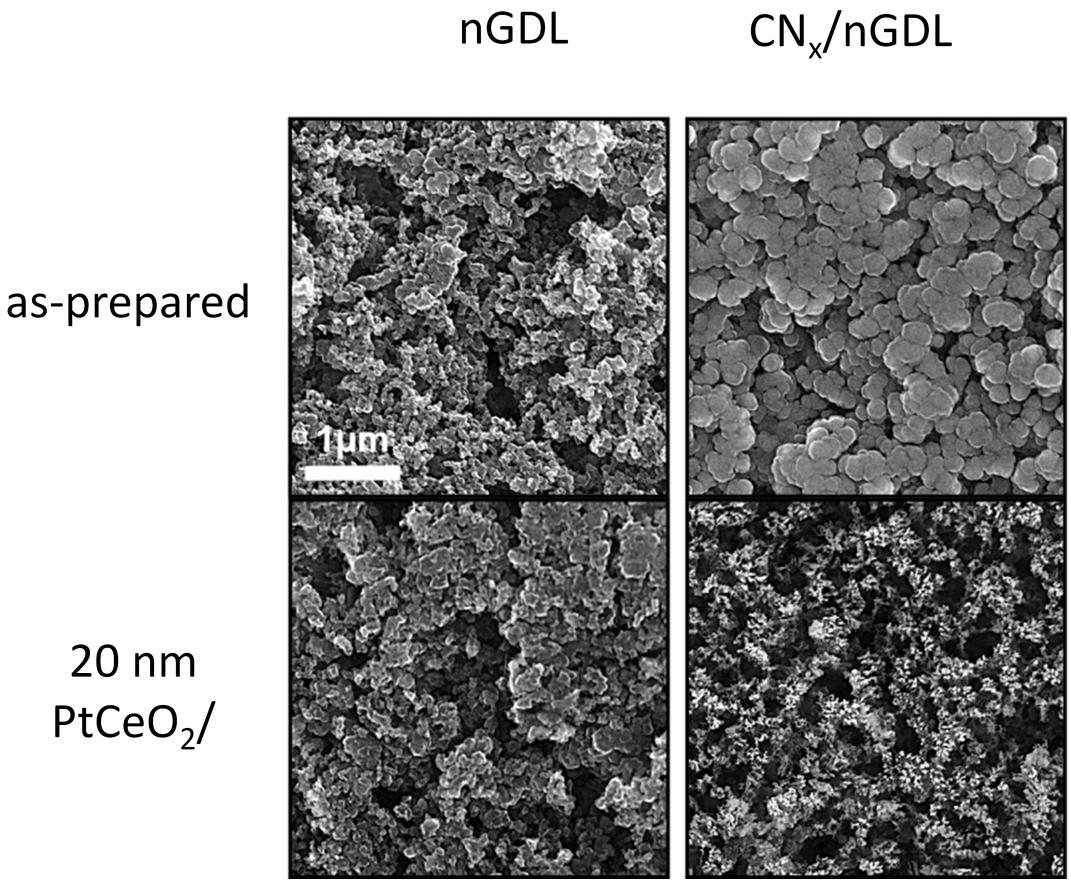

Fig. 16.2: SEM images of catalyst substrates (top row) and substrates coated by 20 nm thick layer of Pt-CeO_2 catalyst (bottom row). The left column represents the use of commercial nGDL support and the right column represents the use of special carbon nitrite coated nGDL as catalyst support.

Figure 16.3 shows a comparison of polarization curves and power density dependencies on current density for Pt-CeO_2/nGDL (I) (0.6 μg(Pt) cm^{-2}) anode with commercial anode catalyst from Alfa Aesar (400 μg(Pt) cm^{-2}). It is clearly seen that our sputtered Pt-CeO_2 anode catalyst with only 0.6 μg(Pt) cm^{-2} exhibited the same power density PD = 1 W cm^{-2} as commercial catalyst with 400 μg(Pt) cm^{-2}. This means that our catalyst caused the 670-fold increase of specific power while any drop of power density was not appeared in comparison with commercial catalyst. The reason why in this case we obtained for Pt-CeO_2 catalyst thin film 3 times higher perfomance than in was in the previous chaper 11 is that the catalyst method preparation was improved and also fuel cell experimental setup was improved.

This result sounds very good but apart from high power density and specific power the catalyst should exhibit also long time stability. The result of endurance test is presented in figure 16.4. This test was performed via the method mentioned in chapter 6.5. In order to accelerate the catalyst degradation, the cycles consisted of 30 s long 1 A cm^{-2} cell load and 30 s long open circuit were applied (see inset). The endurance test was interrupted each $\sim$ 35 h in order to perform IV curves determination and electrochemical characterization (marked by boxes).

It is seen that performance was slightly decreasing in each section of endurance

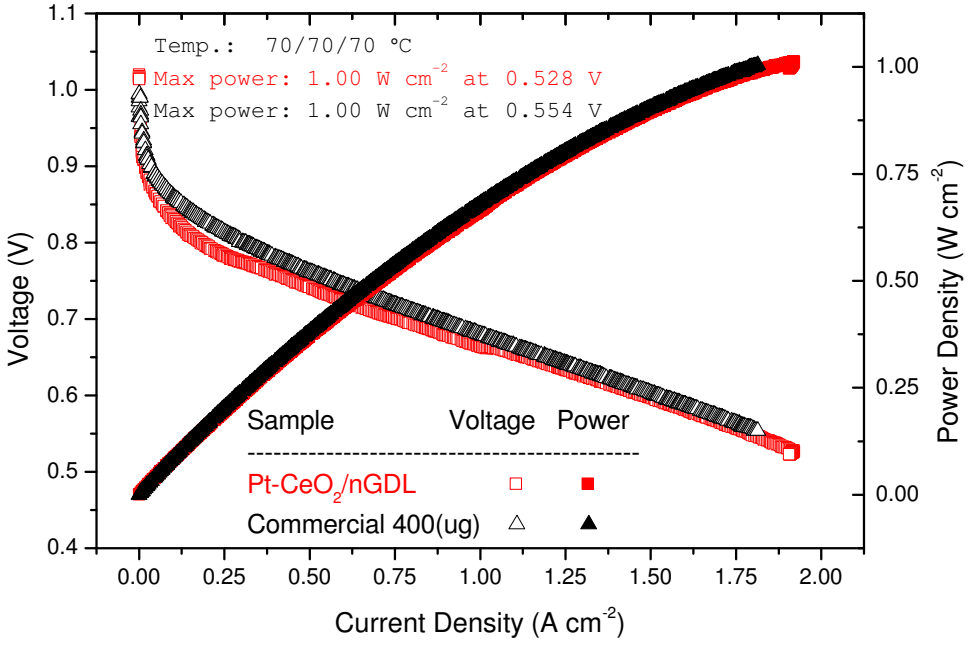

Fig. 16.3: The comparison of polarization curves and power density dependencies on current density for Pt-CeO_2/nGDL (I) (0.6 μg(Pt) cm^{-2}) anode with commercial anode catalyst from Alfa Aesar (400 μg(Pt) cm^{-2}). The cathode was commercial from Alfa Aesar (400 μg(Pt) cm^{-2}) in both cases. Data were obtained at temperatures 70/70/70 °C and at pressure 0.5 Bar. The flow rates were 80 sccm for H_2 and 65 sccm for O_2. Pressure in piston was 8 Bar and active area was 4.41 cm^2.

test. However, what is important, performance was regenerated after electrochemical treatment. This phenomenon is known and explained by reducing of too much oxidized cathode catalyst. The process on the Pt-CeO_2 anode side is not clear but perhaps reducing of too much oxidized CeO_x or other electrochemical processes can regenerate the catalyst and improve the performance again which was also observed and discussed in chapter 17.4. We should note that this effect seems to be 100% reproducible in the investigated time window.

This fact together with the same power density as commercial catalyst and 670-fold increase of specific power makes our Pt-CeO_2 suitable for PEM FC anode application.

Remind that earlier in previous chapters we used the different commercial catalyst with much higher loading of Pt 2700 μg(Pt) cm^{-2} while the performance was even lower (those time better catalyst was not on the market). Therefore the question is what is the optimal Pt loading on the anode and if the decrease of Pt amount will provide still such a high performance. Let's investigate the real difference between Pt doped ceria catalyst and Pt pure catalyst.

Normally all FC results are statistically analyzed but due to the space reason results of analyses have not been shown in detail and just main output was presented (rest of previous chapters). However, in this case, since the data are not publish yet, statistical analysis are presented in order to better understand the behavior of our sputtered catalyst.

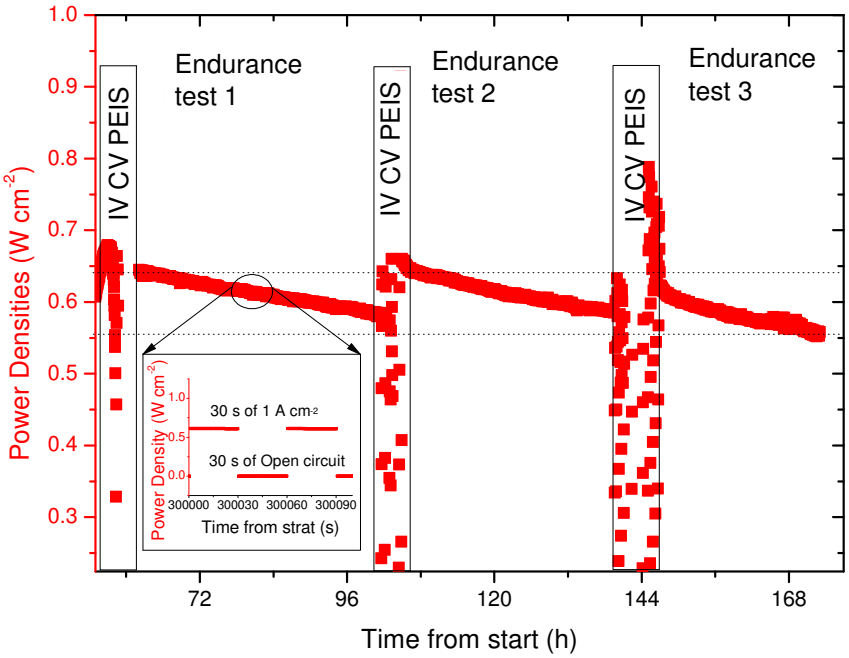

Fig. 16.4: The example of the endurance test of Pt-CeO_2/nGDL (I) (0.6 μg(Pt) cm^{-2}) anode. It is consisted of cycles which are consisted of 30 s long load of cell at current density 1 A cm^{-2} and of 30 s long period of unloaded cell (detail in inset) (see chapter 6.5). Endurance test is interrupted by several sets of polarization curves (IV), cyclic voltammetry (CV) and impedance spectroscopy (PEIS). The cathode was commercial from Alfa Aesar (400 μg(Pt) cm^{-2}). Data were obtained at temperatures 70/70/70 °C and at pressure 0.5 Bar. The flow rates were 80 sccm for H_2 and 65 sccm for O_2. Pressure in piston was 8 Bar and active area was 4.41 cm^2.

FC tests were performed according to the test protocol described in chapter 6.5. FC performance was analyzed before Break-In procedure, after this procedure and after electrochemical measurement as cyclic voltammetry (CV), impedance spectroscopy (PEIS), crossover determination and after endurance test if it was possible or it makes sense. All data obtained in this individual part of test were statistically analyzed and calculated average values (Mean), standard deviation (Snatd. dev.), median (Median) are listed in the table 16.1 where comparison with the rest of investigated samples is also shown. It is seen how FC performance was developing for individual parts of test and for different samples. We can also see that both data obtained for Pt-CeO_2/nGDL (I, II) and Commercial 400(μg) are *Saturated* which means that load used for measurement was not able to decrease its internal resistance to set the cell at maximum power. Thus, it is hard to say how high the real PD would be and differentiate which one would be greater but we admit that this effect could be proportional and thus the same for both samples. It is clearly seen that such a big power density 1 W cm^2 was reached also for pure Platinum catalyst with lower content of Platinum: Commercial 300(μg), Pt(50nm)/nGDL (110 μg(Pt) cm^{-2}), Pt(10nm)/nGDL (20 μg(Pt) cm^{-2}). On the other hand, ten times lower power density was exhibited with the use of pure Pt

catalyst Pt(1nm)/nGDL with loading of 2 μg(Pt) cm^{-2} which still means 33 times higher specific power (SP) in favor of Pt doped ceria catalyst (according to Pt-CeO_2/nGDL (I, II)) in spite of its even lower Pt loading. We can obtain the same result (33 fold increase of SP) if we compare Pt doped ceria Pt-CeO_2/nGDL (I, II) and Pt(10nm)/nGDL.

Phenomenon that PD is not decreasing (up to some limit) with decreasing Pt content in pure Pt catalyst must be better explained and investigated. In order to better compare samples from table 16.1 the PD obtained after stabilization (A-CV) were summarized in the table 16.2 where more information is added: Platinum loading (Loading), calculated specific power (SP) and charge (Q_H) needed for adsorption/desorption of monolayer of hydrogen which is given by integration of hydrogen region 0-0.4 V in voltammogram (see the chapter 6.2) and calculated specific charge per amount of Pt (SQ_H). Error of obtained values for loading, Q_H and SQ_H is estimated as $\sim$10%.

If we compare the SP for Pt-CeO_2/nGDL (I, II) with Pt(10nm)/nGDL and Pt(1nm)/nGDL (see the table 16.2), we obtain the same 33 fold increase in favor of Pt-CeO_2/nGDL (I, II). The fact that samples of Pt doped ceria anode catalysts Pt-CeO_2/nGDL (I, II) are the most convenient catalyst from the studied samples is clearly seen in figure 16.5 (top-left), where PD and SP for different samples are shown, because it exhibits maximum value in both quantities.

Let's again focus to investigation of PD dependency on Pt loading. Correlation coefficient between Q_H and Loading is $r_{Q_H-L} = 0.97 \pm 0.02$ (including all catalyst in the table 16.2 and excluding all Pt-doped ceria catalyst samples, if we include Pt-CeO_2 catalysts the same value is obtained) which is in agreement with assumption that if more Pt nanoparticles are used larger surface area is obtained. However, correlation coefficient between PD and Loading is very low $r_{PD-L} = 0.37 \pm 0.24$ (including all catalyst in the table 16.2 and excluding all Pt-doped ceria catalyst samples). If we include Pt-CeO_2 catalysts samples we obtain $r_{PD-L} = 0.35 \pm 0.24$. Therefore we can say that there is not any significant correlation betwee PD and Loading. This means that Pt loading in commercial catalyst of 300-400 μg(Pt) cm^{-2} is high plenty enough to saturate the cathode reaction by protons and lower Pt amount could be still sufficient. It is seen that Pt loading of 20 μg(Pt) cm^{-2} (Pt(10nm)/nGDL) is still able to proceed the reaction without any performance drop while the content of Pt is lower the decrease of permanence appears as it is seen with the use of the sample Pt(1nm)/nGDL of Pt loading 2 μg(Pt) cm^{-2}. This hypothesis is proved by result revealed by PEIS study (see figure 16.6) where arches representing the resistance to the anode reaction have not clearly appeared for high Pt content catalyst Commercial 400(μg), Commercial 300(μg) and Pt(50nm)/nGDL(110 μg(Pt) cm^{-2} but they are considerably seen for lower Pt content catalyst Pt(10nm)/nGDL(20 μg(Pt) cm^{-2}) and Pt-CeO_2/nGDL (I) (0.6 μg(Pt) cm^{-2}).

We should note that correlation coefficient between Q_H and Loading mentioned above is increased from $r_{Q_H-L} = 0.97 \pm 0.02$ to $r_{Q_H-L} = 0.995 \pm 0.003$ if

the worst pair of values is skipped. This pair of values is for Pt(50nm)/nGDL-($110\,\mu$g(Pt) cm^{-2}) which indicates that specific area (per mg of Pt) of this 50 nm thick sputtered catalyst film is significantly lower than specific area of commercial catalyst. Actually, it is 40 times less in comparison with commercial catalyst (see the table 16.2). This problem is similar for all pure Pt sputtered catalyst. In contrast, specific charge for Pt doped ceria Pt-CeO_2/nGDL (I) $SQ_{H-PtCe} = (250 \pm 30)$C mg^{-1} is 3.0 ± 0.4 times higher than specific charge $SQ_{H-Comm} = (82 \pm 7)$C mg^{-1} for Commercial 400(μg).

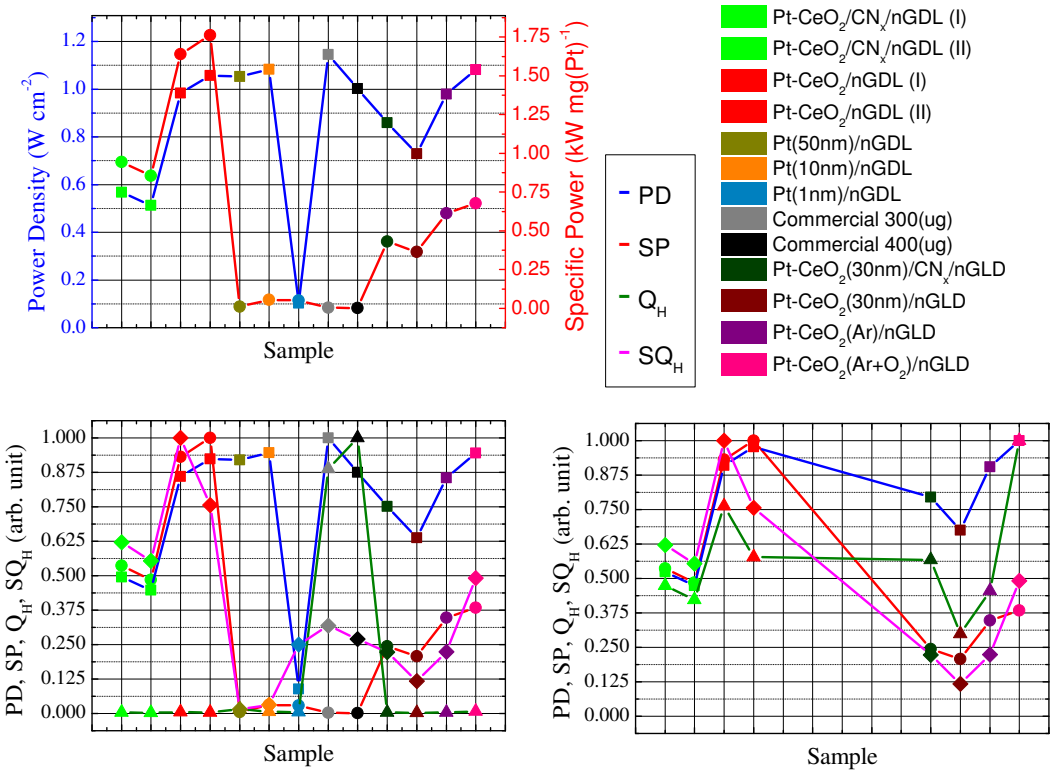

Fig. 16.5: Graphically processed information for samples from the table 16.1 about obtained power density (PD) and specific power (SP) (top-right) and normalized PD, SP, the charge needed for desorption of monolayer of hydrogen (Q_H) and calculated specific charge (SQ_H) (bottom-left). Characterization only for sputtered Pt-CeO_2 layers is shown (bottom-right). FC operating conditions are the same as in figure 16.3 and given by testing protocol 6.5.

Remind the table 16.2. The figure 16.5 (bottom-left) shows an overview of normalized PD, SP, Q_H and SQ_H for all investigated samples. It is again clearly seen that Pt-CeO_2/nGDL (I) exhibits the highest specific power and the highest specific charge (SQ_H) and power density as high as in the case of commercial catalyst. Selection of low Pt content catalysts is seen in figure 16.5 (bottom-right). The next trends and correlations can be estimated e.g. correlation between specific power and specific charge calculated as $r_{SP-SQ_H} = 0.91 \pm 0.05$ in the case of excluding samples with loading higher than $2\,\mu$g(Pt) cm^{-2}.

Impedance spectroscopies for samples listed in the table 16.3 were analyzed. The determined serial resistance is $R_i^A = (0.089 \pm 0.005)\Omega$ cm^2, which is again in agreement with results observed in chapters 9, 11.2 and theory that internal

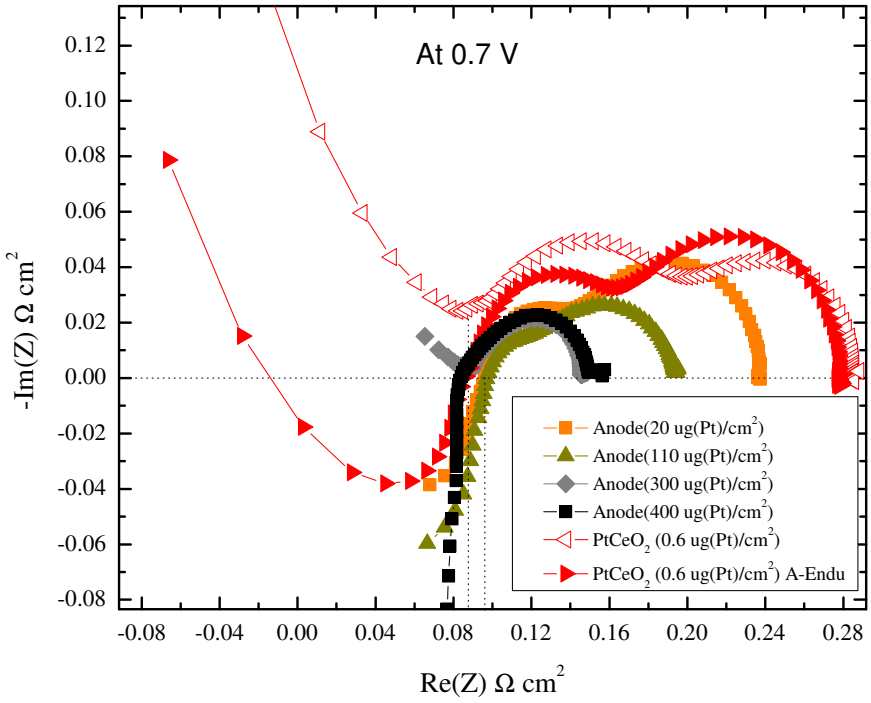

Fig. 16.6: The comparison of impedance spectroscopy for different Pt anode catalysts: Pt(10nm)/nGDL($20\,\mu$g(Pt)$\,$cm^{-2}), Pt(50nm)/nGDL($110\,\mu$g(Pt)$\,$cm^{-2}), Commercial 300(μg) ($300\,\mu$g(Pt)$\,$cm^{-2}) Commercial 400(μg) ($400\,\mu$g(Pt)$\,$cm^{-2}) and Pt-CeO_2/nGDL (I) ($0.6\,\mu$g(Pt)$\,$cm^{-2}) before and after endurance test at 0.7 V. In all cases the same membrane and cathode catalyst were used: Nafion NR212, commercial catalyst from Alfa Aesar ($400\,\mu$g(Pt)$\,$cm^{-2}). Frequency range was 200 kHz - 200 mHz. The active area was 4.41 cm^{-2}. The determined serial resistance is $(0.090\pm0.005)\Omega$ cm^2.

resistance of cell is given mainly by conductivity of the membrane and since the membrane was the same (NR212), the internal resistance is still in the same range. According to the theory presented in chapter 6.4 and literature [166] archers indirectly represent the charge transfer which corresponds directly with the reaction rate. Remind the alternate electrical scheme representing FC reaction parameters in figure 6.5, lengths of archers given by $R_2 + R_3$ were determined and together with its inverse value as $(R_2+R_3)^{-1}$ were summarized in the table 16.3. Additionally, the specific relative reaction rate was calculated as $S(R_2+R_3)^{-1}$ and individual SQ_H were added. The proof of this concept is fact that correlation coefficient between SQ_H and $(SR_2+R_3)^{-1}$; Q_H and $(R_2+R_3)^{-1}$ are $r_{SQ_H-SR} = 0.93 \pm 0.05$ and $r_{Q_H-R} = 0.90 \pm 0.09$; $r_{SQ_H-SR} = 0.999 \pm 0.001$ and $r_{Q_H-R} = 0.96 \pm 0.03$ excluding samples with Pt loading higher than $300\,\mu g(Pt)\,cm^{-2}$, respectively.

Quantities SQ_H and $(SR_2 + R_3)^{-1}$ for Pt-CeO_2/nGDL (I) were increased 18 times and 60 times, respectively, in comparison with Pt(1nm)/nGDL. If we compare these two increases we obtain that reaction rate in the case of Pt doped ceria is 3.4 ± 0.4 times higher than in the case of pure pure Pt catalyst. Similar result can be obtain if we correct the 33 fold increase of specific power for this two compared samples discussed above by factor 10 due to 10 time lower specific area of Pt sputtered layer catalyst Pt(1nm)/nGDL than specific area for commercial samples, $33/10 \cong 3.4 \pm 0.4$. According to the literature the ratio of surface atoms and bulk atoms for commercial catalyst is from 4 to 1 and the optimal particle size is from 1.4 nm to 2 nm. [167–169]. Thus, only less than 20-50% of Pt atom are participated in the reaction (assuming model [167]) in commercial catalyst if it is used in the most effective way. Hence, even with assuming atomically dispersed Pt in our Pt doped ceria, the obtained factor 3.4 ± 0.4 cannot be explained by simple increase of specific area in our catalyst. Hence, reaction must take place faster or it occurs in larger surface than it was seemed from CV. We supposed that Ce atoms around Pt, as it was described in DFT model shown in chapter 11.1, are participated in the hydrogen oxidation reaction. More evidences for this hypothesis are seen in the last chapter 17.

Optimal size of Pt particles in commercial-like catalyst is the above mentioned size (1.4 - 2.0 nm) [168]. Moreover, this result can be explained by the fact that some Pt surface orientation is more effective than others and due to the fact that more than one Pt atom next to each other are necessary to proceed the hydrogen oxidation but interestingly it is not case of our Pt doped ceria catalyst. This means that Pt doped ceria with Pt atomically dispersed caused 5-10 fold increase of specific area principally in comparison with theoretical ideal Pt particles catalyst.

The evidence that sputtered Pt-CeO_2 catalyst is as active as commercial catalyst at the same operating conditions of FC is also seen by using the Tafel analysis in figure 16.7, where obtained exchange current densities are $1.12 \cdot 10^{-5}$ A cm^{-2} and $1.14 \cdot 10^{-5}$ A cm^{-2} for Pt-CeO_2/nGDL (I) and Commercial 400(μg), respectively, are equal to each other according to 10% relative error. In addition, the figure 16.7 shows that sputtered Pt doped ceria catalyst listed in the table 16.3 including Pt-CeO_2/CN_x/nGDL (I) revealed the same activity in comparison with the commercial reference. However, sputtered pure Pt based catalyst, especially Pt(10nm)/nGDL, exhibits small shift of exchange current density to the lower

current ($3 \cdot 10^{-6}$ A cm^{-2}). This can be explained by the fact that Pt sputtered film is not appropriate catalyst because the specific area is lower than in the case of commercial catalyst. In this case it is by factor ~ 10 as it was also explained above in the part discussing obtained Q_H. Relative error of determined exchange current densities are about 10% and obtained values are in agreement with the literature [20].

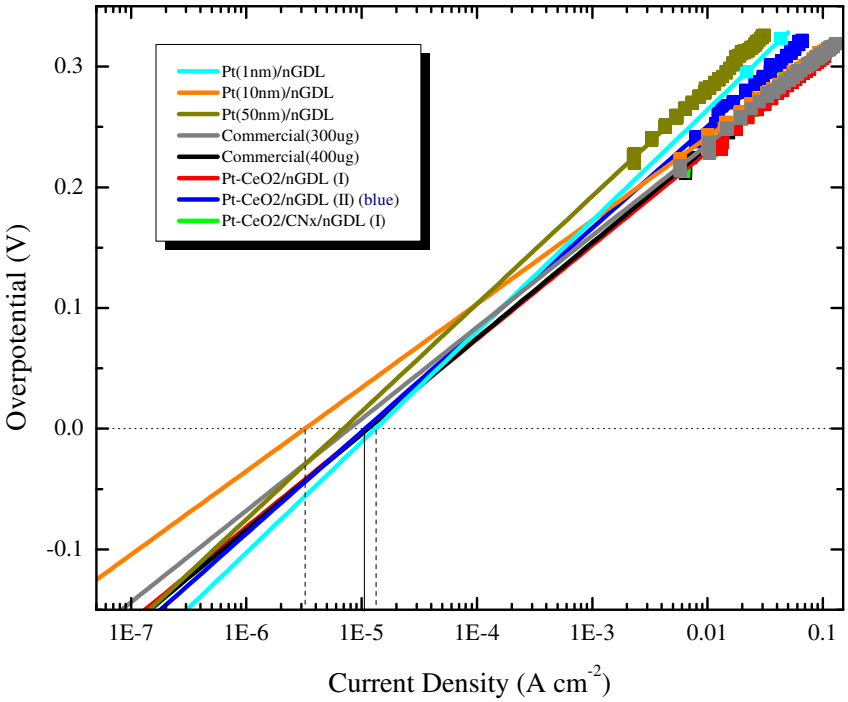

Fig. 16.7: The Tafel plot and the comparison of determined exchange current densities for Pt anode catalysts: Pt(1nm)/nGDL($2\,\mu$g(Pt) cm^{-2}), Pt(10nm)/nGDL($20\,\mu$g(Pt) cm^{-2}), Pt(50nm)/nGDL($110\,\mu$g(Pt) cm^{-2}), Commercial 300(μg) ($300\,\mu$g(Pt) cm^{-2}) Commercial 400(μg) ($400\,\mu$g(Pt) cm^{-2}), Pt-CeO_2/nGDL (I) ($0.6\,\mu$g(Pt) cm^{-2}) (and its twin(II) marked by blue) and Pt-CeO_2/CN_x/nGDL (I). In all cases the same membrane and cathode catalyst were used: Nafion NR212, commercial catalyst from Alfa Aesar ($400\,\mu$g(Pt) cm^{-2}). The active area was 4.41 cm^{-2} and the FC operating conditions are the same as in figure 16.3 and given by testing protocol 6.5.

Sample	Exp.	Mean W cm^{-2}	Stand. dev. W cm^{-2}	Median W cm^{-2}	Trend
Pt-CeO_2/CN_x/nGDL (I)	B-BreakIn	0.71	0.02	0.71	no
	A-BreakIN	0.67	0.08	0.67	down
	A-CV	0.57	0.02	0.57	no
	A-1W-Endu	0.03	0.01	0.04	down
Pt-CeO_2/CN_x/nGDL (II)	B-BreakIn	0.46	0.04	0.48	
	A-BreakIN	0.38	0.06	0.39	down
	A-CV	0.51	0.18	0.54	down
Pt-CeO_2/nGDL (I)	B-BreakIn	0.59	0.02	0.60	
	A-BreakIN	0.60	0.04	0.61	up
	A-CV	0.98	0.02	0.98	no
	B-Endu	0.76	0.02	0.76	saturace
	A-1W-Endu	0.72	0.14	0.65	
	A-Endu2	0.75	0.03	0.75	saturace
Pt-CeO_2/nGDL (II)	B-BreakIn	0.84	0.02	0.85	no
	A-BreakIN	0.92	0.01	0.92	no
	A-CV	1.06	0.07	1.04	saturace
	B-Endu	0.83	0.08	0.85	saturace
	A-1W-Endu	1.12	0.04	1.12	saturace
	A-3W-Endu	0.89	0.04	0.90	saturace
Pt(50nm)/nGDL	B-BreakIn	0.65	0.10	0.64	up
	A-BreakIN	0.85	0.03	0.85	up
	A-CV	1.05	0.03	1.06	saturace
	OnCathode	0.32	0.02	0.31	no
Pt(10nm)/nGDL	B-BreakIn	0.93	0.02	0.92	saturace
	A-BreakIN	1.06	0.01	1.06	saturace
	A-CV	1.08	0.02	1.10	saturace
	OnCathode	0.39	0.02	0.40	no
Pt(1nm)/nGDL	A-BreakIN	0.10	0.04	0.10	no
Commercial 300(μg)	A-BreakIN	1.15	0.01	1.15	saturace
Commercial 400(μg)	A-BreakIN	1.00	0.13	1.01	saturace
Pt-CeO_2(30nm)/CN_x/nGLD	B-BreakIn	0.76	0.02	0.77	no
	A-BreakIN	0.73	0.02	0.73	down
	A-CV	0.86	0.07	0.87	down
Pt-CeO_2(30nm)/nGLD	B-BreakIn	0.58	0.01	0.59	up
	A-BreakIN	0.63	0.03	0.64	no
	A-CV	0.73	0.17	0.70	no
	A-1D-Endu	0.80	0.11	0.78	
Pt-CeO_2(Ar)/nGLD	B-BreakIn	0.70	0.05	0.72	up
	A-BreakIN	0.72	0.04	0.72	no
	A-CV	0.98	0.08	1.02	no
	A-3D-Endu	0.59	0.04	0.61	no
	A-3D-Endu	0.91	0.10	0.95	no
Pt-CeO_2($Ar+O_2$)/nGLD	B-BreakIn	0.90	0.03	0.91	up
	A-BreakIN	1.04	0.01	1.04	saturace
	A-CV	1.08	0.04	1.10	saturace

Tab. 16.1: List of investigated samples with obtained results of FC analyses. There are statistically determined average values (Mean), standard deviation (Snatd. dev.), median (Median) for several different parts of FC experiment (Exp.) which are obtained after or before (A- or B-) some procedures as break-in (BreakIN), electrochemical analyses such as cyclic voltammetry and PEIS (marked together as CV) and different long (XD- means X days long or XW- means x weeks long) endurance experiment (Endu). Two samples were investigated also as a cathode catalyst (OnCathode). Last column (Trend) provides information about statistically significant trends: increasing (Up), decreasing (Down), no trend appeared (No) and if device measurement was overloaded (Saturace). FC operating conditions are the same as in figure 16.3 and given by testing protocol 6.5.

Sample	PD W cm^{-2}	Loading μg(Pt) cm^{-2}	SP W mg(Pt)$^{-1}$	Q_H mC cm^{-2}	SQ_H C mg^{-1}
Pt-CeO_2/CN_x/nGDL (I)	567	0.6	945	0.10	174
Pt-CeO_2/CN_x/nGDL (II)	513	0.6	855	0.09	155
Pt-CeO_2/nGDL (I)	984	0.6	1640	0.17	280
Pt-CeO_2/nGDL (II)	1057	0.6	1762	0.13	212
Pt(50nm)/nGDL	1053	110	10	0.23	2
Pt(10nm)/nGDL	1083	20	54	0.17	9
Pt(1nm)/nGDL	102	2	51	0.03	16
Commercial 300(μg)	1145	300	4	27	89
Commercial 400(μg)	1002	400	2.5	30	75
Pt-CeO_2(30nm)/CN_x/nGLD	860	2	430	0.12	62
Pt-CeO_2(30nm)/nGLD	730	2	365	0.07	33
Pt-CeO_2(Ar)/nGLD	979	1.6	612	0.09	56
Pt-CeO_2(Ar+O_2)/nGLD	1082	1.6	676	0.22	137

Tab. 16.2: FC analyses result for samples presented in the table 16.1 for selected experiment part (Exp. as A-CV) with noted power density (PD) and additional information about Platinum loading (Loading), calculated specific power (SP), the charge needed for desorption of monolayer of hydrogen (Q_H) and calculated specific charge (SQ_H).

Sample	R_i^A Ω cm^2	R_2+R_3 Ω cm^2	$(R_2+R_3)^{-1}$ Ω^{-1} cm^{-2}	$S(R_2+R_3)^{-1}$ Ω^{-1} mg^{-1}	SQ_H C mg^{-1}
Pt(1nm)/nGDL	88	3530	0.0003	0.14	16
Pt(10nm)/nGDL	96	142	0.0070	0.35	9
Pt(50nm)/nGDL	97	96	0.010	0.09	2
Commercial 300(μg)	90	56	0.018	0.06	89
Commercial 400(μg)	83	60	0.017	0.04	75
Pt-CeO_2/nGDL (I)	85	195	0.005	8.55	280
Pt-CeO_2/nGDL (I, A-Endu)	86	190	0.005	8.77	276

Tab. 16.3: List of determined serial resistances (R_i^A) by the PEIS analyses already presneted in figure 16.6, the sum (R_2+R_3) which is length of *arches* and ($(R_2+R_3)^{-1}$) representing reaction rates with its specific value related to the loading of Platinum ($S(R_2+R_3)^{-1}$). Remind the theory presented in 6.4. The charge needed for desorption of monolayer of hydrogen (Q_H) and calculated specific charge (SQ_H) are added.

16.2 Pt-CeO_2/nGDL vs Pt-CeO_2/CN_x/nGDL

Now we are going to investigate the difference between nGDL and CN_x catalyst support. Preparation of CN_x inter layer has been already described above. Illustration of catalyst sandwich structure is seen in figure 19.1 and SEM images promising high specific area of catalyst deposited on CN_x inter layer is presented in figure 16.2. Description of CN_x preparation and explanation of structure formation was reported in [122, 164]. This inter layer is partially decomposed during sputtering of Pt-CeO_2 catalyst on CN_x and structure, which is shown in figure 16.2, is formed.

Comparison of both systems nGDL support and CN_x inter layer is reported in the table 16.2: Pt-CeO_2/CN_x/nGDL (I), Pt-CeO_2/CN_x/nGDL (II) and Pt-CeO_2/nGDL (I), Pt-CeO_2/nGDL (II), respectively. Performances are compared in figure 16.8 for better clarification. It is clearly seen that FC experiment at the same condition and same Pt loading for both system revealed 1.9 ± 0.2 fold decrease of power density in the case of CN_x inter layer in comparison with simple nGDL as catalyst support. Moreover, in the table 16.1 is shown that also endurance of catalyst with CN_x inter layer is not satisfactory. According to these facts and fact that preparation of CN_x layer is more complicated than simple use of commercial nGDL we cannot found the use of CN_x catalyst inter layer as a suitable solution. However, the characteristic structure is also appeared if pure CeO_2 without Pt is sputtered on the CN_x, which means that this CeO_2/CN_x system can be used in some another application.

Suitable application could be e.q. PEM electrolyzer if this system exhibits good stability at higher electrolyzer potential 1.6-2.0 V which is investigated in following section 16.2.1.

16.2.1 Carbon corrosion CN_x vs a-C

In this section the comparisons of corrosion effect with the use of amorphous carbon (a-C) and CN_x catalyst substrates is shown. Corrosion of the a-C film has been already investigated in the literature [170] but, in contrast, authors used a-C film supporting layer on stainless bipolar plates.

We have improved and extended already existed experimental setup for quadrupole mass spectrometry by adding fuel cell testing system to obtain composition of outlet gases from fuel cell. The experimental setup has been published in [171] where more details can be found.

There were prepared two samples: Nafion membrane NR212 was sputtered by 200 nm thick layer of carbon (a-C) in the first case and in second case the membrane was coated by 200 nm of carbon nitride (CN_x) prepared by magnetron sputtering in N_2 atmosphere. Sputtering procedure of this layer has been already published by our colleague (Martin Dubau) [172]. These both layers were coated by 10 nm of Pt as it was described at the begging of this chapter 16.

Samples were clamped in our piston cell introduced in chapter 7.2. Samples of interest were used as a cathode and standard commercial anode ($400\,\mu g(Pt)\,cm^{-2}$) was used. The membrane was humidified by flow of humid N_2 overnight. Then the nitrogen has been changed by process gases of flow rates: H_2 40 sccm on the anode side and mixture of O_2 30 sccm and He 10 sccm on the cathode. The cell was

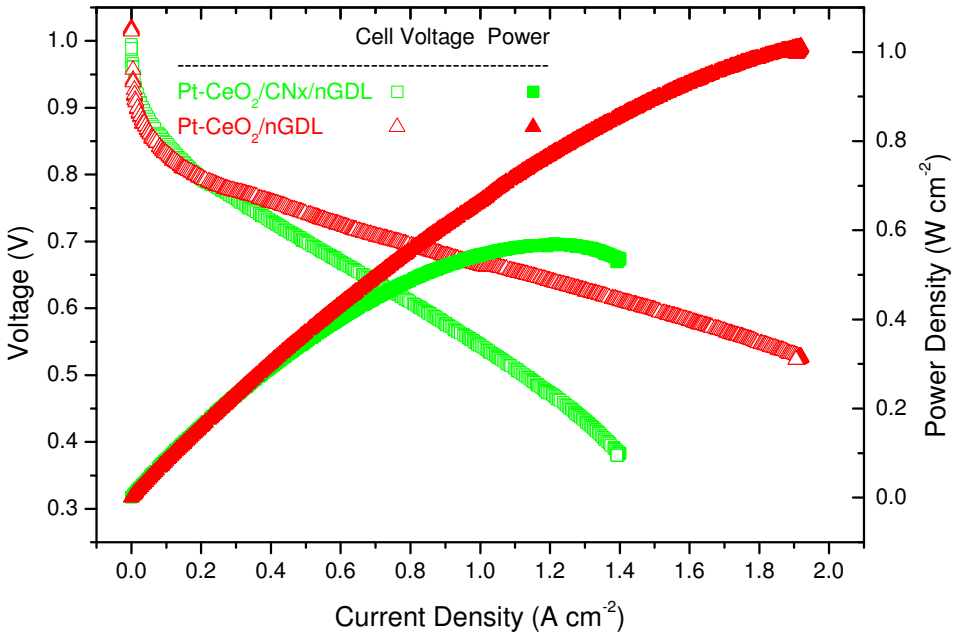

Fig. 16.8: The comparison of polarization curves and power density dependencies on current density for Pt-CeO_2 15 nm thick sputtered catalyst film simply on nGDL as Pt-CeO_2/nGDL (I) (0.6 μg(Pt) cm^{-2}) and on CN_x as Pt-CeO_2/CN_x/nGDL (I) (0.6 μg(Pt) cm^{-2}). The cathode was commercial from Alfa Aesar (400 μg(Pt) cm^{-2}) in both cases. Data were obtained at temperatures 70/70/70 °C and at pressure 0.5 Bar. The flow rates were 80 sccm of H_2, 65 sccm of O_2. Pressure in piston was 8 Bar and active area was 4.41 cm^2.

operating for several hours at normal natural FC working point to stabilize the cell performance. After stabilizing, the voltage of cell started to be increasing by steps up to the potential where carbon corrosion is dominating process (∼1.4 V, when normally air/hydrogen boundaries developed on the anode side discussed also in the section 3) while intesnisties of all relevant masses in the cathode outlet were recording by quadrupole which was installed in the experimental system using a differential pumping.

The results of corrosion effect that was observed with the use of a-C layer (see the figure 16.9) and with the use of CN_x layer (see the figure 16.10) revealed that mass 28 (CO) and 44 (CO_2) occurred for higher voltage in the case of CN_x layer in comparison with the a-C layer. It seems that carbon corrosion for a-C appeared at FC condition in the contrast to CN_x layer where corrosion did not appeared upto 1.75 V.

On the other hand, despite the fact that equilibrium potential for starting oxidation by water described by formula 16.1 is about 0.2 V vs. RHE [173]

$$C + 2H_2O \longrightarrow CO_2 + 4H^+ + 4e^- at \sim 0.2 VvsNHE \qquad (16.1)$$

an occurrence of carbon corrosion at lower overpotential than 1.0 V vs. DHE is normally negligible because the kinetics of carbon corrosion is much slower than oxygen reduction which normally occurs in FC conditions. Therefore the carbon

corrosion effect should not normally appear at voltage lower below ∼1.0 V which is also seen and explained e.g. in [173, 174]. Thus this fact, the observation of CO_2 at normal PEM FC operating voltage could mean some starvation and increase of some impurity in the experimental system.

In order to determine the exact potential of cathode and anode, the experimental setup must be improved and proper reference electrode has to be used. Admitting that more experiments are needed for proper clarification of this behavior, this result reveals no significant carbon corrosion defect with the use of CN_x layer. Hence, we concluded that the CN_x layer could be promising catalyst support for an anode of electrolyzer.

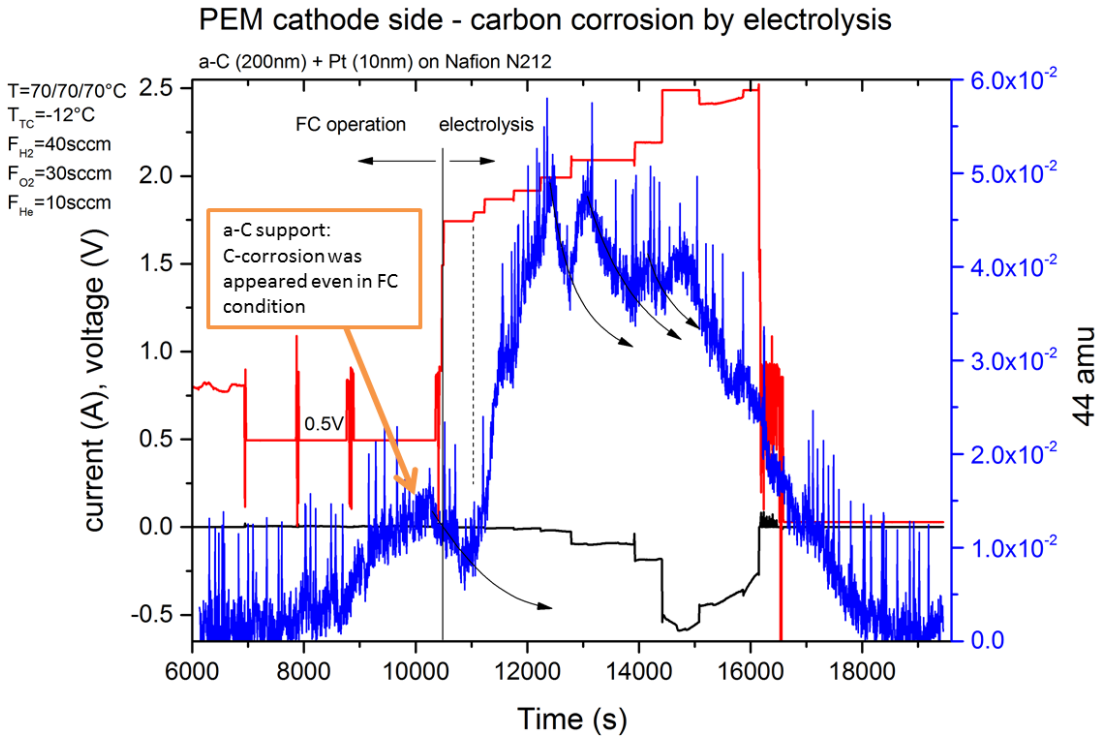

Fig. 16.9: Results of carbon corrosion experiment for amorphous carbon layer coated on Nafion membrane NR212. The normalized signal of mass 44, current and voltage against time is presented.

16.3 Sputtering with Ar vs Ar+O_2

After long time of experimenting of FC we observed that performance of Pt-CeO_2 sputtered catalyst strongly depends on the residual pressure in the process chamber. Later, we have found that it is due to oxygen and water remaining in the residual atmosphere. Thus, we control the partial pressure of oxygen during sputtering process and we have found the optimum partial pressure as 0.001 Pa at process pressure 0.4 Pa as it hase been indicated above. Therefore samples were prepared by procedure described at the beginning of this chapter 16. More information in the literature [122, 164, 165] can be found.

The comparison between FC anode catalyst Pt-CeO_2 sputtered with presence of oxygen Pt-CeO_2(Ar+O_2)/nGLD and without oxygen Pt-CeO_2(Ar)/nGLD is

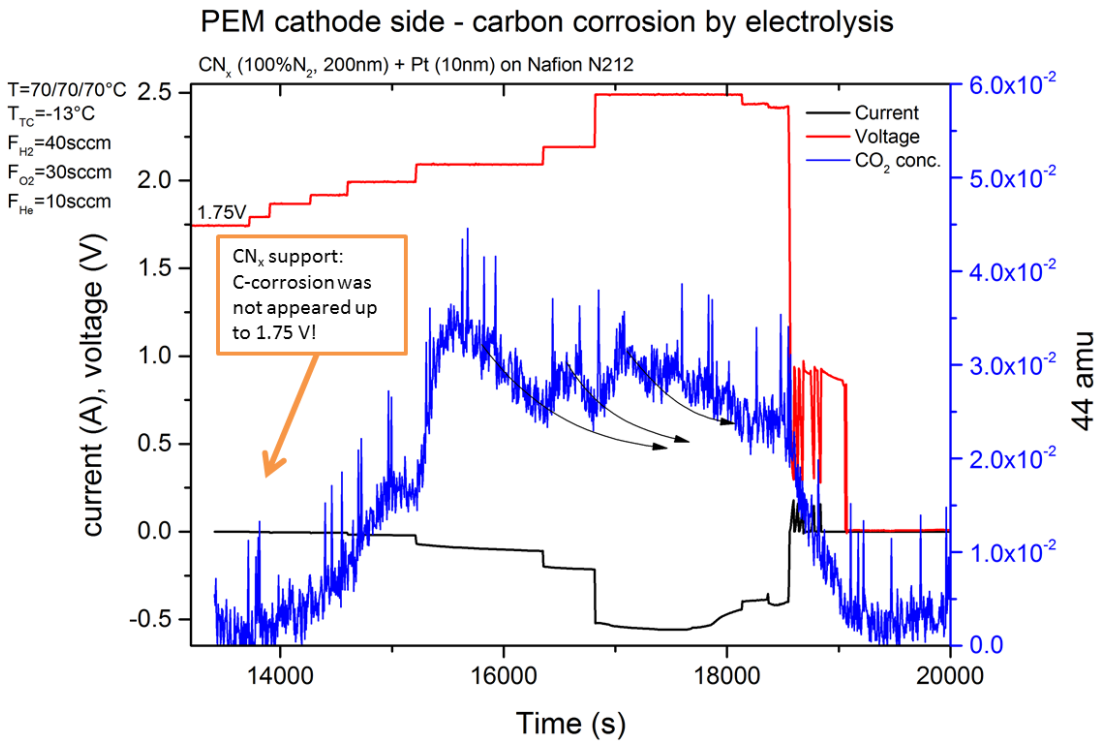

Fig. 16.10: Results of carbon corrosion experiment for CN_x layer coated on Nafion membrane NR212. The normalized signal of mass 44, current and voltage against time is presented.

seen in the table 16.2. For better understanding a comparison of IV curves and power density dependencies on current density are shown in figure 16.11: before electrochemical treatment consisted of several experiment described in the section 6.5 including CV (left) and after the treatment (right). It is seen that before the treatment performance of Pt-CeO_2(Ar)/nGLD is 30% less than performance of Pt-CeO_2(Ar+O_2)/nGLD. However, after the treatment the performance of catalyst prepared without presence of oxygen increases and it is getting to be equal to the performance of catalyst prepared with the presence of oxygen. Thus, performance for both catalyst Pt-CeO_2(Ar+O_2)/nGLD and Pt-CeO_2(Ar)/nGLD is the same after electrochemical treatment. This phenomenon was also observed in voltammogram (not shown) where the charge Q_H increased from 0.09 mC cm^{-2} to 0.23 mC cm^{-2} which is comparable with charge determined for (Ar+O_2) 0.22 mC cm^{-2}.

Additionally, the catalyst Pt-CeO_2(Ar)/nGLD also revealed good durability and long time stability as it shown in the table 16.1.

We can conclude that we are able to sputter Pt-CeO_2 on nGDL at special condition of exact presence of oxygen in Ar process gas to obtain very active catalyst. Then, if pure Ar atmosphere is used, the catalyst can be still activated by electrochemical procedure.

Pt-CeO_2 cycling voltammetry analyses and its comparison with commercial Pt-C based catalyst has been also partially published in [175].

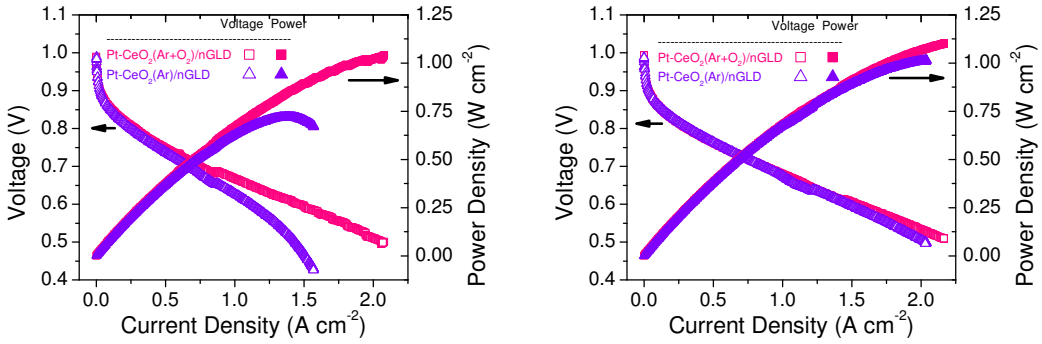

Fig. 16.11: The comparison of polarization curves and power density dependencies on current density for Pt-CeO_2 sputtered catalyst film under presence of oxygen in process gas as Pt-CeO_2(Ar+O_2)/nGLD (0.6 μg(Pt) cm^{-2}) and without presence of oxygen in process gas as Pt-CeO_2(Ar)/nGLD (0.6 μg(Pt) cm^{-2}) before (left) and after cyclic voltammetry treatment (left). The cathode was commercial from Alfa Aesar (400 μg(Pt) cm^{-2}) in both cases. Data were obtained at temperatures 70/70/70 °C and at pressure 0.5 Bar. The flow rates were 80 sccm of H_2, 65 sccm of O_2. Pressure in piston was 8 Bar and active area was 4.41 cm^2.

17. XANES

In this chapter the *in situ* and *in operando* investigation of chemical states of Pt and Ce in Pt doped ceria sputtered catalyst with the use of X-ray absorption near edge structure (XANES) spectroscopy is presented.

This method is also known as near edge X-ray absorption fine structure (NEXAFS). It is a type of absorption spectroscopy that indicates the features in the X-ray absorption spectra (XAS) given by the photoabsorption cross section for electron transitions from a core level to final states. The deexcitation due to refilling of deep core level hole is detected. Typically, the fluorescent X-ray radiation is measured as it was also in our case. More information about this method can be found on the web page [176]. Schematic illustration of this method is seen in figure 17.1 . The extremely intensive monochromatic synchrotron radiation en-

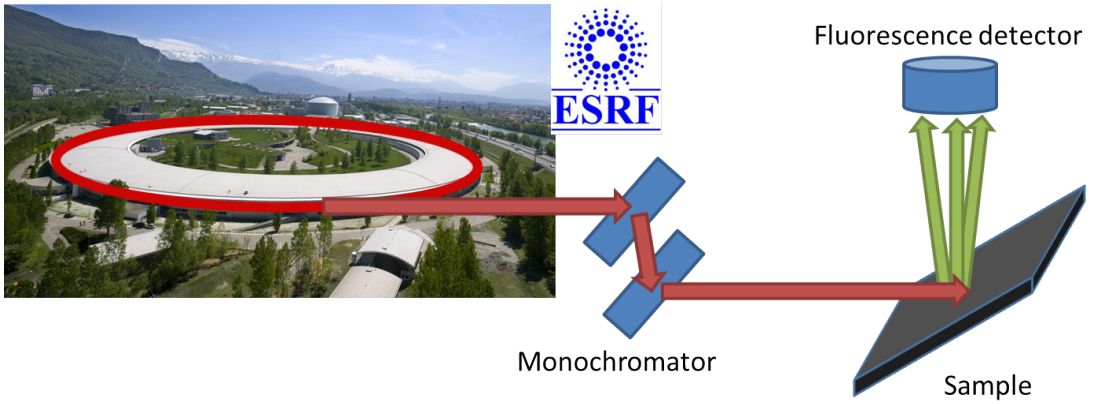

Fig. 17.1: The schematic illustration of X-ray absorption near edge structure (XANES). The fluorescent X-ray is detected.

ables to put samples of interest in to electrochemical environment of the half-cell (see the figure 6.2 left) which simulates operating conditions of FC while characteristic fluorescence for Pt and Ce is appearing. The characteristic energy when the fluorescence appears is called *the edge*. An electrochemical cell made of PEEK (polyether ether ketone) with Kapton window for X-ray was used for the *in situ* XANES measurements.

Since energy of X-ray was high enough (upto 40 keV) the Pt L_3 edge at $\sim$ 11.57 keV and Ce L_3 edge at $\sim$ 5.73 keV were investigated. Therefore, the energy windows measured for Pt and Ce were $11.50 - 11.65$ keV and $5.70 - 5.80$ keV, respectively. The observations of Pt and Ce chemical state changes were reported in the literature [177, 178]. It was reported that Pt L_3 has for all states (Pt^0, Pt^{2+} and Pt^{4+}) only one edge (*peak*) at characteristic energy of 11.56 keV [178, 179] and intensity of this peak increases with increase of oxidation state of Pt.

In contrast, the doublet feature appears at $f_1 = 5.733$ keV and $f_2 = 5.740$ keV in the case of Ce L_3 edge. The ratio f_1/f_2 is close to ~ 1 for stoichiometric CeO_2 and it increases with decrease of oxidation state of Ce [177, 178]. The examples of Ce L_3 edge features for stoichiometric ceria and its reduced form are shown in figure 17.2.

Samples were prepared by magnetron sputtering as it was described in chapter 8. Conditions of sputtering were similar to those presented in chapter 11.1 and 16.

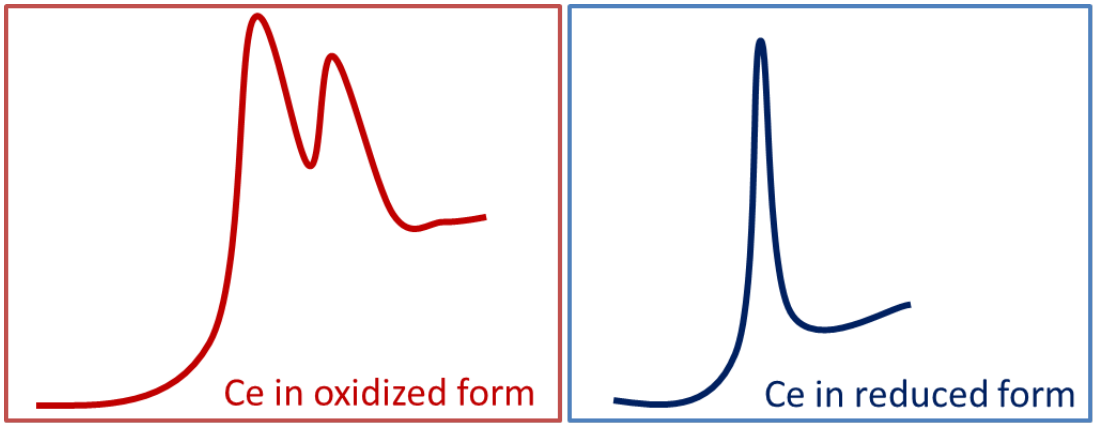

Fig. 17.2: The example of Ce L_3 edge for stoichiometric ceria (left) and its reduced form (left).

Pt-CeO_2 were sputtered with the use of a composed target prepared from CeO_2 target with two Pt wires placed on the target in radial direction.All layers were prepared on several substrates: silicon wafer (Si), carbon foil (CF) and nGDL. Samples with CF were used for investigation by XANES. Thickness of layer was 10 nm.

Four different samples were prepared: metallic Pt, PtO and PtO_2 and Pt-CeO_2.

- Pt was sputtered in Ar atmosphere. Discharge power was set to 10 W which corresponds to 8 nm min^{-1} at this conditions.
- PtO was sputtered in atmosphere consisted of Ar + 30% O_2. Discharge power was set to 10 W which corresponds to 6.2 nm min^{-1} at this conditions.
- PtO_2 was sputtered in O_2 atmosphere. Discharge power was set to 10 W which corresponds to 2 nm min^{-1} at this conditions.
- Pt-CeO_2 was sputtered in Ar atmosphere. Discharge power was set to 20 W which corresponds to 0.18 nm min^{-1} at this conditions. Loading of Pt was determined by XPS analysis and by procedure shown in chapter 19.1 as 3 μg(Pt) cm^{-2}.

XPS measurements of Pt 4f and Ce 3d have been performed and analyzed by the same way as in chapter 11.1 and they revealed absence of metallic state of Pt in our sputtered catalyst film Pt-CeO_2 while the ceria (see the figure 17.4 (left)) was partially reduced as we had expected. This is in agreement with previous results reported in chapter 11.1. The ratio of chemical states was determined: Pt^{2+}/Pt^{4+} is 0.53 and Ce^{3+}/Ce^{4+} is 0.24.

17.1 Verification of the method

At first, the samples Pt/CF, PtO/CF and PtO_2/CF were analyzed as prepared by laboratory XPS and then the same samples were investigated by XAS using

synchrotron radiation in Nitrogen atmosphere. The figure 17.3 shows XPS spectra of PtO/CF (left) and XANES of Pt L_3 edge of the same sample (right). XANES result was fitted by following procedure. Based on XPS result we assumed that XANES of Pt/CF is reference for Pt^0 while PtO_2/CF is reference for state Pt^{4+}. In the case of PtO/CF XPS 4f, apart from the Pt^{2+} the analysis revealed 32% of Pt^{4+}. Thus, we made the fit of obtained Pt L_3 edge for PtO/CF sample by sum of products α[Pt/CF]+β[PtO/CF]+γ[PtO_2/CF] with $\gamma = 0.32$. The results of fitting parameters $\alpha = 0.0$ and $\beta = 0.68$ are in the perfect agreement with the result obtained by XPS and the data are fitted very well.

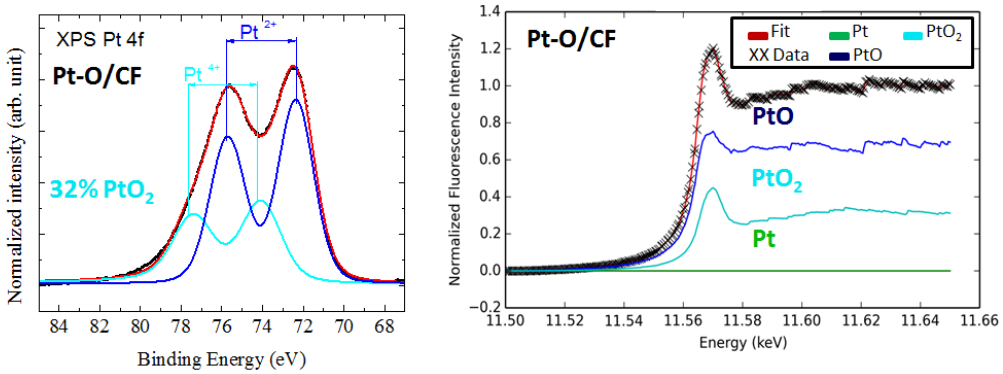

Fig. 17.3: XPS of Pt 4f of sample PtO/CF (left) and NEXAFS Pt L_3 edge of the same sample obtained in N_2 environment fitted by sum of products α[Pt/CF]+β[PtO/CF]+γ[PtO_2/CF] with $\gamma = 0.32$. Calculated parameters: $\alpha = 0.0$ and $\beta = 0.68$.

Similarly, the Ce L_3 edge of Pt-CeO_2/CF was investigated and it was compared with the results obtained by XPS (see fig. 17.4). XPS of Ce 3d for Pt-CeO_2/CF (see figure 17.4 (left)) shows ceria in oxidized form (partially reduced). The ratio of oxidation states was determined as $Ce^{3+}/Ce^{4+} = 0.24$. Figure 17.4 (right) shows NEXAFS Ce L_3 edge for different environment. At first, analysis in the Nitrogen atmosphere was performed and than ceria was reduced in the water environment. Thus, the ceria was not fully reduced because it could be still reduced more which is also in agreement with observation in XPS. Then a change of media from water to 10^{-3}M $HClO_4$ at 0 mV vs Ag/AgCl started causing oxidation of ceria.

According to these facts, the NEXAFS analysis was found as a suitable technique which enables to study the chemical states of individual element of catalyst *in operando*. In following part the interaction between Pt-CeO_2 or CeO_2 and water is presented.

17.2 CeO_2 reduced by water

In the previous section, we did not discuss reducing of ceria in Pt-CeO_2 which was observed in figure 17.4 where the characteristic feature attributed to the ceria reduction after swapping nitrogen for water. This behavior of ceria is really interesting because there exist lots of evidence in the literature that ceria activated by Pd, Pt or Rh with adsorbed water under presence of reducing agent (CO,

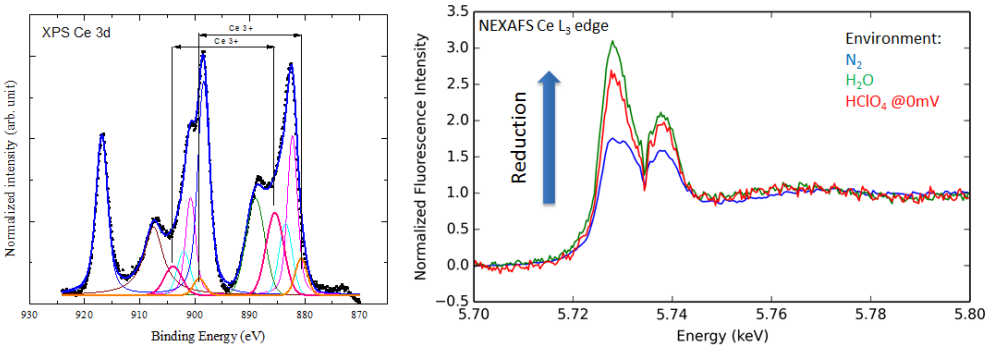

Fig. 17.4: XPS of Ce 3d of sample Pt-CeO_2 (left). The Ce^{3+} content is determined as $Ce^{3+}/Ce^{4+} = 0.24$. NEXAFS Ce L_3 edge for different environment in order of they were used: N_2 atmosphere, H_2O and 10^{-3}M $HClO_4$ environment at $E = 0$ mV vs Ag/AgCl.

CH_3OH,C_2H_5OH) used for the water gas shift reaction (WGS) is oxidized in ultra high vacuum or low pressure conditions e.g. [180] (with more than 600 citations). However, we observed completely opposite behavior because the Pt doped ceria was reduced in the real water media. It is not easy to explain this phenomenon and processes on the surface which lead to appearance of Ce^{3+}. Reduction of ceria can be explained by adsorption of $(OH)^-$ groups and donation of one electron by this way. This hypothesis can be supported by the literature [181] where authors treated Ni doped ceria coated on Ru monocrystal in at very small amount of water and ethanol at low pressure (40 mTorr of ethanol and 200 mTorr of water) in the near ambient pressure XPS and they suspected formation of $Ce(OH)_3$. However, this hydroxide is not stable and more stable form is $Ce(OH)_4$. Interaction between ceria and water molecules adsorbed on the surface at ultra high vacuum condition was also investigated in [182]. Remind the figure 17.4(right) where reduced ceria could be after reduction easily oxidized again by applying of potential (mentioned in previous part), we can expect that this unstable $Ce^{3+} - (OH^-)_3$ complex was formed.

The figure 17.5 shows the same experiment as it was in the case presented in figure 17.4 (right) but now for pure CeO_2 without Pt. It seen that ceria was oxidized in the Nitrogen atmosphere (left) while after change of N_2 atmosphere to water environment ceria was rapidly reduced (right). It should be noted that ceria without Pt was reduced more than uin this case of Pt doped ceria according to the figure 17.4 (right). We suppose that stronger bond between ceria and hydroxyl group was formed in this case which is supported by the fact that reduced ceria was not able to oxidize again by presented method (much more effort was necessary, not shown).

Be that as it may, facts reported in this section are strong evidences that the reaction can be generally proceed by different way in contrast to estimation based on model study in ultra high vacuum (UHV) experiments.

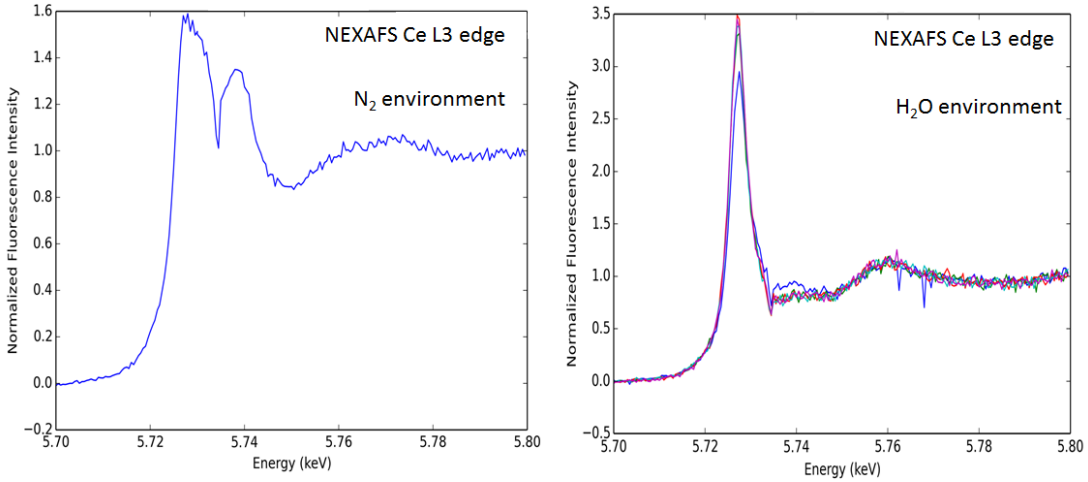

Fig. 17.5: Normalized intensity of Ce L_3 edge of Pt-CeO_2 for different environment: N_2 atmosphere (left) and H_2O environment (right).

17.3 Chemical state investigation at fuel cell conditions

Figure 17.6 shows NEXAFS for Pt L_3 edge at different environments (N_2, H_2O, 10^{-3}M $HClO_4$) and when the reducing potential was applied. It is clearly seen that oxidation state of Pt in PtO/CF sample is changed after applied potential in acidic media and it depends on the media.

In contrast to PtO (the similar can be seen for Pt or PtO_2) where the chemical state of Pt strongly depends even on environment, it is not seen any development of chemical state of Platinum in Pt doped ceria and the only observed oxidized state exhibited excellent stability in the region from -200 mV to 1400 mV vs Ag/AgCl as it is presented in figure 17.7. We have already shown that Pt is ionic in the Pt-CeO_2 and NEXAFS confirmed this fact and additionally we confirmed that ionic Pt appears also in the real FC operating condition (since we investigated the region -200 mV to 1400 mV vs Ag/AgCl). Moreover, we have just shown that this ionic state is stable in this condition.

In contrast to the results presented in figure 17.7, figure 17.8 shows significant development of chemical state of Ce investigated by NEXAFS Ce L_3 edge. Intensity of Ce L_3 edge features and its ration attributed to the chemical state of Ce area were changing in function of applied potential. Reduction of ceria increases with decrease of the potential. Ceria is more reduced at lower potential and again oxidized at higher potential. The fact that chemical state depends on the potential can help us to suggest that ceria participate in the hydrogen oxidation reaction on the FC anode and it supports our hypothesis reported in chapter **??** that ceria attended to the reaction mechanism.

NEXAFS Pt L_3 (see fig. 17.9) and Ce L_3 (see fig. 17.10) for sample Pt-CeO_2/CF have been also investigated during the cycling voltammetry experiment. CV was performed from -200 mV to 1400 mV vs Ag/AgCl with scan rate 50 mV s^{-1} in acidic media 10^{-3}M $HClO_4$ which corresponds to pH 3. It is clearly seen that Pt was in ionic state and there was not any development during the CV experiment and it was not changed up to 70 cycles when the experiment

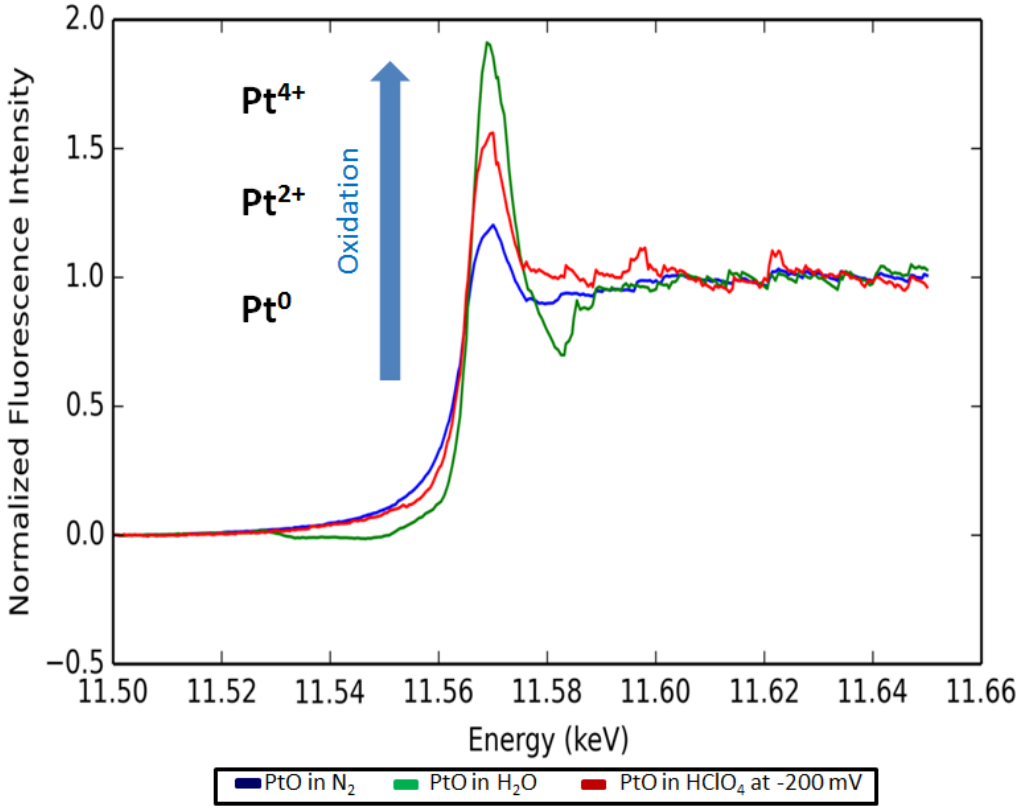

Fig. 17.6: Normalized intensity of Pt L_3 edge of PtO/CF for different environment: N_2 atmosphere, H_2O and 10^{-3}M $HClO_4$ environment at $E = -200$ mV vs Ag/AgCl.

was stopped. In contrast, Ce L_3 revealed the significant development of chemical state of ceria during the CV experiment. It is shown that ceria is more oxidized with time and count of cycles. More significant changes have been shown at the beginning of cycling. The NEXAFS spectra were obtained at 0 mV vs Ag/AgCl.

17.4 Stability of Pt-CeO_2

The stability of $PtCeO_2$ catalyst was investigated for two different pH (pH 3 and pH 1) at the same overpotential. The overpotential shift from pH 1 to pH 3 was calculated as -120 mV using the Nernst equation for standard hydrogen electrode. All experiments in previous sections in this chapter were performed at pH 3. At this pH we have not observed any dissolution of Pt-CeO_2. Immediately after the environment of experiment was switched from pH 3 to pH 1 the reducing of CeO_x was appeared. The dissolution was investigated by focusing on time series of absolute intensity of Pt L_3 edge (see fig. 17.11) and Ce L_3 edge (see fig. 17.12).

The decrease of Ce L_3 gradually is clearly seen and it can be explained by dissolution of ceria. Additionally, it is shown that this dissolution procedure follows exponential decrease (see inserted graph in figure 17.12). The decrease of the intensity to $1/e$ was reached after 45 min and at the end of the experiment it remains less than 10% of ceria in comparison to the amount before experiment. On the other hand, Pt was stable during all experiment and it occurs still at its

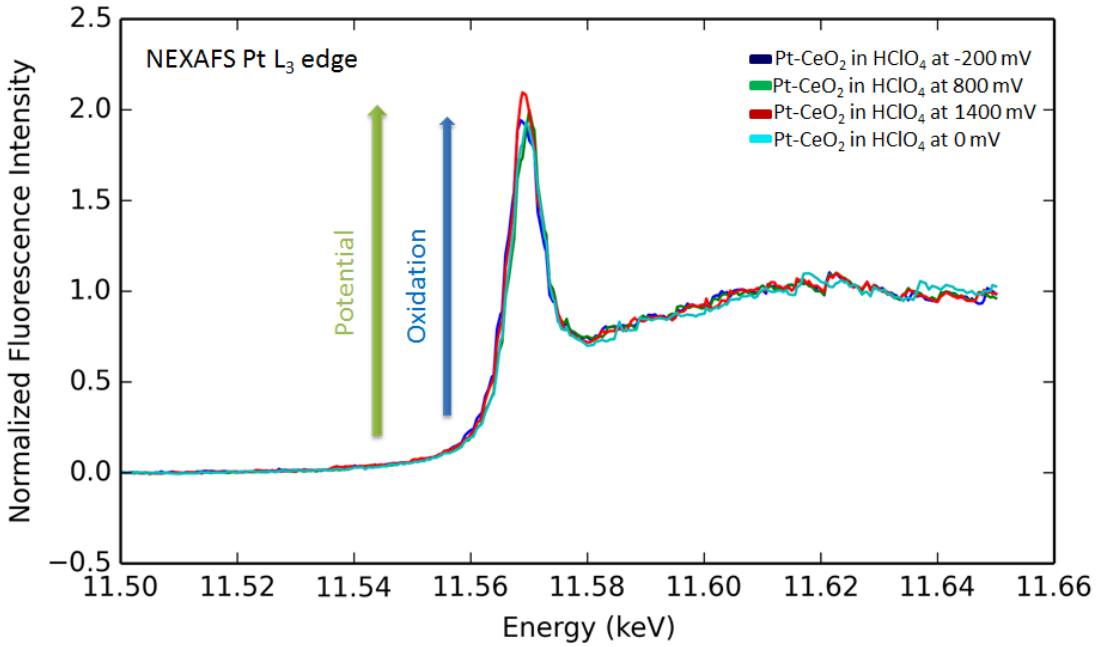

Fig. 17.7: XANES of Pt L_3 edge of Pt-CeO_2 sputtered catalyst on CF performed in acidic media 10^{-3}M $HClO_4$ for different potential vs Ag/AgCl: -200 mV, 800 mV, 1400 mV and 0 mV. Obtained spectra are normalized according to the intensity after edge.

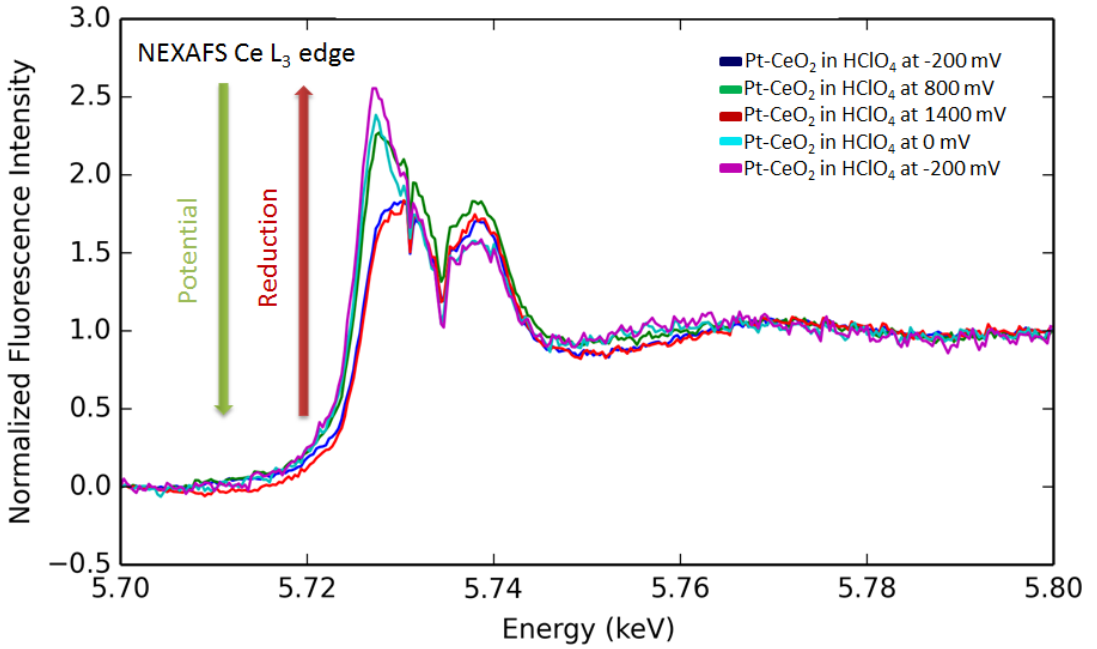

Fig. 17.8: XANES of Ce L_3 edge of Pt-CeO_2 sputtered catalyst on CF performed in acidic media 10^{-3}M $HClO_4$ for different potential vs Ag/AgCl: -200 mV, 800 mV, 1400 mV, 0 mV and 0 mV. Obtained spectra are normalized according to the intensity after edge.

cationic state. Partial reduction of Platinum cations was occurred when the Ce was heavily dissolved (amount of ceria decreased up to lower than 10%.)

Dissolution of Pt-CeO_2 prepared by chemical wet technique in acid media was

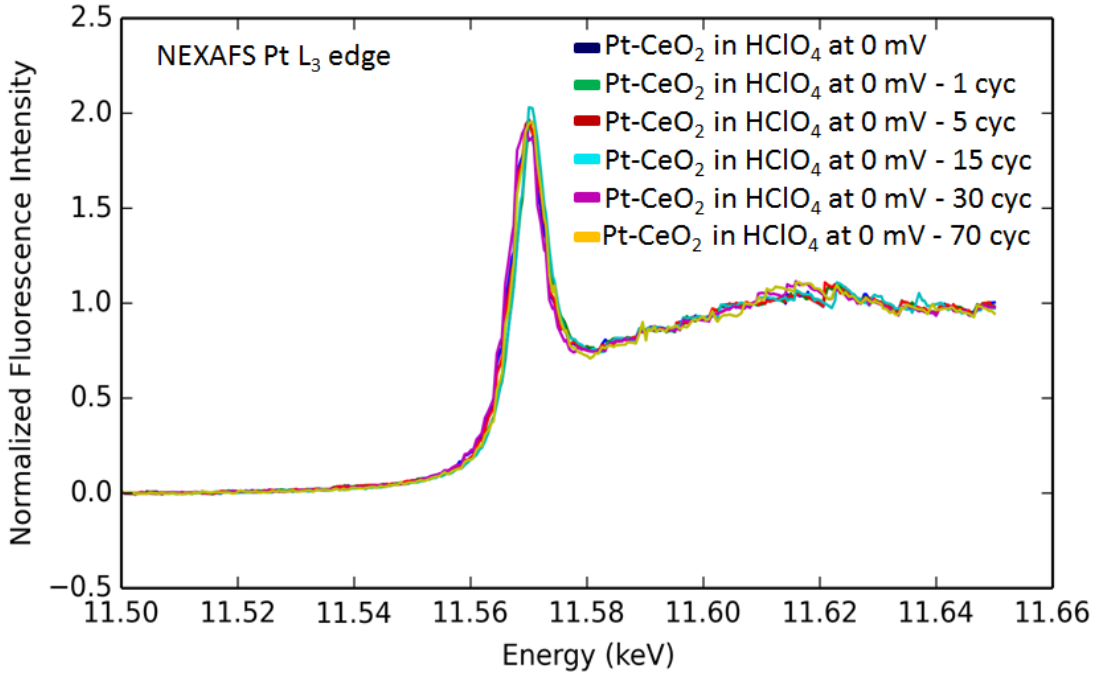

Fig. 17.9: XANES of Pt L_3 edge of Pt-CeO_2 sputtered catalyst on CF obtained in acidic media 10^{-3}M $HClO_4$ after selected cycles of CV performed from -200 mV to 1400 mV vs Ag/AgCl with scan rate 50 mV s^{-1}: initialization, 1 cyc, 5 cyc, 15 cyc, 30 cyc and 70 cyc. Obtained spectra are normalized according to the intensity after edge.

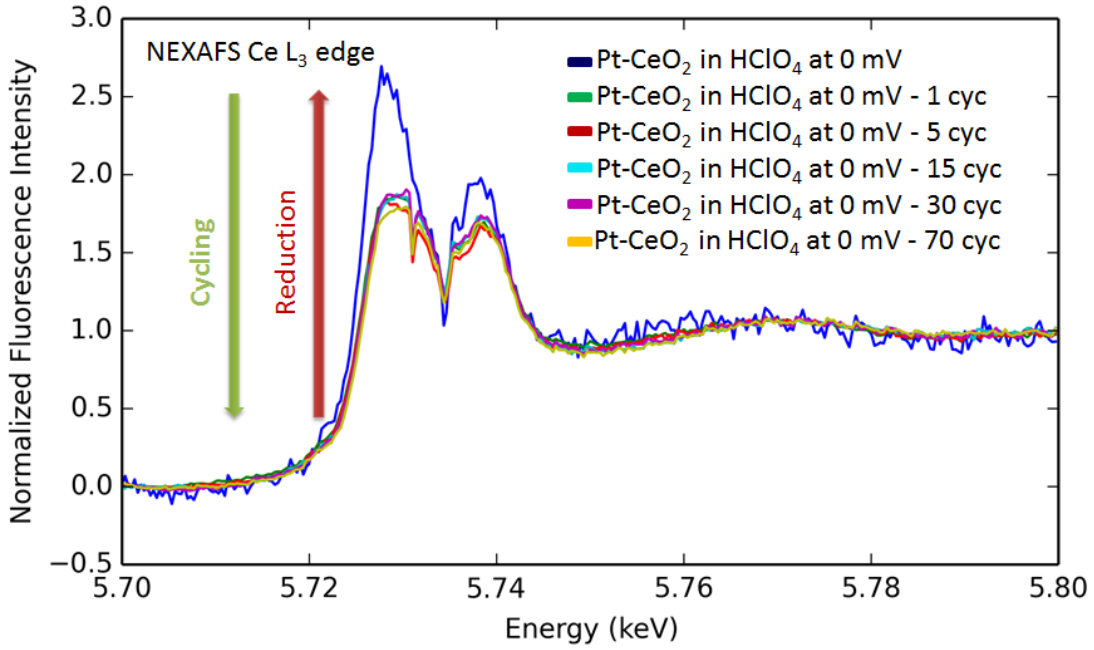

Fig. 17.10: XANES of Ce L_3 edge of Pt-CeO_2 sputtered catalyst on CF obtained in acidic media 10^{-3}M $HClO_4$ after selected cycles of CV performed from -200 mV to 1400 mV vs Ag/AgCl with scan rate 50 mV s^{-1}: initialization, 1 cyc, 5 cyc, 15 cyc, 30 cyc and 70 cyc. Obtained spectra are normalized according to the intensity after edge.

observed in the literature [183, 184]. It is presented that after 30 cycles the ceria was dissolved and only 5% of Ce remains. The most of Ceria was dissolved within

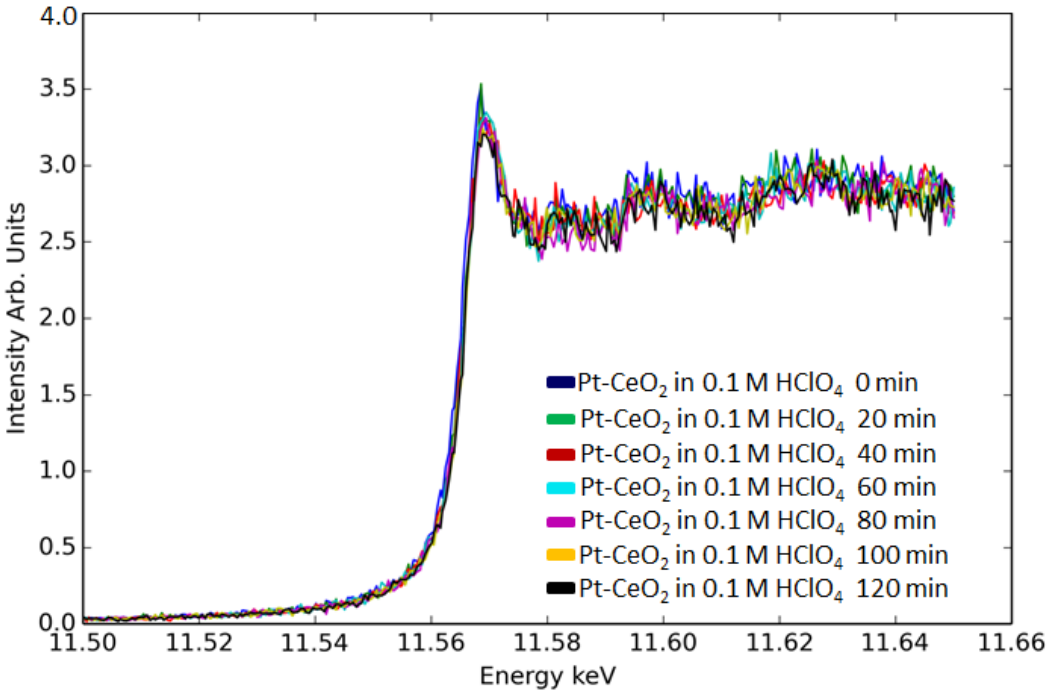

Fig. 17.11: Time dependency of Pt L_3 edge of Pt-CeO_2 sputtered catalyst on CF obtained in acidic media $\mathbf{10^{-1}M}$ $HClO_4$ at -200 mV vs Ag/AgCl at selected elapsed time: initialization, 20 min, 40 min, 60 min, 80 min, 100 min and 120 min. Obtained spectra are **not normalized** according to the intensity after edge in order to compare absolute intensity corresponding to the content of the element on the surface.

5 cycles CV. The dissolution of CeO_2 was also observed and discussed in [184]. However, the authors used standard electrolyte 0.5 M H_2SO_4. We confirmed this result with the use of pH 1 (0.1M $HClO_4$) but at pH 3 (10^{-3}M $HClO_4$) Pt-CeO_2 was not dissolved and it revealed good stability. Additionally, we also observed stability of pure CeO_2 at the pH 1 (not shown). Based on this fact we can suppose that dissolution of Pt-CeO_2 is Pt activated.

We conclude that Pt-CeO_2 anode was found to be suitable to hydrogen oxidation. It reveals great stability and activity and *in operando* NEXAFS study shows that Pt cations are stable while oxidation state of ceria is developing according to environment and applied potential which supports our hypothesis that ceria are participate in hydrogen oxidation reaction directly. We observed that Pt-CeO_2 is not dissolved at pH 3. More information is provided in paper which is under progress.

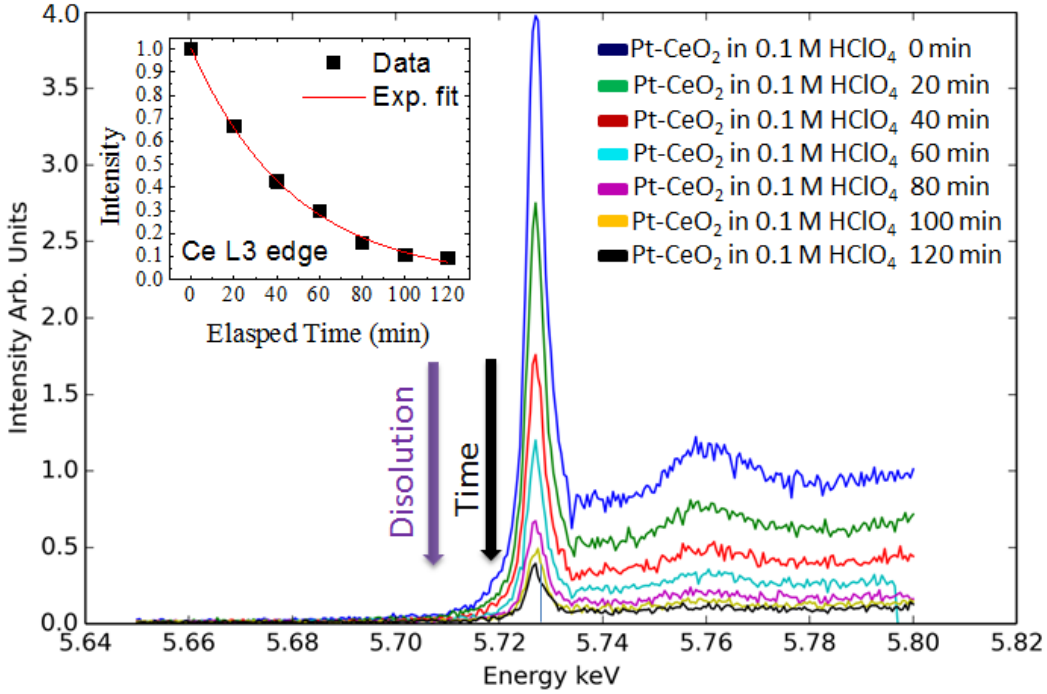

Fig. 17.12: Time dependency of Ce L_3 edge of Pt-CeO_2 sputtered catalyst on CF obtained in acidic media $\mathbf{10^{-1}M}$ $HClO_4$ at -200 mV vs Ag/AgCl at selected elapsed time: initialization, 20 min, 40 min, 60 min, 80 min, 100 min and 120 min. Obtained spectra are **not normalized** according to the intensity after edge in order to compare absolute intensity corresponding to the content of the element on the surface. The inserted graph shows normalized intensity to the initial value corresponding with content of ceria.

18. Online model analyses and calculation

Additionally, FC simulations were programmed using *PHP* and *jQuery*[1] and they are also provided via internet on the web page http://physics.mff.cuni.cz/kfpp/povrchy/vypocty_online/index2.html and mirrored on http://milosfiala.cz/fcsimulator/. See the part *Fuel Cell Simulation*.

The parameters of FC model can be added and the results are presented.

There are two models that were derived *ab-initio* (not shown here due to space reason) and provided for users. The results of model simulations depend on user's input parameters. Apart from model calculation there is presentation of measurement procedure which simulates Potentiostat/galvanostat with all standard functions. Thus, the time-lines for voltage, current and power might be recorded. Moreover, the polarization curve of selected time-line can be plotted. All data can be saved easily. The interface is simple and it is designed user-friendly in order to avoid to complicated and disorganized interface emphasizing on educative role. However, just as well serve as a playground for testing model simulating fuel cell behavior. The website is provided with user help, therefor all functionalities do not need to be explained in detail here. Print screen of the fuel cell simulator is in fig. 18.1.

There are more calculations and simulations presented online. See the list below. All parts of project are created with using of *HTML*, *PHP*, *jQuery* and *CSS*. Web pages have responsive web design[2]

List of topics on the web page:

- **Metal Loading**
  This section enables to determine the weight of noble metal in catalyst. Input parameters are thickness and atomic concentration. Additionally, the specific power and electrochemical active surface area can be calculated.

- **Calculation of Relative Humidity in Fuel Cell**
  This part allows to investigate the relative humidity in the operating cell. The characterization of humidification system and its limits are interactively presented.

- **Calculation of Saturated Vapor Pressure**
  For the needs of the model computing and proper potential calculation was necessary to determine vapor pressure very precisely. The Wagner liquid–vapor pressure equation was used and the results for relevant ranges can be seen online. The reason why we have decided to put the results online is fact that even on the reasonable online database NIST (National Institute of Standards and Technology) http://webbook.nist.gov are still Antoine

[1] PHP is a server-side scripting language designed primarily for web development but also used as a general-purpose programming language. jQuery is a cross-platform JavaScript library designed to simplify the client-side scripting of HTML.

[2] Web pages are viewed in response to the size of the screen or web browser one is viewing with. It offers the same support to a variety of devices for a single website.

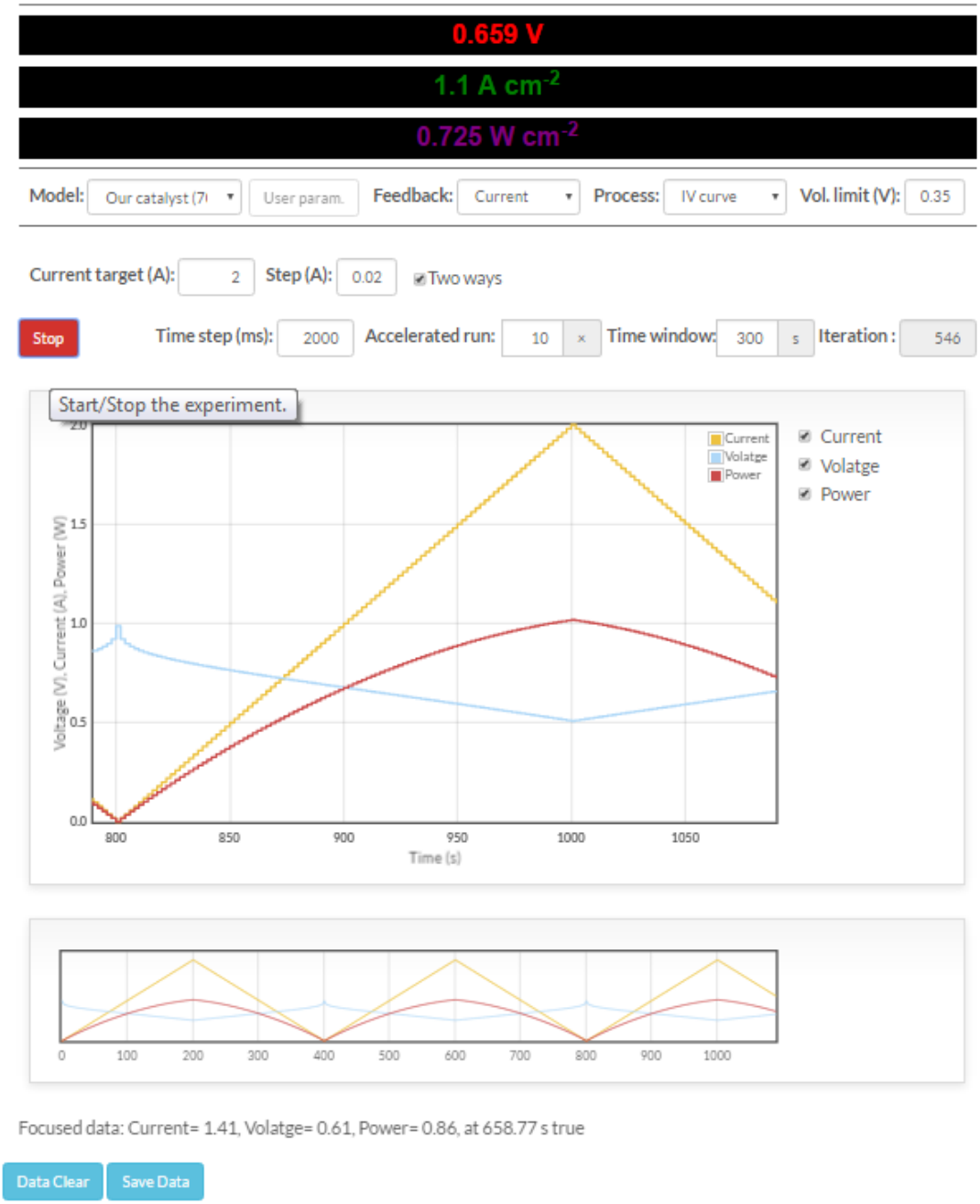

Fig. 18.1: The print screen of online fuel cell simulator demonstrating fuel cell model determined in this work. Additionally, the website works as fuel cell measurement simulator.

equation parameters only which enables to obtain data for limited range dived into several sub ranges.

- **Maximum Cell Voltage**
  In this section of the web page calculation of reversible potential as a function temperature, pressure, partial pressures of reactants and products are presented. The simulated data can be saved. There can be chosen between gaseous or liquid water product and then the 3D potential map is plotted. Example of such a plot is seen in fig. 18.2.

- **Fuel Cell Simulator**
  The simulation software generates the fuel cell simulator presenting real-time measurement of fuel cell and derived models of polarization curves as already described above.

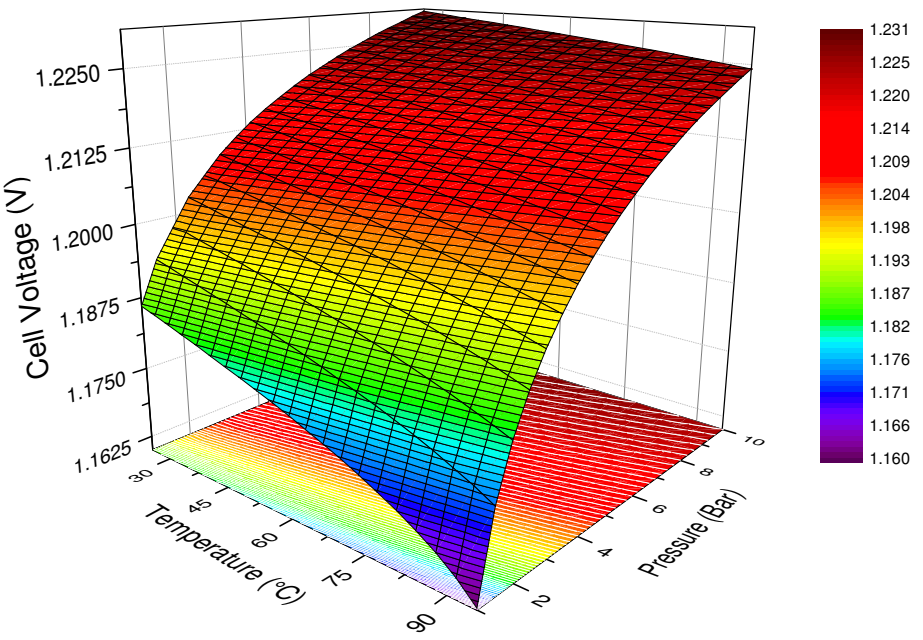

Fig. 18.2: The example of 3D map of reversible potential. In this case: $E(T, P, \alpha, \beta, \gamma) = E(< 25, 95 >, < 1, 10 >, 1, 1 - \gamma, 0.85\frac{P_{sat}}{P})$, where P_{sat} is vapor pressure.

V Closing

"An experiment is a question which science poses to Nature, and a measurement is the recording of Nature's answer."

— Max Planck

19. Conclusion

We have shown that Pt-CeO_2 sputtered anode catalyst exhibits the same power densities in comparison with the state of art commercial catalyst (1 W per cm_2) while we used only 0.6 μg(Pt) cm^{-2} which is more than 600 lower amount than in the case of standard commercial catalyst. Obtained specific power in the case of sputtered Pt-CeO_2 catalyst exceeded 1600 W $mg(Pt)^{-1}$. Additionally, investigation of catalyst durability reveals that Pt-CeO_2 has the same performance up to 6000 of the degradation accelerating cycles when the experiment was stopped. Moreover, the statistical analysis of obtained results from fuel cell analyses of Pt doped ceria and pure Pt catalysts for different Pt loading and electrochemical supporting methods as cycling voltammetry and impedance spectroscopy shows that Pt-CeO_2 sputtered catalyst with atomically dispersed platinum is still at least 3 times active than it would be in the case of hypothetical ideal pure Pt atomically dispersed catalyst keeping the same activite as in the case of Pt nanoparticles.

The XPS studies of Pt 4f and Ce 3d of $PtCeO_2$ revealed Pt in cationic states and partially reduced ceria. Additionally, the NEXAFS study of Pt L_3 and Ce L_3 edges showed that Pt was still in its cationic form at environment simulating the real FC condition at potential range from -200 mV to 1400 mV vs Ag/AgCl. On the other hand, chemical state of Ce significantly depends on applied potential and media which is used. Based on this fact, we assumed that Ce is directly participating in the hydrogen oxidation reaction on the anode which is supported by result of statistical analyses reported above and partially by DFT studies showing low energy barrier for hydrogen adsorption on the Ce atoms in Pt-CeO_2 small cluster.

The NEXAFS study also confirmed that Pt-CeO_2 was dissolved in acidic media of pH 1, as it was reported in the literature, but we did not observe any dissolution at pH 3. Based on this fact, if there would be pH of operating cell around pH 3, the performance of the cell should be stable. However, it is supposed that operating cell has pH less than 3 therefore the dissolution of Pt-CeO_2 must appear. Since the dissolution was not so fast (decrease intensity of Ce L_3 edge to $1/e$ after 45 min) the cell could still might be operated at pulse mode. We have

really observed that the performance of the cell with Pt-CeO_2 decrease in this time scale and after the current density is decreased and at open circuity, catalyst is regenerated the performance is increased again.

Moreover, the dissolution at pH 1 was observed only for Pt-CeO_2 while for CeO_2 it did appear. Based on this observation, we can say that the dissolution must be Pt activated. Interesting result was also a significant reduction of Ce^{4+} state for Pt-CeO_2 as well as for CeO_2 which was opposite result relative to the literature where the oxidation was observed in case of model studies in ultra high vacuum. This result clearly shows that general reaction can be proceed by different way than as it is estimated based on model studies in ultra high vacuum.

Pt-$SnCeO_x$ anode catalyst was also investigated. The XPS analyses revealed cationic Pt similar to the Pt-CeO_2 catalyst case but a feature belonging to the Pt-Sn interaction appeared. Tin was occurred at Sn^{4+} state. Ceria was more reduced than in the case of Pt doped ceria. FC analyses shows a little bit lower performance in comparison to Pt-CeO_2. However, what is interesting, is that Pt-$SnCeO_x$ exhibits the same CO resistance as the Pt-Ru commercial catalyst and at very low CO concentration 25 ppm even higher tolerance occurred. In contrast, Pt-CeO_2 was poisoned very fast from the concentration of 25 ppm. Despite the fact that Pt-$SnCeO_x$ exhibit 10% lower performance in comparison with the Pt-CeO_2 it is still promising FC anode catalyst due to high CO resistance.

We have presented the investigation of Pt-WO_x and Pd-CeO_2 alternative catalyst. XPS analyses showed that Pt was in cationic state ($Pt^{2+}/Pt^{4+} = 0.26$) similarly to the Pt-CeO_2 catalyst while tungsten oxide was oxidized to its maximum oxidation state W^{6+}. Palladium occurred as Pd^{2+}. Both anode catalyst exhibited high specific power 14 W $mg(Pt)^{-1}$ and 1100 W $mg(Pd)^{-1}$ for Pt-WO_x and Pd-CeO_2, respectively. Thus, both catalysts have been found as promising anode catalysts. Additionally, despite the fact that Pd is also a noble metal, the use of Pd can help to diversify natural sources.

Since we obtained very good anode catalysts, for decrease of the amount of Pt in whole fuel cell, the cathode catalyst should be also improved. We investigated the highly reported and cited Pt-Co alloy catalyst but we prepared it by magnetron sputtering in the form of very thin layer of 50 nm. The most active phase Pt_3Co has been prepared after electrochemical treatment which was supported by a shift of the onset potential determined by cycling voltammetry.

We have demonstrated the fully thin catalyst operating fuel cell consisting of Pt-CeO_2 anode and Pt-Co sputtered cathode. The total Pt loading in the cell was 48 $\mu g(Pt)$ cm^{-2} and power density exceeded 125 mW cm^2 which corresponded to the specific power 2.7 W $mg(Pt)^{-1}$ according to the anode together with the cathode. Moreover, this cell exhibited good durability and the performance was not significantly dropped down for 2700 cycles of accelerating degradation processes when the experiment was stopped.

The derivation of the fuel cell model has been done and obtained model was interactively presented online on the web page where the parameters can be changed and the result is immediately seen. On the web page the other useful calculations used in this work are presented. It is possible to interactively calculate on the individual web pages: metal loading, relative humidity of the humidification system of fuel cell, saturated vapor pressure and maximum cell voltage with 3D plot of the cell potential. Additionally, simulation of the fuel

cell measurement based on the model is presented. It can be used for real scientific simulation as well as for education. Calculations described above were programmed by *PHP* and *jQuery* and they are provided via internet http://physics.mff.cuni.cz/kfpp/povrchy/vypocty_online/index2.html and mirrored on http://milosfiala.cz/fcsimulator/.

The presented research could not be performed without development of necessary equipments and devices. The design of piston operated fuel cell was developed. The design of PEM FC stack was developed. The design of the fully automatized test station, which is on the market now, was developed. Design of laboratory with installation of ten of this test station was developed.

VI Appendices

"Physics is like sex: sure, it may give some practical results, but that's not why we do it."

— Richard Feynman

19.1 Catalyst loading

The determination of amount of one substance in binary substances layer is shown. Additional is presented the determination of general formula for any number of substances. Let's assume wight ratio 19.1 and molar ratio 19.2 of two substances A and B as follows

$$\frac{m_{\mathrm{A}}}{m_{\mathrm{B}}} = P \tag{19.1}$$

$$\frac{n_{\mathrm{A}}}{n_{\mathrm{B}}} = R \tag{19.2}$$

The relation between R and P is given by

$$P = R\frac{M_{\mathrm{A}}}{M_{\mathrm{B}}} \tag{19.3}$$

where M_{A} and M_{B} are molar wights and n_{A} and n_{B} are amount of substances of substances A and B, respectively. Define parameters p_{a}, p_{b} determine mass fraction and parameters r_{a}, r_{b} determine molar fraction of substance A and B, respectively. If we assume $p_{\mathrm{a}} + p_{\mathrm{b}} = 1$ and $P = \frac{p_{\mathrm{a}}}{p_{\mathrm{b}}}$ and complementary $r_{\mathrm{a}} + r_{\mathrm{b}} = 1$ and $R = \frac{r_{\mathrm{a}}}{r_{\mathrm{b}}}$ then

$$p_{\mathrm{A}} = \frac{1}{1+\frac{1}{P}} \tag{19.4}$$

$$p_{\mathrm{B}} = \frac{1}{1+P} \tag{19.5}$$

$$r_{\mathrm{A}} = \frac{1}{1+\frac{1}{R}} \tag{19.6}$$

$$r_{\mathrm{B}} = \frac{1}{1+R} \tag{19.7}$$

For obtaining of amount of one substance we need to know the average density. The average density related to mass fraction (p_{a}, p_{b}) is determined with the use of 19.4 and 19.5 by

$$\varrho_{\mathrm{m}} = \frac{\varrho_{\mathrm{A}}\varrho_{\mathrm{B}}}{p_{\mathrm{A}}\varrho_{\mathrm{B}} + p_{\mathrm{B}}\varrho_{\mathrm{A}}} \tag{19.8}$$

$$\Rightarrow \varrho_{\mathrm{m}} = \frac{\varrho_{\mathrm{A}}\varrho_{\mathrm{B}}(1+P)}{P\varrho_{\mathrm{B}} + \varrho_{\mathrm{A}}} \tag{19.9}$$

where ϱ_{A} and ϱ_{B} are mass densities of substance A and B, respectively.

Similarly, the average density according to molar fraction (r_{a}, r_{b}) with the use of 19.9 and 19.3 is given by

$$\varrho_{\mathrm{n}} = \frac{\varrho_{\mathrm{A}}\varrho_{\mathrm{B}}(M_{\mathrm{B}}+RM_{\mathrm{A}})}{RM_{\mathrm{A}}\varrho_{\mathrm{B}}+M_{\mathrm{B}}\varrho_{\mathrm{A}}} \tag{19.10}$$

and with using $R = \frac{r_{\mathrm{A}}}{r_{\mathrm{B}}}$ we obtain the average density according to molar fraction in form as follows

$$\varrho_{\mathrm{n}} = \frac{\varrho_{\mathrm{A}}\varrho_{\mathrm{B}}(r_{\mathrm{B}}M_{\mathrm{B}}+r_{\mathrm{A}}M_{\mathrm{A}})}{r_{\mathrm{A}}M_{\mathrm{A}}\varrho_{\mathrm{B}}+r_{\mathrm{B}}M_{\mathrm{B}}\varrho_{\mathrm{A}}} \tag{19.11}$$

We should note that the average mass density depends on which type of alloy is formed: substitutional alloy or interstitial alloy. Substitutional alloy is created if relative atomic size of all elements are comparable (atomic radius higher than 0.85) while interstitial alloy is formed in the case of different atom sizes of individual elements (atomic radius less than 0.59, usually alloy with small elements like H, C, N, B). The intermediate phase can occur which can be substitutional (atomic radius ratio from 0.85 to 0.6, carbides, nitrides, borides) and in special cases ionic or covalent bond can be created. Thus the average densities can be very different according to which type of alloy is formed. Alternatively, average density can be defined by 19.12

$$\varrho_{\mathrm{Alternation}} = v_{\mathrm{A}}\varrho_{\mathrm{A}} + v_{\mathrm{B}}\varrho_{\mathrm{B}} \tag{19.12}$$

where v_{A} and v_{B} are volume fraction of elements A and B respectively. Define d_{A} and d_{A} as atomic diameters of elements A and B respectively. Than, in the case of the interstitial alloy, the v_{A} and v_{B} can be approximated by

$$v_{\mathrm{A}} = \frac{r_{\mathrm{A}}d_{\mathrm{A}}^3}{r_{\mathrm{A}}d_{\mathrm{A}}^3+r_{\mathrm{B}}d_{\mathrm{B}}^2} \tag{19.13}$$

$$v_{\mathrm{B}} = \frac{r_{\mathrm{B}}d_{\mathrm{B}}^3}{r_{\mathrm{A}}d_{\mathrm{A}}^3+r_{\mathrm{B}}d_{\mathrm{B}}^3} \tag{19.14}$$

For most of usual intersticial alloy mostly consisted of base/solvent (e.g. carbon steel) volume fraction and mass fraction are comparable and volume fraction can be substituted with mass fraction $v_{\mathrm{A}} \cong p_{\mathrm{A}}$, $v_{\mathrm{B}} \cong p_{\mathrm{B}}$. Thus, we obtain approximated formula for average density for intersticial alloy

$$\varrho_{\mathrm{Alternation}} = p_{\mathrm{A}}\varrho_{\mathrm{A}} + p_{\mathrm{B}}\varrho_{\mathrm{B}} \tag{19.15}$$

The presented derived average densities ϱ_{m} and ϱ_{n} suppose an ideal homogeneous solid solution of substitutional alloy with same specific volume of individual species as it is in its natural bulk structure. We will use ϱ_{m} and ϱ_{n} for the rest of calculation but generally any average density can be used.

If we assume the volume of layer V_{l} given by general formula

$$V_{\mathrm{l}} = t_{\mathrm{l}}S \tag{19.16}$$

where t_{l} is thickness of layer and S is area of layer. Thus, with respect to 19.2, 19.16, 19.9, 19.4, the loading of substance A can be expressed as follows

$$L_{\mathrm{m}} = t_{\mathrm{l}}\varrho_{\mathrm{m}}\frac{P}{1+P} \tag{19.17}$$

$$L_{\mathrm{m}} = t_{\mathrm{l}}\frac{\varrho_{\mathrm{A}}\varrho_{\mathrm{B}}(1+P)}{P\varrho_{\mathrm{B}}+\varrho_{\mathrm{A}}}\frac{P}{1+P} \tag{19.18}$$

in the case of weight ratio P (19.1) and similarly with regard to 19.11 and 19.6 is obtained

$$L_{\mathrm{n}} = t_{\mathrm{l}}\varrho_{\mathrm{n}}\frac{RM_{\mathrm{A}}}{M_{\mathrm{B}}+RM_{\mathrm{A}}} \tag{19.19}$$

$$L_{\mathrm{n}} = t_{\mathrm{l}}\frac{\varrho_{\mathrm{A}}\varrho_{\mathrm{B}}\left(M_{\mathrm{B}}+RM_{\mathrm{A}}\right)}{RM_{\mathrm{A}}\varrho_{\mathrm{B}}+M_{\mathrm{B}}\varrho_{\mathrm{A}}}\frac{RM_{\mathrm{A}}}{M_{\mathrm{B}}+RM_{\mathrm{A}}} \tag{19.20}$$

in the case of molar ratio R (19.2). Thus, equations 19.18 and 19.20 determine loading of substance A per cm^2 in binary solution(AB) for given weight ratio (19.1) and molar ratio (19.2), respectively.

For the purpose of general use, the general formulas for any number of substances can be easily determined from equations 19.9, 19.18, 19.11 and 19.20. With regard to mass fraction, the loading of i substance for general solution is as follows

$$L_{\mathrm{m,i}} = t_{\mathrm{l}}p_i\frac{\prod_j \varrho_j}{\sum_j\left(p_j\prod_{k\neq j}\varrho_k\right)} \tag{19.21}$$

where p_i is mass fraction of substance i and it is given by

$$p_i = \frac{m_i}{\sum_j m_j} \tag{19.22}$$

where m_i are wights of substances in solution. The fraction in 19.21 represents the average mass density.

Similarly, with respect to mass fraction 19.22 and due to fact that

$$m_i = n_i M_i \tag{19.23}$$

where n_i is amount of substance i and M_i is molar weight of substance i and with regard to determination 19.11, the fraction 19.24 can be defined as follows

$$X_i = \frac{n_i M_i}{\sum_j n_j M_j} \tag{19.24}$$

Hence, with regard to fraction 19.24 the loading of substance i can be expressed as

$$L_{\mathrm{n,i}} = t_{\mathrm{l}}X_i\frac{\prod_j \varrho_j}{\sum_j\left(X_j\prod_{k\neq j}\varrho_k\right)} \tag{19.25}$$

The fraction in 19.25 represents the average mass density.

Calculations described above were programmed by *PHP* and *jQuery* and they are also provided via internet on the web page `http://physics.mff.cuni.cz/kfpp/povrchy/vypocty_online/index2.html` and mirrored on `http://milosfiala.cz/fcsimulator/`. See the part *Metal Loading*.

Bibliography

1. SORRELL, Steve; SPEIRS, Jamie; BENTLEY, Roger; BRANDT, Adam; MILLER, Richard. Global oil depletion: A review of the evidence. *Energy Policy*. 2010, vol. 38, no. 9, pp. 5290–5295. ISSN 0301-4215. Available from DOI: http://dx.doi.org/10.1016/j.enpol.2010.04.046. Special Section on Carbon Emissions and Carbon Management in Cities with Regular Papers.
2. ALEKLETT, Kjell; HÖÖK, Mikael; JAKOBSSON, Kristofer; LARDELLI, Michael; SNOWDEN, Simon; SÖDERBERGH, Bengt. The Peak of the Oil Age – Analyzing the world oil production Reference Scenario in World Energy Outlook 2008. *Energy Policy*. 2010, vol. 38, no. 3, pp. 1398–1414. ISSN 0301-4215. Available from DOI: http://dx.doi.org/10.1016/j.enpol.2009.11.021. Security, Prosperity and Community – Towards a Common European Energy Policy? Special Section with Regular Papers.
3. ANDREAS ZÜTTEL Andreas Borgschulte, Louis Schlapbach. *Hydrogen as a Future Energy Carrier*. Wiley-VCH, 2011. ISBN 978-3-527-62290-0.
4. KUMP, Lee R. Climate Change: The Last Great Global Warming. *j-SCI-AMER*. 2011-07, vol. 305, no. 1, pp. 56–61. ISSN 0036-8733 (print), 1946-7087 (electronic). ISSN 0036-8733 (print), 1946-7087 (electronic). Available from DOI: http://dx.doi.org/10.1038/scientificamerican0711-56.
5. KLEIN, Tamir; BADER, Martin K.-F.; LEUZINGER, Sebastian; MILDNER, Manuel; SCHLEPPI, Patrick; SIEGWOLF, Rolf T.W.; KÖRNER, Christian. Growth and carbon relations of mature Picea abies trees under 5 years of free-air CO2 enrichment. *Journal of Ecology*. 2016, vol. 104, no. 6, pp. 1720–1733. ISSN 1365-2745. Available from DOI: 10.1111/1365-2745.12621.
6. TEBIBEL, Hammou; LABED, Sifeddine. Performance results and analysis of self-regulated {PV} system in Algerian Sahara. *Renewable Energy*. 2013, vol. 60, pp. 691–700. ISSN 0960-1481. Available from DOI: http://dx.doi.org/10.1016/j.renene.2013.06.032.
7. WIKIPEDIA. *Sahara — Wikipedia, The Free Encyclopedia*. 2016. Available also from: https://en.wikipedia.org/w/index.php?title=Sahara&oldid=743800156. [Online; accessed 11-October-2016].
8. SAMUS, Tobias; LANG, Bastian; ROHN, Holger. Assessing the natural resource use and the resource efficiency potential of the Desertec concept. *Solar Energy*. 2013, vol. 87, pp. 176–183. ISSN 0038-092X. Available from DOI: http://dx.doi.org/10.1016/j.solener.2012.10.011.

9. LILLIESTAM, Johan; ELLENBECK, Saskia.
Energy security and renewable electricity trade—Will Desertec make Europe vulnerable to the "energy weapon"? *Energy Policy*.
2011, vol. 39, no. 6, pp. 3380–3391. ISSN 0301-4215.
Available from DOI: http://dx.doi.org/10.1016/j.enpol.2011.03.035.

10. SKUPINA, ČEZ. *Výroční zpráva 2013*. 2017. Available also from: http://www.cez.cz/edee/content/file/investori/vz-2013/2013-vyrocni-zprava.pdf. [Online; accessed 4-Januar-2017].

11. OECD/IAEA. *Uranium 2014*. OECD Publishing, 2014. ISBN 9789264223516.
Available from DOI: http://dx.doi.org/10.1787/uranium-2014-en.

12. POST, D.E. A review of recent developments in atomic processes for divertors and edge plasmas. *Journal of Nuclear Materials*. 1995, vol. 220, pp. 143–157. ISSN 0022-3115.
Available from DOI: http://dx.doi.org/10.1016/0022-3115(94)00453-6.

13. RYZHKOV, S. V. Current state, problems, and prospects of thermonuclear facilities based on the magneto-inertial confinement of hot plasma.
Bulletin of the Russian Academy of Sciences: Physics.
2014, vol. 78, no. 5, pp. 456–461.
Available from DOI: http://dx.doi.org/10.3103/S1062873814050281.

14. DENDY, R O; MCCLEMENTS, K G. Ion cyclotron emission from fusion-born ions in large tokamak plasmas: a brief review from JET and TFTR to ITER.
Plasma Physics and Controlled Fusion. 2015, vol. 57, no. 4, pp. 044002.
Available from DOI:
http://dx.doi.org/10.1088/0741-3335/57/4/044002.

15. ALLEN, Michael. Europe plans quantum technology flagship. *Physics World*.
2016, vol. 29, no. 6, pp. 8.
Available from DOI: http://dx.doi.org/10.1088/2058-7058/29/6/12.

16. WIKIPEDIA. *Renewable energy — Wikipedia, The Free Encyclopedia*. 2016.
Available also from: https://en.wikipedia.org/w/index.php?title=Renewable_energy&oldid=755800490.
[Online; accessed 20-December-2016].

17. WIKIPEDIA. *Heat of combustion — Wikipedia The Free Encyclopedia*. 2017.
Available also from: https://en.wikipedia.org/w/index.php?title=Heat_of_combustion&oldid=761389722. [Online; accessed 22-June-2014].

18. ČMELÍK, Milan; MACHONSKÝ, Lubor. *Tabulky pro fyziku*.
Liberec: Technická univerzita, 2001. ISBN 80-7083-553-2.

19. MIKULČÁK, Jiří. *Matematické, fyzikální a chemické tabulky pro střední školy*.
SPN, 1990. ISBN 80-04-24962-0.

20. STOLTEN, Detlef.
Hydrogen and fuel cells: fundamentals, technologies and applications.
Ed. by STOLTEN, Detlef. John Wiley & Sons, 2010.
ISBN 978-3-527-32711-9.

21. TEICHMANN, Daniel; ARLT, Wolfgang; WASSERSCHEID, Peter; FREYMANN, Raymond.
A future energy supply based on Liquid Organic Hydrogen Carriers (LOHC).
Energy Environ. Sci. 2011, vol. 4, pp. 2767–2773.
Available from DOI: 10.1039/C1EE01454D.

22. MELAINA, M. W.; ANTONIA, O.; PENEV, M. *Blending Hydrogen into Natural Gas Pipeline Networks: A Review of Key Issues.*
National Renewable Energy Laboratory, 2013-03.
Available from DOI: 10.2172/1068610.

23. BEDEL, Laurent; JUNKER, Michel.
Natural gas pipelines for hydrogen transportation.
16. World Hydrogen Energy Conference Lyon, (France). 2006-06.
Available also from: http://inis.iaea.org/Search/search.aspx?orig%7B%5C_%7Dq=RN:38090887.

24. VISWANATHAN, R.; HENRY, J. F.; TANZOSH, J.; STANKO, G.; SHINGLEDECKER, J.; VITALIS, B.; PURGERT, R. U.S. program on materials technology for ultra-supercritical coal power plants.
Journal of Materials Engineering and Performance.
2005, vol. 14, no. 3, pp. 281–292. ISSN 1544-1024.
Available from DOI: 10.1361/10599490524039.

25. CARMO, Marcelo; FRITZ, David L.; MERGEL, Jürgen; STOLTEN, Detlef.
A comprehensive review on {PEM} water electrolysis.
International Journal of Hydrogen Energy.
2013, vol. 38, no. 12, pp. 4901–4934. ISSN 0360-3199. Available from DOI: http://dx.doi.org/10.1016/j.ijhydene.2013.01.151.

26. SCHALENBACH, Maximilian; TJARKS, Geert; CARMO, Marcelo; LUEKE, Wiebke; MUELLER, Martin; STOLTEN, Detlef.
Acidic or Alkaline? Towards a New Perspective on the Efficiency of Water Electrolysis. *Journal of The Electrochemical Society.*
2016, vol. 163, no. 11, pp. F3197–F3208.
Available from DOI: 10.1149/2.0271611jes.

27. YILANCI, A.; DINCER, I.; OZTURK, H.K. A review on solar-hydrogen/fuel cell hybrid energy systems for stationary applications.
Progress in Energy and Combustion Science.
2009, vol. 35, no. 3, pp. 231–244. ISSN 0360-1285.
Available from DOI: http://dx.doi.org/10.1016/j.pecs.2008.07.004.

28. GROVE, W.R. On Voltaic Series and the Combination of Gases by Platinum.
London and Edinburgh Philosophical Magazine and Journal of Science.
1839, vol. 14, no. 3, pp. 127–130.

29. SCHÖNBEIN, C. F.
On the voltaic polarization of certain solid and fluid substances.
London and Edinburgh Philosophical Magazine and Journal of Science.
1839, vol. 14, no. 3, pp. 43–45.

30. BLOMEN, L.J.M.J.; MUGERWA, M.N. *Fuel Cell Systems.* Springer US, 1994. ISBN 9780306441585.
Available also from: https://books.google.cz/books?id=O0my-RESWYIC.

31. BLOMEN, L.J.M.J.; MUGERWA, M.N. *Fuel Cell Systems*. Springer US, 2013. ISBN 9781489924247.
Available also from: https://books.google.cz/books?id=s9QFCAAAQBAJ.

32. HOOGERS, G. *Fuel Cell Technology Handbook*. CRC Press, 2002. Handbook Series for Mechanical Engineering. ISBN 9781420041552.
Available also from: https://books.google.cz/books?id=%5C_IFmUIRHNH8C.

33. FCHEA. *Fuel Cell and Hydrogen Energy Association*. 2017.
Available also from: http://www.fchea.org/.
[Online; accessed 6-Januar-2017].

34. DWV. *German Hydrogen and Fuel Cell Association (DWV)*. 2017.
Available also from: http://www.dwv-info.de/.
[Online; accessed 6-Januar-2017].

35. NOW. *National Organisation Hydrogen and Fuel Cell Tenchnology*. 2017.
Available also from: www.now-gmbh.de/. [Online; accessed 6-Januar-2017].

36. SHARAF, Omar Z.; ORHAN, Mehmet F.
An overview of fuel cell technology: Fundamentals and applications.
Renewable and Sustainable Energy Reviews. 2014, vol. 32, pp. 810–853.
ISSN 1364-0321.
Available from DOI: http://dx.doi.org/10.1016/j.rser.2014.01.012.

37. KITCO. *Kitco Metals Inc.* 2016. Available also from: http://www.kitco.cz/.
[Online; accessed 6-August-2014].

38. STATISTA. *The Statistics Portal*. 2014. Available also from:
https://www.statista.com/statistics/273624/platinum-metal-reserves-by-country/. [Online; accessed 7-August-2014].

39. GITTLEMAN, C; WALDECKER, J; HIRANO, S; MEHALL, M.
Automotive fuel cell R&D needs. In: *DOE fuel cell pre-solicitation workshop. Department of Energy, Lakewood, Colorado*. 2010.

40. TRIHYBUS. *Triple Hydride Hydrogen Bus*. 2017.
Available also from: http://www.h2bus.cz/.
[Online; accessed 7-January-2017].

41. HONDA. *Clarity Fuel Cell*. 2017.
Available also from: http://automobiles.honda.com/fcx-clarity.
[Online; accessed 7-January-2017].

42. WANG, Guoping; ZHANG, Lei; ZHANG, Jiujun.
A review of electrode materials for electrochemical supercapacitors.
Chem. Soc. Rev. 2012, vol. 41, pp. 797–828.
Available from DOI: 10.1039/C1CS15060J.

43. WANG, Yun; CHEN, Ken S.; MISHLER, Jeffrey; CHO, Sung Chan; ADROHER, Xavier Cordobes. A review of polymer electrolyte membrane fuel cells: Technology, applications, and needs on fundamental research.
Applied Energy. 2011, vol. 88, no. 4, pp. 981–1007. ISSN 0306-2619.
Available from DOI:
http://dx.doi.org/10.1016/j.apenergy.2010.09.030.

44. GENCOGLU, Muhsin Tunay; URAL, Zehra.
Design of a {PEM} fuel cell system for residential application.
International Journal of Hydrogen Energy.
2009, vol. 34, no. 12, pp. 5242–5248. ISSN 0360-3199. Available from DOI:
http://dx.doi.org/10.1016/j.ijhydene.2008.09.038.
{UGHEK} 2008UGHEK 2008.

45. ATWATER, Terrill B.; CYGAN, Peter J.; LEUNG, Fee Chan. Man portable power needs of the 21st century: I. Applications for the dismounted soldier. II. Enhanced capabilities through the use of hybrid power sources.
Journal of Power Sources. 2000, vol. 91, no. 1, pp. 27–36. ISSN 0378-7753.
Available from DOI:
http://dx.doi.org/10.1016/S0378-7753(00)00484-5.

46. KORDESCH, K.V.; SIMADER, G.R.
Environmental impact of fuel cell technology. *Chemical Reviews*.
1995, vol. 95, no. 1, pp. 191–207. Available also from:
https://www.scopus.com/inward/record.uri?eid=2-s2.0-0000094780&partnerID=40&md5=4dd01aab2f439270f90b8ab6fc09729f.
cited By 181.

47. FUELCELLTODAY. *Fuel Cell Use within the US Military*. 2017. Available also from: http://www.fuelcelltoday.com/media/949133/av_11-03-30_fuel_cell_use_within_the_us_military.pdf.
[Online; accessed 7-January-2017].

48. PSOMA, Angela; SATTLER, Gunter.
Fuel cell systems for submarines: from the first idea to serial production.
Journal of Power Sources. 2002, vol. 106, no. 1–2, pp. 381–383.
ISSN 0378-7753. Available from DOI:
http://dx.doi.org/10.1016/S0378-7753(01)01044-8.
Proceedings of the Seventh Grove Fuel Cell Symposium.

49. DU, Xiaoze; CAO, Yannan; YANG, Lijun; YANG, Yongping.
A Characteristic Investigation Of A Combined System Of Solar Hydrogen Production And A Fuel Cell. *International Journal of Green Energy*.
2014, vol. 11, no. 9, pp. 918–935.
Available from DOI: 10.1080/15435075.2013.833513.

50. HOLTON, Oliver T.; STEVENSON, Joseph W.
The Role of Platinum in Proton Exchange Membrane Fuel Cells.
Platinum Metals Review. 2013, vol. 57, no. 4, pp. 259–271. ISSN 0032-1400.
Available from DOI: doi:10.1595/147106713X671222.

51. JAKSIC, Jelena M.; RISTIC, Nikola M.; KRSTAJIC, Nedeljko V.; JAKSIC, Milan M. Electrocatalysis for hydrogen electrode reactions in the light of fermi dynamics and structural bonding FACTORS—I. individual electrocatalytic properties of transition metals.
International Journal of Hydrogen Energy.
1998, vol. 23, no. 12, pp. 1121–1156. ISSN 0360-3199. Available from DOI:
http://dx.doi.org/10.1016/S0360-3199(98)00014-7.

52. NØRSKOV, J. K.; ROSSMEISL, J.; LOGADOTTIR, A.; LINDQVIST, L.; KITCHIN, J. R.; BLIGAARD, T.; JÓNSSON, H.
Origin of the Overpotential for Oxygen Reduction at a Fuel-Cell Cathode. *The Journal of Physical Chemistry B*.
2004, vol. 108, no. 46, pp. 17886–17892.
Available from DOI: 10.1021/jp047349j.

53. DEBE, Mark K.
Electrocatalyst approaches and challenges for automotive fuel cells. *Nature*.
2012-06, vol. 486, no. 7401, pp. 43–51. ISSN 0028-0836.
Available from DOI: 10.1038/nature11115.

54. ZHANG, Zhonghua; LIU, Jie; GU, Junjie; SU, Liang; CHENG, Lifeng.
An overview of metal oxide materials as electrocatalysts and supports for polymer electrolyte fuel cells. *Energy Environ. Sci.*
2014, vol. 7, pp. 2535–2558. Available from DOI: 10.1039/C3EE43886D.

55. GARCIA-MARTINEZ, J.; WANG, Z.L.
Nanotechnology for the Energy Challenge. Wiley, 2013.
ISBN 9783527665129.
Available also from: https://books.google.cz/books?id=T3yXXTTXnzYC.

56. LITSTER, S; MCLEAN, G. PEM fuel cell electrodes.
Journal of Power Sources. 2004, vol. 130, no. 1, pp. 61–76.

57. DEVER, Dennis O; CAIRNCROSS, Richard A; ELABD, Yossef A. Nanofiber Cathode Catalyst Layer Model for a Proton Exchange Membrane Fuel Cell.
Journal of Fuel Cell Science and Technology.
2014, vol. 11, no. 4, pp. 041007.

58. ARICO, Antonino Salvatore; BRUCE, Peter; SCROSATI, Bruno; TARASCON, Jean-Marie; VAN SCHALKWIJK, Walter. Nanostructured materials for advanced energy conversion and storage devices.
Nature materials. 2005, vol. 4, no. 5, pp. 366–377.

59. SRINIVASAN, Supramaniam; MOSDALE, Renaut; STEVENS, Philippe; YANG, Christopher. Fuel cells: reaching the era of clean and efficient power generation in the twenty-first century.
Annual Review of Energy and the Environment.
1999, vol. 24, no. 1, pp. 281–328.

60. DEBE, M. K. *Handbook of Fuel Cells: Fundamentals, Technology, Applications, 3 Volume Set*. Wiley, 2003. ISBN 9780471499268.
Available also from: https://books.google.cz/books?id=0E1SvgAACAAJ.

61. ARICO, AS; SRINIVASAN, S; ANTONUCCI, V1.
DMFCs: from fundamental aspects to technology development. *Fuel cells*.
2001, vol. 1, no. 2, pp. 133–161.

62. SCHMIDT, TJ; NOESKE, M; GASTEIGER, Hubert A; BEHM, RJ; BRITZ, P; BRIJOUX, W; BÖNNEMANN, H.
Electrocatalytic activity of PtRu alloy colloids for CO and CO/H2 electrooxidation: stripping voltammetry and rotating disk measurements.
Langmuir. 1997, vol. 13, no. 10, pp. 2591–2595.

63. MEHTA, Viral; COOPER, Joyce Smith.
Review and analysis of {PEM} fuel cell design and manufacturing.
Journal of Power Sources. 2003, vol. 114, no. 1, pp. 32–53. ISSN 0378-7753.
Available from DOI:
http://dx.doi.org/10.1016/S0378-7753(02)00542-6.

64. GASTEIGER, Hubert A.; MARKOVIC, Nenad; JR., Philip N. Ross;
CAIRNS, Elton J. Methanol electrooxidation on well-characterized
platinum-ruthenium bulk alloys. *The Journal of Physical Chemistry*.
1993, vol. 97, no. 46, pp. 12020–12029.
Available from DOI: 10.1021/j100148a030.

65. PARSONS, R; VANDERNOOT, T. The oxidation of small organic molecules: a
survey of recent fuel cell related research.
Journal of electroanalytical chemistry and interfacial electrochemistry.
1988, vol. 257, no. 1, pp. 9–45.

66. LEGER, J-M; LAMY, C. The Direct Oxidation of Methanol at Platinum Based
Catalytic Electrodes: What is New Since Ten Years?
Berichte der Bunsengesellschaft für physikalische Chemie.
1990, vol. 94, no. 9, pp. 1021–1025.

67. HAMNETT, A; WEEKS, SA; KENNEDY, BJ; TROUGHTON, G;
CHRISTENSEN, PA. Long-Term Poisoning of Methanol Anodes.
Berichte der Bunsengesellschaft für physikalische Chemie.
1990, vol. 94, no. 9, pp. 1014–1020.

68. METIKOS-HUKOVIC, M; BABIC, R; PILJAC, Y.
Kinetics and Electrocatalysis of Methanol Oxidation on Electrodeposited Pt
and Pt˜ 7˜ 0Ru˜ 3˜ 0 Catalysts.
Journal of New Materials for Electrochemical Systems.
2004, vol. 7, no. 3, pp. 179–190.

69. HOBBS, B. S.; TSEUNG, A. C. C.
High Performance, Platinum Activated Tungsten Oxide Fuel Cell Electrodes.
Nature. 1969-05, vol. 222, no. 5193, pp. 556–558.
Available from DOI: 10.1038/222556a0.

70. WAKI, Keiko; MATSUBARA, Kenji; KE, Ke; YAMAZAKI, Yohtaro.
Self-Organized Pt/ SnO2 Electrocatalysts on Multiwalled Carbon
Nanotubes. *Electrochemical and Solid-State Letters*.
2005, vol. 8, no. 10, pp. A489–A491.

71. MATSUI, Toshiaki; FUJIWARA, Katsuhiko; OKANISHI, Takeoh;
KIKUCHI, Ryuji; TAKEGUCHI, Tatsuya; EGUCHI, Koichi.
Electrochemical oxidation of CO over tin oxide supported platinum
catalysts. *Journal of power sources*. 2006, vol. 155, no. 2, pp. 152–156.

72. SKORODUMOVA, N. V.; SIMAK, S. I.; LUNDQVIST, B. I.;
ABRIKOSOV, I. A.; JOHANSSON, B.
Quantum Origin of the Oxygen Storage Capability of Ceria. *Phys. Rev. Lett.*
2002-09, vol. 89, pp. 166601.
Available from DOI: 10.1103/PhysRevLett.89.166601.

73. VAYSSILOV, Georgi N. et al. Support nanostructure boosts oxygen transfer to catalytically active platinum nanoparticles. *NATURE MATERIALS*. 2011-04, vol. 10, no. 4, pp. 310–315. ISSN 1476-1122. Available from DOI: 10.1038/NMAT2976.

74. STAMENKOVIC, Vojislav R.; MUN, Bongjin Simon; ARENZ, Matthias; MAYRHOFER, Karl J. J.; LUCAS, Christopher A.; WANG, Guofeng; ROSS, Philip N.; MARKOVIC, Nenad M. Trends in electrocatalysis on extended and nanoscale Pt-bimetallic alloy surfaces. *Nat Mater*. 2007-03, vol. 6, no. 3, pp. 241–247. ISSN 1476-1122. Available from DOI: 10.1038/nmat1840.

75. GASTEIGER, Hubert A.; KOCHA, Shyam S.; SOMPALLI, Bhaskar; WAGNER, Frederick T. Activity benchmarks and requirements for Pt, Pt-alloy, and non-Pt oxygen reduction catalysts for {PEMFCs}. *Applied Catalysis B: Environmental*. 2005, vol. 56, no. 1–2, pp. 9–35. ISSN 0926-3373. Available from DOI: http://dx.doi.org/10.1016/j.apcatb.2004.06.021. Fuel processing and {PEM} Fuel Cells: advanced cata;ysts, adsorbents and electrocatalysts.

76. KOH, Shirlaine; HAHN, Nathan; YU, Chengfei; STRASSER, Peter. Effects of composition and annealing conditions on catalytic activities of dealloyed Pt–Cu nanoparticle electrocatalysts for PEMFC. *Journal of The Electrochemical Society*. 2008, vol. 155, no. 12, pp. B1281–B1288.

77. FREUND, Andreas; LANG, Jutta; LEHMANN, Thomas; STARZ, Karl Anton. Improved Pt alloy catalysts for fuel cells. *Catalysis Today*. 1996, vol. 27, no. 1, pp. 279–283.

78. MUKERJEE, Sanjeev; SRINIVASAN, Supramaniam; SORIAGA, Manuel P; MCBREEN, James. Role of structural and electronic properties of Pt and Pt alloys on electrocatalysis of oxygen reduction An in situ XANES and EXAFS investigation. *Journal of the Electrochemical Society*. 1995, vol. 142, no. 5, pp. 1409–1422.

79. TAN, XueHai; PRABHUDEV, Sagar; KOHANDEHGHAN, Alireza; KARPUZOV, Dimitre; BOTTON, Gianluigi A.; MITLIN, David. Pt–Au–Co Alloy Electrocatalysts Demonstrating Enhanced Activity and Durability toward the Oxygen Reduction Reaction. *ACS Catalysis*. 2015, vol. 5, no. 3, pp. 1513–1524. Available from DOI: 10.1021/cs501710b.

80. ERLEBACHER, Jonah; SNYDER, Joshua. Dealloyed nanoporous metals for PEM fuel cell catalysis. *ECS Transactions*. 2009, vol. 25, no. 1, pp. 603–612.

81. ERLEBACHER, Jonah; AZIZ, Michael J; KARMA, Alain; DIMITROV, Nikolay; SIERADZKI, Karl. Evolution of nanoporosity in dealloying. *Nature*. 2001, vol. 410, no. 6827, pp. 450–453.

82. CHEN, Shuo; GASTEIGER, Hubert A.; HAYAKAWA, Katsuichiro; TADA, Tomoyuki; SHAO-HORN, Yang. Platinum-Alloy Cathode Catalyst Degradation in Proton Exchange Membrane Fuel Cells: Nanometer-Scale Compositional and Morphological Changes. *Journal of The Electrochemical Society*. 2010, vol. 157, no. 1, pp. A82–A97. Available from DOI: 10.1149/1.3258275.

83. DUBAU, Laetitia; NELAYAH, Jaysen; MOLDOVAN, Simona; ERSEN, Ovidiu; BORDET, Pierre; DRNEC, Jakub; ASSET, Tristan; CHATTOT, Raphaël; MAILLARD, Frédéric. Defects do Catalysis: CO Monolayer Oxidation and Oxygen Reduction Reaction on Hollow PtNi/C Nanoparticles. *ACS Catalysis*. 2016, vol. 6, no. 7, pp. 4673–4684. Available from DOI: 10.1021/acscatal.6b01106.

84. CHATTOT, Raphaël; ASSET, Tristan; BORDET, Pierre; DRNEC, Jakub; DUBAU, Laetitia; MAILLARD, Frédéric. Beyond Strain and Ligand Effects: Microstrain-Induced Enhancement of the Oxygen Reduction Reaction Kinetics on Various PtNi/C Nanostructures. *ACS Catalysis*. 0000, vol. 0, no. 0, pp. 398–408. Available from DOI: 10.1021/acscatal.6b02356.

85. SEROV, Alexey; KWAK, Chan. Review of non-platinum anode catalysts for {DMFC} and {PEMFC} application. *Applied Catalysis B: Environmental*. 2009, vol. 90, no. 3–4, pp. 313–320. ISSN 0926-3373. Available from DOI: http://dx.doi.org/10.1016/j.apcatb.2009.03.030.

86. XING, Tan; ZHENG, Yao; LI, Lu Hua; COWIE, Bruce CC; GUNZELMANN, Daniel; QIAO, Shi Zhang; HUANG, Shaoming; CHEN, Ying. Observation of active sites for oxygen reduction reaction on nitrogen-doped multilayer graphene. *ACS nano*. 2014, vol. 8, no. 7, pp. 6856–6862.

87. WANG, Yichen; JIANG, Xiue. Facile preparation of porous carbon nanosheets without template and their excellent electrocatalytic property. *ACS applied materials & interfaces*. 2013, vol. 5, no. 22, pp. 11597–11602.

88. SNYDER, Joshua; DANILOVIC, Nemanja; PAULIKAS, Arvydas P; TRIPKOVIC, Dusan; STRMCNIK, Dusan; MARKOVIC, Nenad M; STAMENKOVIC, Vojislav R. Thin film approach to single crystalline electrochemistry. *The Journal of Physical Chemistry C*. 2013, vol. 117, no. 45, pp. 23790–23796.

89. ZHU, Guo-Zhen; PRABHUDEV, Sagar; YANG, Jie; GABARDO, Christine M; BOTTON, Gianluigi A; SOLEYMANI, Leyla. In Situ Liquid Cell TEM Study of Morphological Evolution and Degradation of Pt–Fe Nanocatalysts During Potential Cycling. *The Journal of Physical Chemistry C*. 2014, vol. 118, no. 38, pp. 22111–22119.

90. SU, Liang; JIA, Wenzhao; LI, Chang-Ming; LEI, Yu. Mechanisms for Enhanced Performance of Platinum-Based Electrocatalysts in Proton Exchange Membrane Fuel Cells. *ChemSusChem*. 2014, vol. 7, no. 2, pp. 361–378.

91. MOROZAN, Adina; JOUSSELME, Bruno; PALACIN, Serge.
Low-platinum and platinum-free catalysts for the oxygen reduction reaction at fuel cell cathodes. *Energy Environ. Sci.* 2011, vol. 4, pp. 1238–1254. Available from DOI: 10.1039/C0EE00601G.

92. CHRISTIAN, Joel B.; SMITH, Sean P.E.; WHITTINGHAM, M. Stanley; ABRUÑA, Héctor D.
Tungsten based electrocatalyst for fuel cell applications. *Electrochemistry Communications*. 2007, vol. 9, no. 8, pp. 2128–2132. ISSN 1388-2481. Available from DOI: http://dx.doi.org/10.1016/j.elecom.2007.06.001.

93. IZHAR, Shamsul; NAGAI, Masatoshi. Cobalt molybdenum carbides as anode electrocatalyst for proton exchange membrane fuel cell. *Journal of Power Sources*. 2008, vol. 182, no. 1, pp. 52–60. ISSN 0378-7753. Available from DOI: http://dx.doi.org/10.1016/j.jpowsour.2008.03.084.

94. NAGAI, Masatoshi; YOSHIDA, Michiko; TOMINAGA, Hiroyuki.
Tungsten and nickel tungsten carbides as anode electrocatalysts. *Electrochimica Acta*. 2007, vol. 52, no. 17, pp. 5430–5436. ISSN 0013-4686. Available from DOI: http://dx.doi.org/10.1016/j.electacta.2007.02.065.

95. IZHAR, Shamsul; YOSHIDA, Michiko; NAGAI, Masatoshi.
Characterization and performances of cobalt–tungsten and molybdenum–tungsten carbides as anode catalyst for {PEFC}. *Electrochimica Acta*. 2009, vol. 54, no. 4, pp. 1255–1262. ISSN 0013-4686. Available from DOI: http://dx.doi.org/10.1016/j.electacta.2008.08.049.

96. HIGGINS, Drew; ZAMANI, Pouyan; YU, Aiping; CHEN, Zhongwei.
The application of graphene and its composites in oxygen reduction electrocatalysis: a perspective and review of recent progress. *Energy Environ. Sci.* 2016, vol. 9, pp. 357–390. Available from DOI: 10.1039/C5EE02474A.

97. ZENG, L.; ZHAO, T.S.; AN, L.; ZHAO, G.; YAN, X.H.; JUNG, C.Y.
Graphene-supported platinum catalyst prepared with ionomer as surfactant for anion exchange membrane fuel cells. *Journal of Power Sources*. 2015, vol. 275, pp. 506–515. ISSN 0378-7753. Available from DOI: http://dx.doi.org/10.1016/j.jpowsour.2014.11.021.

98. JIANG, Yuanyuan; LU, Yizhong; LV, Xiangyu; HAN, Dongxue; ZHANG, Qixian; NIU, Li; CHEN, Wei.
Enhanced Catalytic Performance of Pt-Free Iron Phthalocyanine by Graphene Support for Efficient Oxygen Reduction Reaction. *ACS Catalysis*. 2013, vol. 3, no. 6, pp. 1263–1271. Available from DOI: 10.1021/cs4001927.

99. WANG, Yu; YUAN, Hao; LI, Yafei; CHEN, Zhongfang.
Two-dimensional iron-phthalocyanine (Fe-Pc) monolayer as a promising single-atom-catalyst for oxygen reduction reaction: a computational study. *Nanoscale*. 2015, vol. 7, pp. 11633–11641. Available from DOI: 10.1039/C5NR00302D.

100. (FIRM), EG G Services; U.S., National Energy Technology Laboratory.
Fuel cell handbook (electronic resource), EG G Technical Services, Inc.
U.S. Dept. of Energy, Office of Fossil Energy, National Energy Technology Laboratory Morgantown, WV, 2004.
Available also from: http://purl.access.gpo.gov/GPO/LPS115918.

101. BRANDON, N.P; BRETT, D.J.
Engineering porous materials for fuel cell applications.
Philosophical Transactions of the Royal Society of London A: Mathematical, Physical and Engineering Sciences. 2006, vol. 364, no. 1838, pp. 147–159.
ISSN 1364-503X. Available from DOI: 10.1098/rsta.2005.1684.

102. JANG, Seung Soon; MOLINERO, Valeria; CAGIN, Tahir; GODDARD, William A. Nanophase-Segregation and Transport in Nafion 117 from Molecular Dynamics Simulations: Effect of Monomeric Sequence.
The Journal of Physical Chemistry B. 2004, vol. 108, no. 10, pp. 3149–3157.
Available from DOI: 10.1021/jp036842c.

103. MAURITZ, Kenneth A.; MOORE, Robert B. State of Understanding of Nafion.
Chemical Reviews. 2004, vol. 104, no. 10, pp. 4535–4586.
Available from DOI: 10.1021/cr0207123. PMID: 15669162.

104. WICKE, Eigen; EIGEN, M; ACKERMANN, Th.
über den Zustand des Protons (Hydroniumions) in wässriger Lösung.
Zeitschrift für physikalische Chemie. 1954, vol. 1, pp. 340–364.

105. LUO, Zhiping; CHANG, Zhangyong; ZHANG, Yuxia; LIU, Zhen; LI, Jing. Electro-osmotic drag coefficient and proton conductivity in Nafion® membrane for PEMFC. *International Journal of Hydrogen Energy*.
2010, vol. 35, no. 7, pp. 3120–3124. ISSN 0360-3199. Available from DOI: http://dx.doi.org/10.1016/j.ijhydene.2009.09.013. 2008 International Hydrogen Forum (HyForum2008)2008 International Hydrogen.

106. HSU, William Y; GIERKE, Timothy D.
Ion transport and clustering in Nafion perfluorinated membranes.
Journal of Membrane Science. 1983, vol. 13, no. 3, pp. 307–326.

107. KREUER, K.D. On the development of proton conducting polymer membranes for hydrogen and methanol fuel cells. *Journal of Membrane Science*.
2001, vol. 185, no. 1, pp. 29–39. ISSN 0376-7388. Available from DOI: http://dx.doi.org/10.1016/S0376-7388(00)00632-3.
Membrances in Fuel Cells.

108. LARMINIE, James; DICKS, Andrew; MCDONALD, Maurice S.
Fuel cell systems explained. J. Wiley Chichester, UK, 2003.

109. KREUER, Klaus-Dieter. Proton conductivity: materials and applications.
Chemistry of Materials. 1996, vol. 8, no. 3, pp. 610–641.

110. KREUER, Klaus-Dieter; RABENAU, Albrecht; WEPPNER, Werner.
Vehicle mechanism, a new model for the interpretation of the conductivity of fast proton conductors.
Angewandte Chemie International Edition in English.
1982, vol. 21, no. 3, pp. 208–209.

111. XIE, Jing; BAN, Shuai; LIU, Bei; ZHOU, Hongjun.
A molecular simulation study of chemical degradation and mechanical deformation of hydrated Nafion membranes. *Applied Surface Science*. 2016, vol. 362, pp. 441–447. ISSN 0169-4332.
Available from DOI: http://dx.doi.org/10.1016/j.apsusc.2015.11.144.

112. MOSHTARIKHAH, S.; OPPERS, N. A. W.; GROOT, M. T. de; KEURENTJES, J. T. F.; SCHOUTEN, J. C.; SCHAAF, J. van der.
Nernst–Planck modeling of multicomponent ion transport in a Nafion membrane at high current density. *Journal of Applied Electrochemistry*. 2017, vol. 47, no. 1, pp. 51–62. ISSN 1572-8838.
Available from DOI: 10.1007/s10800-016-1017-2.

113. KIM, Dong Kyu; CHOI, Eun Jung; SONG, Han Ho; KIM, Min Soo.
Experimental and numerical study on the water transport behavior through Nafion 117 for polymer electrolyte membrane fuel cell.
Journal of Membrane Science. 2016, vol. 497, pp. 194–208. ISSN 0376-7388.
Available from DOI: http://dx.doi.org/10.1016/j.memsci.2015.09.053.

114. DELUCA, Nicholas W; ELABD, Yossef A.
Polymer electrolyte membranes for the direct methanol fuel cell: a review.
Journal of Polymer Science Part B: Polymer Physics.
2006, vol. 44, no. 16, pp. 2201–2225.

115. TENG, Hongxiang.
Overview of the Development of the Fluoropolymer Industry.
Applied Sciences. 2012-05, vol. 2, no. 4, pp. 496–512. ISSN 2076-3417.
Available from DOI: 10.3390/app2020496.

116. COMPANY, SGL Group – The Carbon. *SIGRACET - gas diffusion layer*. 2016.
Available also from:
http://www.sglgroup.com/cms/_common/downloads/products/product-groups/su/fuel-cell-components/White-Paper-SIGRACET-GDL-for-Fuel-Cells.pdf. [Online; accessed 29-August-2016].

117. YUAN, Xiao-Zi Riny; SONG, Chaojie; WANG, Haijiang; ZHANG, Jiujun.
Electrochemical impedance spectroscopy in PEM fuel cells: fundamentals and applications. Springer Science & Business Media, 2009.

118. CELL, FCHEA Fuel; APPLICATIONS, Hydrogen Energy.
USFCC Single Cell Test Protocol. 2016.
Available also from: http://www.members.fchea.org/.
[Online; accessed 28-September-2016].

119. FIALA, Roman.
Investigation of new anode materials for methanol polymer fuel cells. 2010.
M.S. thesis. Charles University.

120. GROUP, Surface Physics. *Fuel Cell*. 2017. Available also from:
http://physics.mff.cuni.cz/kfpp/povrchy/method/fc.
[Online; accessed 7-May-2017].

121. WASA, K.; KANNO, I.; KOTERA, H.
Handbook of Sputter Deposition Technology: Fundamentals and Applications for Functional Thin Films, Nano-materials and MEMS.
William Andrew, 2012. ISBN 9781437734836.
Available also from: https://books.google.cz/books?id=6TYMTZdyWO4C.

122. DUBAU, Martin. *Preparation and Characterization of Porous Cerium Oxide/Carbon Bilayers on Silion Substrates*. 2016.
Available also from: https://is.cuni.cz/webapps/zzp/detail/107965.
Master's thesis.

123. MATOLIN, V.; FIALA, R.; KHALAKHAN, I.; LAVKOVA, J.; VACLAVU, M.; VOROKHTA, M.
Nanoporous Ptn+–CeOx catalyst films grown on carbon substrates.
Int. J. Nanotechnol. 2012, vol. 9, no. 8/9, pp. 680–694. ISSN 1475-7435.
Available from DOI: 10.1504/IJNT.2012.046748.

124. FIALA, R.; KHALAKHAN, I.; MATOLINOVA, I.; VACLAVU, M.; VOROKHTA, M.; SOFER, Z.; HUBER, S.; POTIN, V.; MATOLIN, V.
PtCeO2 Coating of Carbon Nanotubes Grown on Anode Gas Diffusion Layer of the Polymer Electrolyte Membrane Fuel Cell.
Journal of Nanoscience and Nanotechnology.
2011, vol. 11, no. 6, pp. 5062–5067. ISSN 1533-4880.
Available from DOI: doi:10.1166/jnn.2011.4128.

125. MATOLIN, V; FIALA, R; KHALAKHAN, I; LAVKOVA, J; VACLAVU, M; VOROKHTA, M.
Nanoporous Ptn+–CeOx catalyst films grown on carbon substrates.
International Journal of Nanotechnology. 2012, vol. 9, no. 8-9, pp. 680–694.

126. MATOLIN, V. et al. Platinum-Doped CeO2 Thin Film Catalysts Prepared by Magnetron Sputtering. *Langmuir*. 2010, vol. 26, no. 15, pp. 12824–12831.
Available from DOI: 10.1021/la100399t. PMID: 20608706.

127. LAGOWSKI, J.J. *Chemistry: foundations and applications*.
Macmillan Reference USA, 2004. Chemistry: Foundations and Applications.
ISBN 9780028657240.
Available also from: https://books.google.cz/books?id=QT0pAAAAYAAJ.

128. BIRSS, V.I.; CHANG, M.; SEGAL, J. Platinum oxide film formation—reduction: an in-situ mass measurement study.
Journal of Electroanalytical Chemistry. 1993, vol. 355, no. 1, pp. 181–191.
ISSN 1572-6657.
Available from DOI: http://dx.doi.org/10.1016/0022-0728(93)80361-K.
An International Journal Devoted to all Aspects of Electrode Kinetics, Interfacial Structure, Properties of Electrolytes, Colloid and Biological Electrochemistry.

129. WAGNER, N.; BRÜMMER, O.
XPS-study of the interaction of air-oxygen with platinum surfaces.
Kristall und Technik. 1978, vol. 13, no. 12, pp. K71–K73. ISSN 1521-4079.
Available from DOI: 10.1002/crat.19780131223.

130. ELETTRA.EU. *Atomic Calculation of Photoionization Cross-Sections and Asymmetry Parameters*. 2017. Available also from: https://vuo.elettra.eu/services/elements/WebElements.html. [Online; accessed 26-May-2017].

131. YEH, J.J.; LINDAU, I. Atomic subshell photoionization cross sections and asymmetry parameters: 1<Z<103. *Atomic Data and Nuclear Data Tables*. 1985, vol. 32, no. 1, pp. 1–155. ISSN 0092-640X. Available from DOI: http://dx.doi.org/10.1016/0092-640X(85)90016-6.

132. VOORHEES, V.; ADAMS, Roger. THE USE OF THE OXIDES OF PLATINUM FOR THE CATALYTIC REDUCTION OF ORGANIC COMPOUNDS. I. *Journal of the American Chemical Society*. 1922, vol. 44, no. 6, pp. 1397–1405. Available from DOI: 10.1021/ja01427a021.

133. FIALA, Roman et al. High efficiency of Pt 2+-CeO 2 novel thin film catalyst as anode for proton exchange membrane fuel cells. *Applied Catalysis B: Environmental*. 2016, vol. 197, pp. 262–270.

134. MATOLINOVA, I; FIALA, R; KHALAKHAN, I; VOROKHTA, M; SOFER, Z; YOSHIKAWA, H; KOBAYASHI, K; MATOLIN, V. Synchrotron radiation photoelectron spectroscopy study of metal-oxide thin film catalysts: Pt-CeO2 coated CNTs. *Applied Surface Science*. 2012, vol. 258, no. 6, pp. 2161–2164.

135. FIALA, R; VACLAVU, M; REDNYK, A; KHALAKHAN, I; VOROKHTA, M; LAVKOVA, J; POTIN, V; MATOLINOVA, I; MATOLIN, V. Pt–CeO x thin film catalysts for PEMFC. *Catalysis Today*. 2015, vol. 240, pp. 236–241.

136. BRUIX, Albert et al. Maximum Noble-Metal Efficiency in Catalytic Materials: Atomically Dispersed Surface Platinum. *Angewandte Chemie International Edition*. 2014, vol. 53, no. 39, pp. 10525–10530.

137. CHUNG, Chen-Chung; CHEN, Chiun-Hsun; WENG, Der-Cheng; YAN, Yi-Yie; LIN, Hsiang-Hui, et al. Investigation of cell operation conditions for CO tolerance improvement of PEMFC. *Journal of the Chinese Society of Mechanical Engineers*. 2007, vol. 28, no. 6, pp. 563–569.

138. SUNG, Lung-Yu; HWANG, Bing-Joe; HSUEH, Kan-Lin; TSAU, Fang-Hei. Effects of anode air bleeding on the performance of CO-poisoned proton-exchange membrane fuel cells. *Journal of Power Sources*. 2010, vol. 195, no. 6, pp. 1630–1639.

139. MARKOVIĆ, NM; ROSS, Philip N. Surface science studies of model fuel cell electrocatalysts. *Surface Science Reports*. 2002, vol. 45, no. 4, pp. 117–229.

140. GÓMEZ, Roberto; ORTS, José M; ÁLVAREZ-RUIZ, Bernabé; FELIU, Juan M.
Effect of temperature on hydrogen adsorption on Pt (111), Pt (110), and Pt (100) electrodes in 0.1 M HClO4. *The Journal of Physical Chemistry B*. 2004, vol. 108, no. 1, pp. 228–238.

141. WANG, JX; MARKOVIC, NM; ADZIC, RR.
Kinetic analysis of oxygen reduction on Pt (111) in acid solutions: intrinsic kinetic parameters and anion adsorption effects.
The Journal of Physical Chemistry B. 2004, vol. 108, no. 13, pp. 4127–4133.

142. MURTHI, Vivek S; URIAN, R Craig; MUKERJEE, Sanjeev.
Oxygen reduction kinetics in low and medium temperature acid environment: correlation of water activation and surface properties in supported Pt and Pt alloy electrocatalysts.
The Journal of Physical Chemistry B.
2004, vol. 108, no. 30, pp. 11011–11023.

143. QILE, Geer.
Platinum oxide reduction kinetics on polycrystalline platinum electrodes.
2016. PhD thesis. University of Victoria.

144. KOH, Shirlaine; TONEY, Michael F.; STRASSER, Peter.
Activity–stability relationships of ordered and disordered alloy phases of Pt3Co electrocatalysts for the oxygen reduction reaction (ORR).
Electrochimica Acta. 2007, vol. 52, no. 8, pp. 2765–2774. ISSN 0013-4686.
Available from DOI:
https://doi.org/10.1016/j.electacta.2006.08.039.

145. JANG, Ji-Hoon; KIM, Juyeong; LEE, Yang-Hee; KIM, In Young;
PARK, Min-Ho; YANG, Cheol-Woong; HWANG, Seong-Ju;
KWON, Young-Uk.
One-pot synthesis of core-shell-like Pt3Co nanoparticle electrocatalyst with Pt-enriched surface for oxygen reduction reaction in fuel cells.
Energy Environ. Sci. 2011, vol. 4, pp. 4947–4953.
Available from DOI: 10.1039/C1EE01825F.

146. STASSI, A.; GATTO, I.; MONFORTE, G.; BAGLIO, V.; PASSALACQUA, E.; ANTONUCCI, V.; ARICÒ, A.S. The effect of thermal treatment on structure and surface composition of PtCo electro-catalysts for application in {PEMFCs} operating under automotive conditions.
Journal of Power Sources. 2012, vol. 208, pp. 35–45. ISSN 0378-7753.
Available from DOI: https://doi.org/10.1016/j.jpowsour.2012.02.014.

147. CHEN, Shuo; SHENG, Wenchao; YABUUCHI, Naoaki; FERREIRA, Paulo J.; ALLARD, Lawrence F.; SHAO-HORN, Yang.
Origin of Oxygen Reduction Reaction Activity on “Pt3Co” Nanoparticles: Atomically Resolved Chemical Compositions and Structures.
The Journal of Physical Chemistry C. 2009, vol. 113, no. 3, pp. 1109–1125.
Available from DOI: 10.1021/jp807143e.

148. MATOLIN, Vladimir et al.
Pt and Sn doped sputtered CeO2 electrodes for fuel cell applications.
Fuel cells. 2010, vol. 10, no. 1, pp. 139–144.

149. MOULDER, J.F.; STICKLE, W.F.; SOBOL, P.E.; BOMBEN, K.D.
Hanbook of X-Ray Photoelectron Spectrospcopy.
Perkin-Elmer Corporation, 1992. ISBN 0-9627026-2-5.

150. PETITTO, Sarah C; MARSH, Erin M; CARSON, Gregory A; LANGELL, Marjorie A. Cobalt oxide surface chemistry: the interaction of CoO (100), Co 3 O 4 (110) and Co 3 O 4 (111) with oxygen and water. *Journal of Molecular Catalysis A: Chemical*. 2008, vol. 281, no. 1, pp. 49–58.

151. CHUANG, TJ; BRUNDLE, CR; RICE, DW. Interpretation of the x-ray photoemission spectra of cobalt oxides and cobalt oxide surfaces. *Surface Science*. 1976, vol. 59, no. 2, pp. 413–429.

152. LEE, YS; RHEE, JY; WHANG, CN; LEE, YP. Electronic structure of Co-Pt alloys: X-ray spectroscopy and density-functional calculations. *Physical Review B*. 2003, vol. 68, no. 23, pp. 235111.

153. FIALA, R.; VACLAVU, M.; REDNYK, A.; KHALAKHAN, I.; VOROKHTA, M.; LAVKOVA, J.; POTIN, V.; MATOLINOVA, I.; MATOLIN, V. Pt-CeOx thin film catalysts for PEMFC. *CATALYSIS TODAY*. 2015-02, vol. 240, no. B, pp. 236–241. ISSN 0920-5861. Available from DOI: 10.1016/j.cattod.2014.03.069.

154. MATOLIN, V; CABALA, M; CHAB, V; MATOLINOVA, I; PRINCE, KC; ŠKODA, M; SUTARA, F; SKALA, T; VELTRUSKA, K. A resonant photoelectron spectroscopy study of Sn (Ox) doped CeO2 catalysts. *Surface and Interface Analysis*. 2008, vol. 40, no. 3-4, pp. 225–230.

155. SKALA, Tomas; SUTARA, Frantisek; PRINCE, Kevin C.; MATOLIN, Vladimír. Cerium oxide stoichiometry alteration via Sn deposition: Influence of temperature. *Journal of Electron Spectroscopy and Related Phenomena*. 2009, vol. 169, no. 1, pp. 20–25. ISSN 0368-2048. Available from DOI: https://doi.org/10.1016/j.elspec.2008.10.003.

156. MATOLIN, Vladimir et al. Pt and Sn doped sputtered CeO2 electrodes for fuel cell applications. *Fuel cells*. 2010, vol. 10, no. 1, pp. 139–144.

157. XIA, Weiwei; WANG, Haibo; ZENG, Xianghua; HAN, Jie; ZHU, Jun; ZHOU, Min; WU, Shudong. High-efficiency photocatalytic activity of type II SnO/Sn3O4 heterostructures via interfacial charge transfer. *CrystEngComm*. 2014, vol. 16, pp. 6841–6847. Available from DOI: 10.1039/C4CE00884G.

158. SLADKEVICH, S et al. Peroxide induced tin oxide coating of graphene oxide at room temperature and its application for lithium ion batteries. *Nanotechnology*. 2012, vol. 23, no. 48, pp. 485601. Available also from: http://stacks.iop.org/0957-4484/23/i=48/a=485601.

159. TANG, Xiaolan; ZHANG, Baocai; LI, Yong; XU, Yide; XIN, Qin; SHEN, Wenjie. The role of Sn in Pt–Sn/CeO 2 catalysts for the complete oxidation of ethanol. *Journal of Molecular Catalysis A: Chemical*. 2005, vol. 235, no. 1, pp. 122–129.

160. MILITELLO, Maria C.; SIMKO, Steven J. Palladium Oxide (PdO) by XPS. *Surface Science Spectra*. 1994, vol. 3, no. 4, pp. 395–401. Available from DOI: 10.1116/1.1247784.

161. ANTOLINI, Ermete. Palladium in fuel cell catalysis. *Energy Environ. Sci.* 2009, vol. 2, pp. 915–931. Available from DOI: 10.1039/B820837A.

162. PAPAGEORGOPOULOS, DC; KEIJZER, M; VELDHUIS, JBJ; DE BRUIJN, FA. CO Tolerance of Pd-Rich Platinum Palladium Carbon-Supported Electrocatalysts Proton Exchange Membrane Fuel Cell Applications. *Journal of the Electrochemical Society*. 2002, vol. 149, no. 11, pp. A1400–A1404.

163. MAŠEK, K.; BLUMENTRIT, P.; BERAN, J.; SKÁLA, T.; PÍŠ, I.; POLÁŠEK, J.; MATOLÍN, V. Structural and electronic studies of supported Pt and Au epitaxial clusters on tungsten oxide surface. *Vacuum*. 2012, vol. 86, no. 6, pp. 586–589. ISSN 0042-207X. Available from DOI: https://doi.org/10.1016/j.vacuum.2011.07.021. 13TH Joint Vacuum Conference, Štrbské Pleso, Slovakia, June 20-24, 2010 organized by the Slovak Vacuum Society in collaboration with the Vacuum Societies of Austria, Croatia, Czech Republic, Hungary and Slovenia.

164. DUBAU, Martin; LAVKOVA, Jaroslava; KHALAKHAN, Ivan; HAVIAR, Stanislav; POTIN, Valerie; MATOLIN, Vladimír; MATOLINOVA, Iva. Preparation of magnetron sputtered thin cerium oxide films with a large surface on silicon substrates using carbonaceous interlayers. *ACS applied materials & interfaces*. 2014, vol. 6, no. 2, pp. 1213–1218.

165. HAVIAR, Stanislav; DUBAU, Martin; LAVKOVA, Jaroslava; KHALAKHAN, Ivan; POTIN, Valerie; MATOLIN, Vladimir; MATOLINOVA, Iva. Investigation of Growth Mechanism of Thin Sputtered Cerium Oxide Films on Carbon Substrates. *Science of Advanced Materials*. 2014, vol. 6, no. 6, pp. 1278–1285.

166. YUAN, Xiaozi; WANG, Haijiang; SUN, Jian Colin; ZHANG, Jiujun. AC impedance technique in PEM fuel cell diagnosis—A review. *International Journal of Hydrogen Energy*. 2007, vol. 32, no. 17, pp. 4365–4380. ISSN 0360-3199. Available from DOI: http://dx.doi.org/10.1016/j.ijhydene.2007.05.036. Fuel Cells.

167. DAIO, Takeshi; STAYKOV, Aleksandar; GUO, Limin; LIU, Jianfeng; TANAKA, Masaki; LYTH, Stephen Matthew; SASAKI, Kazunari. Lattice strain mapping of platinum nanoparticles on carbon and SnO2 supports. *Scientific reports*. 2015, vol. 5.

168. CHIANG, Yu-Chun; LIANG, Chia-Chun; CHUNG, Chun-Ping. Characterization of Platinum Nanoparticles Deposited on Functionalized Graphene Sheets. *Materials*. 2015, vol. 8, no. 9, pp. 6484–6497.

169. YANO, Hiroshi; INUKAI, Junji; UCHIDA, Hiroyuki; WATANABE, Masahiro; BABU, Panakkattu K; KOBAYASHI, Takeshi; CHUNG, Jong Ho; OLDFIELD, Eric; WIECKOWSKI, Andrzej.
Particle-size effect of nanoscale platinum catalysts in oxygen reduction reaction: an electrochemical and 195 Pt EC-NMR study.
Physical Chemistry Chemical Physics. 2006, vol. 8, no. 42, pp. 4932–4939.

170. BI, Feifei; HOU, Kun; YI, Peiyun; PENG, Linfa; LAI, Xinmin.
Mechanisms of growth, properties and degradation of amorphous carbon films by closed field unbalanced magnetron sputtering on stainless steel bipolar plates for {PEMFCs}. *Applied Surface Science*.
2017, vol. 422, pp. 921–931. ISSN 0169-4332.
Available from DOI: https://doi.org/10.1016/j.apsusc.2017.06.122.

171. JOHANEK, V.; OSTROVERKH, A.; FIALA, R.; REDNYK, A.; MATOLIN, V.
Mass Spectrometry of Polymer Electrolyte Membrane Fuel Cells.
J. Anal. Methods Chem. 2016, vol. 2016, no. 9, pp. 6097285. ISSN 2090-8865.
Available from DOI: 10.1155/2016/6097285.

172. DUBAU, M.; LAVKOVA, J.; KHALAKHAN, I.; HAVIAR, S.; POTIN, V.; MATOLIN, V.; MATOLINOVA, I.
Preparation of Magnetron Sputtered Thin Cerium Oxide Films with a Large Surface on Silicon Substrates Using Carbonaceous Interlayers.
ACS Appl. Mater. Interfaces. 2014, vol. 6, no. 2, pp. 1213–1218.
ISSN 1944-8244. Available from DOI: 10.1021/am4049546.

173. KIM, Jutae; LEE, Junhee; TAK, Yongsug.
Relationship between carbon corrosion and positive electrode potential in a proton-exchange membrane fuel cell during start/stop operation.
Journal of Power Sources. 2009, vol. 192, no. 2, pp. 674–678.
ISSN 0378-7753. Available from DOI:
http://dx.doi.org/10.1016/j.jpowsour.2009.03.039.

174. CASTANHEIRA, Luis; SILVA, Wanderson O.; LIMA, Fabio H.B.; CRISCI, Alexandre; DUBAU, Laetitia; MAILLARD, Frederic.
Carbon Corrosion in Proton-Exchange Membrane Fuel Cells: Effect of the Carbon Structure, the Degradation Protocol, and the Gas Atmosphere.
ACS Catalysis. 2015, vol. 5, no. 4, pp. 2184–2194.
Available from DOI: 10.1021/cs501973j.

175. FIALA, R; MATOLINOVA, I; MATOLIN, V; SEVCIKOVA, K; YOSHIKAWA, H; TAPAN, A.
Electro-Oxidation Activity of Pt-CeOx Carbon Supported Catalysts.
Int. J. Electrochem. Sci. 2013, vol. 8, pp. 10204–10218.

176. XAFS.ORG. *Community site for x-ray absorption fine-structure (XAFS) and related spectroscopies*. 2016. Available also from: http://xafs.org/.
[Online; accessed 19-June-2016].

177. ZHANG, Jing; WU, Ziyu; LIU, Tao; HU, Tiandou; JU, X.
XANES study on the valence transitions in cerium oxide nanoparticles.
Journal of synchrotron radiation. 2001, vol. 8, no. 2, pp. 531–532.

178. MASUDA, Takuya et al.
Role of Cerium Oxide in the Enhancement of Activity for the Oxygen Reduction Reaction at Pt–CeO x Nanocomposite Electrocatalyst-an in Situ Electrochemical X-Ray Absorption Fine Structure Study.
The Journal of Physical Chemistry C.
2012, vol. 116, no. 18, pp. 10098–10102.

179. HYDE, Timothy I; ASH, Peter W; BOYD, David A; RANDLSHOFER, Gabriele; ROTHENBACHER, Klaus; SANKAR, Gopinathan.
X-ray absorption spectroscopic studies of platinum speciation in fresh and road aged light-duty diesel vehicle emission control catalysts.
Platinum Metals Review. 2011, vol. 55, no. 4, pp. 233–245.

180. BUNLUESIN, T.; GORTE, R.J.; GRAHAM, G.W.
Studies of the water-gas-shift reaction on ceria-supported Pt, Pd, and Rh: Implications for oxygen-storage properties.
Applied Catalysis B: Environmental. 1998, vol. 15, no. 1, pp. 107–114. ISSN 0926-3373. Available from DOI: http://dx.doi.org/10.1016/S0926-3373(97)00040-4.

181. LIU, Zongyuan et al.
Ambient pressure XPS and IRRAS investigation of ethanol steam reforming on Ni-CeO2(111) catalysts: an in situ study of C-C and O-H bond scission.
Phys. Chem. Chem. Phys. 2016, vol. 18, pp. 16621–16628.
Available from DOI: 10.1039/C6CP01212D.

182. MATOLIN, V. et al.
Water interaction with CeO2(111)/Cu(111) model catalyst surface.
Catalysis Today. 2012, vol. 181, no. 1, pp. 124–132. ISSN 0920-5861.
Available from DOI: https://doi.org/10.1016/j.cattod.2011.05.032.
Frigyes Solymosi's special issue Planar Model System and Heterogeneous Catalysis.

183. MORI, Toshiyuki; OU, Ding Rong; ZOU, Jin; DRENNAN, John.
Present status and future prospect of design of Pt–cerium oxide electrodes for fuel cell applications.
Progress in Natural Science: Materials International.
2012, vol. 22, no. 6, pp. 561–571.

184. FUGANE, Keisuke et al. Activity of oxygen reduction reaction on small amount of amorphous CeO x promoted Pt cathode for fuel cell application.
Electrochimica Acta. 2011, vol. 56, no. 11, pp. 3874–3883.

List of Tables

List of Abbreviations

a-C	*Amorphous Carbon*
AEI	*Anion Exchange Ionomer*
AFM	*Atomic Force Microscopy*
BEs	*Binding Energies*
CF	*Carbon Foil*
CIL	*Carbon Ionomer Nanoporose Layer*
CN_x	*Carbon Nitride*
CSS	*Cascading Style Sheet*
CV	*Cyclic Voltammetry*
DFT	*Density Functional Theory*
DMF	*Dimethylformamide*
DMFC	*Direct Methanol Fuel Cell*
DWV	*German Hydrogen And Fuel Cell Association*
ECSA	*Electrochemically Active Surface Area*
EIS	*Electrochemical Impedance Spectroscopy*
FC	*Fuel Cell*
FCHEA	*Fuel Cell And Hydrogen Energy Associatio*
FIB	*Focus Ion Beam*
GDL	*Gas Diffusion Layer - Carbon Paper*
GEIS	*Galvanostatic Electrochemical Impedance Spectroscopy*
GHGs	*Green House Gases*
HOR	*Hydrogen Oxidation Recation*
HRTEM	*High Resolution Transmission Microscopy*
HTML	*HyperText Markup Language*
IV	*Current–voltage Characteristic*
jQuery	*Cross-platform JavaScript Library*
LH_2	*Liquid Hydrogen*
LOHC	*Liquid Organic Hydrogen Carrier*
MCFC	*Molten Carbonate Fuel Cell*
MEA	*Membrane Electrode Assembly*
MPL	*Micro-Porous Carbon-based Layer*
MWCNT	*Multi-Walled Carbon Nanotubes*
NEXAFS	*Near Edge X-ray Absorption Fine Structure*
nGDL	*Gas Diffusion Layer With Carbon Nano Porous Layer*
NHA	*National Hydrogen Association*
NPs	*Nanoparticles*
OCV	*Open Circuit Voltage*
ORR	*Oxygen Reduction Reaction*
PD	*Power Density*
PEEK	*Polyether Ether Ketone*
PEFC	*Proton Exchange Fuel Cell*
PEIS	*Potentiostatic Electrochemical Impedance Spectroscopy*
PEM	*Proton Exchange Membrane* or *Polymer Exchange Membrane*
PEM EL	*Polymer Electrolyte Membrane Electrolysis*
PEM FC	*Proton Exchange Membrane Fuel Cell*

PES	*Photoelectron Spectroscopy*
PETM	*Paleocene–Eocene Thermal Maximum*
PHP	*Hypertext Preprocessor*
PTFE	*Polytetrafluorethylen*
rGO	*Reduced Graphene Oxide*
sccm	*Standard Cubic Centimeters Per Minute*
SEM	*Scanning Electron Microscopy*
SOFC	*Solid Oxide Fuel Cell*
SP	*Specific Power*
Stoich	*Stoichiometry*
TEM	*Transmission Electron Microscopy*
TPI	*Triple Phases Interface*
UHV	*Ultra-high Vacuum*
UPD	*Uderpotential Deposition*
USFCC	*U.S. Fuel Cell Council*
XANES	*X-ray Absorption Near Edge Spectroscopy*
XPS	*X-ray Photoelectron Spectroscopy*
XRD	*X-ray Diffraction*

VII Attachments

Att: PEM FC Stack

In the figure 19.1 the 3D model of PEM FC stack of our design is presented. The disassembled stack for better imagination is shown in the figure 19.2.

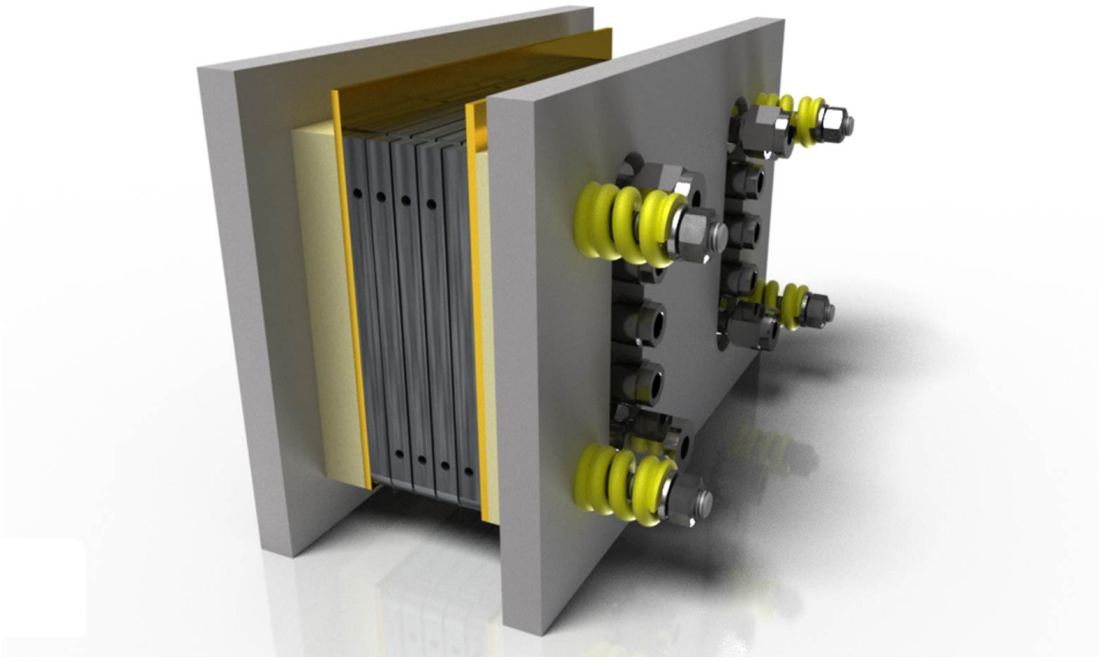

Fig. 19.1: 3D model the PEM FC stack of our design.

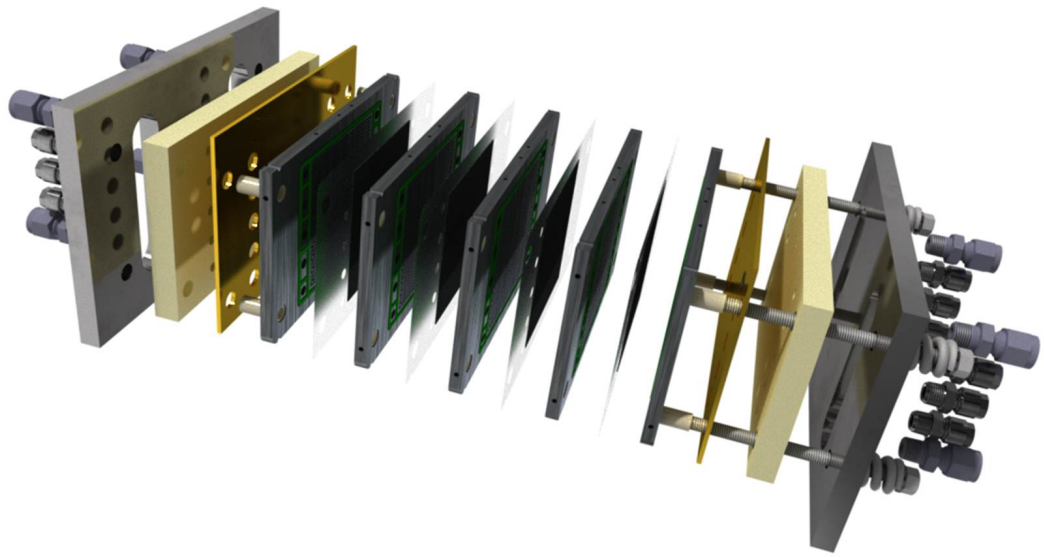

Fig. 19.2: 3D model disassembled PEM FC stack of our design.

Att: New Laboratory

In the figure 19.3 view of 3D model and the final photography of real laboratory which is build on base of technical proposal is shown in the figure 19.4. In the left room is ten new test station organized in two lines and in the right room is central gas distribution of stored gases. There are two 50 L pressure bottles for hydrogen, two pressure bottles for oxygen and two pressure bottles for nitrogen and a spare one for additive gas. The compressed air instead of oxygen can be easy used by manual valve. In the figure next figures are simplified technical drawings of proposal of new laboratory. Apart from the technical room and room with FC test stations there is the control room.

Fig. 19.3: 3D view of laboratory.

Fig. 19.4: A photography of real laboratory.